Functional Dynamics

The relations between dynamics and function studied in yeast cells and bacterial colonies

Sune Danø

Department of Chemistry
H.C.Ørsted Institute
University of Copenhagen

February 2003

Dissertation submitted for obtaining
the Danish Ph.D. degree in chemistry.

Advisors *Assoc. prof. Preben Graae Sørensen*
Chemistry Laboratory III, Dept. of Chemistry,
University of Copenhagen

Assoc. prof. Finn Hynne
Chemistry Laboratory III, Dept. of Chemistry,
University of Copenhagen

To Charlotte

Thank you for making this possible

Preface

This dissertation contains a large part of my research during the last three years. Most of it has been carried out at the University of Copenhagen in the research group of Finn Hynne and Preben Graae Sørensen. A number of people make this a good research group. In particular, I would like to thank Mads Madsen for our fruitful collaboration during the last year. I also owe a lot to Torben Hansen and Aage Nissen; not only for their technical skills but also for being such nice persons. The same goes for Morten Garkier Hendriksen who makes all the computers work. It goes without saying that Preben Graae Sørensen and Finn Hynne have a huge share in my work. Thank you both for all your advise!

Merete Torpe and Malene Zent provided good help in the lab, and my fellow students Anders Bisgaard, Morten Garkier Hendriksen, Mads Madsen, Nicolas Markadieu, Antonio Pons Rivero, Jesper Schmidt and Henrik Skødt made life in the group fun and pleasant.

Silvia De Monte and Francesco d'Ovidio in the group of Erik Mosekilde at the Technical University of Denmark have been invaluable collaborators in our effort to understand the synchronization problems of yeast and in general. It is my hope that we can continue this work in the future.

Together with Kasper Dyring-Andersen, I studied bacterial pattern formation in the laboratory of Prof. James A. Shapiro at the University of Chicago. Kasper, I think we had a great time. I am sorry that you are no longer doing science. Chr. Hansen Holding A/S and the Denmark-America Foundation provided economical support for the research. I am thankful for this support as well as for the hospitality which we were offered by Jim and Joan Shapiro during our stay in Chicago. This research work is still in progress; thank you Thomas Mair and Mads Ipsen for your contributions.

I spent quite some time at the Panum NMR center, and even though this part of my work has not yet made it into print, then I would still like to thank Ib Therkelsen for all the fun I had there.

Sune Danø
Copenhagen, February 2003

Contents

1
Functional dynamics

Dynamics is an integral part of the function of most biological systems. Obvious examples include cell division, morphogenesis, circadian rhythms, nervous activity, muscle contractions, the constant remodelling of the cytoskeleton as well as calcium oscillations and waves in response to hormones. Nevertheless, it is still custom to investigate and describe systems on the mechanistic level rather than on the system level.

There are several reasons why this is so. To some extent it is a matter of tradition. Modern biology has strong bonds to physics and chemistry, and these bonds favour the reductionistic approach as exemplified by the huge interests in genomics and structural biology. The reason for this is mainly historical, as the adoption of quantitative physical and chemical methods in the middle of the 20th century led to the enormous success of contemporary biology. Molecular biology was born from this process, which also has provided numerous important advances in medicine, medical technology and biotechnology.

Another aspect, which favours a mechanistic approach to problems in life science, is commercial interests. In this regard it is essential to be able to take out a patent on a discovery, and this is of course much less complicated if some well defined physical entity is the subject of the patent application.

Despite this, my thesis can be viewed as a case for a strategy which I have termed "Functional Dynamics". In essence, functional dynamics is the idea to utilise dynamics to learn about function[1]: Suppose you want to find out how a car engine works. A complete parts list – maybe even supplemented with a table indicating the effects of removing each of these parts – might not be of

[1]Similar ideas are discussed by Hess *et al.* (1969).

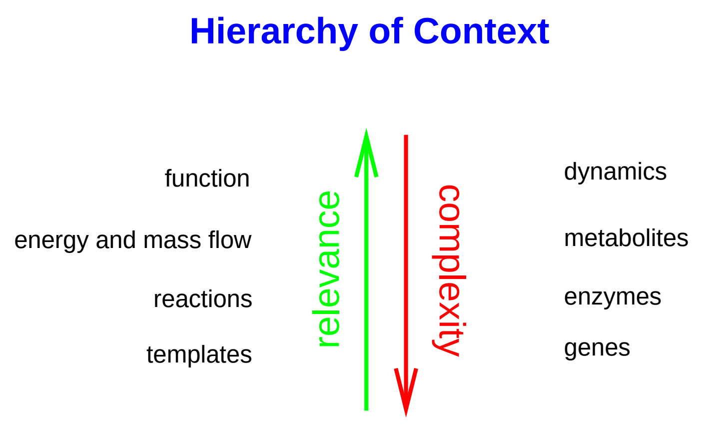

Figure 1.1: Hierarchy of context in cell physiology. See text for discussions.

much help, whereas just watching the engine while it is running will give you a good idea of the main features.

The rationale why this should be analogous to the understanding of cell biology is illustrated by the hierarchy of context in Fig. 1.1. The cell has a number of functions by which it fulfils a purpose[2]. If we want to understand *how* the cell fulfils this purpose, then these functions will be at the top of the contextual hierarchy. In most cases, the function is related to the behaviour of the cell, and thus the cellular dynamics will be the manifestation of the function. The cellular functions are driven by flows of mass and energy, and the manifestation of this is metabolism. The basis for this is the chemical reactions of the cell, which are almost exclusively catalysed by enzymes. The genes, at the bottom of our hierarchy, are merely the templates of these proteins. The striking feature of this hierarchy is that as the functional relevance decreases, the complexity increases. This can be made explicit by considering the yeast *Saccharomyces cerevisiae*, which is the organism under study in most of this thesis. This organism was one of the first eukaryotes to have its

[2] A phenomenon serves a purpose when it contributes to the replication, development or maintenance of the organism.

genome sequenced, and it was found to contain about 6000 genes (Goffeau *et al.*, 1996). This is more than 10 times the number of metabolites, which is estimated to be just below 600. These numbers indicate that even though it is by no means easy to relate function and metabolism, it is an easy puzzle compared to the immense challenge of linking genes and function. Therefore, if we want bridge the gap in understanding between function and mechanism, we should concentrate on the upper part of the hierarchy, since not only is the complexity lower at these levels of description, the gap itself is also much smaller. Again, this can be made more concrete by considering the yeast cell. Here most metabolites have some functional association, whereas some 3000 genes are “ORFans” meaning that their sequence has no homology to any other gene with known function (Dujon, 1996). Thus, these genes are identified in terms of their existence, but not in terms of their function.

These facts are well known and, accordingly, the focus in biochemistry is changing from “genomics” to “proteomics”. Probably, a shift further up the hierarchy to “metabolomics” will follow as soon as high through-put techniques become available. In contrast to this development, dynamics is hardly ever considered in the functional analysis. The idea behind functional dynamics is to make this level accessible by using nonlinear dynamics as a tool for quantitative biochemistry. Of course, nonlinear dynamics is used heavily in the modelling of biochemical systems, but these models are usually simplistic models where the purpose is to obtain a simple model with qualitative correspondence between model and experiment. Thus, these models are meant to be explanatory models, whereas the work presented in chapters 3 and 5 aims at obtaining descriptive models than can account quantitatively for as many experimental facts as possible.

Clyde Tombaugh’s discovery of the planet Pluto in 1930 is an excellent example of the usefulness of descriptive, quantitative models for obtaining mechanistic details. The laws of Newton were discovered in an attempt to explain the planetary motions, so the qualitative understanding of the planetary motions had been there for more than 200 years. However, it was then observed that these laws could not account quantitatively for the motion of the known planets. A search for a trans-Neptunian planet was initiated, and this lead to the discovery of Pluto.

1.1 Experimental systems

Now, since this is not a philosophy thesis, the functional dynamics approach for biochemistry should be tested experimentally. The test system will be yeast glycolysis, and in particular oscillations in the metabolite concentrations that can be observed during glycolysis. This is a well suited test system since yeast glycolysis is particularly well understood, simple to work with, and the dynamics are conveniently monitored by fluorescence. Moreover, a complete mathematical terminology, which is well suited for the description of the dynamics, exists.

The experimental system will be described in detail in chapter 4, and the mathematical concepts will be outlined in chapter 2. Chapter 3 describes a new method for the construction of quantitative, realistic, mathematical models of (bio)chemical systems, and this method is applied to yeast glycolysis in chapter 5. The resulting model is analysed in the following chapter, and in chapter 7 we extend the analysis to the cell synchronization problem which – even in yeast – is still not resolved.

In the last chapter of the thesis I present experiments on bacterial colonies of the species *Proteus mirabilis*. This bacterial system is special in that it consists of two different cell types; a vegetative type and a type showing collective motility. In this sense, the Proteus system is among the simplest possible multicellular systems. As a result of cell-cell interactions and cell-environment interactions, these colonies form beautiful patterns that can be seen as prototypes for biological pattern formation. By applying functional dynamics to the pattern formation process we have uncovered its phenomenology and assigned different functional roles to different nutritional components. This is one of the first applications of functional dynamics to a living system. It is my sincere hope that this thesis will inspire the readers to more.

2 Complex kinetics

When describing a chemical reaction system, we first want to be able to write down a description of it. Then, we want to be able to answer the question "what is the behaviour of this system?" These issues are the topics of this chapter and, accordingly, it is merely a recapitulation of certain aspects of nonlinear dynamics systems theory, which serve as useful tools for the work presented in the rest of the thesis. Therefore, readers who are familiar with nonlinear dynamics are encouraged to jump ahead to chapter 3. The discussion is not meant to be complete in a strict mathematical sense, nor is it meant to be exhaustive. For more formal and in-depth discussions, the reader is referred to Wiggins (1990), Hale and Kocak (1991) or Perko (1996). The mathematically inclined reader might also consult Guckenheimer and Holmes (1983), whereas readers without a solid mathematical background should start with Strogatz (1994) or just stick with this chapter.

2.1 Describing (bio)chemical reaction kinetics

The first thing to consider is the type of equations to be used for the description of the system. It is by far most convenient to work with a set of ODEs, but it might not always give an adequate description of the system. There are two issue to consider: Is the number of molecules big enough for fluctuations to be averaged out, and is the system spatially homogeneous? The answers to these questions are of course dependent on the system under study, and therefore such considerations will not be made here. Instead, they are postponed until we consider a specific system. For now, we will simply assume that a description in terms of ODEs is suitable. Given this, we can make an explicit description f_s of the changes in concentration c_s for each of the n chemical species s in the reaction system:

$$\begin{aligned}\frac{\mathrm{d}c_1}{\mathrm{d}t} &= f_1(c_1,\ldots,c_n)\\ &\vdots\\ \frac{\mathrm{d}c_n}{\mathrm{d}t} &= f_n(c_1,\ldots,c_n)\end{aligned}$$

or, in a more compact notation

$$\dot{\mathbf{c}} = \mathbf{f}(\mathbf{c}) \tag{2.1}$$

where $\mathbf{c}$ and $\mathbf{f}$ are n dimensional vectors, and the dot denotes differentiation. The vector $\mathbf{c}$ describes a point in concentration space, and the solution of the vector field defined by $\mathbf{f}$ is called the flow of the system.

For our purpose of linking the dynamic and the mechanistic description, this formalism is particularly useful, because the stoichiometry and reaction mechanisms of the system can be expressed through $\mathbf{f}$. By writing f_s as a sum of contributions from the different reactions involving s we can rewrite Eq. 2.1 as

$$\frac{\mathrm{d}c_s}{\mathrm{d}t} = \sum_r \nu_{sr} v_r \quad \text{or in matrix notation} \quad \dot{\mathbf{c}} = \boldsymbol{\nu}\cdot\mathbf{v} \tag{2.2}$$

where v_r is the velocity of reaction r and ν_{sr} is the stoichiometric coefficient of species s in reaction r. Likewise, the functional form of v_r can be chosen to reflect some mechanistic understanding of the reaction r. For example, one could choose $v_r = \frac{V_{\mathrm{max}}[\mathrm{S}]}{K_{\mathrm{m}}+[\mathrm{S}]}$ in order to express that a single-substrate enzymatic reaction is irreversible and follows Michaelis-Menten kinetics.

At this point it should be noted that although this is the principle for describing chemical reaction systems, this is in practice not the usual approach when biochemical systems are modelled. Instead, most species and reactions are ignored "for the sake of simplicity" and only a few "essential" components are retained. The obvious advantage of this is, indeed, the simplicity of the model which allows for conclusive analysis to be made. If the purpose of the modelling is to give a phenomenological explanation of an experimental observation, then this is a very effective approach which has often proved successful.

However, there are problems related to this approach. First, it is only in very rare cases that there is a clear cut way of deciding which components are essential and which are not. Moreover, if one has no quantitative framework for making this decision, it will necessarily be based on the intuition of the modeller, and therefore the model should be viewed more as a hypothesis about the system than a description of it. Secondly, if a few well-defined essential components cannot be identified, then the variables c_s of the simple model should more be thought of as "pools" of species sharing the same functional roles, and, accordingly, the reactions v_r should be thought of as more or less unphysical reactions relating these pools. These considerations are exceptionally clear in the classical modelling paper by Sel'kov (1968). Nevertheless, this has not held his successors from overdoing the interpretation of such simple models.

2.2 Dynamics

The analysis of the persistent behaviour of a dynamical system is based on its *stability*. We will first be concerned with the stability of a stationary state of the system towards small perturbations, and then analyse the system as parameter changes lead to changes in stability.

2.2.1 Stationary states

A stationary state $\mathbf{c}^\mathrm{s}$ is simply a state of the system which does not change in time:

$$\mathbf{f}(\mathbf{c}^\mathrm{s}) = \mathbf{0}. \tag{2.3}$$

The dynamics of such a stationary state are trivially simple, and any real, closed chemical system has at least one stationary state, namely chemical equilibrium. A stationary state is not very expressive, but it is nevertheless a very nice starting point for the analysis of a dynamical system, since it can be treated in terms of simple mathematics. Consider the effect of a small perturbation to a system in the state $\mathbf{c} = \mathbf{c}^\mathrm{s}$: heuristically, the state of the system will either decay back to $\mathbf{c}^\mathrm{s}$ or diverge, and in both cases the response can be fast, moderate or slow compared to some relevant timescale. We will now formalise the idea that the system will either return to $\mathbf{c}^\mathrm{s}$ or not, and postpone the question of timescales to section 2.2.2.

A stationary state is said to be *asymptotically stable* if there exists a constant $b > 0$ such that, if $|\mathbf{c}(t_0) - \mathbf{c}^\mathrm{s}| < b$, then $\lim_{t\to\infty} |\mathbf{c}(t) - \mathbf{c}^\mathrm{s}| = 0$. A system that is not stable is said to be *unstable*. With this definition, we are concerned with the longterm effects of infinitesimal perturbations, so the obvious way to make this definition operational is to consider the Taylor expansion of $\mathbf{f}$ around $\mathbf{c}^\mathrm{s}$. This is most practical to do if we first make a change in coordinates so that only the derivations from $\mathbf{c}^\mathrm{s}$ are considered: $\mathbf{x} = \mathbf{c} - \mathbf{c}^\mathrm{s}$. Since $\dot{\mathbf{x}} = \dot{\mathbf{c}} - \dot{\mathbf{c}^\mathrm{s}} = \dot{\mathbf{c}} = \mathbf{f}(\mathbf{c})$, the Taylor expansion reads

$$\dot{\mathbf{x}} = \mathbf{J} \cdot \mathbf{x} + O(\mathbf{x}^2) \tag{2.4}$$

where $J_{ij} = \left.\frac{\partial f_i}{\partial x_j}\right|_{\mathbf{c}=\mathbf{c}^\mathrm{s}}$ are the components of the Jacobian matrix. In most cases, the linearised dynamics in Eq. 2.4 give a good description of the system behaviour (see below). Since Eq. 2.4 is linear, it is conveniently analysed in terms of its eigenvalues λ_i and the associated eigenvectors $\mathbf{e}_i$ defined in term of the eigenvector problem $\mathbf{J}\mathbf{e}_i = \lambda_i \mathbf{e}_i$ with $\mathbf{e}_i \neq \mathbf{0}$. Shortly, we will also need the left eigenvectors $\mathbf{e}_i^*$ defined in terms of the transposed eigenvector problem $\mathbf{e}_i^* \mathbf{J} = \lambda_i \mathbf{e}_i^*$, $\mathbf{e}_i^* \neq \mathbf{0}$. If $\mathbf{J}$ has n linearly independent eigenvectors, then $\mathbf{J}$ can be diagonalized, and, as I will show now, the system can then be analysed in terms of n uncoupled modes, each corresponding to the motion along an eigenvector (but see below for complex eigenvalues). This is the case for most ODEs describing real systems. The diagonalization has the following form:

$$\mathbf{J} = \mathbf{U}\mathbf{D}\mathbf{U}^{-1} = \begin{bmatrix} | & & | \\ \mathbf{e}_1 & \cdots & \mathbf{e}_n \\ | & & | \end{bmatrix} \begin{bmatrix} \lambda_1 & 0 & \cdots & 0 \\ 0 & \lambda_2 & \cdots & 0 \\ \vdots & \vdots & \ddots & \vdots \\ 0 & 0 & \cdots & \lambda_n \end{bmatrix} \begin{bmatrix} - & \mathbf{e}_1^* & - \\ & \vdots & \\ - & \mathbf{e}_n^* & - \end{bmatrix},$$

from which it follows that $\mathbf{U}^{-1}\dot{\mathbf{x}} = \mathbf{D}\mathbf{U}^{-1}\mathbf{x}$. By writing this out explicitly as

$$\begin{bmatrix} - & \mathbf{e}_1^* & - \\ & \vdots & \\ - & \mathbf{e}_n^* & - \end{bmatrix} \begin{bmatrix} \dot{x}_1 \\ \vdots \\ \dot{x}_n \end{bmatrix} = \begin{bmatrix} \lambda_1 & 0 & \cdots & 0 \\ 0 & \lambda_2 & \cdots & 0 \\ \vdots & \vdots & \ddots & \vdots \\ 0 & 0 & \cdots & \lambda_n \end{bmatrix} \begin{bmatrix} - & \mathbf{e}_1^* & - \\ & \vdots & \\ - & \mathbf{e}_n^* & - \end{bmatrix} \begin{bmatrix} x_1 \\ \vdots \\ x_n \end{bmatrix} \tag{2.5}$$

we see that the projections $\mathbf{e}_i^* \mathbf{x} = \mathbf{y}_i$ from concentration space on to the eigenvectors $\mathbf{e}_i$ transforms the linearised ODEs to the simple, uncoupled form $\dot{\mathbf{y}} = \mathbf{D}\mathbf{y}$ with the well-known solution $y_i(t) = y_i(0)e^{\lambda_i t}$.

It follows that for each $\lambda_i < 0$ there is an exponential decay towards $\mathbf{c}^\mathrm{s}$ in the direction of the associated eigenvector $\mathbf{e}_i$, so these modes are stable. On the other hand, the flow of the system will diverge exponentially from $\mathbf{c}^{\mathrm{s}}$ in directions $\mathbf{e}_i$ where the corresponding eigenvalues λ_i are positive, and hence these modes are unstable.

In the case of complex eigenvalues $\lambda_i = \alpha + i\beta$ and $\lambda_{i+1} = \overline{\lambda}_i = \alpha - i\beta$ with the associated eigenvectors $\mathbf{v} \pm i\mathbf{w}$, the diagonal matrix now becomes a block-diagonal matrix, and the solution corresponding to these modes is given by

$$\begin{aligned} \mathbf{x}(t) &= ae^{(\alpha+i\beta)t}(\mathbf{v}+i\mathbf{w}) + \overline{a}e^{(\alpha-i\beta)t}(\mathbf{v}-i\mathbf{w}) \\ &= e^{\alpha t}(a(\cos\beta t + i\sin\beta t)(\mathbf{v}+i\mathbf{w}) + \overline{a}(\cos\beta t - i\sin\beta t)(\mathbf{v}-i\mathbf{w})) \end{aligned} \tag{2.6}$$

in concentration space. This describes an elliptical motion with exponentially varying amplitude in the plane spanned by $\mathbf{v}$ and $\mathbf{w}$. The sign of $\mathrm{Re}(\lambda_i) = \alpha$ determines whether the oscillatory motion is towards or away from the stationary state, so the real part of the complex eigenvalues determine the stability whereas the imaginary part of the complex eigenvalues sets the frequency of oscillation.

Topology

The subspace of concentration space spanned by the set of eigenvectors with negative real part of the eigenvalues is called the stable subspace E^s, and the subspace spanned by the eigenvectors with positive real part of the corresponding eigenvalues is known as the unstable subspace E^u. In the case $\mathrm{Re}(\lambda_i) = 0$ there is no first-order term associated with the mode $\mathbf{e}_i$, so the linearised dynamics of Eq. 2.4 are not sufficient to account for the behaviour of the system, and higher-order terms must be taken into account. The eigenvectors with $\mathrm{Re}(\lambda_i) = 0$ form the basis of the center subspace E^c, and the direct sum $\mathbf{R}^n = E^s \oplus E^c \oplus E^u$ spans the entire concentration space. In this context, an important theorem is the Hartman-Grobman theorem, which states that the flow of a nonlinear system, Eq. 2.1, in the neighbourhood of a stationary point $\mathbf{c}^{\mathrm{s}}$ is topologically equivalent to the flow of the linearised system Eq. 2.4, provided that $\mathrm{Re}(\lambda_i)|_{\mathbf{c}^{\mathrm{s}}} \neq 0$ for all i. (A stationary state that fulfils this criterion is said to be hyperbolic). Thus, the qualitative behaviour of any such nonlinear system can be understood by combining the phase portraits of Figs. 2.1, 2.2 and 2.3, and remembering that the stability of each of these modes is given by the real part of the corresponding eigenvalues. The closer to $\mathbf{c}^{\mathrm{s}}$ one gets, the better the agreement between the flow of the linearised dynamics and the full system. Fig. 2.4 shows a phase portrait of a center, an example of a mode with $\mathrm{Re}(\lambda_i) = 0$.

Transformations

From Eq 2.5 it can be seen that $\mathbf{U}^{-1}\mathbf{U} = \mathbf{I}$ from which it follows that the left and the right eigenvectors form a biorthogonal basis: $\mathbf{e}_i^*\mathbf{e}_j = \delta_j^i$. Based on these observations, I will now summarise the transformations between concentration space and the eigenspace of $\mathbf{J}$ as well as the projections from concentration space onto an eigenmode of the system:

$$\begin{array}{rcll} \mathbf{y} & = & \mathbf{U}^{-1}\mathbf{x} & \text{transformation from concentration space to eigenspace} \\ \mathbf{x} & = & \mathbf{U}\mathbf{y} & \text{transformation from eigenspace to concentration space} \\ y_i & = & \mathbf{e}_i^*\mathbf{x} & \text{projection from concentration space onto } \mathbf{e}_i \\ \mathbf{x} & = & \mathbf{e}_i y_i & \text{transformation from } \mathbf{e}_i \text{ to concentration space} \end{array}$$

Similar transformations are found for the kinetics of complex modes (Eq. 2.6). If we denote the complex coordinates in eigenspace by $z = z' + iz''$ and write the complex eigenvector as $\mathbf{u} = \mathbf{v} + i\mathbf{w}$, we have

$$\mathbf{x} = z\mathbf{u} + \overline{z\mathbf{u}}$$

for the transformation from the z coordinates of the oscillatory mode to concentration space, and

$$z = \mathbf{u}^*\mathbf{x}$$

which describes the projection from concentration space onto the plane of the oscillatory mode. (As before, we have $\mathbf{u}^*\mathbf{u} = 1$).

All transformations described here are between concentration space and the space spanned by the eigenvectors of the Jacobian matrix. These eigenvectors give a first order approximation of the dynamical structures of the system. If a more accurate description is needed, then higher-order terms must be included in the transformations. (See Ipsen *et al.* (1998); practical examples are found in Schmidt (2000) and in Table 11 of Hynne *et al.* (2001)).

2.2.2 Bifurcations

We have seen that the stability of a system, and thus its qualitative behaviour, is determined by the sign of the real part of its eigenvalues at least when we are sufficiently close to $\mathbf{c}^{\mathrm{s}}$. Therefore, a change in the qualitative behaviour

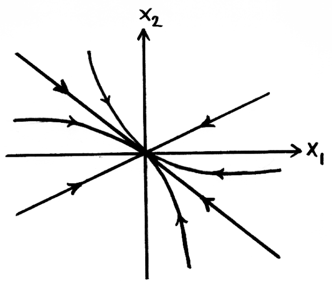

Figure 2.1: A stable node; an example of a hyperbolic stationary point. $E^s = \mathbf{R}^2$.

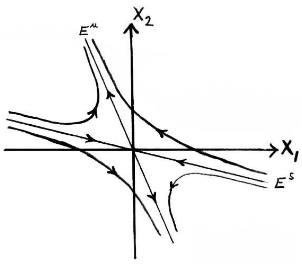

Figure 2.2: A saddle; an example of an unstable hyperbolic stationary point.

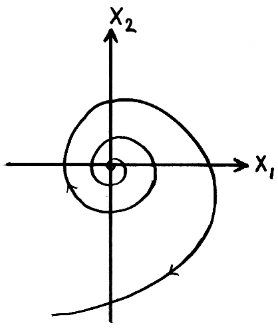

Figure 2.3: An unstable focus; an example of a hyperbolic stationary point. $E^u = \mathbf{R}^2$.

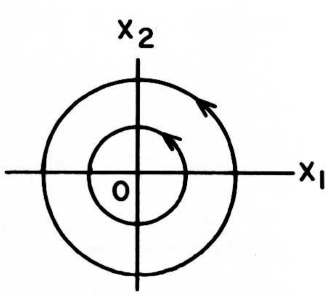

Figure 2.4: A center; an example of neutral stability and therefore a non-hyperbolic stationary point. $E^c = \mathbf{R}^2$. Reproduced from Perko (1996).

is expected when the real part of an eigenvalue changes sign. This is called a bifurcation. As it should be evident from the previous section, such a change in stability can have important consequences for the system under study, and bifurcations are therefore realizable in experiments.

We change the sign of an eigenvalue by changing some parameter of the system. This is expressed by rewriting Eq. 2.1 in the form

$$\dot{\mathbf{x}} = \mathbf{f}(\mathbf{x}, \mu) \tag{2.7}$$

where μ is some parameter of the system: the activity of a specific enzyme, some tunable parameter in the experimental setup, or some other effector which is not in itself a variable of the ODEs.

At the bifurcation point $\mu = 0$ we have $\mathrm{Re}(\lambda) = 0$ for the bifurcating mode, and the system is no longer hyperbolic. Accordingly, it should no longer be analysed solely in terms of its linearised dynamics. For μ values close to 0, $|\lambda|$ of the bifurcating mode will be very small. Physically, this means that the timescale associated with this mode will be much slower than any other timescale of the system, and therefore we can base our analysis of the dynamics on a timescale argument. For this we will consider the case usually encountered, which is that all modes except the bifurcating mode are stable. On the timescale of this mode, all other modes of the system will collapse in the course of a short transient, and the persistent behaviour of the system will then be given by the dynamics of the slow bifurcating mode. Therefore, the dynamics of systems close to a given type of bifurcation are universal: all such systems will show the same kind of dynamics, and this can be described by the same set of low-dimensional equations describing only the dynamics of the slow mode. System specificity enters through the parameters of these equations. (These ideas generalise to cases with more than one bifurcating mode).

The simplest form of the equations describing the dynamics of the slow manifold at a bifurcation is called the *normal form* of that bifurcation. Through *unfolding* of this normal form, we can use the low-dimensional description of the system dynamics not only at the bifurcation point, but also in the neighbourhood of the bifurcation with the distance from the bifurcation point set by the bifurcation parameter μ. See Ipsen (1996), Roberts (1997), Ipsen *et al.* (1998) and Schmidt (2000) for specific details.

The Hopf bifurcation

The Hopf bifurcation plays a major role in the work presented in this thesis, and at the same time it provides an example to illustrate the concepts introduced above. The scenario is the following: A stable stationary point becomes unstable as a pair of complex conjugate eigenvalues crosses the imaginary axis, and a limit cycle emerges around the unstable stationary point. The following conditions apply at a Hopf bifurcation:

- The Jacobian matrix of the stationary state has exactly one set of purely imaginary eigenvalues $\lambda_j = \bar{\lambda}_{j+1} = i\beta_j$. All other eigenvalues have negative real part.
- The transversality condition which states that the complex pair λ_j, λ_{j+1} actually crosses the imaginary axis, *i.e.*

$$\left.\frac{d\mathrm{Re}(\lambda_j)}{d\mu}\right|_{\mu=0} \neq 0$$

- A limit cycle with zero amplitude and frequency $\frac{\beta_j}{2\pi}$ emerges.

To third order the unfolded normal form is

$$\dot{z} = (i\omega_0 + \mu\sigma)z + gz|z|^2 \tag{2.8}$$

where $z = z' + iz''$, $\sigma = \sigma' + i\sigma''$ and $g = g' + ig''$. This equation is known as the *Stuart-Landau equation.* The system has the stationary state $z = 0$, and the Jacobian matrix of the system evaluated at this state is

$$\mathbf{J}|_{z=0} = \begin{bmatrix} \mu\sigma' & -(\omega_0 + \mu\sigma'') \\ \omega_0 + \mu\sigma'' & \mu\sigma' \end{bmatrix}.$$

The eigenvalues of this matrix are $\lambda_\pm = \mu\sigma' \pm i(\omega_0 + \mu\sigma'')$, so the first two conditions are fulfilled as long as $\sigma' \neq 0$ and $\omega_0 \neq 0$. The emergence of a limit cycle can be seen by rewriting the system in polar coordinates $z = re^{i\theta}$:

$$\begin{aligned} \dot{r} &= \mu\sigma' r + g' r^3 \\ \dot{\theta} &= \omega_0 + \mu\sigma'' + g'' r^2. \end{aligned}$$

For $g' < 0$ and $\mu\sigma' \leq 0$ there is only one stationary radius $r = 0$, which is stable. For $\mu\sigma' > 0$ the stationary radius $r = \sqrt{\frac{\mu\sigma'}{-g'}}$ is asymptotically stable whereas $r = 0$ is unstable. Hence, a small-amplitude stable limit cycle with radius $r_{\text{lc}} = \sqrt{\frac{\mu\sigma'}{-g'}}$ and frequency $\omega_{\text{lc}} = \omega_0 + \mu\left(\sigma'' - \frac{g''\sigma'}{g'}\right)$ emerges. This is called a *supercritical Hopf bifurcation* – a graphical presentation is given in Fig. 2.5, which shows the solution diagram and simulations of Eq. 2.8 for five different values of μ.

If the system is just beyond the supercritical Hopf bifurcation, the geometry of its concentration space will be as depicted in Fig. 2.7: the stationary state has an unstable plane which is the unstable subspace E^u. All other $N-2$ directions are stable, so in that sense the stationary state is a saddle point (see Fig. 2.2). The small-amplitude limit cycle is found on the unstable manifold, which can be well approximated by E^u. (The picture generalises to N dimensions with $N > 2$). Small perturbations – here in the form of additions of small amounts of chemicals taking part in the oscillations – can be used to probe the geometry of concentrations space. If a pure substance is added to the system, then the state of the system is shifted in the direction of the axis denoting the concentration of that species. In the general case, there will be exactly one angle of addition (*i.e.* location on the limit cycle) and one amount of added substance that will take the system from the limit cycle on to the stable manifold. This is readily seen from Fig. 2.7. Such a perturbation response is easily recognised in experiments, since it results in a momentary quenching of the oscillations as the state of the system moves along the stable manifold (approximated by E^s) and passes close by the unstable stationary point. Fig. 4.8 shows two such quenchings. In the degenerate case where the stable subspace is parallel to the axis of the added species, one cannot quench the oscillations with this substance. In practise, it is also impossible to quench the oscillations with a species which has its axis almost parallel to the stable subspace. The chemical interpretation is that such species do not affect the oscillations, because the plane of oscillations is orthogonal to these species in concentration space (see Table. 5.8).

The quenching angle and amplitude for a given species can be calculated from the Jacobian matrix of the system, so data from quenching experiments can be used for validation of kinetic models. This is done in chapters 3 and 5. If quenching with all species relevant to the reaction system can be made, then it is possible to calculate a number of properties of the system directly from the quenching data. However, this will generally not be the case for biological systems, since quenchings of cellular oscillations cannot be made with substances that are unable to pass the cell membrane. Quenching experiments

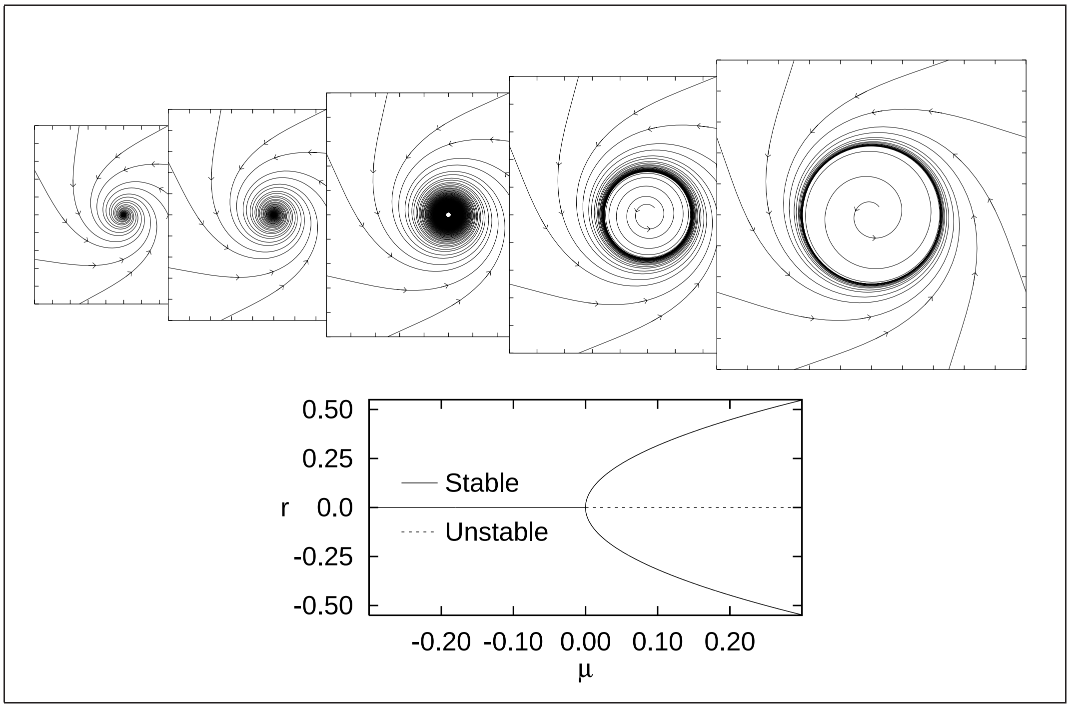

Figure 2.5: Phase portraits of Eq. 2.8 for different values of μ together with the solution diagram for the supercritical Hopf bifurcation. The values of μ in the phase portraits are (from left to right): -0.2, -0.1, 0, 0.1 and 0.2. The other parameters are: $g = 1$, $\sigma = 1$ and $\omega_0 = 1$. The figure is reproduced from Lorenzen (1996).

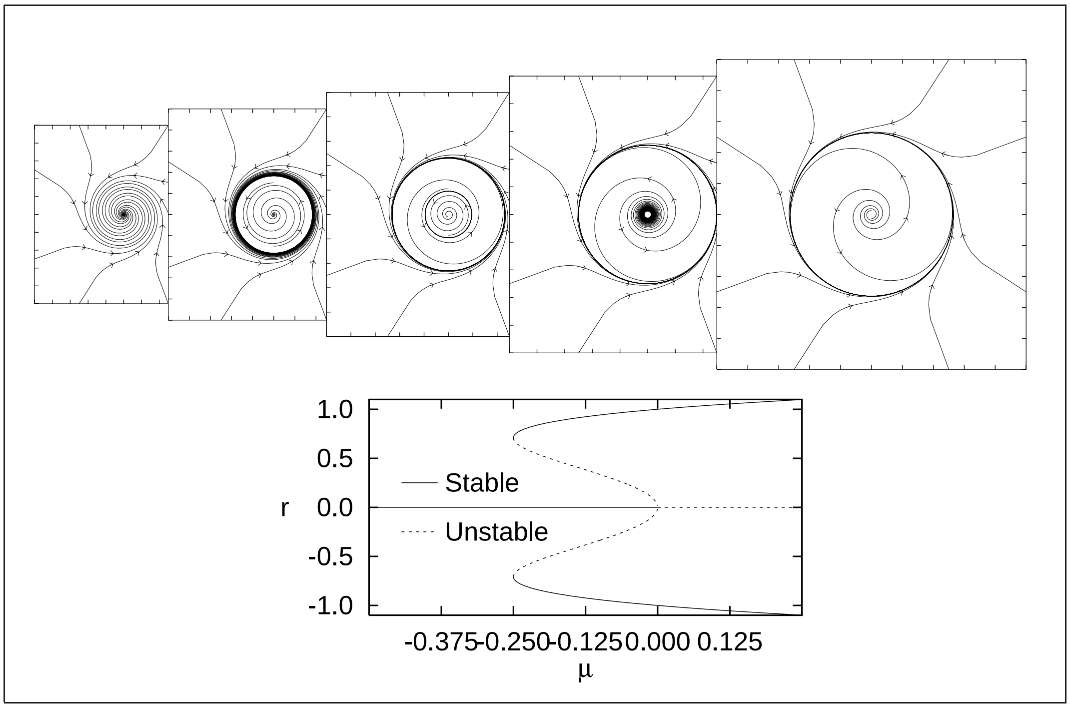

Figure 2.6: Subcritical Hopf bifurcation with a limit cycle stabilised by the fifth order term. Phase portraits for different values of μ together with the solution diagram. The values of μ in the phase portraits are (from left to right): -0.375, -0.25, -0.125, 0 and 0.125. The figure is reproduced from Lorenzen (1996).

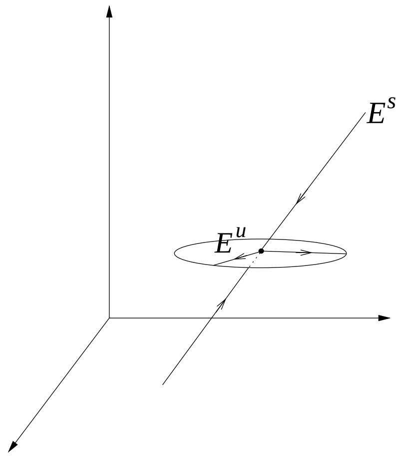

Figure 2.7: A sketch of concentration space close to a supercritical Hopf bifurcation. The limit cycle is the ellipse in the plane spanned by the unstable subspace, and the unstable stationary point (marked by a •) is at the intersection of the stable and the unstable subspace.

with glycolytic oscillations in yeast cells is treated in more detail in Danø (1999). For general quenching theory the reader should consult Hynne *et al.* (1990).

If $\mathrm{Re}(g)$ is positive, then an unstable limit cycle is found for $\mu\sigma' < 0$, and for $\mu\sigma' > 0$ there is only one stationary radius $r = 0$ which is unstable. In this case, one needs to consider higher order terms of Eq. 2.8 in order to describe the persistent behaviour of the system. These terms can give rise to a stable limit cycle, but in this case there will be hysteresis around the bifurcation point, and the state of the system will jump from the stationary point to a large-amplitude limit cycle when the bifurcation parameter is changed so that the sign of $\mu\sigma'$ becomes positive (Fig. 2.6). Therefore, experimental solution diagrams (Figs. 4.6 and 4.7) will clearly show whether a Hopf bifurcation is supercritical or subcritical.

3

The direct method of optimization

In this chapter I will present "The Direct Method of Optimization" which is a method for constructing realistic, (bio)chemical models in quantitative agreement with experiments. The method is primarily developed by one of my supervisors, Finn Hynne. Our application of the method to a real biochemical system is the topic of chapter 5; the purpose of the present chapter is merely to present the method as already described in Hynne *et al.* (1993a,b).

It is important to realise that the direct method is not a fitting algorithm *per se*. Instead, it is a strategy for doing a brute force search in parameter space in an intelligent way. The method takes advantage of the inherent simplicity of stationary states which allows models properties for a given set of parameters to be validated against experimental findings through algebraic calculations. Therefore, a point in parameter space can be validated without the need for newton iterations to locate stationary states or numerical integrations of ODEs. This makes the direct method at least two orders of magnitude faster than the methods usually used.

3.1 The aim of the modelling

A few considerations about the aim of the modelling will be made before introducing the direct method. Generally, three types of models exist:

- *Explanatory models* where the purpose of the modelling is to construct a model which explains a given phenomenon. Occam's Razor is often applied in this context: Entia non sunt multiplicanda praeter necessitatem. (Latin for "Entities should not be multiplied more than necessary"). That is, if two possible explanations exist, the simplest one will be preferred. An example of an explanatory model in line with the topics of this thesis would be a model explaining the occurrence of metabolic oscillations in glycolysis in a simple and unambiguous way (Sel'kov, 1968).

- *Predictive models* are meant to predict in the sense that they should foretell properties which are not already known. In the physics community, the predictive power of a model is often taken as a measure of how good the model is. If a model can be made very simple while retaining its predictive power, it is concluded that the model describes the essential features of the system under study. A law of nature can be seen as a simple, predictive model which is generally applicable and which has not been falsified. Another example would be to model planets as a spheres. This predicts that you would end up at your starting place if you walk straight ahead and continue for long enough; the conclusion drawn from Magellan's circumnavigation of the Earth (1480-1521) would be that it is essentially a sphere. The phenomenological model which we propose for the circularity of the bacterial patterns in chapter 8 is an example of a simple predictive model.

- *Descriptive models* (or "realistic models") contrast the two previous categories of models in that simplicity is not a goal in itself. Instead, a descriptive model should be as accurate as possible in describing a given phenomenon, and the description should preferably be in mechanistic terms. Obviously, descriptive models are often both very detailed and very specific. As a descriptive model of the Earth, a sphere would not suffice; one would need to draw a detailed map indicating oceans, mountains, countries, cities etc. This globe would now be specific in the sense that it would no longer be a good model of, say, Mars. Descriptive models are often of great practical value, *e.g.* flight simulators for the training of pilots or pigs used as substitutes for humans in experimental surgery. They can even be useful for making predictions. An example of this is atmospheric models for weather forecasts.

The direct method is intended for the construction of descriptive, mathematical models of (bio)chemical reaction systems where large amounts of experimental data is available. The aim of the modelling will then be to construct a model which gives a concise, mathematical description of the current knowledge of the reaction system. I other words, the aim will be to obtain a set of ODEs which is in quantitative agreement with all experimental findings of the particular system under study.

The paramount problem of such a task it the so-called "parameter explosion". In order to be able to make comparisons with all experimental findings, the model needs to include the measured species and account for many mechanistic details of the reaction system. This leads to a set of ODEs with a large number of parameters. When searching for the best fit, all possible (although realistic) parameter combinations should in principle be tested. However, the number of combinations increases exponentially with the number of unknown parameters, and this combinatorial explosion makes it impossible to do an exhaustive scan of parameter space within a realistic time even for moderately sized reaction systems: a bold brute force strategy will not work.

3.2 Basic concepts

The direct method offers a pragmatic solution to this problem by decreasing the size of the fitting problem, and by increasing the computational efficiency.

3.2.1 Specification of a model at a stationary state

The size of the fitting problem is decreased be exploiting physical and chemical constraints on the reaction system at a stationary state $\dot{\mathbf{c}} = \mathbf{0}$ (Eq. 2.3). To see how this is done, consider a chemical reaction system as composed of the stoichiometry of its reactions and the kinetics of each of these. The connection between stoichiometry and concentrations is given by Eq. 2.2: $\dot{\mathbf{c}} = \boldsymbol{\nu} \cdot \mathbf{v}$. We work only with the stationary states of the reaction system, and these states can be found from Eq. 2.2 as the null space of $\boldsymbol{\nu}$, which is the space of all vectors $\mathbf{v}$ for which $\boldsymbol{\nu} \cdot \mathbf{v} = \mathbf{0}$. The use of these ideas in chemistry was pioneered by Clarke (Clarke, 1980) in the context of stability of chemical networks. Geometrically, the relevant part of velocity space is a polygonal cone (colloquially: a pyramid of infinite height) extending from origo, and it is generally of lower dimension than the velocity space. (In the modelling presented in chapter 5, the dimension of velocity space is 36, whereas the space of stationary reaction velocities is 16 dimensional). The cone is known as the current cone, and the velocity vectors defining the edges of the cone are known as the extreme currents ("current" is short for stationary velocity). These concepts are illustrated in Fig. 3.1. Any stationary velocity $\mathbf{v}$ can be represented by a point in the current cone and expressed as a linear combination with non-negative coefficients j_i of the extreme currents $\mathbf{E}_i$:

$$\mathbf{v} = \sum_i j_i \mathbf{E}_i, \tag{3.1}$$

a "convex combination". (Hence the name of the coefficients: convex coefficients). This parameterisation can be used to scan over all possible models in all stationary states using a minimum of independent parameters. See Appendix B of Hynne *et al.* (2001) for a brief discussion of redundancy and some considerations regarding the implementation, and see Clarke (1980) chapter II, Section C for proofs and additional technical details.

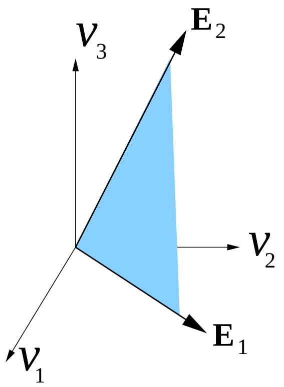

Figure 3.1: Sketch of a two-dimensional current cone in a three-dimensional velocity space. v_1, v_2 and v_3 are the velocities of three reactions, and $\mathbf{E}_1$ and $\mathbf{E}_2$ are the extreme currents defining the edges of the current cone (shaded). These edges appear because all velocities are non-negative. In this fictitious three-reaction system, stationary states are only found on the two-dimensional current cone. The figure is from Hynne *et al.* (2003).

3.2.2 Incorporation of chemical kinetics

Chemical kinetics must be included in the description in order to make it complete. The rate of a chemical reaction r can generally be written as

$$v_r = \kappa_r g_r(\mathbf{c}, \mathbf{K}_r) \tag{3.2}$$

where κ_r is the *velocity parameter* of the reaction, $\mathbf{c}$ is a vector containing the concentrations of the metabolites of the reaction system, and $\mathbf{K}_r$ is a vector containing the *intrinsic parameters* of the reaction (*i.e.* all remaining parameters after the velocity parameter has been factored out). Consider, for example, the Michaelis-Menten rate equation $v = \frac{V_{\max}[\mathrm{S}]}{K_\mathrm{m}+[\mathrm{S}]}$. Here $\kappa_r = V_{\max}$, $g_r = \frac{[\mathrm{S}]}{K_\mathrm{m}+[\mathrm{S}]}$,

$\mathbf{K}_r$ is simply K_m, whereas $\mathbf{c}$ is the concentration vector of the entire reaction system.

The splitting of the parameters into velocity parameters and intrinsic parameters makes it straight forward to take advantage of the possibility to specify stationary velocities from the stoichiometry of the reaction system. We pick a set of stationary velocities $\mathbf{v}$, a set of intrinsic parameters $\mathbf{K}_r$ for each of the reactions, and any set of concentrations $\mathbf{c}$ which we want to become stationary concentrations of the model. From these, we can now calculate the velocity parameters of all the reactions as $\kappa_r = v_r/g_r(\mathbf{c}, \mathbf{K}_r)$. This way we fit one parameter *per reaction* by invoking the stationarity condition, and we also obtain a model which – by construction – has a stationary state with the experimentally determined concentrations and fluxes. This is achieved solely through algebraic operations, which are extremely efficient when compared to the usual fitting procedures involving numeric integration of the kinetic equations or repeated Newton iterations of the rate expressions describing the reaction system. This is the key idea of the direct method, and it is also the origin of its name.

Note that as long as the functional form of the rate equations is known, then a unique model is determined by a set of $\mathbf{K}_r$ for all reactions, a set of stationary velocities $\mathbf{v}$ and a set of stationary concentrations $\mathbf{c}$. We will refer to the three sets together as a *point*.

3.3 Validation of a model at a stationary state

Thus far we have only utilised experimental data on concentrations and fluxes, but we need to be able to exploit any possible kind of experimental information in order not to have vastly under-determined parameters in the fitting. Most properties will be included by means of model validation. That is, for each point the property is calculated from the model and compared with the experimental value. Our brute force fitting strategy is to scan as many points as possible, varying unknown intrinsic parameters, unknown concentrations and unknown fluxes. Each of the resulting points are then validated, and finally the one which is in best agreement with experiments is selected. The remainder of this chapter will explain how this validation is performed in the most efficient way.

Direct comparison

The simplest way to validate a point is to make a direct comparison of the calculated velocity parameters with their experimental values. However, these values are often unknown.

Despite the fact that it is possible to fix all known intrinsic parameters, concentrations and fluxes at their experimental values, it might be desirable to set them to slightly different values in order to obtain a better fit to other properties. Also, ambiguous data might be available, so that one cannot determine precisely what the correct experimental value is. Such comparisons are exemplified by Tables 5.5, 5.7, 5.8 and 5.9. Table 5.5 also serves to exemplify the problem of ambiguous data.

If the stationary state of more than one operating point is well described experimentally, then direct validation could also be used to incorporate this additional, non-local information about the system.

3.3.1 Properties of a stationary state: dynamics and more

When considering only stationary states, one might think that the dynamical properties of the system cannot be included in the parameter fitting. This is, however, not the case. As explained in chapter 2, the local dynamics near a stationary state can be described quite accurately by the linearised kinetics around this state; Eq. 2.4. The Jacobian matrix in this equation can be calculated for any stationary state of a given system. In cases where the velocity parameters are not used for validation, it is advantageous to evaluate the Jacobian matrix as $J_{sp} = \sum_r \nu_{sr} \frac{\partial v_r}{\partial c_p} = \sum_r v_r \nu_{sr} \frac{\partial \ln v_r}{\partial c_p}$ which has no explicit dependence on the velocity parameters, since these disappear as a result of the logarithmic derivation.

The ideal dataset for validation would be a full experimental determination of the elements of the Jacobian matrix. The very general method of "Kinetic spectrometry" (Mihaliuk *et al.*, 1999) will in principle give these data from perturbation experiments, but the method is not yet fully developed experimentally.

The Hopf bifurcation

If the system under study possesses a supercritical Hopf bifurcation, then it is particularly useful to do the optimization at this bifurcation point. Here, in a sense, one has the expressiveness of the oscillatory state and the simplicity of the stationary state at the same time. As already described in chapter 2, the real part of the bifurcating eigenvalue is zero at the bifurcation point, and the imaginary part equals the frequency of the oscillations:

$$\mathrm{Re}(\lambda) = 0, \quad \mathrm{Im}(\lambda) = \omega_0.$$

This immediately yields two additional validation parameters, which can be included in the fitting procedure by calculating the eigenvalues of $\mathbf{J}$ for each point. Since these calculations are fast, they are well suited for a large scale scan of parameter space. In fact it is possible to use a root finding algorithm to limit the search to points which have a Hopf bifurcation at the experimental operating point. An example is found in Tables 5.7 and 5.10.

Stuart-Landau parameters of the Hopf bifurcation

In most cases, the direction and the type of the bifurcation will be known, so at least the signs of the Stuart-Landau parameters σ' and g' can be used in the validation. (The Stuart-Landau equation was introduced in chapter 2). In some experimental settings it will be possible to estimate the value of some of the Stuart-Landau parameters from perturbation experiments (see Fig 4.8). If the experimental setup is well controlled, then it is also possible to measure the dependence of the frequency and the amplitude on the bifurcation parameter. In the neighbourhood of the bifurcation these dependencies are given in terms of the Stuart-Landau parameters:

$$\begin{aligned} r_{\mathrm{lc}} &= \sqrt{\frac{-\sigma'\mu}{g'}} \\ \omega_{\mathrm{lc}} &= \omega_0 + \left(\sigma'' - \frac{\sigma' g''}{g'}\right)\mu. \end{aligned}$$

Even though they cannot be calculated from the Jacobian matrix alone, it is possible to calculate the Stuart-Landau parameters for a given bifurcating stationary state. This is conveniently done by the method described in Ipsen *et al.* (1998). Still, these calculations are rather expensive, and should therefore only be performed for a small subset of points showing a good fit when simpler properties are validated. See Table 5.10 for an example, but note that the high computational costs prohibited the use of Stuart-Landau parameters in the actual fitting described in chapter 5.

Small amplitude oscillations close to a Hopf bifurcation

The unstable subspace $\mathbf{E}^u$ in concentration space is spanned by the complex right eigenvectors $\mathbf{u}$ and $\bar{\mathbf{u}}$ associated with the two complex bifurcating eigenvalues. Sufficiently close to the bifurcation point $\mathbf{E}^u$ gives a good approximation of the plane of oscillations, and therefore the relative amplitudes a_s and phases θ_s of an oscillating chemical species s can be calculated from the corresponding component of $\mathbf{u}$

$$u_s = a_s e^{i\theta_s}.$$

It is feasible to calculate the eigenvectors of $\mathbf{J}$ for a rather large number of points, so each additional species which has been measured during small amplitude oscillations contributes with two additional validation criteria. An example is found in Table 5.8.

Quenching analysis close to a Hopf bifurcation

In analogy with the right eigenvectors associated with the two complex, bifurcating eigenvalues, the corresponding components of the left eigenvectors $\mathbf{u}^*$ and $\bar{\mathbf{u}}^*$ describe the quenching phase ϕ_s and quenching amplitude q_s of species s if the quenching experiments have been made sufficiently close to a supercritical Hopf bifurcation (quenching experiments were briefly discussed in chapter 2; see Hynne *et al.* (1990) for details):

$$u_s^* = -\frac{1}{q_s} e^{i\phi_s}$$

As for the right eigenvectors, the left eigenvectors are feasible to calculate for a large number of points in the scan. Moreover, quenching data is in general easier to obtain experimentally, since the quenching experiments only involves additional well controlled perturbations for each additional species under study. This is in contrast to the direct observation of oscillations of a number of species, which often involves different sophisticated measurements to follow the time course of different chemical species. Table 5.8 exemplifies the use of quenching data in the fitting.

Other possible validation properties

Other validations of stationary states are possible. So, for completeness, I will briefly mention some additional methods. However, we have not worked with validation of these properties in any depth.

In the field of cell metabolism, many experimental studies in the context of metabolic control analysis have been made. Therefore, a lot of MCA data already exist in the literature (see Fell (1997) for an introduction). MCA characterises a stationary state in term of the elasticities $\epsilon_p^{v_i} = \frac{\partial \ln v_i}{\partial \ln p}$ of an enzyme i towards a parameter p (typically, an enzyme activity modulated either by an inhibitor or a change in the concentration of a metabolite) and the control coefficients $C_{v_i}^X = \frac{\partial \ln X}{\partial \ln v_i}$ of an enzyme i on a variable X (typically the flux through the system). These properties are local properties of a stationary state, which could easily be calculated and compared with experimental values for each point in the scan.

Another source of experimental data well suited for the direct method would be Eigen's relaxation method (see *e.g.* Bernasconi (1976)). However, this approach is limited by the problems arising when one tries to extract a number of similar exponential modes from a monotonous decay. An alternative might be found in one or some of the methods discussed in the review by Chevalier *et al.* (1993). These methods are very promising in that they allow a full reconstruction of the Jacobian matrix, but – unlike the method of Kinetic Spectrometry – most of these methods are limited by the requirement that all species of the reaction system should be measured. A very specific property which might be included in the model validation is the cell synchronization property dealt with in chapter 7. Further discussions of this issue can be found there.

Still, many experimental findings can only be incorporated in the validation by direct integration of the ODEs defining a point. This approach is extremely time consuming, and should therefore only be applied at very late stages of the optimization, where points which reproduce all other properties well have been selected. Nevertheless, this approach is sometimes applied as the only way of validating a model (e.g. Rizzi *et al.* (1997)). In some contexts, validation by integration might still be useful since non-local properties (for example in the form of transients following large perturbations) could be included in the fitting. Another possibility for the inclusion of non-local properties would be the use of continuation methods (Kohout *et al.*, 2002) to map out the location of additional known bifurcations of the system.

3.4 Choosing the best fit

A virtue of the direct method is the possibility of including a very broad range of experimental data in the fitting. However, this also raises the question of how to tell which fit is the better, because the different properties are not directly comparable. So, although it is possible to construct a quantitative measure for the “goodness of fit”, one cannot construct an objective measure in a justifiable way. Therefore, the final choice of the parameter set with the best fit is a subjective judgement, which relies on the modeller’s personal understanding of the system and the available experimental data. Moreover, compromises between conflicting interests will unavoidably be needed during the search, so the search itself is to some extent guided by the intuition of the modeller.

4

Glycolytic oscillations in yeast cells

Oscillations in the metabolite concentrations in yeast cells were one of the first biochemical systems where dynamics were studied (Duysens and Amesz, 1957; Chance *et al.*, 1964; Ghosh and Chance, 1964), so a lot of data is already at hand in the literature. Furthermore, glycolysis is probably the biochemical pathway which is best understood (see *e.g.* Mathews and van Holde (1990)). For these reasons, glycolytic oscillations in yeast cells makes a perfect model system for the first application of functional dynamics to a living system. Since so much work has already been made on this system, as well as on the related system of yeast extracts showing glycolytic oscillations, a full account of the available knowledge cannot be made here. Instead, I will limit the description to the experimental findings relevant for the characterisation of the dynamics of the system, and for the modelling of the system described in the following chapter. More work on the oscillatory transients can be found in chapter 6. For additional information about glycolysis and glycolytic oscillations in yeast cells the reader is referred to the theses by Teusink (1999) and Danø (1999) or to the reviews by Hess and Boiteux (1971) and Hess (1979).

4.1 The occurrence of glycolytic oscillations

Glycolytic oscillations are usually observed by adding a pulse of glucose and subsequently a pulse of potassium cyanide to a thick suspension of yeast cells, which have been grown in batch culture and harvested at the point of glucose depletion. This procedure, which I will refer to as a "transient experiment", has become the standard procedure, because the phenomenon is both robust and pronounced when initiated in this simple way (see Fig. 4.1).

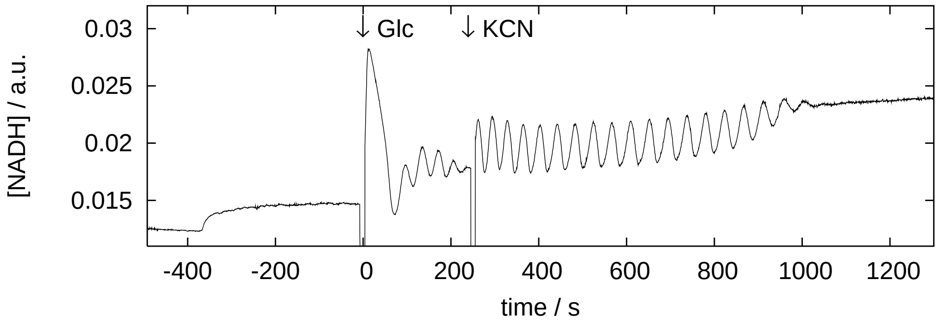

Figure 4.1: A typical transient experiment. At time $t = 0$ glucose was added to a final concentration of 20 mM, and 4 min later KCN was added to a final concentration of 5 mM. The jump in fluorescence just after $t = -400$ s is caused by a transition from aerobic to anaerobic conditions. The initial cell density was 29.2 (mg d.w.)/mL.

4.1.1 Growth and make-up of the yeast cells

In order to be able to study pronounced, long lasting trains of oscillations in intact yeast cells, one must grow and harvest the yeast cells in a rather specific manner. A number of studies have been concerned with the questions involved in this problem; see in particular the papers by Hess and Boiteux (1968), Kreuzberg and Betz (1979) and Richard *et al.* (1993). Hess and Boiteux showed that the oscillations are most pronounced when the yeast cells are harvested at the diauxic shift (*i.e.* at the point of glucose depletion).

In the very thorough study by Kreuzberg and Betz it is shown that starvation increases the amplitude of the oscillations and decreases their frequency. The starvation response is more complex with fructose grown cells than with glucose grown cells. With glucose, there is a saturation effect of the starvation above 2-3 h. The period of the oscillations is also affected by the harvesting point. Fructose generally induces oscillations with a longer period and smaller amplitude than glucose does. In particular, the window of experimental parameters where oscillations are found is smaller for fructose than for glucose. When oscillations are induced with increasing hexose concentrations, a saturation response is seen with glucose, whereas the period is found to change throughout the range of fructose additions, and the amplitude of fructose induced oscillations first increases and then decreases with the amount of hexose added until oscillations are no longer observed.

The relevance of the work on these problems by Richard *et al.* is to remap these findings for a more well defined growth protocol and for oscillations induced by glucose and cyanide addition as opposed to hexose addition after transition to anaerobiosis (see next section). The growth protocol defined in their papers is also used in our experimental work. In short, the yeast cells (*Saccharomyces cerevisiae* x2180) are grown under semi-aerobic conditions in batch culture in Erlenmeyer flasks in a rotary shaker at 30°C to the point of glucose depletion. The medium consists of YNB and glucose in a phtalic acid buffer at $p\mathrm{H} = 5$. (See Danø (1999) for details on the growth procedures used in our lab).

Biochemical background of the growth dependence

Some progress towards a biochemical understanding of the growth phase dependence of the glycolytic oscillations has been made. It was shown by Becker and Betz (1972) that the differences in the oscillatory dynamics observed when either fructose or glucose is used as a glycolytic substrate, can be explained in terms of the differences in fructose and glucose transport affinities. In the same study, the hexose transport was identified as an important control point for the flux and the dynamics of the pathway. The first finding fits well with the study by Teusink *et al.* (1998a) where a pronounced growth phase dependence in the K_m of glucose transport was found: 55 mM when harvested in the first exponential growth phase as opposed to 1.7 mM when harvested at the diauxic shift. The V_max of glucose transport remains more or less constant. The second finding was rediscovered by Reijenga *et al.* (2001) and quantified by means of MCA.

These findings are reflected in the calorimetric measurements by Teusink *et al.* (1996b). In this study, a glucose pulse (20 mM) and a cyanide pulse (4 mM) is added to a suspension of starved yeast cells in a micro-calorimeter; the generated heat reflects the glycolytic flux. Cells harvested before glucose depletion show a high initial glycolytic flux which decreases rapidly. As the flux decreases, the oscillations damp out. When cells are harvested at the diauxic shift, the oscillatory transient lasts much longer, and during these oscillations the flux remains rather constant. The mean flux for cells harvested at a later stage during ethanol growth is comparable to that of cells from the diauxic shift, but these oscillations damp out quickly. A possible explanation for this is offered in chapter 7.

Additional biochemical differences between cells harvested during growth on glucose and cells harvested at the point of glucose depletion were reported by Richard *et al.* (1994): HK activity increases by at least a factor of two at the diauxic shift, whereas PDC activity remains more or less unchanged.

In contrast to this rather complicated picture, glycolytic oscillations in yeast extracts are readily seen, regardless of the exact make-up of the yeast cells. In fact, the first step in the standard procedure for producing yeast extract for the study of glycolytic oscillations involves a short trip to the supermarket to buy large quantities of commercial, compressed bakers yeast. Our preliminary studies have shown that the largest source of variations in the oscillatory dynamics of this system stems from variations in the concentrations of metabolites, cofactors and metal ions in the commercial yeast: batch differences can be almost eliminated by dialysis of the extract and subsequent well-defined additions of the required substances. When comparing extracts and intact cells, many things will be different. However, obvious differences will be the absence of the cell membrane and cellular organelles such as the mitochondria or the nucleus. An important observation is that – in contrast to intact yeast cells – oscillations are not observed when a single pulse of glucose is added to a yeast extract (Becker and Betz, 1972). With the yeast extracts, the sugar must instead be supplied in a continuous manner, either by a flow system or by means of slow, enzymatic degradation of trehalose. This again points to the membrane transport as an important factor, since saturation of the glucose transport capacity will result in a rather steady flux through the glycolytic pathway, regardless of the way glucose is being administered (Danø *et al.* (1999); see also section 6.2).

On the basis of these findings, it is tempting to suggest that the main biochemical factor of the growth dependence is the change in affinity of the hexose transport system. The effect of the starvation is less obvious, but one possibility is that the glycogen storage of the yeast cells is used up during the starvation. When the oscillations are induced, a substantial flux out of the glycolytic pathway at G6P into glycogen synthesis is observed (Betz and Hinrichs (1968); the flux corresponds to almost 50% of the total glucose uptake). Such a large flux will definitely affect the dynamics of the pathway, but it is uncertain whether it is essential for the appearance of the glycolytic oscillations.

4.1.2 Transient experiments

When yeast cells are prepared as described above, glycolytic oscillations can be observed when glucose is added to a suspension of the cells with anaerobic metabolism. The oscillations are monitored by fluorescence with excitation at 365 nm and emission above 420 nm. (See Danø (1999) for a detailed description of our setup). This signal reflects the concentration of NADH and NADPH in the yeast cells plus an offset. Changes in the signal are proportional to changes in the concentration of NAD(P)H, but the proportionality constant is unknown. It is not possible to make a direct calibration of the system, since the fluorescence is measured in the surface region of a cuvette with a milky suspension of yeast cells. It has been established that the fluorescence changes correspond to changes in NADH rather than NADPH under the conditions where oscillations are observed (Richard *et al.*, 1993), so I will refer to the signal simply as NADH-fluorescence. It should be noted that the fluorescence intensity of enzyme bound NADH is approximately five times higher than that of unbound NADH (Bjørn Quistorff and Ian Max Møller, personal communication). See also Hess *et al.* (1973).

Anaerobiosis and the effects of cyanide

The anaerobiosis is either caused by some not fully understood endogenous respiration by the starved yeast cells (the small "jump" just after $t = 400$ s in Fig. 4.1), or it is achieved by blocking the respiration by the addition of cyanide or other chemical effectors like for example azide. Ghosh *et al.* (1971) showed that cyanide is particularly effective in promoting oscillations, because it blocks the respiration and at the same time it is a nucleophilic agent, which reacts with the acetaldehyde produced by the yeast cells. These two "roles" were examined independently by using sodium azide or antimycin A to block the respiration, and extracellular acetaldehyde traps in the forms of ADH + NADH, Girards reagent P or semicarbazide. From these studies, it was concluded that more pronounced oscillations are observed when an acetaldehyde trap is present along with the respiratory inhibitor. The dual role of CN^- was later rediscovered by Richard *et al.* (1994), who apparently were unaware of the work by Ghosh *et al.* (1971). See also Betz and Chance (1965a) where the ability of KCN to prolong the transient oscillations is first described.

As already discussed, it seems that the rather stable transient oscillations observed following the addition of the glucose and the cyanide pulse is a conse-

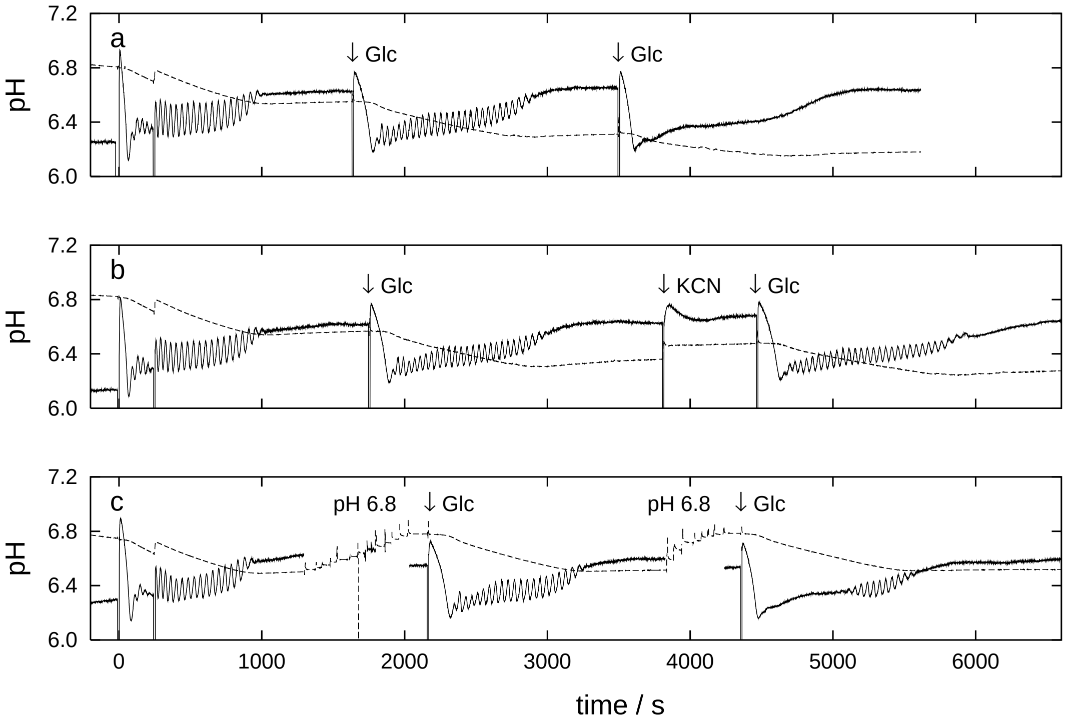

Figure 4.2: Addition of multiple glucose pulses. As reported by Teusink *et al.* (1996b), an additional train of oscillations can be induced by adding a second pulse of glucose after the first pulse has been used up, but no oscillations are seen upon addition of a third pulse (a). Teusink *et al.* also found that if additional KCN is administered after the first two trains of oscillations, a third train of oscillations can be seen (b). We found that a third train of oscillations can be seen without additional cyanide if instead we use KOH to adjust the *p*H back to 6.8 after each train of oscillations, but these oscillations are not very pronounced (c). All glucose pulses are 20 mM, KCN pulses are 5 mM and 16 mM of KOH was needed in each of the two *p*H adjustments. All three experiments were initiated by a glucose pulse at time $t = 0$ s and a cyanide pulse at $t = 240$ s. The initial cell densities were 29.2 (mg d.w.)/mL.

quence of the saturated glucose transporter, which sets up an almost constant flow of glucose into the cells. This flow stops abruptly when the glucose is consumed, and the oscillations come to a sudden halt. If another glucose pulse is added, a new train of oscillations is seen, but this time with a reduced amplitude. Oscillations are not observed on a third addition, unless additional cyanide is added as well (Teusink *et al.* (1996b); Fig. 4.2a,b).

The lower amplitude in the second train of oscillations might be due to changes in the extracellular medium caused by the glycolysing yeast cells (ethanol buildup, cyanide depletion through reaction with ACA, lowering of the *p*H *etc.*), or it might be due to changes within the yeast cells (*e.g* glycogen buildup or changes in the enzyme composition). If we wash and resuspend the cells in fresh phosphate buffer after the first train of oscillations, we find that the second train of oscillations displayed by these cells is indistinguishable from the first (data not shown), so the changes from the first to the second trains of oscillations in Fig. 4.2a must be due to changes in the medium. Fig. 4.2b shows that some of these changes can be compensated by addition of more cyanide (Teusink *et al.*, 1996b), whereas Fig. 4.2c shows that KOH additions to keep the *p*H close to the initial *p*H of 6.8 also has a compensating effect. Further experiments have shown that the oscillations disappear both at high and low *p*H values (roughly, at *p*H 7.7 and 6.2) with an optimum around 7. Possibly, the effect of the *p*H changes is to change the reactivity of cyanide towards ACA: The reactive species CN^- is a base, so reactivity decreases with decreasing *p*H. We have, however, not looked further into this. Strangely, if transient experiments are carried out with the cells in water (*i.e.* without the 0.1 M potassium buffer), then we observe a train of oscillations that appears normal, even though the *p*H falls below 4.5 during the oscillations. We have no explanation for this observation. See Hocker *et al.* (1994) for expriments and modelling concerned with *p*H in yeast extracts and Hess *et al.* (1969) for measurements of *p*H and pCO_2 in yeast extracts.

Metabolite measurements

Detailed biochemical measurements of glycolytic metabolites have been made by Betz and Chance (1965b) and Richard *et al.* (1996b) (reproduced in Table 5.8). Such measurements are made by stopping all reactions in a small sample as fast as possible, and subsequently determining the total (*i.e.* enzyme bound and unbound) concentrations of the relevant metabolites enzymatically. As described in the previous chapter, such data are very valuable for modelling purposes. It should be noted that the two sets of experiments differ in several ways. The experiments by Richard *et al.* (1996b) are performed with *S. cerevisiae* as opposed to *S. carlsbergensis*, and the oscillations are induced by KCN addition following a glucose pulse. Accordingly, these oscillations are rather stable compared to the short transients investigated by Betz and Chance (1965b), who initiated the oscillations by removing the oxygen from the suspension. The newer dataset is also more complete due to the use of a more sophisticated extraction technique (De Koning and van Dam, 1992). Nevertheless, such data should be used with caution: see the thought-provoking discussion in Teusink (1999), section 1.4.2, where it is shown that different extraction procedures can give very different results, which cannot always be explained.

Additional data of this kind can be found in Ghosh and Chance (1964) (initial observations), Richard *et al.* (1993) (NADH and G6P), Richard *et al.* (1996a) (extracellular ACA) and Teusink *et al.* (1996b) (heat flux in phase with NADH and with an amplitude of 5-10% of the mean value). See also the phase-relation plots for yeast extracts given in Hess *et al.* (1969) (reproduced in Hess and Boiteux (1971); Boiteux and Hess (1974)).

4.1.3 Cell synchronization

When observed as described above, glycolytic oscillations are a macroscopic phenomenon: we observe the average signal from many million yeast cells. Consequently, when no oscillations are observed, this can either be due to the absence of oscillations, or because the cells are oscillating out of phase with each other. On the other hand, when macroscopic oscillations – sometimes called "bulk oscillations" – are observed, this implies that the oscillations in the yeast cells are at least partly synchronized.

A key experiment is the mixing experiment (originally devised by Pye (1969)), where two suspensions of oscillating yeast cells with different phases are mixed. If the two suspensions are in opposite phases, then the amplitudes cancel out upon mixing. However, the amplitude quickly recovers, indicating strong and active synchronization among the yeast cells. A very nice example of a mixing experiment with a 180° phase difference can be found in Richard *et al.* (1996a). This work is of particular importance to our modelling, since it shows strong synchronization under conditions very similar to those of our CSTR experiments (see the following section). Still, the key reference to mixing experiments remains Ghosh *et al.* (1971) where an elaborate series of mixing experiments with different mixing phases and phase differences is presented. See also Winfree (1980) for an analysis of these data.

Another approach to the synchronization problem is to observe the NADH fluctuations directly by fluorescence microscopy, and compare them with the bulk oscillations. Several attempts have been made at this, but so far only Chance *et al.* (1973) have been successful. Using *S. carlsbergensis* and an experimental procedure where strongly damped bulk oscillations are seen, they

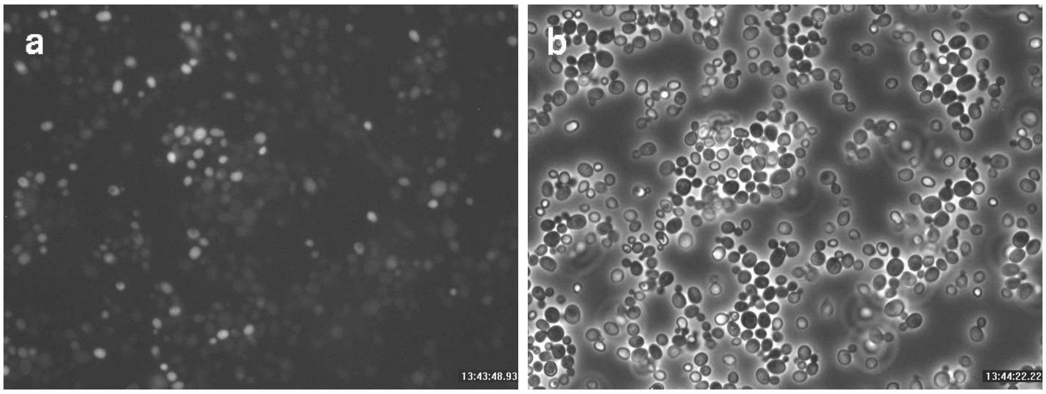

Figure 4.3: Yeast cells visualised by means of fluorescence microscopy (a) and phase contrast microscopy (b). The two pictures are recorded with approximately 40 s interval at the end of a transient experiment (*i.e.* 30 min after glucose addition). The two pictures illustrate the heterogeneity of the yeast population both in terms of size, shape and fluorescence intensity.

observe single cell oscillations which are clearly less damped than those of the corresponding suspension. This indicates – of course – that in this particular setting the damping of the bulk oscillations is partly due to desynchronization of the oscillators. Note that the shape of the single-cell oscillations is comparable to the sinusoidal shape of the bulk oscillations, and far from the relaxation-like shape often seen with yeast extracts.

The conclusion drawn from these experiments is that, depending on the exact experimental conditions, the yeast cells can be actively synchronizing their oscillations in phase or slowly drifting apart. with the growth and harvesting procedures which we have adopted from Richard *et al.*, the strong in-phase synchronization is seen.

The synchronization mechanism

A central question remains, however: what mediates this synchronization of the oscillations? Figure 4.3 shows yeast cells grown and harvested according to our protocol and photographed by means of fluorescence microscopy (a) and phase contrast microscopy (b) at the end of a transient experiment. Clearly, the yeast cell population is heterogeneous in many respects. The cells differ in both size, budding stage and fluorescence intensity. If any of these parameters are important for the oscillations, or if similar differences exist in other relevant parameters, then the need for an explanation of the coupling phenomenon seems even more pronounced.

A necessary condition for a chemical species to act as a synchronizer is that it can penetrate the cell membrane, and that an instantaneous change in its concentration will influence the oscillations and give rise to an amplitude or phase change. Many different substances known to pass the cell membrane have been tested by perturbation experiments. Proper responses are observed with ACA (Pye, 1969; Richard *et al.*, 1996a; Danø *et al.*, 1999), O_2 (Winfree, 1972) and – when the glucose transporter is not saturated – glucose (Danø *et al.*, 1999). Substances which have been tested, but without proper responses, are H^+ (Pye, 1969), K^+ (Pye, 1969), pyruvate (Pye, 1969; Danø *et al.*, 1999), Mg^{2+} (Ghosh *et al.*, 1971), EtOH (Ghosh *et al.*, 1971; Danø *et al.*, 1999), phosphate (Ghosh *et al.*, 1971), cyanide (Danø *et al.*, 1999) and glycerol (Nicolas Markadieu, personal communication).

Another necessary condition for a species to act as a synchronizer is that it oscillates in the extracellular medium as a result of periodic excretion or absorption by the cells. This condition excludes O_2 as a synchronizer in anaerobic experiments or experiments where respiration is inhibited, so we are left with ACA, glucose and possibly unknown substances as synchronizer candidates.

Because of a limitation of the acetaldehyde assay it was concluded that no synchronizing species could be identified unambiguously (Ghosh *et al.*, 1971; Winfree, 1980). A method for measuring the extracellular concentration of acetaldehyde in the presence of cyanide (Richard *et al.*, 1996a) showed, however, that the extracellular concentration of acetaldehyde exhibited large-amplitude oscillations. This behaviour was taken as a strong indication that acetaldehyde is an important species for the synchronization, but there are still a number of loose ends. As pointed out by Winfree (1980), the amount of ACA which the yeast cells should be able to produce will not be enough to perturb the oscillations. The data published by Richard *et al.* (1996a) seems to prove Winfree's calculations false, but the correction to the work by Richard *et al.* given on page 27 in Teusink (1999) states that the large ACA amplitude originally published is an error due to a mis-calibration. So, after-all, the experimentally observed ACA amplitude agrees with Winfree's conclusion that, after dilution of the ACA into the extracellular medium, the fluctuations will no longer be large enough to affect the oscillations.

Glucose is also a problematic candidate since, in the experiments with transient oscillations, the glucose transporter is saturated, and this renders the yeast cells insensitive to changes in the extracellular glucose concentration. To conclude, the mechanism of cell synchronization remains an open question, even though ACA seems to be the most promising candidate.

This ends the account of the current knowledge of transient glycolytic oscillations. However, in chapter 6 further explanations of the appearance of the transient oscillations will be offered on the basis of the model developed in chapter 5, just like the cell synchronization problem will be revisited in chapter 7, when we have a detailed model at hand.

4.2 Characterisation of the dynamics

From the above discussion of the experiments with oscillatory transients it is seen that, although they are perfectly well defined in terms of experimental procedures, they are not that well defined mathematically because of slow changes in the extracellular environment and possibly also in the cells themselves. This makes it hard to characterise the dynamics on basis of such experiments, and it also makes the quantitative use of measured dynamical properties more difficult.

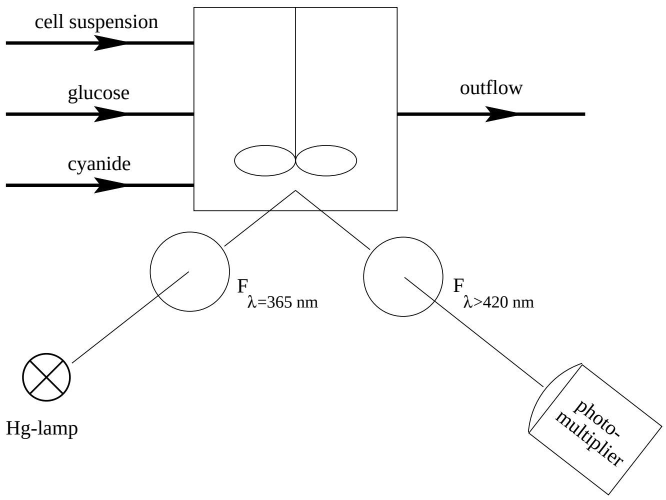

Figure 4.4: The CSTR setup. The stirred open flow reactor has a main inflow of cell suspension and two minor inflows of glucose and cyanide suspension. The fluorescence of the dense, milky suspension is monitored on the surface of the cuvette. F designates filters. (See appendix B in Danø (1999) for technical details).

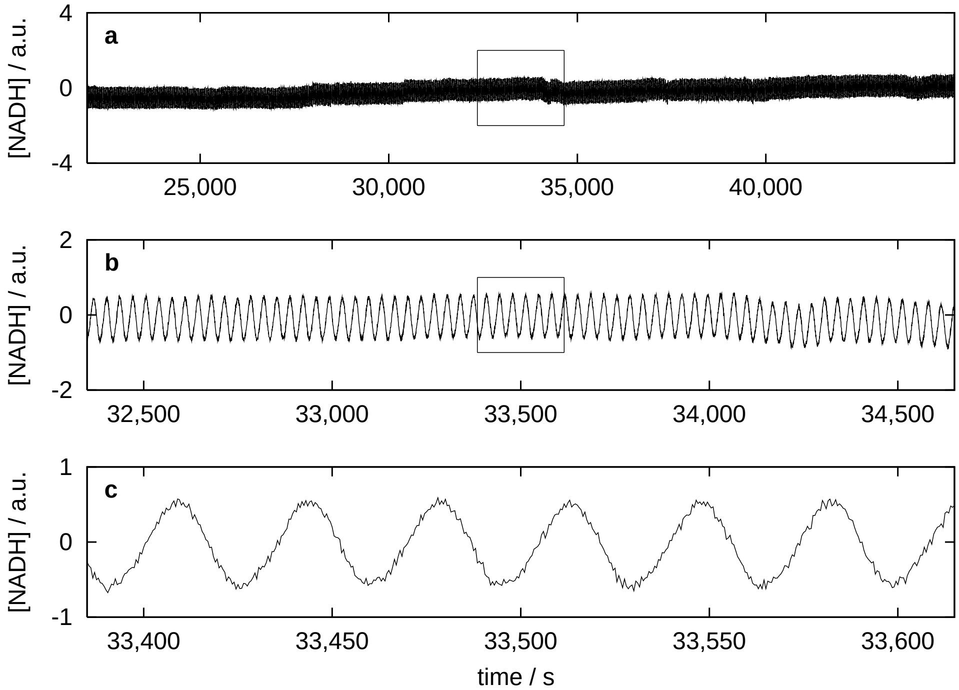

Figure 4.5: Sustained glycolytic oscillations in the CSTR. The period of the oscillation is 34.8 ± 0.2 s, and the amplitude is constant with a relative standard deviation of 3%. Panel (b) shows an expansion of the box in panel (a). Likewise, panel (c) is an expansion of the box in panel (b). The cell density is 30.5 (mg d.w.)/mL, and the specific flow rate is $k_0 = 0.051\ \mathrm{min}^{-1}$. The mixed flow concentrations are $[\mathrm{Glc_x}]_0 = 35.0$ mM and $[\mathrm{CN_x^-}]_0 = 5.4$ mM. Time is measured from the start of the experiment.

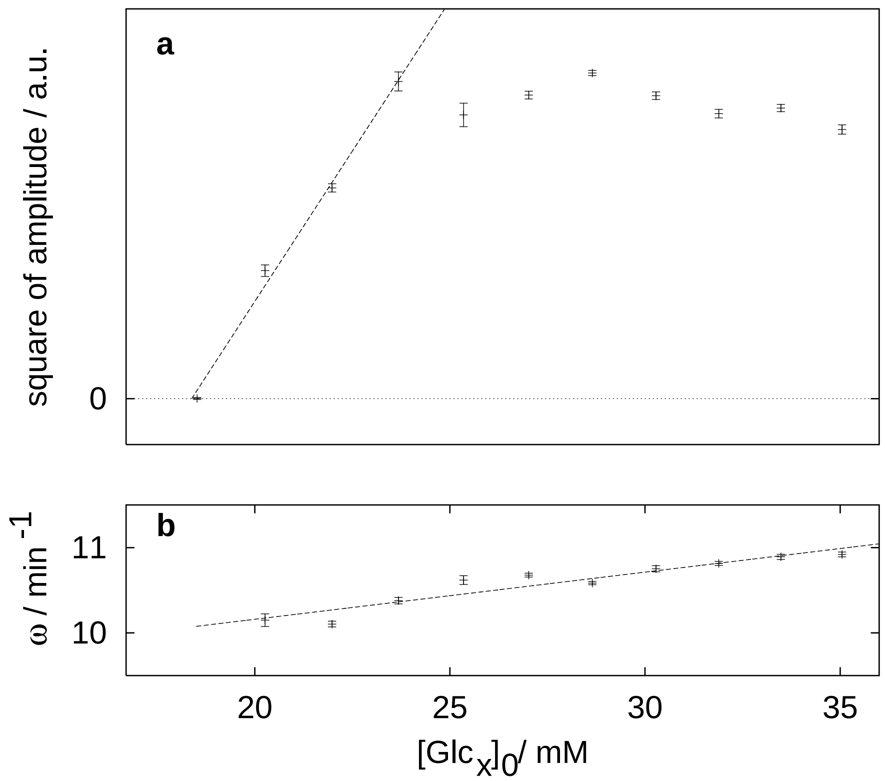

Figure 4.6: Solution diagram showing the square of the amplitude (a) and the angular frequency (b) of the oscillations as a function of the mixed flow glucose concentration. The bifurcation point at 18.5 mM corresponds to an extracellular glucose concentration of 1.6 mM. Cell density, mixed flow cyanide concentration and specific flow rate were fixed at 30.5 (mg d.w.)/mL, 5.6 mM, and 0.048 min^{-1}, respectively. The rate of change of the angular frequency is 0.055 min^{-1} mM^{-1}.

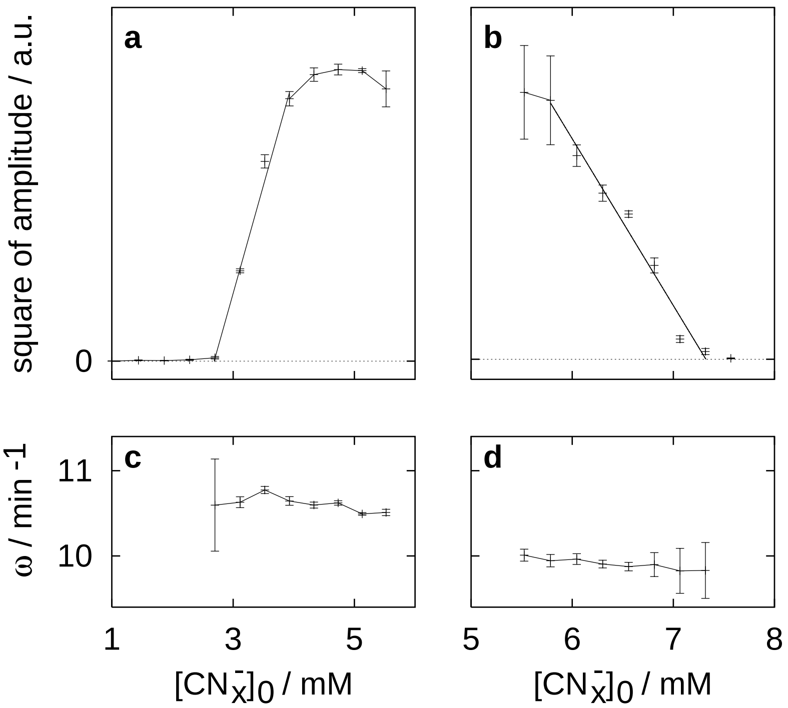

Figure 4.7: Solution diagram showing the square of the amplitude of the oscillations as a function of the mixed flow cyanide concentration in (a) the low end and (b) the high end. Panels (c) and (d) show the corresponding variation of the angular frequency. In (a) and (c), the cell density, the mixed flow glucose concentration $[\mathrm{Glc_x}]_0$, and the specific flow rate k_0 were fixed at 31.1 (mg d.w.)/mL, 28 mM, and 0.048 min^{-1}, respectively. In (b) and (d) these parameters were 30.5 (mg d.w.)/mL, 27 mM, and 0.050 min^{-1}, respectively.

Therefore, an experimental setup which allows us to study the yeast cells in well-defined dynamical states is needed. We have achieved this by conducting the yeast experiments in a CSTR; an open flow system as depicted in Fig. 4.4 (Danø *et al.*, 1999). In this flow system, there is a constant flow of glucose, cyanide and cell suspension into the stirred and thermostated (25°C) reactor, and there is an equally constant outflow ensuring constant volume. The stock of cell suspension is kept at 2°C in a stirred flask. See Danø *et al.* (1999) and Danø (1999) for more details. With this setup it is possible to work at a well defined state indefinitely (in practise: for as long time as fresh cell suspension can be supplied), as illustrated in Fig. 4.5. Moreover, this state can be accurately controlled by changing the various inflows of the reactor.

Solution diagrams

The main goal of this work is to locate the onset of the macroscopic oscillations, and to determine whether this onset corresponds to synchronization of the oscillations in a population of oscillating yeast cells, or, alternatively, to the simultaneous onset of oscillations in each the individual yeast cells. By changing the mixed flow concentration[1] of either glucose or cyanide, we have measured solution diagrams as shown in Figs. 4.6 and 4.7. These diagrams define the onsets of oscillations for the two bifurcation parameters quantitatively. It is also seen that close to the bifurcation points the amplitude of the oscillations grows proportional to the square root of the bifurcation parameter. As described in chapter 2, this is what one would expect if the onset of the oscillations corresponds to a supercritical Hopf bifurcation. With $[\mathrm{Glc}_x]_0$ as the bifurcation parameter, a gradual but rather sudden stabilisation of the amplitude is seen. This coincides with the operation point where the yeast cells become insensitive to Glc perturbations (see Danø *et al.* (1999) and below), so a plausible explanation could be that the stabilisation is due to glucose transporter saturation as already discussed. Also, the wave form remains sinusoidal even for very high values of $[\mathrm{Glc_x}]_0$.

However, the observed amplitude scaling and the sudden stabilisation is also what one would expect from a collection of certain types of coupled oscillators when the coupling strength K is increased above the critical coupling strength K_c as described by Kuramoto (1975, 1984) and discussed in a more comprehensible way by Strogatz (1993). These coupled oscillators are so-called

[1]The mixed flow concentration $[\mathrm{S}]_0$ of a substance S is the concentration [S] that would be found in the flow reactor if no reactions took place.

phase oscillators, which are one-dimensional oscillators with a fixed amplitude and a distribution in their natural frequencies. According to Daido (1994), however, the generic scaling for limit-cycle oscillators with all-to-all coupling is a linear increase of the amplitude as the coupling strength is increased. This result is supported by Crawford (1995).

Perturbation experiments

Therefore, we have also used quenching experiments to characterise the geometry of the dynamical structures in concentration space[2]. We found that quenching of the oscillations was possible either by ACA perturbations or by Glc perturbations (Fig. 4.8), and established that the quenching amounts $q_{\mathrm{ACA_x}}$ and $q_{\mathrm{Glc_x}}$ as well as the quenching phases $\phi_{\mathrm{ACA_x}}$ and $\phi_{\mathrm{Glc_x}}$ are unique. As mentioned, glucose perturbations were only effective at low values of $[\mathrm{Glc_x}]_0$. Other substances were tested (see section 4.1.3 and Table 5.8), but we did not find any with which it is possible to quench the oscillations. This is simply because these substances are unable to cross the cell membrane, or does so rather slowly.

The perturbation experiments seem to be consistent with what one should expect close to a supercritical Hopf bifurcation. In order to test this observation, we fitted the Stuart-Landau equation (Eq. 2.8) to the fluorescence traces of the perturbations as shown in Fig. 4.8. Two slow modes are added to the Stuart-Landau equation in order to catch the slow modes of the experiments; see Danø *et al.* (2000) or Appendix B for details of the fitting. The fits are quite good; discrepancies are only seen immediately after the perturbations. This is probably due to the fact that even with Glc and ACA it takes some time for the perturbation substance to get into the cells. As indicated in the legend of the figure, the same set of Stuart-Landau parameters fit both perturbations even though they are made at different mechanical operating points of the reactor. Again, this is probably an effect of saturation of the glucose transporter: at some point there is no longer any effect of increasing the extracellular glucose concentration, so the dynamics remain the same.

[2]It should be noted here that Winfree (1972) has previously used oxygen perturbations in an attempt to characterise the dynamics of glycolytic oscillations. The experiments are impressive, and so are the ideas behind the analysis; especially considering that the work was done 30 years ago. However, the transient nature of the oscillations in that study confused the analysis, and led to erroneous conclusions.

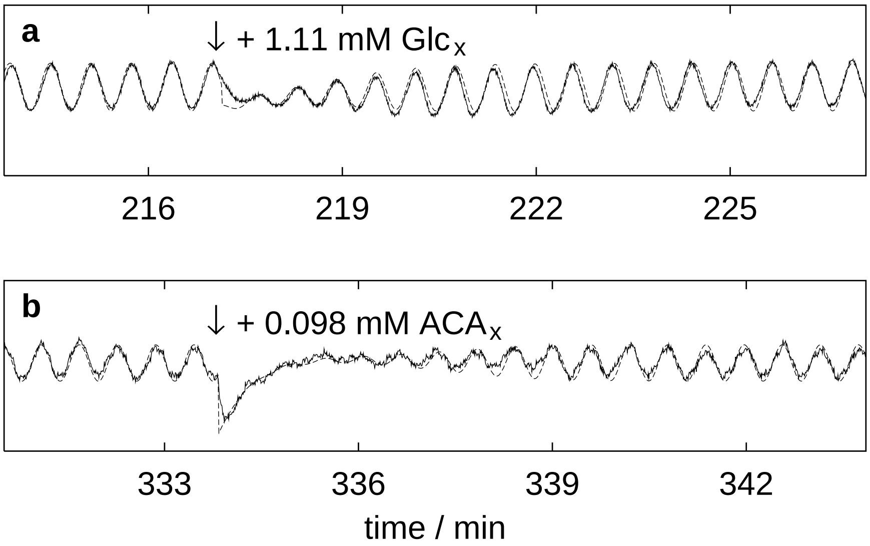

Figure 4.8: Quenching of the oscillations by addition of Glc and ACA. A fit of a Stuart-Landau equation (Eq. 2.8) with two slow modes is also shown (dashed lines). Differences in perturbation response arise because perturbations with different metabolites excite the slow modes differently. (a) quenching of the oscillations by addition of 1.1 mM $\mathrm{Glc_x}$ at 4°. The cell density is 30.7 (mg d.w.)/mL, $[\mathrm{Glc_x}]_0 = 23.1$ mM, $[\mathrm{CN_x^-}]_0 = 4.26$ mM, and $k_0 = 0.0506\ \mathrm{min}^{-1}$. (b) quenching of the oscillations by addition of 0.098 mM $\mathrm{ACA_x}$ at 172°. The cell density is 31.4 (mg d.w.)/mL, $[\mathrm{Glc_x}]_0 = 35.0$ mM, $[\mathrm{CN_x^-}]_0 = 5.37$ mM, and $k_0 = 0.0479\ \mathrm{min}^{-1}$. In both fits $\mu\sigma' = -g' = 0.86\ \mathrm{min}^{-1}$, $\eta = g''/g' = -0.21$, and the relaxation times of the slow modes are 0.58 min and 1.3 min. In each of the fits ω_{lc} is adjusted according to Fig. 4.6b. See Appendix B for details of the fitting.

Conclusion

As I will now summarise, all available experimental findings are consistent with a scenario of simultaneous supercritical Hopf bifurcations in a population of synchronized yeast cells, whereas the alternative cell synchronization scenario has a number of shortcomings:

- The yeast cells are known to be strongly coupled under similar conditions (Richard *et al.*, 1996a).

- The amplitude is proportional to the square root of the bifurcation parameter (Danø *et al.*, 1999). This could also support the cell synchronization scenario, but in general one would not expect the square root dependence for this scenario Daido (1994); Crawford (1995).

- The perturbation response is in accordance with the universal geometry of dynamical structures of systems close to a supercritical Hopf bifurcation (Danø *et al.*, 1999), and it can be modelled by the Stuart-Landau equation (Danø *et al.*, 2000). This would be unlikely for the alternative scenario.

- The oscillations are sinusoidal as expected close to a supercritical Hopf bifurcation. This holds both at the macroscopic and the microscopic level (Chance *et al.*, 1973).

- In yeast extract experiments it is indeed found that an increase of the glucose inflow will take the system from a stationary state to an oscillatory state (Hess and Boiteux, 1973). In contrast, it is unclear how an increase in the glucose inflow should cause synchronization.

- The rather sudden stabilisation of the amplitude as $[\mathrm{Glc_x}]$ increases can be explained by glucose transporter saturation or, alternatively, by all oscillators reaching complete synchronization. A similar effect is not found when cyanide inflow is used as bifurcation parameter (Fig. 4.7). This is as expected for the glucose saturation explanation, but seems odd for the synchronization scenario.

On the basis of this, we draw two conclusions. First, the most plausibly description of the system at the onset of oscillations is that of simultaneous supercritical Hopf bifurcations in a population of phase-synchronized cells. Second, under our experimental conditions this description of the yeast cells is generally applicable, since the saturation of the glucose transporter ensures that the yeast cells are never taken far away from the Hopf bifurcation. These two conclusions provide an important starting point for the work presented in the following three chapters.

5

Biochemical application of the direct method

In this chapter I will present the first biochemical application of the Direct Method of Optimization, which was presented in chapter 3. For this, we use the system of oscillating yeast cells described in the previous chapter. Thus, a purpose of the modelling is to test the method on a real biochemical system. Yeast glycolysis is a particularly well suited model system for this purpose, because glycolysis is one of the best understood biochemical pathways, and because a host of experimental data is available for this system. Still, a realistic model of glycolytic oscillations in intact yeast cells will be a valuable tool in the ongoing research on the cell synchronization problem and on glycolytic oscillations in general, so the modelling serves a dual purpose. A quantitative, realistic model will also be valuable in various biotechnological contexts, but we did not have any specific applications in mind for the model presented here. The common goal is a model which is in quantitative agreement with as many experimental findings as possible.

The main reference for this chapter is Hynne *et al.* (2001) where we give a detailed account of the work. A more introductory text is also available (Hynne *et al.*, 2003).

5.1 Existing models

Glycolytic oscillations have been modelled extensively in extracts. In broad terms, these models are either simple ones focusing on the dynamics of PFK (*e.g.* Sel'kov (1968); Goldbeter (1996)) or elaborate models encompassing most of the glycolytic reactions (Richter *et al.*, 1975; Termonia and Ross, 1981; Hocker *et al.*, 1994; Nielsen *et al.*, 1998). In particular, the models presented by Richter *et al.* (1975) and by Nielsen *et al.* (1998) both include the NAD^+/NADH system. However, none of the yeast extract models include the branching of the reaction network.

Modelling of glycolytic oscillations in intact yeast cells is somewhat more sparse. One reason for this might be the difficulties of using parameters obtained from *in vitro* studies for modelling an *in vivo* system. Often the V_{max} values of enzymes seem to be much higher *in vivo* than when they are measured *in vitro* (*e.g.* Babul *et al.* (1993); Benevolensky *et al.* (1994); Teusink *et al.* (2000)). Several explanations have been offered for such phenomena (see *e.g.* Ovádi and Srere (1996)). A less exotic explanation of why this problem seems more pronounced for V_{max} values than for K_{m} values might be that the enzyme activity depends both on the chemical nature of the enzyme and on its concentration, so both the specific activity as well as the enzyme concentration needs to be determined; this increases the risk for experimental error. The Direct Method circumvents this problem, since V_{max} parameters are not needed in the optimization.

From the cell synchronization perspective, qualitative (Wolf and Heinrich, 1997; Bier *et al.*, 2000) and semi-quantitative (Wolf *et al.*, 2000; Wolf and Heinrich, 2000) models have been published which address the question of cell synchronization in yeast cells explicitly. Only a limited amount of biochemical detail has been incorporated in these models.

Quantitative, full-scale models of glycolysis in intact yeast cells have previously been published (Rizzi *et al.*, 1997; Teusink *et al.*, 2000). These models have detailed biochemistry, including the NAD^+/NADH system and branchings from glycolysis. In the work by Rizzi *et al.* model parameters were fitted to the glucose response of yeast cells that were otherwise in steady-state growth. Since the cells were growing, this model includes steady-state fluxes from glycolysis to several other pathways. A reasonable agreement with the observed perturbation response was obtained through extensive fitting.

In the recent modelling work by Teusink *et al.* (2000), the fluxes and concentrations in a quasi-stationary state, as well as a large number of enzyme kinetic parameters, were measured in non-growing, anaerobic yeast cells. The metabolite concentrations are then inserted into the equations of the model, and the calculated fluxes are compared with the experimental ones. Such a procedure has previously been described by Wurster and Schneider (1970) and by Barwell and Hess (1972), and similar calculations are discussed by Danø (1999). Despite the huge amount of high-quality biochemical data considered, the Teusink model fails to describe the experiments quantitatively because no actual optimization is performed. Neither Rizzi *et al.* nor Teusink *et al.* address glycolytic oscillations in their modelling.

5.2 Available data

As discussed in chapter 3, the main problem in constructing a realistic model of a real biochemical system is the rather large number of parameters which needs to be included in the fitting. The Direct Method cannot circumvent this problem, so the experimental data available for the optimization is of utmost importance. These data will be discussed now in terms of their origin, their usability, and their reliability. I will not account for the ways the various types of data enter the optimization procedure here, since this issue has already been addressed in chapter 3.

Operating point

First of all, we need to define an operating point for the optimization. This will be the Hopf bifurcation point observed when increasing the mixed flow glucose concentration in the CSTR as defined by Fig. 4.6. This point is chosen because it is a well defined stationary state, and because it allows us to include a number of experimental findings regarding the glycolytic oscillations in the optimization.

The CSTR setup permits reproducible, well-controlled experimental conditions for prolonged periods of time. This means that frequencies and relative amplitudes can be measured accurately, and therefore positions of bifurcation points can be determined precisely. So for each individual run, the CSTR provides very accurate data. Unfortunately, there is inevitable variation between batches of cell suspensions used in the inflow (due to differences in cell density and exact harvesting time). Nevertheless, the data from these experiments are quite reproducible from run to run.

Data on stationary concentrations

Richard *et al.* (1996b) provide data on oscillating metabolite concentrations in experiments with oscillatory transients in yeast cells grown and prepared in the same manner as those used in the CSTR experiments. Since we have established that the glucose transporter saturation keeps the dynamical state of the yeast cells close to the Hopf bifurcation, it is feasible to include this rich dataset in the optimization. We use the mean values of the biochemical measurements of the oscillating metabolites as an approximation of the stationary concentrations at the operating point of the optimization. As we will see in section 6.1, this approach is – to a large extent – self-consistent in that the model retains almost all of the mean values of the metabolite concentrations at their values at the bifurcating point when integrated at higher concentrations of extracellular glucose.

As with all biochemically determined concentrations, these data are determined with at least 10% error, but it helps that they are averaged over a number of data points. As pointed out by Teusink (1999), systematic errors can be expected in data from extraction experiments either because the extraction procedure itself introduces errors or because of problems related to the difficulties of stopping all reactions immediately. (A special technique, where the reactions are stopped by spraying the sample into $-40°C$ cold methanol, was used to limit this problem (De Koning and van Dam, 1992)).

Still, the concentration measurements is a key dataset in the optimization. It can be found in Table 5.8 along with a few more data on stationary concentrations from Richard *et al.* (1994), Richard *et al.* (1996a) and Hynne *et al.* (2001). Note that for extracellular species, the data from the transient experiments are not directly applicable ($\mathrm{EtOH_x}$, $\mathrm{Glyc_x}$ and $\mathrm{ACA_x}$).

The purely mechanical rate constant k_0 (see below) is known, and others are being scanned (the membrane diffusion constants of glycerol, EtOH and ACA). Therefore, a number of concentrations are calculated during the optimization and cannot be fixed at a desired value ($[\mathrm{Glc_x}]$, $[\mathrm{CN_x^-}]$, $[\mathrm{EtOH}]$, $[\mathrm{EtOH_x}]$, $[\mathrm{ACA}]$, $[\mathrm{ACA_x}]$, $[\mathrm{glycerol}]$ and $[\mathrm{glycerol_x}]$). Instead, these concentrations are used for model validation if their experimental values are known.

Flux data

Another essential set of data is the data defining the fluxes through the system. Again, the glucose transporter saturation allows us to exploit the data from the transient experiments of Richard *et al.* (1994). As pointed out in the previous chapter, the starved cells build a substantial part of the glucose taken up into glycogen, and this should be taken into account when estimating the metabolic fluxes. Unfortunately, data on glycogen buildup is not available for *Saccharomyces cerevisiae.* Instead, we use data from experiments on glycolytic oscillations in *Saccharomyces carlsbergensis* (Betz and Hinrichs, 1968). Therefore, the estimates of metabolic flux distributions (normalised convex parameters) are made by combining the data in Richard *et al.* (1994) and Betz and Hinrichs (1968), so these estimates might not be very accurate for the situation considered (Table 5.9). Consequently, we scan a fairly narrow interval of these parameters.

When calculating the magnitudes of the fluxes, the ratio, y_{vol}, of the extracellular volume to the cytosolic volume is a key parameter. This ratio is inversely proportional to the cell density, and the conversion factor between cell density (measured either as wet weight or as protein mass pr. volume) and y_{vol} is given in Richard *et al.* (1996b). We tried to use these conversion factors to determine y_{vol} for the CSTR experiments, but the two conversion factors give inconsistent results. Therefore, we have no accurate value for y_{vol} but use the estimate $y_{\mathrm{vol}} \approx 45$ as a reasonable starting point. With this value and the data in Richard *et al.* (1994) we estimate the glycolytic flux (defined in our work as the flux through PGI, PFK or ALD) to 27 mM/min. (See p. 111 in Danø (1999)). Since the magnitude of the glycolytic flux becomes an important parameter in the optimization process, we define it as $j_0 v_0$ with $v_0 = 27$ mM/min.

Local dynamical properties

Since we are working at a supercritical Hopf bifurcation, it is possible to include local dynamical properties. From the extraction experiments with oscillatory transients reported by Richard *et al.* (1996b) and Richard *et al.* (1996a) we have data on 13 amplitudes and nine relative phases of oscillating metabolites. We will see later that use of these data yields self-consistent results in the same way as described above for the quasi-stationary concentrations.

Of course, these data are subject to the same limitations as described above for the quasi-stationary metabolite concentrations, but a larger error will be associated with these properties, since they are defined by fewer measurements. This is clearly illustrated by the data in Table 5.8 where the amplitudes of the metabolites for the moiety conserved sets NAD^+/NADH and ATP-ADP-AMP do not match (see also Richard *et al.* (1996b)). At least for the NAD^+/NADH set, independent measurements by the same authors suggest that, indeed, there is moiety conservation (Richard *et al.*, 1993).

At the bifurcation point the oscillations have zero amplitude, so only the relative amplitude of the metabolites can be exploited in the optimization.

Another set of local dynamical data is the quenching data from the CSTR experiments (Danø *et al.*, 1999). (Quenching phases ϕ_s and amplitudes q_s of extracellular Glc and ACA as well as the information that the remaining three extracellular species cannot quench the oscillations). For the reasons given above, these quenching amplitudes and phases can be measured with high accuracy and without any complications arising from extraction procedures *etc.* However, a problem with the CSTR experiments is, that the measured fluorescence is proportional to the intracellular NADH concentration but the proportionality constant is unknown. So we loose an absolute measure of the magnitude of the [NADH] oscillations, which is needed in order to scale the quenching amplitudes for comparison at the bifurcation point. Therefore, only the ratio of the two quenching amplitudes can be used in the optimization.

The CSTR experiments have also provided a precise determination of the angular frequency of oscillation, ω_0, by extrapolation. Some qualitative information of the bifurcation is also included: the Hopf bifurcation should be supercritical ($g' < 0$), and the direction of the bifurcation should be so that the stationary state looses stability for increasing $[\mathrm{Glc_x}]_0$ ($\sigma' > 0$).

Intrinsic parameters

Enzyme kinetic parameters constitute most of the intrinsic parameters which we need to specify. Literature values from yeast can be found for many of the enzymes (glucose transport, HK, PGI, TIM, PK, ADH and G3PDH), and several values are often available (Table 5.5). This gives a good impression of the uncertainty associated with these parameters. Other enzymes, however, have no or limited enzyme kinetic information available (PFK,ALD,PDC; note in Table 5.5 that values in parenthesis are values used in other models). Enzyme kinetic parameters are generally *in vitro* values. As mentioned, this might cause discrepancies, but it remains uncertain to which extend *in vivo* and *in vitro* values differ.

Unused experimental data

Despite our aim of including as much experimental data as possible, we have had to leave out some data for various reasons. This is mainly due to the high computational cost of calculating Stuart-Landau parameters for a large number of points. From the fitting of Stuart-Landau parameters to the quenching perturbations (Fig. 4.8) we have an estimate of g'/g'' which is not used. Likewise, the rate of change of angular frequency of the limit cycle as a function of μ has been measured (we found $\sigma'' - \sigma' g''/g' = 0.055\ \mathrm{min}^{-1}$; Fig. 4.6b), but this has not been included in the optimization.

The synchronization issue has been omitted as well. One way to include this would have been by optimizing a model describing two cells and an extracellular medium instead of one cell and a medium. This would not have introduced more parameters, but it would have been computationally expensive. Alternatively, the methods described in chapter 7 could have been applied, but they were not developed at the time the modelling was done, and they also depend on the calculation of Stuart-Landau parameters.

5.3 Model

Our use of the direct method enables us to include a wide range of biochemical and dynamical data in the optimization of a detailed biochemical model, so when setting up this model we need to include the reactions which are necessary for a meaningful comparison with all relevant experimental data. Because of the extensive set of data, this results in a full-scale model. However, it should be emphasised that completeness is not attempted for its own sake; on the contrary, we have attempted to simplify the model wherever possible.

5.3.1 The type of equations

Before these ideas can be made concrete, we need to consider the type of equations to be used. It is by far most convenient to work with a set of ODEs, but that might not always give an adequate description of the system. There are two issues to consider: Is the number of molecules big enough, and is the system spatially homogeneous?

In metabolism one is generally in the millimolar range of concentrations, so within a typical yeast cell of say 6 μm diameter one will find $N \approx 10^7$ for each of the metabolites. Stochastic fluctuations are on the order of $\sqrt{N} \approx 3 \cdot 10^3$ which is less than 1‰ of N. However, one might run into trouble when modelling other cellular systems, notably regulatory networks of the genome.

Intracellular spatial homogeneity is ensured by diffusion if the volume of the cell is small enough. That is, the characteristic time for diffusive mixing in the spatial compartment should be less than the characteristic time of the dynamics in question. Again, for a typical yeast cell we have $t_{\text{mix}} \approx \frac{L^2}{\pi^2 D} < 0.1\text{s}$ when the diffusion constant D is taken to a typical value for metabolites in water, $5 \cdot 10^{-6}\text{cm}^2/\text{s}$. This seems small when compared to the 35–40s period of the observed oscillations. Nevertheless, travelling NADH waves have been observed in neutrophiles which are elongated cells with a typical length of 20 μm (Petty *et al.*, 2000), so in general one cannot rule out the possibility of spatial heterogeneity. Still, the wavelength of the NADH waves observed in that study is so large that they would not fit in a yeast cell. Consequently, we will assume that the yeast cells are spatially homogeneous.

Another assumption will be that the enzyme activity is the same for all experiments used in the optimization. Note that this only makes sense if the experimental values are obtained for identical cells which are truly in the same proteomic state, and that this state remains constant during the experiments. As Fig. 4.3 shows, the cells are not completely identical but have, for example, a size distribution. For now, we will nevertheless assume that the cells have identical behaviour due to the strong coupling, and return to the issue in chapter 7. The time constancy of cell properties is only approximately valid in the transient experiments, but is confirmed for the CSTR by the remarkable long-time stability of the oscillatory amplitude (Fig. 4.5).

5.3.2 Reaction network

We are now ready to define the structure of the reaction network. The experiments supplying the data for the optimization have setups that help to minimise the size of the biochemical network which we need to include in the model. The cyanide blocks the cytochrome c oxidase of the electron transport chain, and consequently, pyruvate is not oxidised through the citric acid cycle; instead it is fermented to ethanol. Since the yeast cells of the present work are starved beforehand and have no external nitrogen source available during the experiments, they will not be able to change their enzyme composition significantly during the experiments. Therefore, we model them as non-growing cells with a fixed enzyme composition, and we need only consider the reactions in a very limited part of yeast metabolism.

Table 5.1: Reactions of the model

r	reaction			
1:		$\rightleftharpoons$	Glc_x	inGlc
2:	Glc_x	$\rightleftharpoons$	Glc	GlcTrans
3:	Glc + ATP	$\rightarrow$	G6P + ADP	HK
4:	G6P	$\rightleftharpoons$	F6P	PGI
5:	F6P + ATP	$\rightarrow$	FBP + ADP	PFK
6:	FBP	$\rightleftharpoons$	GAP + DHAP	ALD
7:	DHAP	$\rightleftharpoons$	GAP	TIM
8:	GAP + NAD^+	$\rightleftharpoons$	BPG + NADH	GAPDH
9:	BPG + ADP	$\rightleftharpoons$	PEP + ATP	lpPEP
10:	PEP + ADP	$\rightarrow$	Pyr + ATP	PK
11:	Pyr	$\rightarrow$	ACA	PDC
12:	ACA + NADH	$\rightarrow$	EtOH + NAD^+	ADH
13:	EtOH	$\rightleftharpoons$	$EtOH_x$	difEtOH
14:	$EtOH_x$	$\rightarrow$		outEtOH
15:	DHAP + NADH	$\rightarrow$	Glyc + NAD^+	lpGlyc
16:	Glyc	$\rightleftharpoons$	$Glyc_x$	difGlyc
17:	$Glyc_x$	$\rightarrow$		outGlyc
18:	ACA	$\rightleftharpoons$	ACA_x	difACA
19:	ACA_x	$\rightarrow$		outACA
20:	ACA_x + CN_x^-	$\rightarrow$		lacto
21:		$\rightleftharpoons$	CN_x^-	inCN
22:	G6P + ATP	$\rightarrow$	ADP	storage
23:	ATP	$\rightarrow$	ADP	consum
24:	ATP + AMP	$\rightleftharpoons$	2 ADP	AK
	$[NAD^+] + [NADH]$	$=$	constant	
	$[ATP] + [ADP] + [AMP]$	$=$	constant	

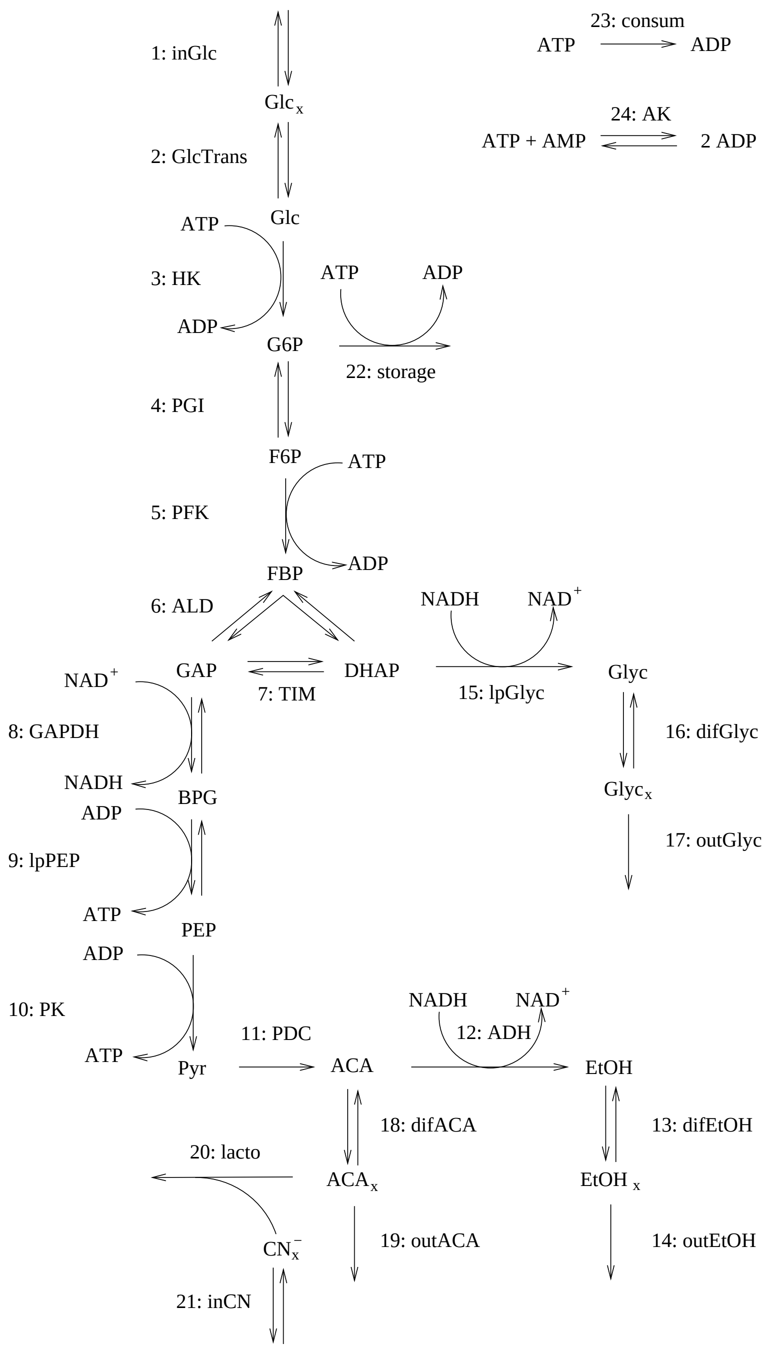

Figure 5.1: Reaction network.

This principle of functionally isolating the pathway of interest *in vivo* is generally applicable. It offers a dramatic reduction of the complexity of the system, which could make detailed modelling of a number of other pathways possible.

Network structure

The stoichiometry of glycolysis (including the identity of the metabolites participating and the branching/connectivity of the network) has been known for a long, time but some reactions can be lumped and some metabolites ignored in the modelling without sacrificing agreement with experiments. As I will now describe, this process results in the reaction network shown in Table 5.1 and Fig. 5.1. The known branching ratios of the system (Table 5.9) account well for the mass flow under our experimental conditions, so the only relevant parts of yeast metabolism are glycolysis (reactions 3-10), fermentation (reactions 11 and 12), glycerol production (reaction 15) and glycogen buildup (reaction 22; the UTP required for this reaction is counted simply as ATP). For the relevant metabolites, transport across the cell membrane is modelled by reactions 2, 13, 16 and 18. Since we model glycolysis in a stationary state, it is necessary to include processes consuming ATP. These reactions are modelled schematically as reaction 23. We may think of this ATP hydrolysis as driving some basic cellular demands like the maintenance of membrane potentials. Reaction 24 – the AK reaction – is included for the sake of dynamics. As mentioned, the lactonitrile-forming reaction between acetaldehyde and cyanide seems to be important for the dynamics of synchronized glycolytic oscillations, so this reaction is included as reaction 20.

Describing the flow system

In the CSTR setup there are constant inflows of glucose solution, cyanide solution and cell suspension, and a constant outflow of reaction mixture. Therefore, all the metabolites in the model should in principle be modelled with an inflow and an outflow. However, flows of intracellular metabolites are not taken into account. Including these flows in the model would complicate the model significantly without gaining much in terms of biochemistry or realism. This is easily seen from a simple calculation: The intracellular glycolytic metabolite with the highest known concentration is pyruvate with a concentration of 8.7 mM. Since the specific flow rate of the CSTR is 0.048 min^{-1}, the outflow of pyruvate due to outflow of cells is 0.4 mM/min which is negligible compared to the glycolytic flux of 27 mM intracellular glucose per minute. Therefore, we model the CSTR as if the cells were fixed in the reactor, while there is an inflow of glucose and cyanide solutions and an outflow of the extracellular reaction mixture (reactions 1,14,17,19 and 21; see Fig. 5.2). Apart from the immediate simplification of the model, this approximation also introduces two conservation equations (Table 5.1), which simplify the optimization further.

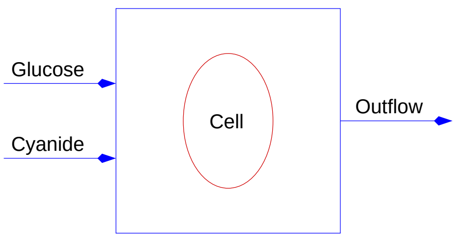

Figure 5.2: Schematic figure showing the situation described by the model: a single yeast cell fixed in a CSTR. In the experiments the reactor contained 1.6 billion cells, and fresh cells were flowed into the reactor. The dynamics of a one-cell reactor is identical to the dynamics of a many-cell reactor provided the state of the cells are identical, and the (absolute) flow rate and volume is increased in proportion with the number of cells. See text for further discussions.

Because of the complication of two phases (intracellular and extracellular), we need to be careful with our definition of reaction velocity, so we first define the rate of conversion of reaction r as $\dot{\xi}_r$, the rate of change of the extent of reaction r. By definition, a change $\Delta\xi_r$ of the extent of reaction r results in a change of the amount n_s of species s equal to $\Delta n_s = \nu_{sr}\Delta\xi_r$, so that

$$\dot{n}_s = \sum_r \nu_{sr}\dot{\xi}_r, \tag{5.1}$$

in which ν_{sr} is the stoichiometric coefficient of species s in reaction r, an element of the stoichiometric matrix $\boldsymbol{\nu}$.

It is convenient to define the rate of reaction r as $v_r = \dot{\xi}_r/V$ with V the total intracellular cytosol volume *regardless* of the character of the reaction (whether it is intracellular, extracellular, or it transfers some species across the membrane from one phase to the other). As already mentioned, we denote the ratio of the extracellular volume to the total volume of intracellular cytosol by $y_{\rm vol}$. We may then write Eq. 5.1 as

$$y_s\dot{c}_s = \sum_r \nu_{sr}v_r, \tag{5.2}$$

in which $y_s = y_{\rm vol}$ if s is extracellular and $y_s = 1$ for intracellular s.

It is straightforward to take the special definition of reaction velocities into account in the calculation of dynamical properties of the model, in the calculation of rate constants and maximum velocities, and in the integration of the final model.

Further simplifications

We have lumped the glycerol producing branch (G3PDH and glycerol phosphatase), and describe its kinetics by the kinetics of G3PDH because we have no data available on intracellular glycerol concentrations, nor do we have any data on the glycerol phosphatase kinetics. The glycerol phosphatase reaction is energetically favourable, so we do not expect it to be rate limiting for the glycerol branch. Likewise, we have lumped the PGK, PGM and ENO reactions because we have no data on 2PG, and because the enzyme kinetics of the three enzymes are not well described.

Using Eq. 3.2 and the stationarity condition we fix one velocity parameter per reaction. But, since we have experimental data on net stationary velocities (*i.e.* $w = v_\mathrm{f} - v_\mathrm{r}$), this is in fact only one parameter per net reaction. Therefore, we need additional parameters specifying the ratio between v_f and v_r for each reversible reaction. (Usually, we do this in the form of a K_eq parameter). This means that we can reduce the number of parameters significantly by modelling reactions with large $-\Delta G$ values as irreversible reactions, and therefore reactions 3, 5, 10, 11, 12 and 15 are modelled this way. (See Danø (1999) for calculations). The observations that there is no effect of EtOH and Glyc perturbations give direct experimental support to this simplification.

Extreme currents

With the structure of the reaction network in place, we can now calculate the extreme currents needed for the application of the direct method. The model has 36 components in the velocity vector $\mathbf{v}$, of which 12 are reverse reactions of reversible pairs. Thus, the velocity space has 36 dimensions. For convenience, we shall work in the space of net velocities $\mathbf{w}$ which is 24 dimensional. The extreme currents of this space are calculate as indicated in chapter 3 and shown in Table 5.2. A biochemical argument for this representation of stationary velocities can also be made; see Appendix C. Since the space of stationary net velocities is four dimensional and there are 12 reverse reactions, the space of stationary velocities in the model is 16 dimensional. As indicated above, the

12 reversible reactions are handled independently via equilibrium constants, known rate constants or a parameter describing the ratio between the forward and reverse reaction (*e.g.* $K_{4\text{eq}}$ and $k_{9\text{f}}/k_{9\text{r}}$).

According to Eq. 3.1, we can now express any stationary net velocity as a linear combination with non-negative coefficients of these four extreme stationary net velocities,

$$\mathbf{w} = j_{\text{ferm}}\,\mathbf{E}_{\text{ferm}} + j_{\text{glyc}}\,\mathbf{E}_{\text{glyc}} + j_{\text{lact}}\,\mathbf{E}_{\text{lact}} + j_{\text{stor}}\,\mathbf{E}_{\text{stor}}. \tag{5.3}$$

A set of four nonnegative coefficients (convex coefficients) uniquely determines the net velocity for our particular model. (But see the brief discussion of redundancy in the general case in Appendix B of Hynne *et al.* (2001)).

The components of the four extreme currents are integers which are directly related to the stoichiometry of the reaction chains. As velocities they are measured in a common unit which we choose to be v_0, the estimated glycolytic flux (that is, the rate of flow of glucose into the cells, apart from that built into glycogen).

The precise normalisations are not really important to the optimization, but a rational choice may help us understand the significance of any particular set of convex coefficients. Our normalisation is such that each of the extreme currents alone would have a glycolytic flux of v_0. For convenience, we define

$$j_0 = j_{\text{ferm}} + j_{\text{glyc}} + j_{\text{lact}} + j_{\text{stor}} \tag{5.4}$$

and refer to a linear combination of (normalised) extreme currents with non-negative convex coefficients satisfying $j_0 = 1$ as a normalised net velocity. With this definition we can uniquely specify any possible stationary reaction velocity for our model by supplying 16 values: three normalised convex coefficients, a set of 12 velocities for the reverse reactions, and j_0 which (together with v_0) gives the magnitude of the glycolytic flux.

5.3.3 Rate equations

A rate expression can often be expressed in a definite functional form containing kinetic parameters such as Michaelis constants in which the mathematical form is believed to be correct. Much of the variability and the least known aspects of glycolysis can be associated with the precise values of kinetic parameters for any given system.

Table 5.2: Extreme net currents based on velocities defined on the basis of the intracellular volume as described near Eq. 5.2. The indices refer to the irreducible subpathways representing fermentation, glycerol production with outflow of ACA, glycerol production with lactonitrile formation, and storage buildup, respectively (depicted in Fig. C.1).

r	reaction	$\mathbf{E}_{\mathrm{ferm}}/v_0$	$\mathbf{E}_{\mathrm{glyc}}/v_0$	$\mathbf{E}_{\mathrm{lact}}/v_0$	$\mathbf{E}_{\mathrm{stor}}/v_0$
1	inGlc	1	1	1	2
2	GlcTrans	1	1	1	2
3	HK	1	1	1	2
4	PGI	1	1	1	1
5	PFK	1	1	1	1
6	ALD	1	1	1	1
7	TIM	1	0	0	1
8	GAPDH	2	1	1	2
9	lpPEP	2	1	1	2
10	PK	2	1	1	2
11	PDC	2	1	1	2
12	ADH	2	0	0	2
13	difEtOH	2	0	0	2
14	outEtOH	2	0	0	2
15	lpGlyc	0	1	1	0
16	difGlyc	0	1	1	0
17	outGlyc	0	1	1	0
18	difACA	0	1	1	0
19	outACA	0	1	0	0
20	lacto	0	0	1	0
21	inCN	0	0	1	0
22	storage	0	0	0	1
23	consum	2	0	0	0
24	AK	0	0	0	0

Therefore, the strategy of our modelling is to work from a fairly complete, fixed 'skeleton' of rate equations building on the extensive biochemical knowledge of glycolysis, and use the experimental data described in the previous section to fit the set of unknown parameters. The precise choice of equations will, of course, influence the properties of the final model. I emphasise that the functional forms of the rate expressions have not been subject to optimization in this study although, some details have been adjusted in the course of the project.

Since we want to include as large a set of experimental data as possible in the optimization, we need rate equations expressing all the experimentally measured properties. To this end, we expand existing glycolytic models of yeast extract. This approach results in a fairly large model, which includes processes associated with the membrane and the extracellular phase. This way, we have focused on the application of the Direct Method of Optimization and the incorporation of experimental data in the optimization, rather than the actual formulation of the model.

As basis for our model, we have chosen the yeast extract model by Nielsen *et al.* (1998) (which builds on previous work by Termonia and Ross (1981) in particular), since this model describes the dynamics of cell extracts quite well: It predicts the same sequence of bifurcations and waveforms as is seen in a CSTR with yeast extract when the specific flow rate is varied, and it gives a quite good description of the response to perturbations. However, to obtain a model describing the reaction network outlined above, some changes and extensions are needed. Our main source for these extensions has been the model by Richter *et al.* (1975).

In appendix D I explain how such changes and additions result in the model presented in Table 5.3 by commenting on the rate equations of the individual reactions. However, a detailed discussion of the forms of the rate equations and the significance of the parameters is out of the scope of this work. For such information, please see the papers referenced in the appendix.

With this huge model, we can capture most of the available experimental observations of our specific system. An obvious drawback is that the model now has a large number of parameters. Furthermore, the dynamics of the unoptimized model does not fit the experimental observations *at all*. However, since most of the equations are taken from other models or directly from enzyme kinetic studies, we have some reasonable parameter values for the start of the optimization, and, as we shall see, most of the kinetic parameters can retain their literature values.

r	rate equation (v_r)
1:	$v_{\rightarrow} = y_{\mathrm{vol}} k_0 [\mathrm{Glc_x}]_0$ $v_{\leftarrow} = y_{\mathrm{vol}} k_0 [\mathrm{Glc_x}]$
2:	$v_{\rightarrow} = \frac{V_{2\mathrm{m}} \frac{[\mathrm{Glc_x}]}{K_{2\mathrm{Glc}}}}{1+\frac{[\mathrm{Glc_x}]}{K_{2\mathrm{Glc}}}+\frac{P_2 \frac{[\mathrm{Glc_x}]}{K_{2\mathrm{Glc}}}+1}{P_2 \frac{[\mathrm{Glc}]}{K_{2\mathrm{Glc}}}+1}\left(1+\frac{[\mathrm{Glc}]}{K_{2\mathrm{Glc}}}+\frac{[\mathrm{G6P}]}{K_{2\mathrm{IG6P}}}+\frac{[\mathrm{Glc}][\mathrm{G6P}]}{K_{2\mathrm{Glc}} K_{2\mathrm{IIG6P}}}\right)}$ $v_{\leftarrow} = \frac{V_{2\mathrm{m}} \frac{[\mathrm{Glc}]}{K_{2\mathrm{Glc}}}}{1+\frac{[\mathrm{Glc}]}{K_{2\mathrm{Glc}}}+\frac{P_2 \frac{[\mathrm{Glc}]}{K_{2\mathrm{Glc}}}+1}{P_2 \frac{[\mathrm{Glc_x}]}{K_{2\mathrm{Glc}}}+1}\left(1+\frac{[\mathrm{Glc_x}]}{K_{2\mathrm{Glc}}}\right)+\frac{[\mathrm{G6P}]}{K_{2\mathrm{IG6P}}}+\frac{[\mathrm{Glc}][\mathrm{G6P}]}{K_{2\mathrm{Glc}} K_{2\mathrm{IIG6P}}}}$
3:	$v_{\rightarrow} = \frac{V_{3\mathrm{m}}[\mathrm{ATP}][\mathrm{Glc}]}{K_{3\mathrm{DGlc}} K_{3\mathrm{ATP}}+K_{3\mathrm{Glc}}[\mathrm{ATP}]+K_{3\mathrm{ATP}}[\mathrm{Glc}]+[\mathrm{Glc}][\mathrm{ATP}]}$
4:	$v_{\rightarrow} = \frac{V_{4\mathrm{m}}[\mathrm{G6P}]}{K_{4\mathrm{G6P}}\left(1+\frac{[\mathrm{F6P}]}{K_{4\mathrm{F6P}}}\right)+[\mathrm{G6P}]}$ $v_{\leftarrow} = \frac{V_{4\mathrm{m}} \frac{[\mathrm{F6P}]}{K_{4\mathrm{eq}}}}{K_{4\mathrm{G6P}}\left(1+\frac{[\mathrm{F6P}]}{K_{4\mathrm{F6P}}}\right)+[\mathrm{G6P}]}$
5:	$v_{\rightarrow} = \frac{V_{5\mathrm{m}}[\mathrm{F6P}]^2}{K_5\left(1+\kappa_5 \frac{[\mathrm{ATP}]^2}{[\mathrm{AMP}]^2}\right)+[\mathrm{F6P}]^2}$
6:	$v_{\rightarrow} = \frac{V_{6\mathrm{f}}[\mathrm{FBP}]}{K_{6\mathrm{FBP}}+[\mathrm{FBP}]+\frac{[\mathrm{GAP}] K_{6\mathrm{DHAP}} V_{6\mathrm{f}}}{K_{6\mathrm{eq}} V_{6\mathrm{r}}}+\frac{[\mathrm{DHAP}] K_{6\mathrm{GAP}} V_{6\mathrm{f}}}{K_{6\mathrm{eq}} V_{6\mathrm{r}}}+\frac{[\mathrm{FBP}][\mathrm{GAP}]}{K_{6\mathrm{IGAP}}}+\frac{[\mathrm{GAP}][\mathrm{DHAP}] V_{6\mathrm{f}}}{K_{6\mathrm{eq}} V_{6\mathrm{r}}}}$ $v_{\leftarrow} = \frac{V_{6\mathrm{f}} \frac{[\mathrm{GAP}][\mathrm{DHAP}]}{K_{6\mathrm{eq}}}}{K_{6\mathrm{FBP}}+[\mathrm{FBP}]+\frac{[\mathrm{GAP}] K_{6\mathrm{DHAP}} V_{6\mathrm{f}}}{K_{6\mathrm{eq}} V_{6\mathrm{r}}}+\frac{[\mathrm{DHAP}] K_{6\mathrm{GAP}} V_{6\mathrm{f}}}{K_{6\mathrm{eq}} V_{6\mathrm{r}}}+\frac{[\mathrm{FBP}][\mathrm{GAP}]}{K_{6\mathrm{IGAP}}}+\frac{[\mathrm{GAP}][\mathrm{DHAP}] V_{6\mathrm{f}}}{K_{6\mathrm{eq}} V_{6\mathrm{r}}}}$
7:	$v_{\rightarrow} = \frac{V_{7\mathrm{m}}[\mathrm{DHAP}]}{K_{7\mathrm{DHAP}}+[\mathrm{DHAP}]+\frac{K_{7\mathrm{DHAP}}}{K_{7\mathrm{GAP}}}[\mathrm{GAP}]}$ $v_{\leftarrow} = \frac{V_{7\mathrm{m}} \frac{[\mathrm{GAP}]}{K_{7\mathrm{eq}}}}{K_{7\mathrm{DHAP}}+[\mathrm{DHAP}]+\frac{K_{7\mathrm{DHAP}}}{K_{7\mathrm{GAP}}}[\mathrm{GAP}]}$
8:	$v_{\rightarrow} = \frac{V_{8\mathrm{m}}[\mathrm{GAP}][\mathrm{NAD^+}]}{K_{\mathrm{GAP}} K_{\mathrm{NAD}}\left(1+\frac{[\mathrm{GAP}]}{K_{\mathrm{GAP}}}+\frac{[\mathrm{BPG}]}{K_{\mathrm{BPG}}}\right)\left(1+\frac{[\mathrm{NAD^+}]}{K_{\mathrm{NAD}}}+\frac{[\mathrm{NADH}]}{K_{\mathrm{NADH}}}\right)}$ $v_{\leftarrow} = \frac{V_{8\mathrm{m}} \frac{[\mathrm{BPG}][\mathrm{NADH}]}{K_{8\mathrm{eq}}}}{K_{\mathrm{GAP}} K_{\mathrm{NAD}}\left(1+\frac{[\mathrm{GAP}]}{K_{\mathrm{GAP}}}+\frac{[\mathrm{BPG}]}{K_{\mathrm{BPG}}}\right)\left(1+\frac{[\mathrm{NAD^+}]}{K_{\mathrm{NAD}}}+\frac{[\mathrm{NADH}]}{K_{\mathrm{NADH}}}\right)}$
9:	$v_{\rightarrow} = k_{9\mathrm{f}}[\mathrm{BPG}][\mathrm{ADP}]$ $v_{\leftarrow} = k_{9\mathrm{r}}[\mathrm{PEP}][\mathrm{ATP}]$

Table 5.3: The rate equations of the model

r	rate equation (v_r)
10:	$v_{\rightarrow} = \frac{V_{10\mathrm{m}}[\mathrm{ADP}][\mathrm{PEP}]}{(K_{10\mathrm{PEP}}+[\mathrm{PEP}])(K_{10\mathrm{ADP}}+[\mathrm{ADP}])}$
11:	$v_{\rightarrow} = \frac{V_{11\mathrm{m}}[\mathrm{Pyr}]}{K_{11}+[\mathrm{Pyr}]}$
12:	$v_{\rightarrow} = \frac{V_{12\mathrm{m}}[\mathrm{ACA}][\mathrm{NADH}]}{(K_{12\mathrm{NADH}}+[\mathrm{NADH}])(K_{12\mathrm{ACA}}+[\mathrm{ACA}])}$
13:	$v_{\rightarrow} = k_{13}[\mathrm{EtOH}]$ $v_{\leftarrow} = k_{13}[\mathrm{EtOH_x}]$
14:	$v_{\rightarrow} = y_{\mathrm{vol}}k_0[\mathrm{EtOH_x}]$
15:	$v_{\rightarrow} = \frac{V_{15\mathrm{m}}[\mathrm{DHAP}]}{K_{15\mathrm{DHAP}}\left(1+\frac{K_{15\mathrm{INADH}}}{[\mathrm{NADH}]}\left(1+\frac{[\mathrm{NAD^+}]}{K_{15\mathrm{INAD}}}\right)\right)+[\mathrm{DHAP}]\left(1+\frac{K_{15\mathrm{NADH}}}{[\mathrm{NADH}]}\left(1+\frac{[\mathrm{NAD^+}]}{K_{15\mathrm{INAD}}}\right)\right)}$
16:	$v_{\rightarrow} = k_{16}[\mathrm{glycerol}]$ $v_{\leftarrow} = k_{16}[\mathrm{glycerol_x}]$
17:	$v_{\rightarrow} = y_{\mathrm{vol}}k_0[\mathrm{glycerol_x}]$
18:	$v_{\rightarrow} = k_{18}[\mathrm{ACA}]$ $v_{\leftarrow} = k_{18}[\mathrm{ACA_x}]$
19:	$v_{\rightarrow} = y_{\mathrm{vol}}k_0[\mathrm{ACA_x}]$
20:	$v_{\rightarrow} = y_{\mathrm{vol}}k_{20}[\mathrm{ACA_x}][\mathrm{CN_x^-}]$
21:	$v_{\rightarrow} = y_{\mathrm{vol}}k_0[\mathrm{CN_x^-}]_0$ $v_{\leftarrow} = y_{\mathrm{vol}}k_0[\mathrm{CN_x^-}]$
22:	$v_{\rightarrow} = k_{22}[\mathrm{ATP}][\mathrm{G6P}]$
23:	$v_{\rightarrow} = k_{23}[\mathrm{ATP}]$
24:	$v_{\rightarrow} = k_{24\mathrm{f}}[\mathrm{AMP}][\mathrm{ATP}]$ $v_{\leftarrow} = k_{24\mathrm{r}}[\mathrm{ADP}]^2$

Table 5.3: The rate equations of the model

5.4 Optimization

With the reaction network, the rate equations, and the extreme currents in place, we can now perform the actual optimization where we scan relevant parts of the space of unknown parameters and variables. The convex coefficients are scanned with selected step intervals. For all other parameters and variables, the possible values sometimes span several decades, so these are scanned with selected step factors.

Recall from chapter 3 that a large number of experimental properties can be included in the model validation, and that the computational costs of these validations are very different. Therefore, we use an optimization strategy where we first do broad scans with only a few simple validations. At later stages of the optimization, more expensive validations are included. See also section 5.2.

Optimization software

The program used for the optimization is written in pascal by Finn Hynne and runs on HP workstations only. This software is no longer maintained, but a complete re-implementation of the program in C++ for the linux platform is currently under development by Morten Garkier Hendriksen at our department. In this new implementation, clusters of computers can be utilised for parallel computations, and a huge database will be used to store previously encountered good points. The program design is highly modular, so it will be possible to adopt advanced search strategies and data visualisation procedures.

I will briefly indicate the structure of Finn Hynne's program, which was used in the present work. After initialisation, partly from an input file specifying the run mode, where to search, and criteria for output etc, the main part consists of nested loops for scanning intrinsic parameters, convex coefficients, reverse reactions, and concentrations.

The inner loop basically treats one point. It calculates net velocities from convex coefficients, then all velocities using also information about reverse velocities. At this stage, variables are adjusted for interdependencies which would be awkward to account for in the loop structure. Now the Jacobi matrix is calculated and diagonalized. If only eigenvalues are needed, we use a QR algorithm for a matrix obtained from $\mathbf{J}$ by balancing and reduction to Hessenberg form as described in Press *et al.* (1989). When the eigenvectors are needed as well, the algorithm by Eberlein is used; see Wilkinson and Reinsch (1971). Depending on the current stage of the optimization, each of the calculations from the inner loop is either output to a file or used in further calculations as indicated below.

Initial stages of the optimization

The first task is to find regions (of the set of unknown variables and parameters) where the system shows oscillations, *i.e.* where the spectrum of eigenvalues of the Jacobi matrix includes a complex conjugate pair. When regions with oscillatory modes have been located, we consider the stability of the modes. We need regions where one oscillatory mode can become unstable, whereas all other modes are stable. In these initial searches, it is sufficient to determine the set of eigenvalues of each point, which is much faster than finding also the eigenvectors. In these stages of the optimization we simply output one character which summarises the properties of the stationary state calculated in the inner loop, and go on to the next loop iteration. On an HP 715/75 workstation this can be done at a rate of about 5000 points per minute.

Late stages of the optimization

In the late stages of the optimization, we search relevant regions found in the initial phase, locate Hopf bifurcations, calculate the relevant dynamical properties of the model at the bifurcations, and compare these with the experimental values.

Eigenvectors need only be calculated for points describing a Hopf bifurcation and where the frequencies of oscillation meet given criteria. In order to locate points a at Hopf bifurcations, we look for points where the real part of the eigenvalue of the (relevant) oscillatory mode becomes zero using a root-finding algorithm.

So, for each iteration in the inner loop, we test whether there is an oscillatory mode, if the previous point had an oscillatory mode as well, and if there is a change of sign of the real part of the eigenvalue, λ, associated with that mode between the previous point and the present one. (The inner loop variable is carefully selected to suit the search for Hopf bifurcations; in the present optimization, we search with the intracellular glucose concentration). If these tests indicate that a Hopf bifurcation might be found for some value of the inner loop variable in the interval between the last two points, we enter a search for the bifurcation point, using an algorithm due to van Wijngaarden, Dekker, and Brent, see Press *et al.* (1989). The algorithm finds a zero of $\mathrm{Re}(\lambda)$ and the frequency of oscillation at that point as $\omega_0 = \mathrm{Im}(\lambda)$.

When scanning over all stationary net velocities, it is convenient to first scan over all relevant normalised velocities (see Eq. 5.4), and subsequently scan over all relevant magnitudes of the velocity $j_0 v_0$. A normalised velocity determines the fractions of the glycolytic flow that go through the different branches. The magnitude of the velocity vector determines in a rough sense the total glycolytic flux, and this magnitude is a prime factor determining the frequency of oscillations near a Hopf bifurcation (see the section "A scaling principle" in Hynne *et al.* (1993b)). It also determines the experimentally known extracellular glucose concentration $[\mathrm{Glc_x}]$, and maintaining agreement with frequency and $[\mathrm{Glc_x}]$ simultaneously constitutes an important restraint during the optimisation.

If the frequency agrees with the experimental value to within assigned limits, the eigenvectors associated with the oscillatory mode are calculated, and from these, the desired dynamical properties of the model are found, in particular amplitudes and phases of oscillatory concentrations, and quenching concentrations and quenching phases of species as explained in chapter 3. During the optimization, we also calculate the normal form parameter σ' with a special method building on an interpretation of the normal form. The sign of this parameter determines the "direction" of the bifurcation, and it was necessary to check it because it was wrong in a large fraction of the bifurcation points found.

The calculated dynamical properties are compared with experimental values, and if all properties agree to within assigned limits, all or selected parts of the data for the bifurcating stationary point are output. In any case the calculation proceeds to the next loop iteration. The speed at which these computations can be made depends very much on how often eigenvectors must be calculated. In our final scans with a large fraction of Hopf points, we could treat well over 400 points per minute on the HP 715/75 workstation.

Final calculations

When the best possible fit of model properties to experimental values has been found, the resulting rate constants and maximum velocities are obtained from Eq. 3.2, and all data of the optimum model are collected. In practice, we do not obtain one perfect fit, but must choose the "best" one through a somewhat subjective compromise between conflicting criteria. Therefore, we record data for all points meeting less strict criteria, and select a best fit by searching and filtering the output.

At this stage, candidates for the best model have been found, but we still need to make sure that their bifurcations are indeed supercritical Hopf bifurcations – they could just as well be subcritical, and in this case the model would not be acceptable as the final result. We do this by calculating their Stuart-Landau parameters as described in Ipsen *et al.* (1998); these calculations were not done during the optimization because they are much too time consuming.

As a check, we integrate the kinetic equations of the model with all the parameters as determined at the optimum, and using the optimum concentrations as initial values. Since, by design, the concentrations correspond to a stationary state, all concentrations must remain absolutely constant in the integration provided the values for all parameters and initial concentrations are given with high accuracy. This check on the consistency of data set and model is extremely sensitive to errors.[1]

5.5 Result of the optimization

As the result of the optimization just described, we have chosen a single point as "the best fit", and this point will be presented here. To select this point, we have investigated the properties of more than 100 million points. Of course, this is not at all an exhaustive scan of parameter space. On the other hand, points with good fits are only rarely encountered, and of those this one is the one which we have judged to give the best fit. So, even though it is impossible to guarantee that this is the best point, it is nevertheless special in the sense that it produces an exceptionally good fit compared to many millions of other possible points.

An important limitation of the optimization is that it is local. This is essential for the efficiency the method, but it also limits the properties that can be taken into account. I will now present the properties of the model defined by this point at the operating point of the optimization. Further integration of the kinetic equations to investigate the behaviour of the model in

[1]Users of our data, who wish to make a such check, should consult the tables of section 7 in Hynne *et al.* (2001) where we gave the model parameters with much higher precision than would otherwise be appropriate.

the neighbourhood of the bifurcation point, determine bifurcation diagrams, study synchronization behaviour etc. are reported in chapter 6.

Parameters defining the model

In some sense, the immediate result of the optimization is the set of velocity parameters presented in Table 5.4. They merely serve to define the model, since no experimental data are available for comparison. The other parameters needed to define the model are the intrinsic parameters which are displayed in Table 5.5. These parameters are generally in good agreement with the literature values. (The rate constants k_{13}, k_{16}, and k_{18} are repeated from Table 5.4 to exhibit their interrelation used in the optimization.)

The only major discrepancies between experimentally determined intrinsic parameters and those of the model are the values of $K_{3\mathrm{Glc}}$ and $K_{4\mathrm{eq}}$. These parameters could not come closer to the experimentally reported values without seriously impairing the overall fit of the model. The constant $K_{15\mathrm{DHAP}}$ may appear to disagree with the experimental value, but this is due to the fact that $K_{15\mathrm{DHAP}}$ in the model includes the effect of inorganic phosphate (11 mM; Richard *et al.* (1996b)) found in the yeast cells (see Cai *et al.* (1996) for details on the effect of $\mathrm{P_i}$ on G3PDH). The equilibrium constant $K_{7\mathrm{eq}}$ is also somewhat off. This is due to an internal inconsistency of the experimental data which is discussed below in connection with the result for the stationary metabolite concentrations.

To completely define the model, the kinetic parameters must be supplemented with the value of the ratio between the extracellular volume and the total cytosolic volume, y_{vol}, given in Table 5.7. It can be considered part of the specification of the operating point insofar as it depends on the cell density of the suspension, but it may be said to enter the kinetic equations of the two-phase model in a more fundamental way than other operating point data (see Eq. 5.2). As we mentioned in section 5.2, we could not determine a consistent value for y_{vol} from data in the literature, but for an order of magnitude comparison, we quote a value deduced from comparable transient experiments (Richard *et al.*, 1996b).

Operating point and stationary concentrations

It is particularly important to evaluate the model for the specific conditions used for the optimization. These are specified by the operating point shown

Table 5.4: Calculated maximum velocities and rate constants. For extracellular reactions, the values have been corrected (by y_{vol}) so that they refer to the extracellular volume.

r	reaction	parameter	forward	reverse
1	inGlc	k_0/min^{-1} †	0.048	0.048
2	GlcTrans	$V_{2\mathrm{max}}/\mathrm{mM\,min}^{-1}$	1.015×10^3	1.015×10^3
3	HK	$V_{3\mathrm{max}}/\mathrm{mM\,min}^{-1}$	5.175×10^1	
4	PGI	$V_{4\mathrm{max}}/\mathrm{mM\,min}^{-1}$	4.960×10^2	4.960×10^2
5	PFK	$V_{5\mathrm{max}}/\mathrm{mM\,min}^{-1}$	4.543×10^1	
6	ALD	$V_{6\mathrm{max}}/\mathrm{mM\,min}^{-1}$	2.208×10^3	1.104×10^4
7	TIM	$V_{7\mathrm{max}}/\mathrm{mM\,min}^{-1}$	1.164×10^2	1.164×10^2
8	GAPDH	$V_{8\mathrm{max}}/\mathrm{mM\,min}^{-1}$	8.339×10^2	8.339×10^2
9	lpPEP	$k_9/\mathrm{mM}^{-1}\,\mathrm{min}^{-1}$	4.439×10^5	1.529×10^3
10	PK	$V_{10\mathrm{max}}/\mathrm{mM\,min}^{-1}$	3.431×10^2	
11	PDC	$V_{11\mathrm{max}}/\mathrm{mM\,min}^{-1}$	5.313×10^1	
12	ADH	$V_{12\mathrm{max}}/\mathrm{mM\,min}^{-1}$	8.980×10^1	
13	difEtOH	k_{13}/min^{-1} ‡	1.672×10^1	1.672×10^1
14	outEtOH	k_0/min^{-1} †	0.048	
15	lpGlyc	$V_{15\mathrm{max}}/\mathrm{mM\,min}^{-1}$	8.148×10^1	
16	difGlyc	k_{16}/min^{-1} ‡	1.9	1.9
17	outGlyc	k_0/min^{-1} †	0.048	
18	difACA	k_{18}/min^{-1} ‡	2.47×10^1	2.47×10^1
19	outACA	k_0/min^{-1} †	0.048	
20	lacto	$k_{20}/\mathrm{mM}^{-1}\,\mathrm{min}^{-1}$	2.838×10^{-3}	
21	inCN	k_0/min^{-1} †	0.048	0.048
22	storage	$k_{22}/\mathrm{mM}^{-1}\,\mathrm{min}^{-1}$	2.259	
23	consum	k_{23}/min^{-1}	3.208	
24	AK	$k_{24}/\mathrm{mM}^{-1}\,\mathrm{min}^{-1}$	4.329×10^2	1.333×10^2

†: not calculated; fixed during the optimization.
‡: not calculated; varied during the optimization.

Table 5.5: Comparison with literature: Intrinsic parameters (defined in Table 5.3). Literature values in parenthesis are parameters from other models which are cited because no biochemical data are available. a: isozyme PII. b: isozyme PI. c: this equilibrium constant is inconsistent with the measurements of metabolite concentrations and fluxes. d: apparent equilibrium constant with the concentration of inorganic phosphate fixed at the mean value 11 mM (Richard *et al.*, 1996b). e: isozyme I. f: See Appendix D. g: the apparent value of $K_{15\mathrm{DHAP}}$ will be significantly higher due to the presence of inorganic phosphate (Cai *et al.*, 1996). Conditions: 25°C, pH = 7.0 where possible. See Table 5.6 for references.

reaction	parameter	model	literature	reference index
GlcTrans	$K_{2\mathrm{Glc}}$	1.7	1.1, 1.7	[1,2]
	$K_{2\mathrm{IG6P}}$	1.2	1.2	[3]
	$K_{2\mathrm{IIG6P}}$	7.2	7.2	[3]
	P_2	1	1, 1.87	most plausible value, [4]
HK	$K_{3\mathrm{ATP}}$	0.1	0.1, 0.15^a, 0.2^b, 0.29^a, 0.3^b	[5,6,6,7,7]
	$K_{3\mathrm{Glc}}$	0	0.1, 0.12^b, 0.12^a,0.12^b	[5,8,8,6]
			0.23^a, 0.2-0.3^b, 0.25-0.6^a	[6,7,7]
	$K_{3\mathrm{DGlc}}$	0.37		
PGI	$K_{4\mathrm{G6P}}$	0.8	0.27, 0.3, 0.7, 0.8, 1.5	[9]
	$K_{4\mathrm{F6P}}$	0.15	0.11, 0.15, 0.23	[9]
	$K_{4\mathrm{eq}}$	0.13	0.3	[10,11]
PFK	K_5	0.021	(0.0016)	[12]
	κ_5	0.15	(0.017)	[12]
ALD	$V_{6\mathrm{r}}/V_{6\mathrm{f}}$	5	(5)	[13]
	$K_{6\mathrm{eq}}$	0.081	0.08, 0.081	[14,15]
	$K_{6\mathrm{FBP}}$	0.3	(0.3)	[13]
	$K_{6\mathrm{GAP}}$	4.0	(2.0)	[13]
	$K_{6\mathrm{DHAP}}$	2.0	(2.0)	[13]
	$K_{6\mathrm{IGAP}}$	10.0	(10.0)	[13]
TIM	$K_{7\mathrm{DHAP}}$	1.23	1.23	[16]
	$K_{7\mathrm{GAP}}$	1.27	1.27	[16]
	$K_{7\mathrm{eq}}$	0.055	0.045^c	[10]
GAPDH	$K_{8\mathrm{GAP}}$	0.6	0.6	[17]
	$K_{8\mathrm{BPG}}$	0.01		
	$K_{8\mathrm{NAD}}$	0.1	0.1	[17]
	$K_{8\mathrm{NADH}}$	0.06		
	$K_{8\mathrm{eq}}$	0.0055^d	0.0055^d	[18]
PK	$K_{10\mathrm{ADP}}$	0.17	0.16 - 0.17, 0.36	[9,19]
	$K_{10\mathrm{PEP}}$	0.2	0.099, 0.2	[20,19]
PDC	K_{11}	0.3	(0.3)	[12]
ADH	$K_{12\mathrm{ACA}}$	0.71	0.84, 0.93, 1.1^e	[21,22,23]
	$K_{12\mathrm{NADH}}$	0.1	0.084, 0.096, 0.110^e	[21,22,23]
difEtOH	k_{13}	$k_{16} \times 8.8$	$k_{16} \times 8.8^f$	[24]
G3PDH	$K_{15\mathrm{NADH}}$	0.13	0.13, 0.023, 0.016 - 0.027	[25,26,9]
	$K_{15\mathrm{DHAP}}$	25	0.54^g, 1.6^g	[26,25]
	$K_{15\mathrm{INADH}}$	0.034	0.034	[25]
	$K_{15\mathrm{INAD}}$	0.13	0.13, 0.93	[25,26]
difGlyc	k_{16}	1.9		
difACA	k_{18}	$k_{16} \times 13$	$k_{16} \times 13^f$	[24]

Table 5.6: Reference lookup table for Table 5.5.

index	reference	index	reference
[1]	Azam and Kotyk (1969)	[14]	Goldberg and Tewari (1995a)
[2]	Teusink *et al.* (1998a)	[15]	Enzyme handbook (1969)
[3]	Rizzi *et al.* (1996)	[16]	Krietsch (1975)
[4]	Kotyk (1967)	[17]	Byers (1982)
[5]	Crane (1962)	[18]	Goldberg *et al.* (1993)
[6]	Kopetzki and Entian (1985)	[19]	Barwell and Hess (1972)
[7]	Barnard (1975)	[20]	Aust *et al.* (1975)
[8]	Fernández *et al.* (1985)	[21]	Dickenson and Dickinson (1976)
[9]	BRENDA (2000)	[22]	Dickinson and Monger (1973)
[10]	Goldberg and Tewari (1995b)	[23]	Ganzhorn *et al.* (1987)
[11]	Goldberg (1999)	[24]	Jain and Wagner (1980)
[12]	Nielsen *et al.* (1998)	[25]	Cai *et al.* (1996)
[13]	Richter *et al.* (1975)	[26]	Albertyn *et al.* (1992)

in Table 5.7. Besides the volume ratio y_{vol} expressing the cell density of the suspension, this is given by the flow rates of the CSTR at the bifurcation point: the specific flow rate and the mixed flow concentrations of extracellular glucose and cyanide. These flow rates agree exactly with the conditions of the experiment, *i.e.* it is possible for the model to work at the experimental operating point. (Table 5.7 also shows two fluxes characteristic of the metabolic activity. These are discussed below).

Table 5.7: Comparison with experiments: Operating point. (Experimental data from Richard *et al.* (1994, 1996b); Danø *et al.* (1999) as described in section 5.2).

	parameter	model	exp
Volume ratio	y_{vol}	59	$\sim$45
Specific flow rate at bifurcation	k_0/min^{-1}	0.048	0.048
Mixed flow glucose concentration	$[\mathrm{Glc_x}]_0/\mathrm{mM}$	18.5	18.5
Mixed flow cyanide concentration	$[\mathrm{CN_x^-}]_0/\mathrm{mM}$	5.60	5.60
Glycolytic flux	$j_0 v_0/\mathrm{mM\,min}^{-1}$	28	$\sim$27
Cellular glucose uptake rate	$k_0\left([\mathrm{Glc_x}]_0 - [\mathrm{Glc_x}]\right) y_{\mathrm{vol}}/\mathrm{mM\,min}^{-1}$	48	

Table 5.8: Comparison with experiments related to metabolites: concentration c_s of species s, oscillation amplitude, a_s, in units of the NADH-amplitude, a_{NADH}. Oscillation phase θ_s, in degrees relative to the phase of NADH, quenching concentration q_s in units of $q_{\mathrm{ACA_x}}$, and quenching phase in degrees relative to the oscillation phase of NADH. Experimental data are from Richard *et al.* (1994, 1996a,b); Danø *et al.* (1999); Hynne *et al.* (2001) as described in section 5.2.

species	c_s/mM		a_s/a_{NADH}		θ_s/deg		$q_s/q_{\mathrm{ACA_x}}$		ϕ_s/deg	
	mod	exp	mod	exp	mod	exp	mod	exp	mod	exp
$\mathrm{Glc_x}$	1.55	1.6	0.013		135		5.3	11	355	4
Glc	0.57		1.83		12		18		81	
G6P	4.2	4.1	15.8	21	190	260	1.7		67	
F6P	0.49	0.5	2.16	2.7	178	250	1.7		72	
FBP	4.64	5.1	22.2	26	32	70	4.4		218	
GAP	0.115	0.12	0.295	0.04	30		7.0		255	
DHAP	2.95	2.5	6.97	0.5	38		7.9		195	
BPG	$3{\cdot}10^{-4}$	n.d.	0.002		136		0.53		287	
PEP	0.04	0.04	0.023	0.07	18		1.1		286	
Pyr	8.7	8.7	4.06	7	79		125		180	
ACA	1.48		0.894		196		2.5		268	
EtOH	19.2		1.22		26		∞		undef	
$\mathrm{EtOH_x}$	16.5	$7.1^{\dagger}$	0.035		114		∞	n.p.	undef	
Glyc	4.2		1.68		98		∞		undef	
$\mathrm{Glyc_x}$	1.68	$1.3^{\dagger}$	0.005		188		∞	n.p.	undef	
$\mathrm{ACA_x}$	1.29	$0.07^{\dagger}$	0.037	$0.3^{\ddagger}$	284	200	1	1	181	172
$\mathrm{CN_x^-}$	5.2		$5{\cdot}10^{-5}$		193		2400	n.p.	271	
ATP	2.1	2.1	10.8	8	139	180	0.50		289	
ADP	1.5	1.5	6.32	9.4	319	0	1.0		290	
AMP	0.33	0.33	4.5	3.6	319	0				
NADH	0.33	0.33	1	1	0	0	0.68		106	
$\mathrm{NAD^+}$	0.65	0.65	1	0.6	180	180				

†: Transient experiment; not directly comparable with CSTR results for extracellular metabolites.
‡: According to Teusink (1999), the amplitude of $\mathrm{ACA_x}$ is three to five times smaller than the value given here.
n.p.: quenching was attempted but was not possible.
n.d.: not detectable.

Once the operating point has been specified, we have a self-contained model for which the properties can be investigated by integration. However, we know beforehand that if the operating point is chosen as in Table 5.7, the model has a stationary state with stationary concentrations given by Table 5.8, and indeed that a supercritical Hopf bifurcation occurs exactly at that point (with the mixed flow glucose concentration as bifurcation parameter). These properties were used to select the best point in the optimization process. Note however, that the stationary point shown in Table 5.8 need not be unique: there could be other (stable or unstable) stationary states for the same model and operating point, and other persistent states like *e.g.* stable limit cycles could also coexist with the stationary point of Table 5.8.

These remarks on possible non-uniqueness are really irrelevant to the optimization insofar as we have no knowledge of such behaviour either in the model or in the experiments. We only mention the possibility to emphasise that, once the model has been obtained, it remains well defined even without knowledge about the point in concentration space shown in Table 5.8. That said, the fact that we have a bifurcating stationary point, that is designed to model a specific bifurcating stationary point in a well defined experiment, is very important. It is a rich source of additional experimental data, that can be immediately compared with the model. Table 5.8 makes that comparison as well.

By design, the stationary concentrations predicted by the model agree very well with experiments. The concentrations of G6P, F6P, FBP, GAP, PEP, Pyr, ATP, ADP, AMP, NADH and NAD^+ agree with the transient experiments within experimental error, assuming that these intracellular concentrations do not change much from the bifurcation point used to the conditions of the transient experiments; DHAP is 18% higher than the reported value. However, this is due to an inconsistency in the experimental data: with the experimental values of [GAP] and [DHAP] and the experimental equilibrium constant $K_{7\mathrm{eq}}$, the TIM reaction is almost at equilibrium; in fact, it has a small net velocity in the direction from GAP to DHAP, *i.e.* opposite to the substantial net flux (≈ 23 mM/min) from DHAP to GAP required by other reliable experimental data. Therefore, [DHAP] has been increased a little in order to obtain a reasonable value for the equilibrium constant $K_{7\mathrm{eq}}$ of this reaction, somewhat higher than the experimental value (see Table 5.5).

As mentioned already, the extracellular species measured in transient experiments ($\mathrm{EtOH_x}$, $\mathrm{ACA_x}$ and $\mathrm{Glyc_x}$) are not directly comparable to those at the Hopf bifurcation in the CSTR. We have measured the extracellular glucose concentration in the CSTR, and the model agrees with this value within 5%.

Flux distributions and magnitude

A property of the model of considerable biochemical importance is the total glycolytic flux (defined *e.g.* as the velocity of the PFK-reaction) and the contributions to that flux from the various branches: fermentation, glycerol formation (with or without lactonitrile formation), and glycogen buildup. Table 5.7 shows the total glycolytic flux. It agrees with estimates from comparable transient experiments. A related measure of overall metabolic rate is the cellular glucose uptake activity, also shown in Table 5.7, which includes the glucose build into glycogen. By our convention, it is given as an intracellular velocity (and equals *e.g.* the velocity of the HK reaction because of stationarity).

Table 5.9: Comparison with experiments: Branching of glycolysis in terms of normalised convex coefficients, see Eqs. (5.3) and (5.4). (Experimental data from Betz and Hinrichs (1968) and Richard *et al.* (1994) as described by Danø (1999) p. 117-118).

branch	convex coef	model	exp
Glycolysis and fermentation	j_{ferm}	0.12	0.12
Glycerol production	j_{glyc}	0.13	0.13
Lactonitrile formation	j_{lact}	0.04	0.04
Glycogen buildup	j_{stor}	0.71	0.71

Table 5.9 shows the branching fractions of the glycolytic flux together with values deduced from experiments as discussed in section 5.2. We see that the model branchings agree with the experimental estimates. As an illumination of the meaning of these figures, we note that the storage process contributes $j_{\text{stor}} j_0 v_0$ to the glycolytic flux and the same to glycogen buildup, so the total glucose uptake rate can also be calculated as $(1 + j_{\text{stor}}) j_0 v_0$, which agrees with the figure quoted in Table 5.7 (to within rounding errors).

Dynamics

Comparison of dynamical properties of the model with experiments forms a significant part of the optimization, and Tables 5.8 and 5.10 show how close an agreement it was possible to attain. First of all the model has a Hopf bifurcation at the experimental value of the mixed flow glucose concentration. The bifurcation is supercritical (g' is negative) and occurs in the correct 'direction' (σ' is positive) so the limit cycle oscillations appear for increasing values of the mixed flow glucose concentration; these features agree with the experiments.

Table 5.10: Comparison with experiments: Dynamics. (Experimental data from Danø *et al.* (1999) as described in section 5.2. See also Fig. 4.8).

	parameter	model	exp
Angular frequency at bifurcation	ω_0/min^{-1}	10.05	10.05
Rate of change of instability[a]	σ'/min^{-1}	0.0579	> 0
Rate of change of frequency[a]	σ''/min^{-1}	−0.112	
Nonlinearity parameter, real part	g'/min^{-1}	−1124	< 0
Nonlinearity parameter, imaginary part	$g''/\text{ min}^{-1}$	−1586	> 0
Rate of change of amplitude[b]	$2\sqrt{-\sigma'/g'}$	0.0144	
Rate of change of frequency[c]	$(\sigma'' - \sigma' g''/g')/\text{min}^{-1}$	−0.194	0.055

[a]at the stationary point as a function of μ.
[b]of the limit cycle as a function of $\sqrt{\mu}$ in units of mM NADH.
[c]of the limit cycle as a function of μ.

The angular frequency ω_0 of the model (which is $2\pi/T_0$ with T_0 the period of oscillations near the stationary point at the bifurcation), is in perfect agreement with the CSTR experiments as Table 5.10 shows. The rate of change of frequency of the limit cycle oscillations with the mixed flow glucose concentration can also be compared with experiments. It has a wrong sign in the model, which predicts that the frequency decreases with the mixed flow concentration whereas in fact it increases. According to the fit of Stuart-Landau parameters to the quenching experiments (Fig. 4.8), the ratio g''/g' has the wrong sign too, so we cannot say whether the error in the frequency variation of the limit cycle with $[\text{Glc}_\text{x}]_0$ as the bifurcation parameter is due to a wrong sign of σ'' or g''.

Other dynamical properties that have played an important role in the optimization are compared with experiments in Table 5.8. These include first of all the fairly accurate quenching data obtained from the CSTR experiments. We see from Table 5.8 that the quenching phases ϕ_s for extracellular glucose and for extracellular acetaldehyde agree to within 9 degrees with the experimental values. The experimental quenching concentrations must be scaled with the amplitude of the [NADH] oscillations for the comparison, but the fluorescence measurements of the CSTR experiments did not provide absolute values, unfortunately. Consequently we can only compare the ratio of $q_{\mathrm{Glc_x}}$ and $q_{\mathrm{ACA_x}}$. It is 5.3 in the model as compared to 11.3 in the experiments.

Thanks to work by Richard and coworkers, we also know a number of oscillation amplitudes and phases approximately. The relative amplitudes of most of the metabolites also agree rather well with those determined in the transient experiments – especially when considering the rather large experimental errors discussed in section 5.2. Still, the relative amplitudes of GAP, DHAP and $\mathrm{ACA_x}$ in the model are much smaller than observed experimentally. The phases relative to NADH are wrong. However, groups of related metabolites have similar errors in their phases relative to NADH. Thus, there is a phase change of -12 degrees from G6P to F6P in the model as compared to -10 degrees in the experiments, and the relative phases of FBP, ATP, ADP, and AMP are also correct (as are $\mathrm{NAD^+}$ and NADH as a consequence of a stoichiometric constraint).

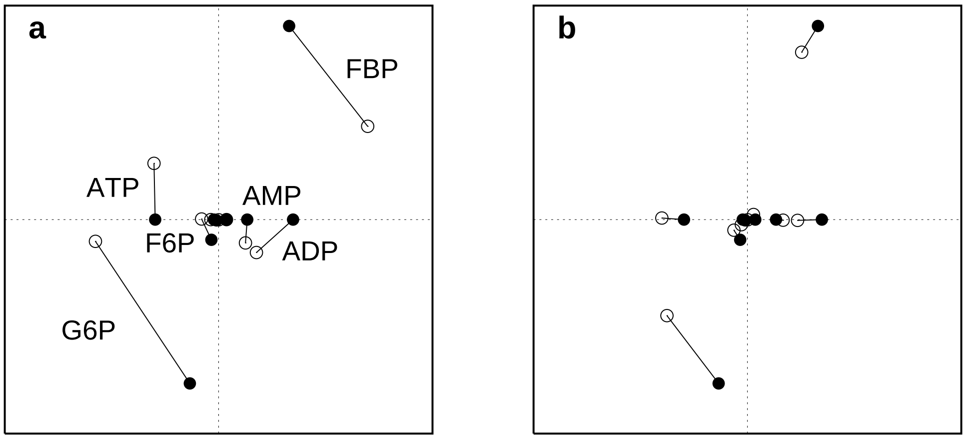

Figure 5.3: Comparison with experiments: plane of oscillations. Polar plots with the relative phases as the angles and the relative amplitudes as the moduli. This representation reflects the relative positions of the different metabolites in the coordinate system of the eigenmode corresponding to one of the two bifurcating complex eigenvalues. Since a complex eigenvector multiplied by any non-zero complex number is still an eigenvector of the system, the unit of the modulus is arbitrary as are the absolute angles. All available experimental data is plotted as •, and the corresponding data points of the model are plotted as ∘. The lines connect corresponding datapoints. The left-hand panel shows the raw data, whereas the panel on the right shows the data with all model phases shifted by +40°. (For graphical reasons NADH, $\mathrm{NAD^+}$ and $\mathrm{ACA_x}$ could not be annotated).

This is illustrated in Fig. 5.3a where the experimental values of the relative phases and amplitudes are plotted together with the corresponding values from the model. The plot is a polar plot where, for each metabolite, the angle is the relative phase and the modulus is the relative amplitude. Since the component of metabolite s of the complex eigenvector in the plane of oscillations is given by $u_s = a_s \exp(i\theta_s)$, this representation reflects the relative positions of the different metabolites in the coordinate system of the complex (oscillatory) eigenmode. Fig. 5.3b depicts the same data, but this time with all metabolites of the model phase-shifted by $+40°$. It is evident that this corrects most of the discrepancies between the model and the available experimental data (but an error of roughly $30°$ still exists for G6P and F6P).

This might indicate an inherent difficulty with stopping all cellular reactions momentarily: a phase-shift of $+40°$ corresponds to round 4s delay in the stopping reaction; a quite reasonable value for this explanation. Alternatively, the difference might signal that NADH is not handled entirely correct in the model. However, the fact that the quenching phases relative to NADH agree with the experiments seems to contradict this.

5.6 Conclusion

We have successfully applied the Direct Method of Optimization to a biochemical system and obtained a full-scale model of glycolysis and glycolytic oscillations which describes the reaction system in terms of biochemical rate expressions. The resulting model is in quantitative agreement with almost all available experimental data at the operating point of the optimization: stationary concentrations and fluxes, most enzyme kinetic parameters, the parameters defining the operating point, as well as many dynamic properties. (Analysis of the model away from the operating point of the optimization will be made in the following chapter).

To the best of my knowledge, this is a unique result. It suggests that the combined use of automated or semi-automated measurements of fluxes and metabolite concentrations, well controlled experimental setups like the CSTR, the strategy of isolating pathways *in vivo* chemically, as well as the Direct Method of Optimization offers a solution to the fundamental problem of accurately modelling an entire pathway.

6
Analysis of the full-scale model

"A Detailed model is as hard to understand as the system itself." This argument is often raised against the development of full-scale models like the one described in the previous chapter. Of course, we do not share this view. The present chapter serves to demonstrate that, indeed, it is possible to reach meaningful conclusions from an analysis of our glycolysis model. A complementary approach to the analysis of the detailed model is to reduce it systematically to a simple model, and then use this simplified model for further analysis. This approach is taken in the following chapter.

In the first part of the present chapter, we investigate the model in the neighbourhood of the operating point of the optimization with the purpose of documenting to what extent the model agrees with experimental findings when one moves away from the this operating point.

Given the detailed model, it should be possible to gain a better understanding of a number of experimental observations. The model offers an explanation for the nature of the overshoot seen when the initial glucose pulse is added in the transient experiments, and it predicts an almost constant glycolytic flux even in the transient experiments. We verify these suggestions experimentally, and present further experimental observations on the transient oscillations in the second part of the chapter.

A quantitative description can also be used to address the "classical" question of oscillating glycolysis: what makes it oscillate? This question is treated in the last part of this chapter.

6.1 Evaluation of the optimized model

The optimization leading to the results presented in the previous chapter were strictly local in the sense that only properties of the system in an (arbitrary small) neighbourhood of some stationary point were considered. The fit is quite satisfactory as far as local properties go. However, the model is meant to apply more generally, and consequently we should evaluate it outside the special point used for the optimization, the bifurcating stationary point. This evaluation is made in this section, which follows section 8 of Hynne *et al.* (2001) closely. The numerical integrations of the model were done using CHEM (Sørensen, 1999) which is based on CVODE (Cohen and Hindmarsh, 1994), and continuations were performed with the software CONT (Kohout *et al.*, 2002).

Hopf bifurcation

We first confirm explicitly that we do in fact have a supercritical Hopf bifurcation at $[\mathrm{Glc_x}]_0 = 18.5\,\mathrm{mM}$. The results of the integration of the kinetic equations are shown for the concentration of NADH in Fig. 6.1: damped oscillations decaying to a stationary state for $[\mathrm{Glc_x}]_0 = 17.0\,\mathrm{mM}$; a stationary state at the bifurcation value $[\mathrm{Glc_x}]_0 = 18.5\,\mathrm{mM}$; and oscillations growing from an unstable stationary state towards a stable limit cycle for $[\mathrm{Glc_x}]_0 = 20.0\,\mathrm{mM}$. (The change of stability of the stationary point can be demonstrated for an arbitrarily small interval around $[\mathrm{Glc_x}]_0 = 18.5\,\mathrm{mM}$, but the change can be more easily seen if the interval is not too small.)

A more detailed representation of the change of behaviour as the mixed flow glucose concentration is varied is presented in figure 6.2. Below the bifurcation, there is a stable stationary state, shown for the concentration of NADH (solid curve), which becomes unstable beyond the bifurcation (dashed curve). Beyond the bifurcation, stable limit cycle oscillations appear, indicated as a 'profile' with solid curves showing the minimum and maximum NADH concentrations during the oscillations. These two curves have vertical tangents in the bifurcation point, a behaviour characteristic of a supercritical Hopf bifurcation where the amplitude grows as the square root of the bifurcation parameter. We shall return to that question shortly.

We note that the square root dependence applies approximately only in a (fairly small) interval beyond the bifurcation. For higher values of the mixed flow glucose concentration, the amplitude of the oscillations does not change much. This behaviour agrees with the saturation of the glucose transporter

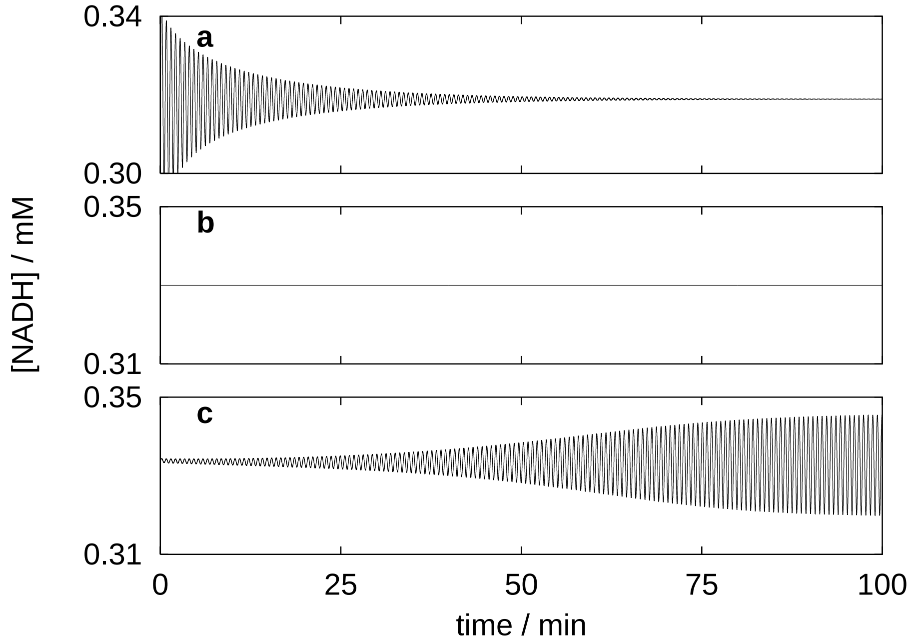

Figure 6.1: Integration of the model before the Hopf bifurcation, at the Hopf bifurcation and after the Hopf bifurcation. The mixed flow concentration of glucose, $[\mathrm{Glc_x}]_0$, is 17.0 mM in (a), 18.5 mM in (b), and 20.0 mM in (c). All other parameters as indicated in the tables of section 5.5.

observed in the experiments and, indeed, both the model and the experiments retain near-Hopf behaviour for very large values of the mixed flow glucose concentration.

Limit-cycle oscillations

During limit-cycle oscillations, all metabolites oscillate with the same frequency, but with different amplitudes and phases. Fig. 6.3 shows the oscillations of most of the metabolites at a mixed flow glucose concentration of 24 mM. This figure allows us to test the assumption, used in the optimization, that the mean intracellular metabolite concentrations at glucose saturation (in

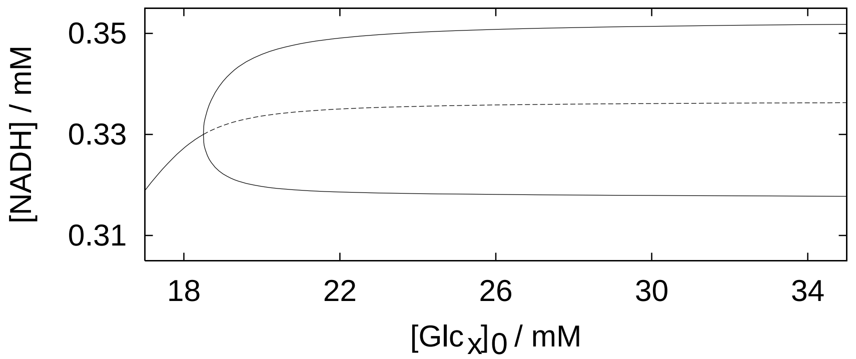

Figure 6.2: Stationary point and profile of oscillations as functions of the mixed flow concentration of glucose, $[\mathrm{Glc_x}]_0$. All other model parameters are as indicated in the tables of section 5.5.

transient experiments) will be similar to those at the bifurcation point.

We find that the assumption holds for all intracellular metabolites except Glc and Pyr, for which the average concentrations increase significantly as the mixed flow glucose concentration is increased (compare Fig. 6.3 and Table 5.8). No data from transient experiments were available on the intracellular glucose concentration, so this discrepancy is irrelevant to our optimization. Therefore, the only problem caused by this assumption is the pyruvate concentration. These considerations show that the use of concentration data from the transient experiments for the optimization of our model leads to a result which – to a large extent – is self-consistent, thus justifying the approach.

Note that the cause of the specific problem with the mean pyruvate concentration can be explained simply by the kinetics: the K_m value of the PDC reaction is so low that the enzyme is practically saturated already at the bifurcation point, so even a minor increase in glycolytic flux will cause excessive pyruvate buildup. As indicated in Table 5.5, this particular K_m value was adopted initially from another glycolytic model because we were unable to find relevant biochemical data, and tentative changes did not improve the agreement of local properties. This exemplifies the importance of having realistic parameters for the optimization of models as large as this: in practice, it is impossible to predict all possible problems that might arise outside the local optimization as a consequence of a parameter set chosen.

The assumption of slow variation with the bifurcation parameter also holds for the relative amplitudes and phases. For most species, these are practi-

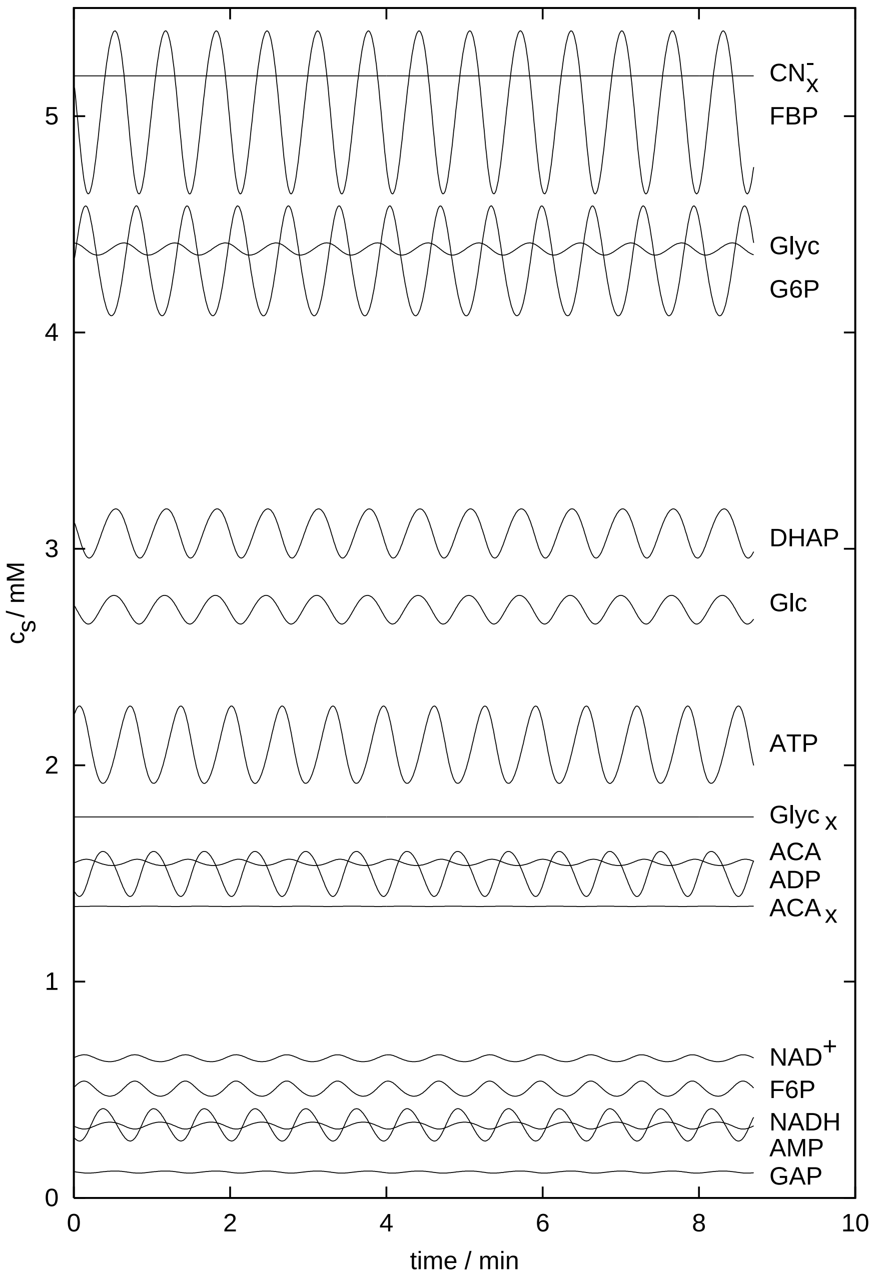

Figure 6.3: Integration of the model at a mixed flow glucose concentration of $[\mathrm{Glc_x}]_0 = 24.0$ mM. All other parameters as indicated in the tables of section 5.5. c_s designates the concentration of species s. Mean values of concentrations of metabolites that do not fit in the figure are: $[\mathrm{Glc_x}] = 6.7$ mM, $[\mathrm{BPG}] = 0.0003$ mM, $[\mathrm{PEP}] = 0.041$ mM, $[\mathrm{Pyr}] = 22$ mM, $[\mathrm{EtOH}] = 20$ mM, and $[\mathrm{EtOH_x}] = 17$ mM.

cally unchanged when the mixed flow glucose concentration is increased from 18.5 mM to 24 mM. The only exceptions are Glc_x and Glc. (At $[Glc_x]_0 =$ 24 mM we have $a_{Glc_x} = 0.049\, a_{NADH}$, $\theta_{Glc_x} = -160°$ and $a_{Glc} = 4.15\, a_{NADH}$, $\theta_{Glc} = 30°$, relative to NADH.

We may also use Fig. 6.3 to compare the absolute amplitudes of the different metabolites at $[Glc_x]_0 = 24$ mM with those of the transient experiments by Richard *et al.* (1996b). We see that the amplitudes are generally much smaller in the model. This may be so because the instability does not grow fast enough with $[Glc_x]_0$ to reach a proper size of the limit cycle before the saturation of the glucose transporter sets in. So, this discrepancy may be caused by the biochemistry of the glucose transporter and by a rather low value of σ' or high value of $|g'|$ (see Table 5.10).

Bifurcation and solution diagrams

The CSTR experiments provide detailed data on the effect of increasing the mixed flow glucose concentration, which can be directly compared with the model. Sufficiently close to a supercritical Hopf bifurcation, the amplitude of the oscillations will grow as the square root of the distance from the bifurcation point, as we have said. So, by plotting the square of the amplitude as a function of the bifurcation parameter, we should get a curve with tangent in the bifurcation point of finite slope (neither infinite nor zero). Fig. 6.4a compares the square of the amplitude of the oscillations (defined here as half the difference between the maximum and minimum NADH concentration) as a function of the bifurcation parameter $[Glc_x]_0$. Because the NADH concentration is only known to within an unknown proportionality factor, we use a least squares fit for the ordinates.

As can be seen, Fig. 6.4a confirms the generic Hopf behaviour close to the bifurcation point (tangent of finite slope) and the gradual but rather sudden transition into the behaviour resulting from the saturation of the glucose transporter. The prediction by the model is rather good. The bifurcation occurs at precisely the right value of $[Glc_x]_0$, but the saturation of the glucose transporter sets in too early in the model – the curve is initially too steep (and remember the fit for the scale of NADH concentrations).

The variation with $[Glc_x]_0$ of the frequency of the limit cycle oscillations is shown for the model and the experiments in Fig. 6.4b. They agree exactly at the bifurcation point, but the frequency decreases with $[Glc_x]_0$ in the model whereas it increases in the experiments as discussed in the previous chapter.

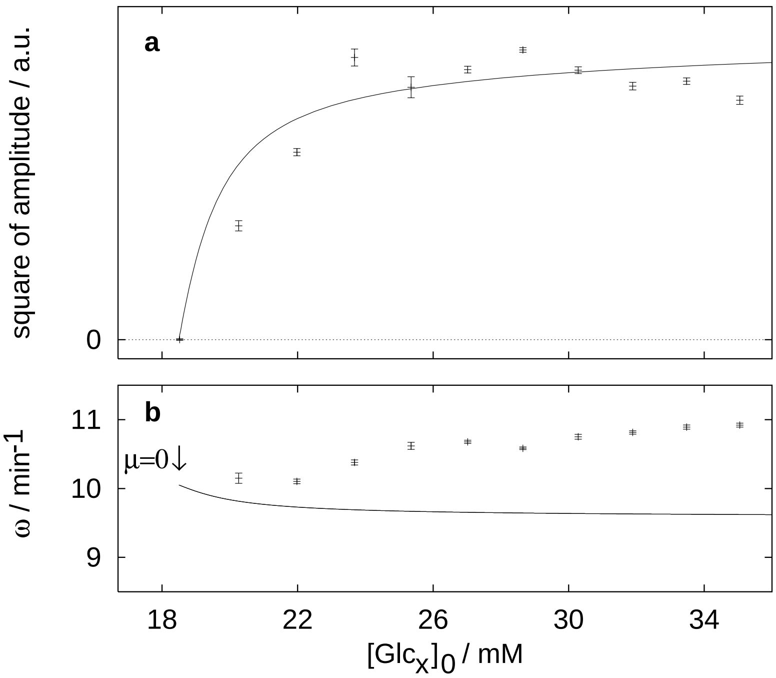

Figure 6.4: Comparison with experiments (Fig. 4.6; Danø *et al.* (1999)): Square of amplitude (a) and angular frequency (b) versus the mixed flow concentration of glucose, $[\mathrm{Glc_x}]_0$. All other model parameters as indicated in the tables of section 5.5. Discrete data points are from experiments and solid lines are model predictions. Because the experimental NADH concentration is only known to within an unknown proportionally factor, we have used a least squares fit for the ordinates in (a).

However, Fig. 6.4b shows that the frequency in the model remains close to the experimental value. For example, the period of oscillations at $[\mathrm{Glc_x}]_0 = 24\,\mathrm{mM}$ is 36 s in the experiments whereas the model predicts 39 s.

The CSTR experiments provide similar bifurcation data for $[\mathrm{CN_x^-}]_0$ as the bifurcation parameter (Fig. 4.7). The bifurcation diagram in Fig. 6.5 shows that the Hopf bifurcation at high $[\mathrm{CN_x^-}]_0$ is found in both the model and the CSTR experiments, but at different mixed flow cyanide concentrations. The Hopf bifurcation at low $[\mathrm{CN_x^-}]_0$ is not found in the model. However, this is to be expected since the initial effect of the cyanide is to block the respiratory chain of the mitochondria which are not included in the present model. So,

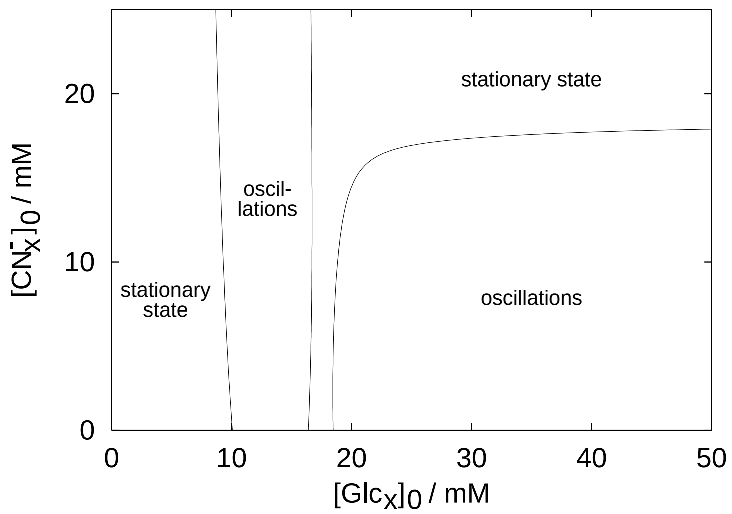

Figure 6.5: Bifurcation diagram of the model. The mixed flow concentrations $[\mathrm{Glc_x}]_0$ and $[\mathrm{CN_x^-}]_0$ are used as bifurcation parameters as in the CSTR experiments. All other parameters as indicated in the tables of section 5.5.

the model agrees qualitatively – but not quantitatively – with the solution diagrams presented in chapter 4.

The bifurcation diagram indicates that a second region of oscillations exists in the model. However, there is no experimental evidence for the existence of such region. Probably, it is an artefact which arises because the surface of Hopf bifurcations is crossed almost tangentially, and therefore happens to be intersected three times. This interpretation fits well with the observation that the value of σ' seems too low (see the discussion of absolute amplitudes above).

Simulation of quenching experiments

The model has already been compared with the quenching experiments in Table 5.8; in fact it was used in the optimization. However, that comparison applies to the bifurcation point and may be said to compare the behaviour for infinitesimally small limit cycles. It is therefore of interest to compare the quenching behaviour also for realistic, finite limit cycles.

We simulate a quenching experiment by integrating the limit cycle oscillations until some time for which the oscillation has the desired phase. Then we

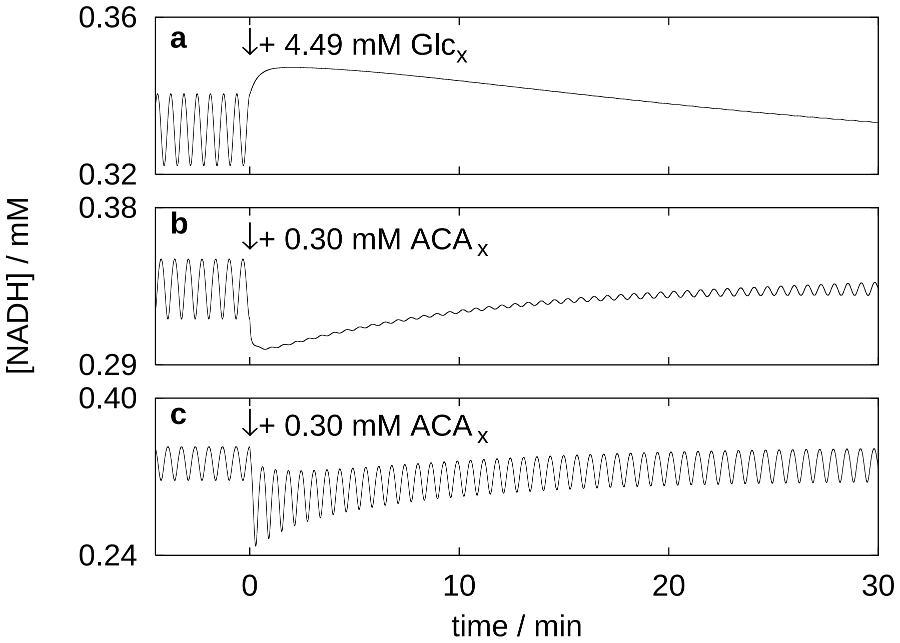

Figure 6.6: Simulations of perturbations with Glc_x and ACA_x (arrows indicate time of perturbations). (a) quenching with Glc_x at -3° (mixed flow glucose concentration $[Glc_x]_0 = 19.0$ mM, mixed flow cyanide concentration $[CN_x^-]_0 = 5.6$ mM, specific flow rate $k_0 = 0.048$ min^{-1}). (b) quenching with ACA_x at -170° ($[Glc_x]_0 = 35.0$ mM, $[CN_x^-]_0 = 5.37$ mM, $k_0 = 0.0479$ min^{-1}). (c) ACA_x perturbation at 10° (operating conditions as in panel (b)). All other parameters as indicated in the tables of section 5.5. Compare with Fig. 4.8.

shift the concentration of the metabolite added in the simulated experiment by any chosen value while keeping all the other concentrations fixed at the values they had at the point of the simulated addition. We then continue the integration with the new set of concentrations as initial values. The phase and concentration change to be used in order to quench the oscillations is unique and must be determined by trial and error, but the values calculated at the bifurcation point form excellent initial guesses, so the correct quenching data for the simulation are not hard to find.

So in order to simulate an 'actual' quenching experiments with addition of Glc_x or ACA_x as described above, we must integrate the kinetic equations away from the bifurcation point. In the quenching with ACA_x, we work at the experimental operating point. The quenching with Glc_x can only be performed when the glucose transporter is not saturated. (This is true both in the model and in the experiments). As just mentioned, the saturation occurs too early in the model, so the glucose quenching cannot be performed exactly at the working point of the experimental quenching. Instead, we work at a point where the degree of saturation is comparable to that in the experiment.

Fig. 6.6 shows the results of these simulations. In panel (a), the concentration of extracellular glucose, $[Glc_x]$, is suddenly changed by 4.49 mM at a phase of -3°, close to experimental quenching phase of 4°, resulting in quenching of the oscillations. (In the experiments, 1.11 mM of Glc_x was needed to quench the oscillations in a comparable, but not identical, working point). Panel (b) shows the simulation of the experimental quenching by addition of ACA_x with a change of concentration of 0.3 mM at a phase of 190°. This should be compared with the experimental quenching obtained by adding 0.098 mM ACA_x at 172°.

The simulated quenching with ACA_x may be compared with panel (c) which shows the result of the same instantaneous concentration change at the opposite phase. Whereas (a) and (b) show successful quenchings, (c) shows instead a small increase of the instantaneous amplitude, thus exemplifying the characteristic phase dependence of the response. Summarising, the quenching phases differ from the experimental values by $-7°$ and 18°, respectively, and the quenching concentrations differ by factors 4 and 3, respectively, for Glc_x and ACA_x.

Fig. 6.6 should be compared with the experimental quenchings in Fig. 4.8. We note the presence of slow non-oscillatory transients in the model results. The one for acetaldehyde agrees qualitatively with the one seen in the experiments. This behaviour is due to the excitation of one or more of the slow stable monotonous (non-oscillatory) modes. The non-oscillatory transient seen in the model quenching with glucose is not present in the experiments. Comparison also shows that the spiralling return to the limit cycle is too slow in the model. Again, this points to a too low value of σ' or possibly a too high value of $|g'|$.

Cell synchronization

As discussed in chapter 4, the experiments suggest that the synchronization of the yeast cells is strong. In fact, this is what allows us to use macroscopic data in the optimization as if the data applied to a single cell. It is straightforward to extend the present model so that it describes two (identical) cells and a common extracellular phase (see *e.g.* Wolf and Heinrich (1997, 2000)). We have integrated this 35-dimensional extended model with various initial conditions and at various operating points of the CSTR. In all cases tested, we found that the stable solution is synchronized with the two cells oscillating in opposite phases, and that the in-phase synchronization is unstable.

Furthermore, the synchronization process seems to be an order of magnitude too slow. So, the present model (extended as indicated) cannot simulate Pye's mixing experiment (Pye, 1969; Ghosh *et al.*, 1971; Richard *et al.*, 1996a), and there is a lack of self-consistency in that the model cannot reproduce the strong coupling seen in the experiments. Further investigations of this problem will be the topic of chapter 7.

Conclusion

The integrations and continuations described above show, that the detailed glycolytic model is in good qualitative agreement with experimental observations also when one moves away from the operating point of the optimization. However, the agreement is not quantitatively correct. The lack of quantitative agreement is to be expected for a strictly local optimization. The qualitative agreement can probably be attributed to the use of biochemical rate equations, thus illustrating an advantage of models based on mechanistic rate equations.

The model fails to describe the cell synchronization observed experimentally, so in this regard the model is inconsistent with its underlying assumptions. This is also unsatisfactory from a biological point of view, since the cell synchronization problem is left unsolved.

6.2 Transient oscillations revisited

Since we have now shown that the model works quite well in the neighbourhood of the operating point of the optimization, we can use it to investigate a number of phenomena observed in the transient experiments. In particular, we will be concerned the initial glucose response and the time course of the flux through the system and its branchings. The motivation for these investigations is to test our understanding of yeast glycolysis: since yeast glycolysis is believed to be very well understood, and since we now have a detailed biochemical model describing its biochemical dynamics, we should be able to account for the observed effects in this model organism. If this is indeed so, then more difficult problems can be addressed with the tools used here.

From a technological point of view it is also interesting to try to understand the flux distribution patterns of the transients, as well as the initial glucose response, since microorganisms in industrial fermentors are faced with a changing and heterogeneous environment due to the way nutrients are supplied, and due to stirring problems in such large-scale fermentors.

A typical transient experiment is shown in Fig. 4.1, and a similar experiment but with the opposite addition sequence is shown in Fig. 7.7a. In both cases, a very dramatic response is seen when the glucose is added to the starved yeast cells. Richard *et al.* (1994) provide data on the time course of the accumulations of $EtOH_x$ and extracellular glycerol, and these data are reproduced in Fig. 6.7. The EtOH time course seems more or less linear in time, maybe with a lag phase immediately following the glucose addition, but this is only clear for the experiment without added cyanide. The glycerol time course is more complex. Following an initial lag phase, the glycerol production rate increases and is markedly higher than average from 2 to 8 min after glucose addition. The rate then decreases and stays at a lower constant value throughout the rest of the time course. These observations were not explained by Richard *et al.* (1994), whereas they did account for the flux changes observed when different amounts of KCN were added.

Simulation of transient oscillations

Using our glycolysis model, we can simulate these transient experiments simply by setting the specific flow rate $k_0 = 0$ and choosing adequate initial concentrations for the numerical integration. The initial concentration of Glc_x is set to 20 mM and $[CN_x^-](0)$ is set to 5 mM. "Starved cells" are simulated by set-

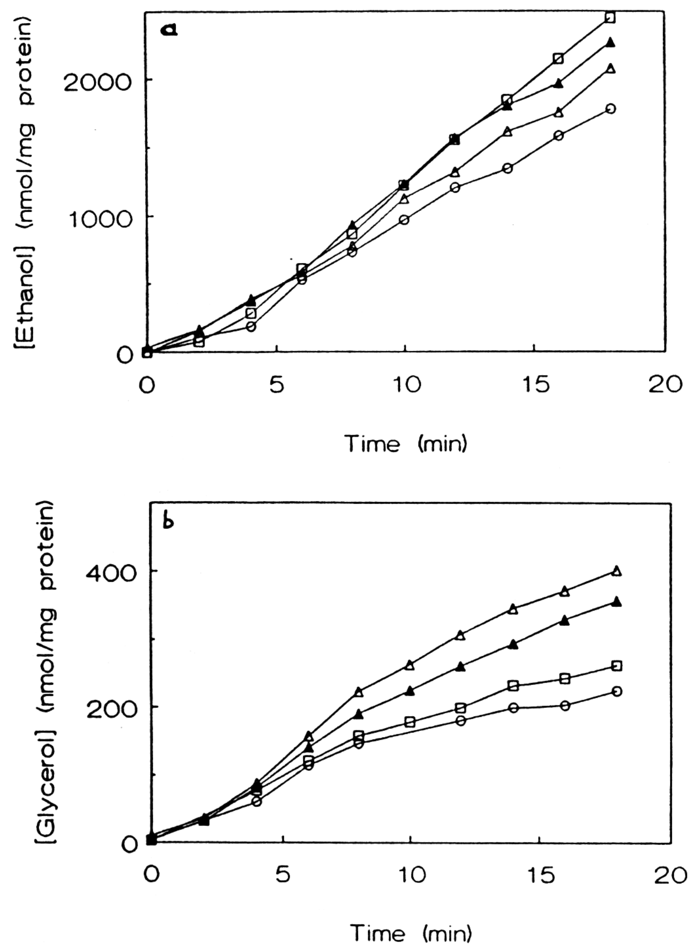

Figure 6.7: Ethanol production (a) and glycerol production (b) during transient experiments as reported by Richard *et al.* (1994). Cell density is reported to be 6.6 (g protein)/L, so 2000 (nmol EtOH)/(mg protein) corresponds to 13.2 mM EtOH, and 400 (nmol glycerol)/(mg protein) corresponds to 2.64 mM glycerol. The starved cells were given 20 mM of glucose and either 0 mM (○), 0.5 mM (□), 2 mM (▲) or 8 mM (△) KCN. (Reproduced from Richard *et al.* (1994)).

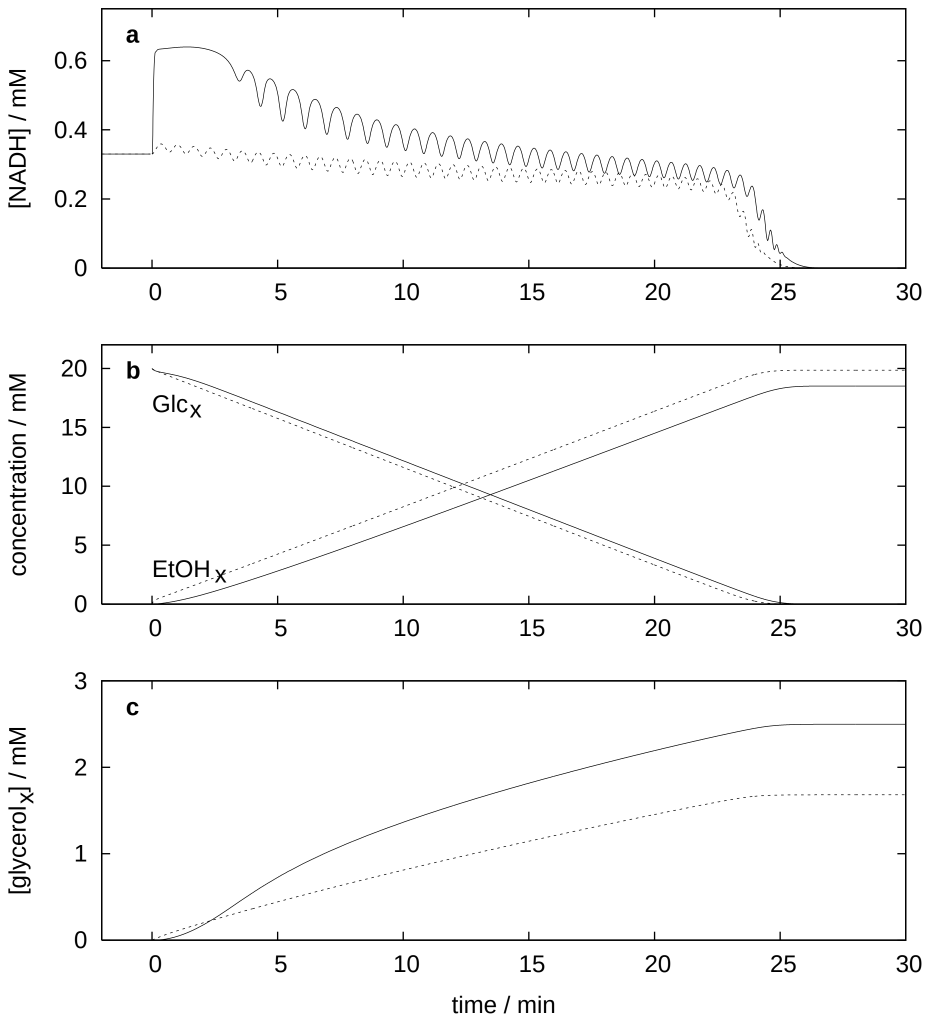

Figure 6.8: Simulation of transient experiments with "starved cells" (solid lines) and "unstarved cells" (dashed lines) as explained in the text. The initial NADH overshoot (a) as well as the multi-phasic time-course of [glycerol$_x$] (c) are reproduced by the starved cells, but not by the unstarved cells. Both the glucose consumption and the ethanol production rates are constant, except for a 1-2 min lag phase with the starved cells (b).

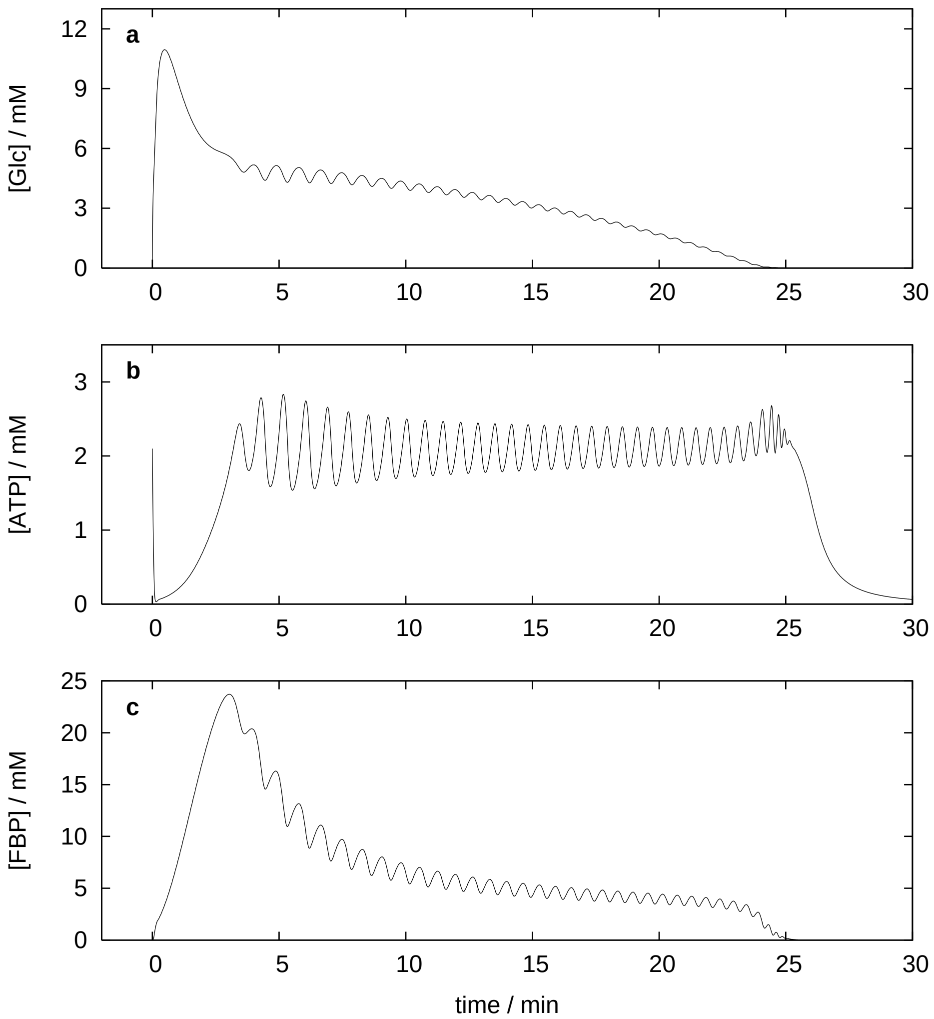

Figure 6.9: Time-traces of metabolites in a simulated transient experiment with "starved cells". The data are from the same simulation as those of Fig. 6.8. Details of this simulation can be found in the text. The metabolites depicted in the panels are (a) Glc; (b) ATP (very similar to G6P, F6P and BPG, and rather similar to PEP and Pyr); (c) FBP (similar to GAP and DHAP).

ting the initial concentrations of all metabolites to zero, except those of the conserved sets ATP, ADP, AMP and NADH, NAD^+ which retain their values from Table 5.8 as initial concentrations. For comparison, "unstarved cells" are simulated with initial concentrations $[Glc_x](0) = 20$ mM, $[CN_x^-](0) = 5$ mM, $[EtOH_x](0) = 0$ mM and $[glycerol_x](0) = 0$ mM, but all other initial concentrations as indicated in Table 5.8. The results of these simulations are show in Figs. 6.8 and 6.9. In Fig. 6.8 it is seen that – at least qualitatively – the simulation of the starved cells shows the initial NADH overshoot as a response to glucose (compare panel (a) with Figs. 4.1 and 7.7a), and the multi-phasic glycerol time course is reproduced quite well (compare panel (c) with Fig. 6.7b). In contrast, the simulation with unstarved cells cannot reproduce these phenomena, so – at least with the model – the starvation is the immediate cause of these effects.

The last part of the NADH time-course is wrong for both starved and unstarved cells. This is, however, to be expected since a number of enzymes were modelled as irreversible reactions due to large values of $-\Delta G$ at the operating point of the optimization. But towards the end of the transient experiments, the glycolytic flux goes to zero, and the reactions equilibrate. Obviously, this will not happen in our model. In particular, the final NADH concentration in the simulated transient experiments is zero, as opposed to the high state seen in the experiments, because ADH is modelled irreversibly.

Further inspections of the simulation results show, that the glucose response of the starved cells can be understood in terms of an interplay between the stoichiometric constraints caused by the conservation relations $[ATP]+[ADP]+[AMP] = \text{constant}$ and $[NAD^+] + [NADH] = \text{constant}$.

In Fig. 6.9a it is seen that the intracellular glucose concentration builds up rapidly, and reaches high values. The subsequent phosphorylations of this substance depletes the ATP pool (Fig. 6.9b) in analogy to the "turbo effect" described by Teusink *et al.* (1998b). The ATP depletion is prolonged because the GAPDH reaction initially has shifted the redox balance towards high NADH concentrations. The low NAD^+ concentration slows down the GAPDH reaction, and, consequently, both the ATP synthesis in the lower part of glycolysis and the fermentative re-oxidation of NADH are slow. Therefore, the NAD^+/NADH ratio must recover mainly through glycerol production, which explains the increased glycerol production in the first part of the transient. Likewise, G6P, F6P, BPG, PEP and Pyr can only slowly build up to the levels observed during glycolytic oscillations (G6P, F6P and BPG have time courses very similar to that of ATP (Fig. 6.9b), whereas PEP and Pyr show somewhat

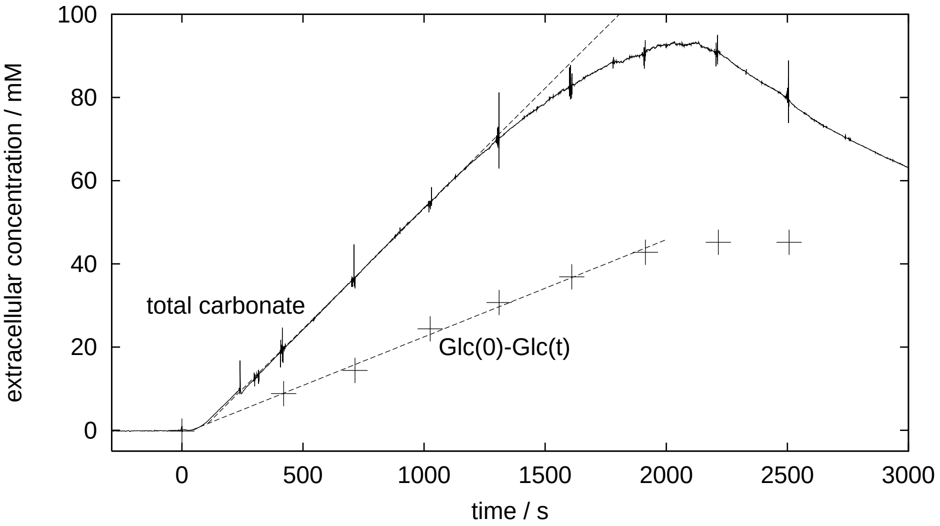

Figure 6.10: Consumed glucose and total carbonate in the extracellular medium. Starved yeast cells (30.7 (mg d.w./mL)) were given 46 mM of glucose at time $t = 0$ and 5 mM of KCN four min later. Total carbonate is calculated from pH measurements as described in appendix E. Glucose was measured in samples removed by sterile filtration (0.45μm) and analysed using an enzymatic Sigma glucose kit. pH was 6.8 at the start of the experiment and reached a minimum of 6.2 round $t = 2000$ s. The glucose consumption rate and the CO_2 production rate were determined by fitting straight lines to the data (dashed lines), and values of 1.4 mM/min and 3.5 mM/min were found, respectively. As discussed in the text, the amount of CO_2 produced by the yeast cells can only be determined from the first part of the dataset, and hence the fit was made in the time interval [110s:1000s].

more damped responses). A qualitatively different response is seen for FBP, GAP and DHAP. Due to the allosteric regulation of PFK, it increases its reaction rate as the ATP level goes down and the AMP level increases. This leads to an accumulation of these three metabolites (exemplified by Fig. 6.9c).

Note that this explanation of the overshoot phenomenon and the changes in glycerol flux is only qualitatively correct: the transient Glc and FBP concentrations seem unrealisticly high, and some of the timescales of the transient are not correct.

Both the glucose consumption and the ethanol production are constant in time except for a 1-2 min lag phase (Fig. 6.8b, solid lines). The EtOH time trace compares well with Fig. 6.7a. For comparison with the Glc data, we measured extracellular glucose concentration in a transient experiment as indicated in

Fig. 6.10 and found constant glucose consumption rate during the transient experiment. This result fits well with the model and previous considerations in this thesis. (The "total carbonate" measurements in the figure are treated below).

The effects of different initial cyanide concentrations seen in Fig. 6.7 can also be analysed by simulation of transient experiments with starved cells. All effects on glycerol production can be reproduced qualitatively, but not quantitatively (the effect is too small in the simulations, probably because the value of k_{20} in the model is too low). This is also true for EtOH, except that the model does not predict a low EtOH production in the absence of cyanide. This low EtOH production is due to a drain of pyruvate into the TCA cycle and the oxidative phosphorylation, which is not described by the model. The conclusion drawn from the modelling agrees with that reached by Richard *et al.* (1994): an increased cyanide concentration removes more ACA from the fermentative branch, and the need to re-oxidise NADH then increases the flux through the glycogen branch.

Experimental observation of the lag phase

In order to test the explanation for the NADH overshoot and the changing flux distribution during the transient oscillations given by the model, we note that the effect is basically due to the "starvation" which means that the pathway needs to fill up before glycolysis can proceed as normal. In the simulations, this is reflected in the lag phases seen for the extracellular metabolites Glc, EtOH, ACA and Glyc as well as for the CO_2 production when "starved" cells are simulated. We will use on-line measurements of the CO_2 production to look for this lag phase.

For this purpose, we use a glass electrode to monitor pH changes during transient oscillations. The changes in pH are caused by the CO_2 produced by the PDC reaction; all irreducible subpathways are pH neutral (see appendix C). The glycolytic flux is so large, that significant pH changes occur despite the fact that the experiments are carried out in 0.1 M potassium phosphate buffer. This way of monitoring the flux is both simple and convenient, since the electrode provides an online measurement which can be related directly to the flux through a single reaction. In order to calculate the amount of CO_2 produced from the time course of the electrode potential, we will first assume equilibrium of the acid-base reactions which is a quite reasonable assumption. This allows us to calculate the total carbonate concentration in the solution. If, further-

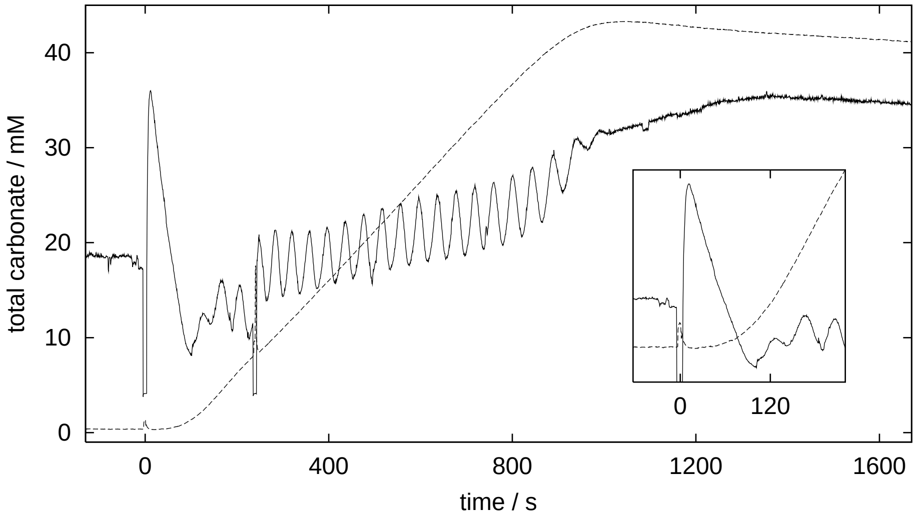

Figure 6.11: Total carbonate concentration calculated from pH measurements in a transient experiment. The NADH fluorescence trace is also shown. The yeast cells were given 20 mM of glucose at $t = 0$ s and 5 mM of KCN at $t = 240$ s. The cell density was 33 (mg d.w.)/mL. The inset shows an enlargement of the initial part of the experiment. The lag phase due to the filling-up of the pathway is evident (the characteristic response time of the electrode has been measured to 16 s in the setup). After the lag phase, the total carbonate concentration builds up at a constant rate until the point of glucose depletion. See appendix E for details of the calculations.

more, we assume that no CO_2 leaves the solution and goes into the gaseous phase above it, then this is equivalent to the total amount of CO_2 produced by the yeast cells. The validity of this second assumption is very dependent on the chemical state of the solution: the solution will degas much faster at lower pH and higher total carbonate. Therefore, we will underestimate the CO_2 production, but in the beginning of the transient experiments this underestimation will be negligible as shown in appendix E. Other details concerning the calculations are also given in this appendix.

Fig. 6.11 shows such an experiment. The lag phase is clearly visible in the inset of the figure. The characteristic response time of the electrode has been measured to 16 s in the setup, so the lag phase is significant and in accordance with the simulations. After the lag phase, the CO_2 production rate is constant as expected.

Magnitude of the CO_2 flux

Measurements of pH were also made in the experiment shown in Fig. 6.10. This allows us to compare the glucose consumption rate to the CO_2 production rate. At the cell density of the figure, we measure a glucose consumption rate of 1.4 mM/min and a CO_2 production rate of 3.5 mM/min. Surprisingly, the ratio of the glucose consumption rate to the CO_2 production rate is 2.5, whereas the expected ratio is 1 (either from experiments as described in section 5.2 or from simulations of transient experiments), and the highest possible ratio with the reaction network of the model is 2. This could be an indication that other parts of metabolism are active with a substantial flux, but another probable explanation is that the total carbonate calculations are wrong due to errors in some of the many parameters that enter the equations, or due to a too crude correction for the ionic strength of the solution. The additions of KOH at the ends of the transient experiments in Fig. 4.2c can be viewed as titrations of the acid-base system, and as such they can be used to check the accuracy of our calculations. In these experiments an addition of 16 mM KOH was made in order to bring the pH back to the starting value of 6.8, whereas we calculate the sizes of the additions to 14 mM from the measured pH values. This error is approximately 15%, so it seems unlikely that our total carbonate calculations should be off by more than a factor of 2.

Still, a better method for measuring the CO_2 production rate would be to implement a pH-stat in the setup, thus avoiding the need for elaborate calculations. This has, however, not been done.

Conclusion

From the simulations of transient experiments and the pH measurements, we conclude that the initial overshoot when the glucose pulse is given results from a filling up of glycolysis. This overshoot is the cause of the changes seen in the glycerol production rate. Despite the transient nature of the experiment and the changing glycerol production, glucose consumption and CO_2 production are constant throughout most of the experiment; this is in agreement with the simulations. The CO_2 production rate appears to be a factor of two higher than expected. We have no biochemical explanation for this observation.

In some biotechnological applications, it is desirable to maximise the EtOH production and minimise the glycerol production. In this context, it is interesting to note that without changing the biochemical system, one can have significant changes in the flux through the glycerol branch while the glucose consumption remains constant. However, much more detailed studies are needed in order to tell whether or not this effect can actually be exploited.

6.3 The origin of the oscillations

A questions about oscillatory glycolysis which I have often been asked is "what makes glycolysis oscillate". In earlier work PFK with its allosteric regulation (in particular inhibition by ATP and activation by AMP and FBP) has been pointed out as the "oscillophore", *i.e.* the enzyme responsible for the oscillations (Ghosh and Chance, 1964; Higgins, 1964). The analysis of these early observations, as well as a substantial amount of additional experimental evidence supporting the conclusion that PFK is the oscillophore, is summarised in section 2.1 of Goldbeter (1996). See also the work by Benno Hess and coworkers (Hess *et al.*, 1969; Hess and Boiteux, 1971; Boiteux and Hess, 1974; Hess, 1979).

Still, PFK need not be the only part of the network exerting control on the dynamic properties of glycolysis. Based on the phase angles of the glycolytic intermediates in yeast extracts, Boiteux and Hess (1974) point to PK and the GAPDH-PGK pair as additional control points conveying the adenine nucleotide signal from PFK to other parts of the network. Becker and Betz (1972) point to the hexose transport step as an important control point of the oscillatory dynamics, but still suggest PFK as the primary source of the oscillations. Moreover, the stoichiometry of glycolysis makes the pathway autocatalytic in ATP (Aon *et al.*, 1991), and the conserved sum of NAD^+/NADH constitutes yet another feedback loop.

Indeed, more recent work has disputed the idea of PFK as the oscillophore. Instead, it is advocated by the Amsterdam group that the control of the oscillations is distributed throughout the network (Bier *et al.*, 1996; Teusink *et al.*, 1996a; Reijenga *et al.*, 2002), and in Reijenga *et al.* (2001) they point to hexose transport as having "most but not all" control of dynamics. However, this is a somewhat dubious conclusion to draw: the control coefficients determined in their study can be positive as well as negative (see *e.g.* Fig. 6.12), so one cannot judge the importance of a single step from its control coefficient and a summation theorem without knowing the control coefficients of the other relevant steps too. Still, their experiments emphasise and quantify the importance of hexose transport kinetics.

Given the full-scale model it should be possible to answer the "oscillophore question" by model analysis. Still, the question is not as simple to answer as one might think, since it is unclear how one should quantify the ability to make a reaction system oscillatory; *i.e.* the oscillophore concept is not rigorously defined.

Stoichiometric Network Analysis can classify reaction networks according to the possibilities of instabilities to occur, and in certain cases also according to the possibilities for Hopf bifurcations to occur (Clarke, 1980). However, this analysis only works for reaction systems with mass-action kinetics, and hence cannot be applied to our glycolysis model.

6.3.1 Control analysis of glycolytic oscillations

Another approach is Metabolic Control Analysis (MCA; a form of sensitivity analysis), which has previously been used in the analysis of models describing glycolytic oscillations (Bier *et al.*, 1996; Teusink *et al.*, 1996a; Reijenga *et al.*, 2002). These models, however, were merely qualitative or semi-quantitative models with limited biochemical detail. The conclusions drawn in these papers were that no single enzyme could be identified as the oscillophore; instead control was found to be distributed over the reaction network.

The sensitivity analysis of our glycolysis model which I present below is developed in close collaboration with Mads Madsen at our department, who has also performed the actual calculations.

In control analysis, the control coefficient $C_p^X = \frac{\partial \ln X}{\partial \ln p}$ describes the control of a parameter p on a property X (see, *e.g.*, Fell (1997)). We want to discuss the control of the oscillations, so the natural choice for the properties is frequency and amplitude of the oscillations. However, it is still unclear whether an oscillophore should have a strong control over frequency, amplitude or both.

Close to the supercritical Hopf bifurcation, the Stuart-Landau equation $\dot{z} = (i\omega_0 + \sigma\mu)z + gz|z|^2$ gives a good description of our system. For use with MCA we choose $\mu = (p - p_0)/p_0$. This results in new values of σ' and σ'' for each parameter p, but the values of ω_0 and g remain the same. The frequency and amplitude of the oscillations are

$$\begin{aligned} \omega_{\mathrm{lc}} &= \omega_0 + \left(\sigma'' - \frac{\sigma' g''}{g'}\right)\mu \\ r_{\mathrm{lc}} &= \sqrt{\frac{-\sigma'\mu}{g'}}, \end{aligned}$$

respectively (chapter 2). The frequency control coefficient at the bifurcation point then becomes

$$C_p^\omega = \frac{d\ln(\omega)}{d\ln(p)} = \frac{1}{\omega}\frac{d(\omega)}{d(\mu)} = \frac{1}{\omega_0}\left(\sigma'' - \sigma'\frac{g''}{g'}\right), \tag{6.1}$$

whereas the usual MCA definition of control coefficients cannot be used for the amplitude due to the presence of a singularity at the bifurcation point. Instead we introduce the *relative rate of change of stability*

$$\frac{d\mathrm{Re}(\lambda)}{dp/p_0} = \frac{d\mathrm{Re}(\lambda)}{d\mu} = \sigma', \tag{6.2}$$

which is a scaled measure of the change of the square of the amplitude. However, this quantity is more clearly interpreted as the rate of change of stability of the stationary state as the parameter in question is increased.

We have calculated these control coefficients at the Hopf bifurcation point which was also the operating point of the optimization. The results are presented in Figs. 6.12 and 6.13. The shading denotes the sign of the coefficients: white is negative and black is positive. Due to the large amount of parameters in the model, only the parameters corresponding to enzyme concentrations (V_{max} values and mass-action rate constants) have been included in the analysis. In addition, the specific flow rate k_0 has been included in order to present the effects resulting from time scaling: control coefficients sum to 1, and the relative rates of change of stability sum to 0 min^{-1}.

If we want to use the results from the control of the frequency (Fig. 6.12) to identify an oscillophore, then we must conclude that it does not exist since the control is distributed among a number of enzymes, and these enzymes are located in different parts of the network. If, on the other hand, we want to identify it from the data on rate of change of stability (Fig. 6.13), then we see that the reactions resulting in large coefficients are all located in the upper part of glycolysis, possibly including the unspecific ATP consuming reaction. From this we must conclude that PFK and the adenine nucleotides are the essential parts of the reaction system. This ambiguity shows clearly that the question "what is the oscillophore" is ill posed since there is no clear definition of an oscillophore. Instead, we can conclude that, for the present model, the instability of the system stems from the PFK kinetics and the kinetics of the adenine nucleotides, whereas the control of the frequency of oscillations is distributed over the entire network. This means that a reduced biochemical PFK

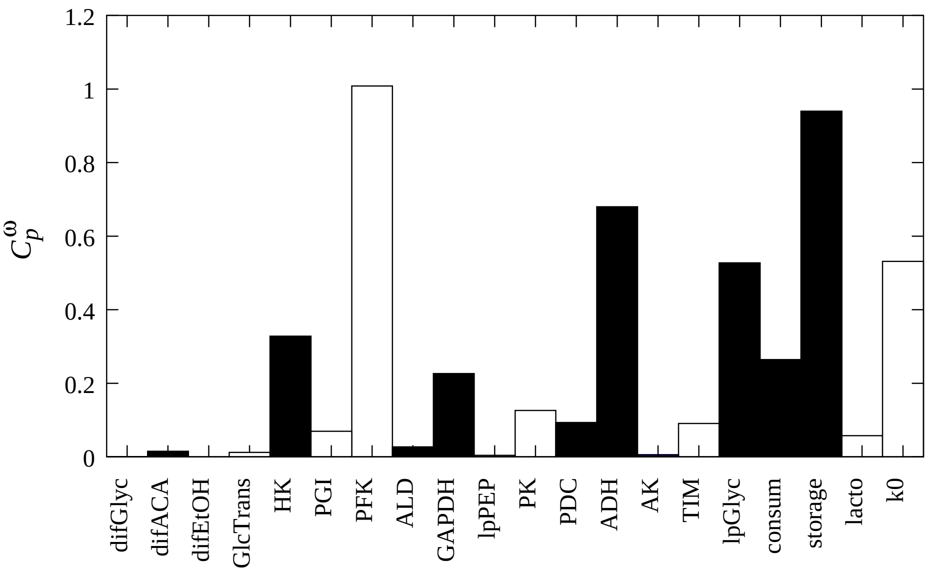

Figure 6.12: Frequency control coefficients for $V_{\max}$ or mass-action rate constants for all reaction in our glycolysis model. For reversible reactions, the control coefficients for the forward and reverse reactions are added, in order to reflect the effect of increasing the concentration of the enzyme. Black bars are positive and white bars are negative.

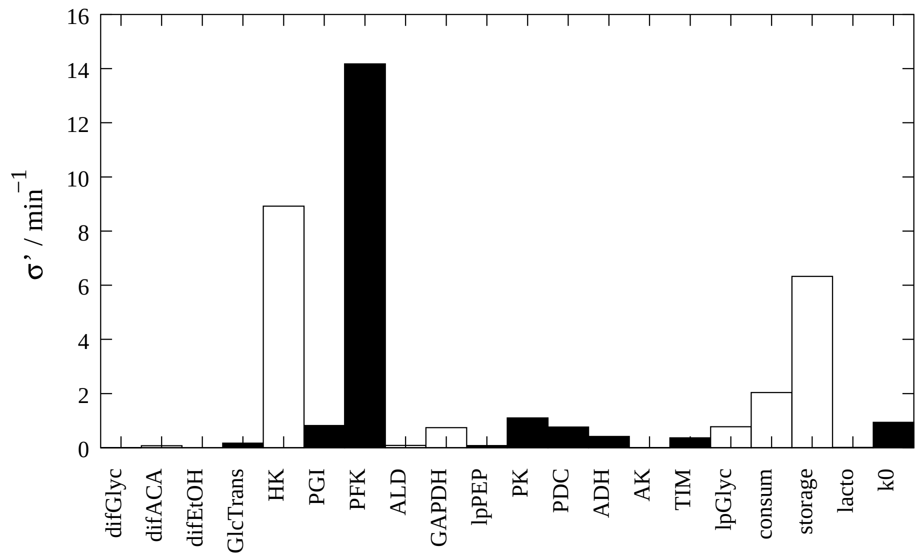

Figure 6.13: Relative rate of change of stability for $V_{\max}$ or mass-action rate constants for all reaction in our glycolysis model. For reversible reactions, the coefficients for the forward and reverse reactions are added, in order to reflect the effect of increasing the concentration of the enzyme. Black bars are positive and white bars are negative.

based model might be good for understanding the basis of the oscillations, but for more detailed analysis – and in particular analysis involving the frequency of the oscillations – a full-scale model is needed.

Recent experiments by Reijenga *et al.* (2001) have shown that the glucose transporter exerts substantial control of both total flux and frequency during glycolytic oscillations in yeast. Apparently, our analysis does not fit this result. However, the experiments were performed as transient experiments where the glucose transporter is saturated or at least close to saturation, whereas the above analysis is made at the bifurcation point using the mixed flow glucose concentration as bifurcation parameter. In this case, the glucose transporter is not saturated. Obviously, the first enzyme in a pathway will exert more control when it is saturated than when it is not, and this is probably the reason for the apparent discrepancy.

The reactions which play an important role in the control of the frequency but not in the generation of the instability are ADH, GAPDH, the glycerol forming reaction and the mechanical flow of the reactor. ADH, GAPDH and glycerol formation are all linked to the rest of the network by the moiety conservation of NAD^+ and NADH, so it seems that the primary importance of this feedback system is its modulation of the frequency of the oscillations.

In this regard it is interesting to note that the expression for C_p^ω has two terms, the magnitudes of which are determined either by σ' or by σ'', whereas the rate of change of stability is given only by σ'. Consequently, we have the following possibilities:

1. $|\sigma'|$ is large compared to $|\sigma''|$. Such a reaction modulates both stability and frequency, and the frequency modulation is through $|\sigma'|$. In our case, this results in opposite signs of the two coefficients C_p^ω and σ'. The PFK, the ATP consumption and the glycogen production reactions are good examples of such a reaction.

2. $|\sigma'|$ is small compared to $|\sigma''|$. Such a reaction modulates frequency without affecting the stability. In the present model, good examples are the ADH, GAPDH and glycerol formation reactions as well as the mechanical flows of the reactor.

3. The contributions from the σ' and σ'' terms cancel out so that the reaction affects stability but does not affect the frequency. There are no clear cut examples of this in our model, but the frequency modulation exerted by the HK reaction is lowered in this way.

4. Finally, it is possible that the contributions from the two terms are comparable but add up. The effect of this is control over both stability and frequency. This is of no importance in the analysis of the present model.

To conclude, we see that enzyme concentration variations of PFK and of the reactions which are intimately connected to the adenine nucleotides affect the dynamics through their σ' values, whereas variations in the concentrations of enzymes connected to the NAD^+/NADH system affect the dynamics through their σ'' values. Therefore, the former group of reactions gives rise to the instability and modulates the frequency of the reactions, whereas the reactions of the NAD^+/NADH control system only affect the frequency of the oscillations. So, at least in our model, the oscillations arise in the upper part of glycolysis in a few reactions around PFK, but the frequency of these oscillations is modulated by a large part of the reaction network.

This conclusion disagrees with that reached by the Amsterdam group in their control analysis of a number of simple models of glycolytic oscillations, but agrees with earlier work pointing to PFK as an essential part of oscillatory glycolysis.

6.3.2 Phase plane analysis

The above analysis is based on the reactions of the reaction system. Alternatively, one can discuss the origin of the oscillations in terms of the chemical species involved. The simplest form of phase plane analysis would be to look for the metabolites with the largest relative amplitudes, disregarding the phase information. Britton Chance and Benno Hess took the opposite approach and used Chance's cross-over theorem to analyse the metabolite oscillations in terms of their relative phases, disregarding the amplitude information (Ghosh and Chance, 1964; Hess *et al.*, 1969).

However, I will now show that it is possible to utilise both the phase and the amplitude data through phase plane analysis[1]. In order to do this, we will first write the real and imaginary parts of the Stuart-Landau equation explicitly

$$\begin{aligned} \dot{z}' &= \mu\sigma' z' - (\omega_0 + \mu\sigma'')z'' + g' z'(z'^2 + z''^2) - g'' z''(z'^2 + z''^2) \\ \dot{z}'' &= \mu\sigma' z'' + (\omega_0 + \mu\sigma'')z' + g' z''(z'^2 + z''^2) + g'' z'(z'^2 + z''^2) \end{aligned} \tag{6.3}$$

[1] I have not seen the present approach used elsewhere, but considering its straight forward nature, I would be surprised if it is not already described in the literature

and from this calculate the Jacobian matrix at the stationary state $z = 0$

$$\mathbf{J}|_{z=0} = \begin{bmatrix} \mu\sigma' & -(\omega_0 + \mu\sigma'') \\ \omega_0 + \mu\sigma'' & \mu\sigma' \end{bmatrix} \tag{6.4}$$

which, after the onset of the oscillations, is on the form $\begin{bmatrix} + & - \\ + & + \end{bmatrix}$. We can interpret the dynamics in the plane of oscillations as composed of two abstract (unphysical) chemical species z' and z''. Above the bifurcation point (*i.e.* for $\mu\sigma' > 0$), both of these abstract species are autocatalytic, and the strength of the autocatalysis is given by $\mu\sigma'$. The tendency to oscillate is due to the asymmetry in the two off-diagonal terms $\pm(\omega_0 + \mu\sigma'')$. In a chemical interpretation this means that the abstract species z' is an activator of the other abstract species z'', whereas this species is an inhibitor of z'.

In concentration space, these abstract chemical species correspond to two directions in the plane of oscillations, but these two modes are not uniquely defined. However, *if* it were possible to uniquely identify the directions corresponding to z' and z'' in concentration space, then these directions could be interpreted as an activating and an inhibiting mode, respectively. If such modes had large components from a few metabolites, then we could conclude that these metabolites were essential, and what the roles of these metabolites were in the oscillations. If, on the other hand, these modes were composed of many metabolites without any of them being dominating, we would conclude that all metabolites contributed to the oscillations without any of them being more important than the others.

The equation for the transformation from the part of eigenspace corresponding to the center manifold to concentration space shows why these modes are not uniquely defined. To lowest order it reads

$$\mathbf{c} = \mathbf{c}^{\mathrm{s}} + z\mathbf{u} + \overline{z\mathbf{u}}$$

as described in chapter 2. (The bar denotes complex conjugation). Any complex vector $\mathbf{u}' = \alpha\mathbf{u}$ obtained by multiplying a complex eigenvector $\mathbf{u}$ by a non-zero complex number α is itself an eigenvector associated with the same eigenvalue, so by choosing α we can scale modulus of all components of the complex eigenvector and shift their phases. Accordingly, only the relative amplitudes and the relative phases contain information about the dynamics of the system. This information can be visualised in plots like those of Figs. 5.3 and 6.14. Recall that the component of metabolite s of the complex eigenvector in the plane of oscillations is given by $u_s = a_s \exp(i\theta_s)$, so such plots

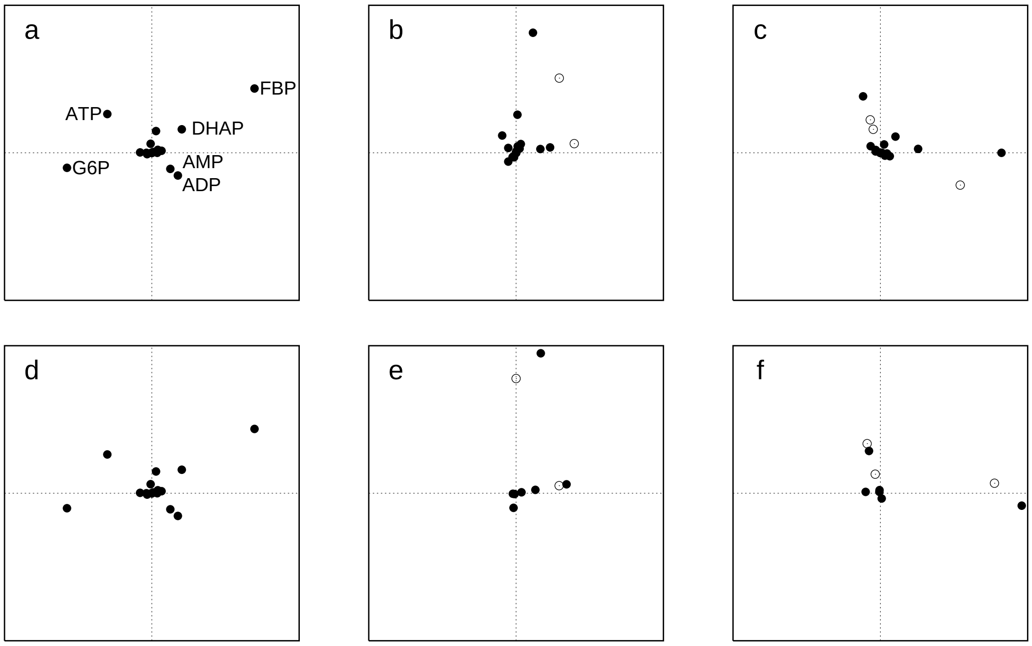

Figure 6.14: Plane of oscillations. Polar plots with the relative phases as the angles and the relative amplitudes as the moduli. This representation reflects the relative positions of the different metabolites in the coordinate system of the eigenmode corresponding to one of the two bifurcating complex eigenvalues. Since a complex eigenvector multiplied by any non-zero complex number is still an eigenvector of the system, the unit of the modulus is arbitrary as are the absolute angles. Panels (a)-(d) are model data, and panels (e)-(f) are data from Richard *et al.* (1996b). Data points plotted as ∘ are shifted by 180°, whereas normal data points are plotted as •. Panels (a),(d) show the uninterpreted model data with and without annotations. Panels (b),(e) and panels (c),(f) show data interpretations as discussed in the text.

reflect the relative positions of the different metabolites in the coordinate system of the complex (oscillatory) eigenmode. These plots have the advantage that the directions corresponding to the real and imaginary axis will form a 90° angle, whereas this would not be the case if we had just plotted the plane of oscillations in concentration space.

Fig. 5.3 shows that the phase planes of the experiments and the model are in good agreement. Fig. 6.14a and d show the phase plane of the model with all components plotted; indeed, some structure is present in the plot. Panels (b) and (c) show two possible interpretations of this structure, and panels (e) and (f) show the corresponding plots for the experiments. FBP is the metabolite with the largest relative amplitude in both model and experiments, so we will base the interpretation on this metabolite.

In panels (b) (model data) and (e) (experimental data), FBP is part of the inhibitory mode. To obtain this, G6P and ATP have been shifted 180°. In this interpretation, the "activator" is a mode with ADP, AMP and absence of ATP, and the "inhibitor" is a mode with FBP (possibly also DHAP) and absence of G6P. The activation in this interpretation corresponds to the regulation of PFK by the adenine nucleotides and to a decrease in the HK velocity due to a decrease in the concentration of its substrate ATP. The inhibitory feedback can be seen as a consequence of the stoichiometry of the adenine nucleotides in glycolysis: high FBP and low G6P increases the production of ATP and decreases that of ADP and AMP accordingly, because it increases the flux in the lower part of glycolysis and decreases it in the upper part (see Hess *et al.* (1969); Pye (1969)).

The 90° structure in the phase plots is most evident when the experimental data are plotted. In particular, "absence of G6P" belongs more clearly to the FBP mode in the experimental data than it does in the model data. This observation might be relevant to the ongoing discussion of a possible feedback of T6P or G6P to HK or the glucose transporter (see Teusink (1999) and references therein), since it might be an indication that an important regulatory element is modelled incorrectly. This also holds for the next possible interpretation to be discussed.

This interpretation is given in panels (c) (model) and (f) (experiment); now with FBP as the main component of the activating mode. To obtain this, we have shifted G6P, ADP and AMP by 180° and rotated the plot accordingly, so the "activator" is now mainly FBP and absence of G6P, and the "inhibitor" is ATP and absence of ADP as well as AMP. The activating and inhibiting feedbacks can be explained by the same reasoning as given for the first interpretation.

Conclusion

Other interpretations are possible, so there is no idea in telling which mode is the "activator" and which is the "inhibitor". Instead, the interesting point to note is that two modes with approximately 90° separation in the phase plot and with a limited number of components are found in both model and experiments, and that the feedback between these modes (regardless of the interpretation chosen) can be rationalised in terms of PFK kinetics and the glycolytic stoichiometry of the adenine nucleotides. As with our control analysis, this leads to the conclusion that PFK and the ATP-ADP-AMP system are key elements of the glycolytic oscillator. However, the basis of the conclusion is now not just one single glycolysis model, but also the experimental data of Richard *et al.* (1996b).

7
From enzyme kinetics to population dynamics

The topic of this chapter is the cell synchronization problem: how do the yeast cells synchronize their oscillations in phase? This question is relevant not only for the yeast cells oscillations, but also for the understanding of coupling phenomena in a number of other cell types like insulin secreting β-cells (Chou *et al.*, 1992; Yaney *et al.*, 1995; Cunningham *et al.*, 1996; Nilsson *et al.*, 1996; Prentki, 1996; Civelek *et al.*, 1996, 1997), neutrophiles showing oscillations in time and space (Petty *et al.*, 2000), heart cells exhibiting metabolic oscillations (Frenkel, 1968a,b,c; O'Rourke *et al.*, 1994, 1995), or skeletal muscles showing glycolytic oscillations at least in extracts (Tornheim and Lowenstein, 1974, 1975; Tornheim, 1988; Tornheim *et al.*, 1991; Marynissen *et al.*, 1992; Siegel *et al.*, 1997). The chapter is the last chapter dealing with oscillating yeast cells, and it is based on Danø *et al.* (2001) with a number of extensions.

The experimental and biochemical background of the synchronization problem was discussed in chapter 4. With a entirely correct, detailed biochemical model of oscillatory yeast glycolysis, it should be possible to account biochemically for the coupling phenomenon in mechanistic detail, so as to match the experimental observations. But, much to our surprise, our glycolysis model cannot account for the in-phase synchronization even though it is in good agreement with most other properties of the yeast oscillating yeast cells: recall from section 6.1 that when our model is modified to described two cells coupled by a common extracellular medium, they synchronize slowly and in opposite phase; their in-phase solution is unstable. The purpose of this chapter is to give possible explanations for this discrepancy, and through this process obtain a better understanding of the phase synchronization process.

7.1 Modelling a population of identical oscillators

The synchronization phenomenon occurs on the population level, so we will consider the dynamics of many coupled cells. On the other hand, we want to use the detailed glycolysis model as our starting point. Phase synchronization is basically the mutual modulation of the frequency of oscillation among the cells in the population. We saw in section 6.3 that the control of the frequency is distributed throughout the reaction network in our glycolysis model, so the phenomenon will involve the entire metabolic network of glycolysis and fermentation, and consequently it cannot be addressed at the level of a single enzyme or a single key metabolite, nor can we expect a simplified glycolysis model ("core model") to be a good starting point for the analysis. We could instead perform a direct numerical study of a population of yeast cells each modelled by the full-scale model, but this will be prohibitively time consuming since the system is very stiff (the timescales of the system span seven orders of magnitude; see Table 10 in Hynne *et al.* (2001)). Moreover, it will probably be equally difficult to draw any clear conclusions from the results.

To overcome these problems, we model the system of yeast cells in a CSTR quantitatively as a population of Stuart-Landau oscillators interacting by exchange of metabolites through the extracellular medium. (The Stuart-Landau equation was introduced in chapter 2). This approach reduces the complexity of the problem without sacrificing the biochemical realism, since the Stuart-Landau parameters of the model can be derived by a systematic expansion from any full-scale model of the yeast cell kinetics with a supercritical Hopf bifurcation as described in Ipsen *et al.* (1998). Alternatively, the parameters can be obtained by fitting the Stuart-Landau equation to perturbation experiments as we did in chapter 4.

We will consider N identical cells, each with volume ω, in an extracellular medium with volume Ω. Each cell is surrounded by a cell membrane able to transport certain chemical species between the intracellular and the extracellular medium. Concentrations of the M chemical species are $\mathbf{c}_i(t)$ in cell i and $\mathbf{c}(t)$ in the medium, and we denote the specific flow rate of the CSTR by j and the mixed flow concentrations by $\mathbf{c}^f$. As in our full-scale model, enzyme concentrations are assumed to be constant, and we neglect the changes in amounts of metabolites caused by the state difference between cells flowing in and out of the reactor. Then, the kinetic equations for this system are

$$\begin{aligned} \dot{\mathbf{c}}_i &= \mathbf{F}(\mathbf{c}_i) + \mathbf{G}(\mathbf{c}_i, \mathbf{c}) \\ \dot{\mathbf{c}} &= -\frac{\omega}{\Omega}\sum_i \mathbf{G}(\mathbf{c}_i, \mathbf{c}) + \mathbf{H}(\mathbf{c}) + j(\mathbf{c}^f - \mathbf{c}) \end{aligned} \tag{7.1}$$

where $\mathbf{F}(\mathbf{c}_i)$,$\mathbf{G}(\mathbf{c}_i, \mathbf{c})$ and $\mathbf{H}(\mathbf{c})$ describe the intracellular reactions, the transport across the cell membrane, and reactions in the extracellular medium, respectively.

$\mathbf{G}$ and $\mathbf{H}$ are expanded to first order from the stationary state $(\mathbf{c}_I^s, \mathbf{c}^s)$ of a system where all $\mathbf{c}_i$ are equal to $\mathbf{c}_I^s$. The stationary state is defined by

$$\begin{aligned} \mathbf{F}(\mathbf{c}_I^s) + \mathbf{G}(\mathbf{c}_I^s, \mathbf{c}^s) &= \mathbf{0} \\ -\frac{N\omega}{\Omega}\mathbf{G}(\mathbf{c}_I^s, \mathbf{c}^s) + \mathbf{H}(\mathbf{c}^s) + j(\mathbf{c}^f - \mathbf{c}^s) &= \mathbf{0}, \end{aligned} \tag{7.2}$$

and the expansion gives

$$\begin{aligned} \mathbf{G}(\mathbf{c}_i, \mathbf{c}) &= \mathbf{G}(\mathbf{c}_I^s, \mathbf{c}^s) + \left.\frac{\partial \mathbf{G}}{\partial \mathbf{c}_i}\right|_{(\mathbf{c}_I^s, \mathbf{c}^s)} (\mathbf{c}_i - \mathbf{c}_I^s) + \left.\frac{\partial \mathbf{G}}{\partial \mathbf{c}}\right|_{(\mathbf{c}_I^s, \mathbf{c}^s)} (\mathbf{c} - \mathbf{c}^s) \\ &= \mathbf{G}(\mathbf{c}_I^s, \mathbf{c}^s) - \mathbf{D}_I(\mathbf{c}_i - \mathbf{c}_I^s) + \mathbf{D}_E(\mathbf{c} - \mathbf{c}^s) \end{aligned}$$

and

$$\mathbf{H}(\mathbf{c}) = \mathbf{H}(\mathbf{c}^s) + \left.\frac{\partial \mathbf{H}}{\partial \mathbf{c}}\right|_{\mathbf{c}^s} (\mathbf{c} - \mathbf{c}^s) = \mathbf{H}(\mathbf{c}^s) + \mathbf{H}_E(\mathbf{c} - \mathbf{c}^s).$$

In this approximation the kinetic equations are

$$\begin{aligned} \dot{\mathbf{c}}_i &= \mathbf{F}(\mathbf{c}_i) + \mathbf{G}(\mathbf{c}_I^s, \mathbf{c}^s) - \mathbf{D}_I(\mathbf{c}_i - \mathbf{c}_I^s) + \mathbf{D}_E(\mathbf{c} - \mathbf{c}^s) \\ \dot{\mathbf{c}} &= -\frac{\omega}{\Omega}\sum_i (\mathbf{G}(\mathbf{c}_I^s, \mathbf{c}^s) - \mathbf{D}_I(\mathbf{c}_i - \mathbf{c}_I^s)) - \frac{N\omega}{\Omega}\mathbf{D}_E(\mathbf{c} - \mathbf{c}^s) \\ &\quad + \mathbf{H}(\mathbf{c}^s) + \mathbf{H}_E(\mathbf{c} - \mathbf{c}^s) + j(\mathbf{c}^f - \mathbf{c}) \end{aligned} \tag{7.3}$$

Defining $\mathbf{x}_i = \mathbf{c}_i - \mathbf{c}_I^s$, $\mathbf{x} = \mathbf{c} - \mathbf{c}^s$, $\tilde{\mathbf{F}}(\mathbf{x}_i) = \mathbf{F}(\mathbf{c}_i) - \mathbf{F}(\mathbf{c}_I^s)$ and using Eq. 7.2 we get

$$\begin{aligned} \dot{\mathbf{x}}_i &= \tilde{\mathbf{F}}(\mathbf{x}_i) - \mathbf{D}_I\mathbf{x}_i + \mathbf{D}_E\mathbf{x} \\ \dot{\mathbf{x}} &= \frac{\omega}{\Omega}\sum_i (\mathbf{D}_I\mathbf{x}_i) - \frac{N\omega}{\Omega}\mathbf{D}_E\mathbf{x} + (\mathbf{H}_E - j)\mathbf{x} \\ &= \frac{N\omega}{\Omega}(\mathbf{D}_I\frac{1}{N}\sum_i \mathbf{x}_i - \mathbf{D}_E\mathbf{x}) + (\mathbf{H}_E - j)\mathbf{x} \end{aligned} \tag{7.4}$$

In the somewhat unphysical limit of $\Omega \to 0$ we have $\frac{1}{N}\mathbf{D}_I \sum_k \mathbf{x}_k - \mathbf{D}_E \mathbf{x} \to 0$ which by substitution in Eq. 7.4 gives,

$$\dot{\mathbf{x}}_i = \tilde{\mathbf{F}}(\mathbf{x}_i) + \mathbf{D}_I(\frac{1}{N}\sum_k \mathbf{x}_k - \mathbf{x}_i). \tag{7.5}$$

This equation describes a population of cells with a linear mean-field coupling. We will refer to this limit as "direct coupling", since the cells are now coupled directly, whereas they were coupled through the medium before. The same approximation is obtained in the limit of $\mathbf{D}_I$ and $\mathbf{D}_E \to \infty$ at constant $\mathbf{D}_I/\mathbf{D}_E$.

It is seen that if $\mathbf{X}(t)$ satisfies $\dot{\mathbf{X}} = \tilde{\mathbf{F}}(\mathbf{X})$ then $\mathbf{x}_i(t) = \mathbf{X}(t)$ for all i is a solution of Eq. 7.5. If this solution is stable, then the dynamics of the population is identical to the dynamics of a single cell in the CSTR. This is the situation which we assumed in the development of our glycolysis model in chapter 5. In the opposite limit of $(N\omega/\Omega) \to 0$ or $\mathbf{D}_I$ and $\mathbf{D}_E \to 0$ at constant $\mathbf{D}_I/\mathbf{D}_E$, the cells will become independent of each other. This corresponds to loss of synchronization at low cell densities, as exemplified in Fig. 7.1.

7.1.1 Incorporating the Stuart-Landau description

The orders of the systems of kinetic equations Eqs. 7.4 and 7.5 are $(N+1)M$ and NM, respectively. For a large number of cells these are huge numbers, but they can be considerably reduced by taking advantage of the conclusion of section 4.2, namely that each yeast cell is well described as an oscillator close to a supercritical Hopf bifurcation. Except for short transients, the cellular dynamics will be confined to a two dimensional manifold embedded in the high dimensional concentration space. On this slow manifold, the original large system of kinetic equations can then be reduced to two differential equations describing the evolution of suitably chosen local coordinates on the manifold. As already discussed in chapter 2, this equation is the Stuart-Landau equation

$$\dot{z}_i = (\imath\omega_0 + \sigma\mu)z_i + g z_i |z_i|^2. \tag{7.6}$$

Both the Stuart-Landau parameters and the transformation from the local coordinates to actual concentrations can be explicitly calculated from a kinetic model (Ipsen *et al.*, 1998). For fast transients from any point in concentration space, the evolution is essentially an instantaneous projection onto the slow manifold, after which the state evolves in accordance with the local kinetic

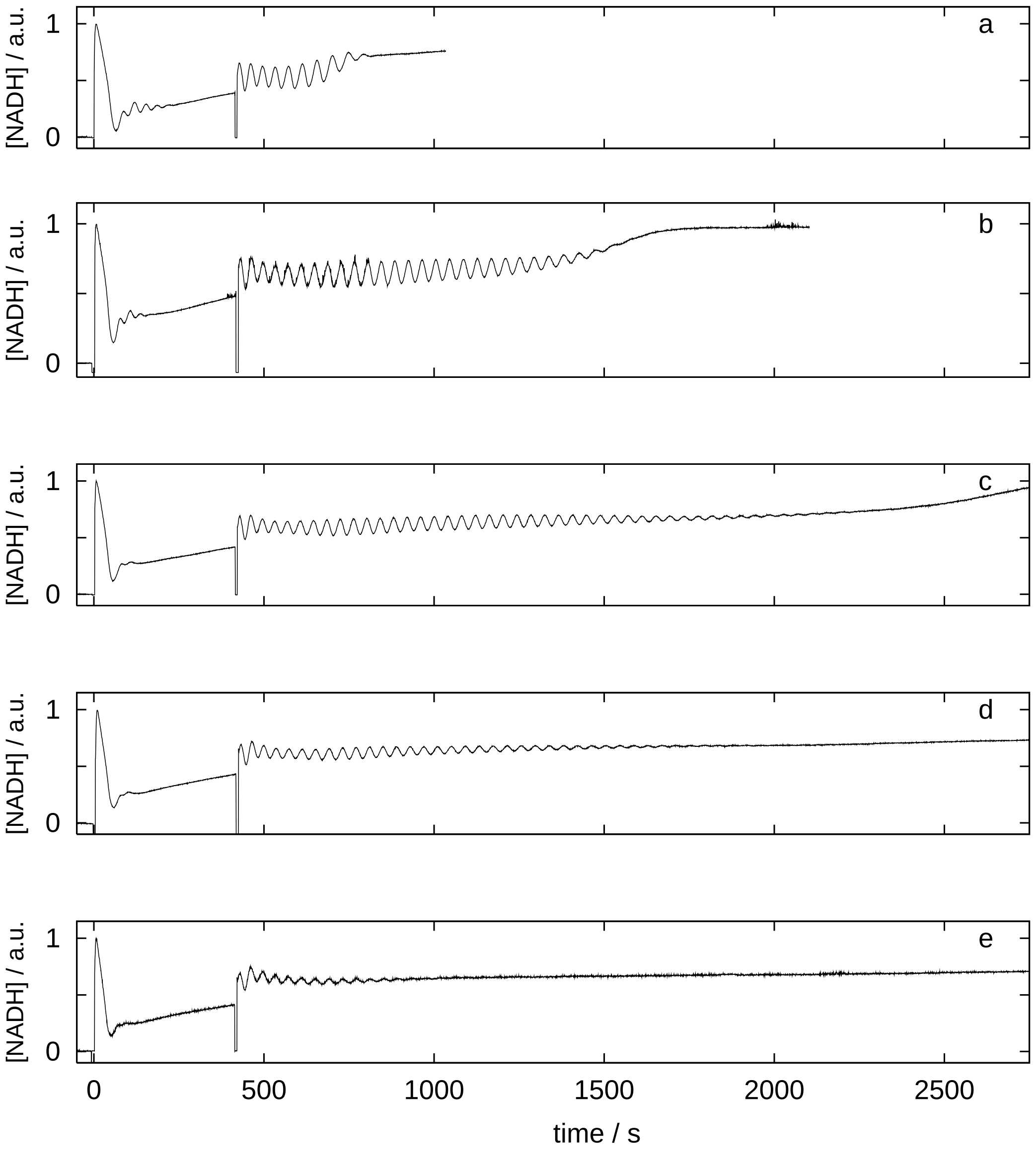

Figure 7.1: Dilution experiments. Transient experiments showing the effect of different cell densities: 39 (mg d.w.)/mL (a); 20 (mg d.w.)/mL (b); 13 (mg d.w.)/mL (c); 7.9 (mg d.w.)/mL (d); 3.9 (mg d.w.)/mL (e). The signal intensity has been scaled so that the height of the initial peak is one. In all experiments, glucose was added to a final concentration of 20 mM at time $t = 0$ s, and followed by 5 mM of KCN 7 min later.

equations. This projection of a point in concentration space onto the slow manifold is given by

$$z_i = \mathbf{u}^* \mathbf{x}_i \tag{7.7}$$

where $\mathbf{u}^*$ is the left eigenvector of the Jacobian matrix corresponding to the eigenvalue with the imaginary part $\imath\omega_0$. The presence of slow, hyperbolic modes is evident both in the experiments and in the model (see Fig. 4.8, Fig. 6.6 and Table 10 in Hynne *et al.* (2001)), but even though they can in some cases have a drastic influence on the dynamics (Ipsen *et al.*, 2000), we do not take them into account here.

Recall that, to lowest order, the transformation from z_i to the metabolite concentration vector $\mathbf{x}_i$ is given by

$$\mathbf{x}_i = z_i \mathbf{u} + \overline{z_i \mathbf{u}} \tag{7.8}$$

where $\mathbf{u}$ is the right eigenvector of the Jacobian matrix corresponding to the eigenvalue with the imaginary part $\imath\omega_0$. The bar denotes complex conjugation. The complex eigenvectors should be normalised such that $\mathbf{u}^*\mathbf{u} = 1$ and $\mathbf{u}^*\overline{\mathbf{u}} = 0$.

The slow manifold of the oscillating kinetics is not present in the extracellular medium, so we cannot use the Stuart-Landau description there. Accordingly, we will retain the concentration space coordinates for the description of this part of the system, and utilise the above transformations to connect the two descriptions.

To obtain an equation for a population of Stuart-Landau oscillators coupled through an extracellular medium, we first substitute the $\tilde{\mathbf{F}}$ term describing intracellular dynamics in Eq. 7.4 with Eq. 7.6, and transform the linear transport terms to Stuart-Landau coordinates by multiplication from the left by $\mathbf{u}^*$ (Eq. 7.7). We then use Eq. 7.8 to express $\mathbf{x_i}$ in terms of z_i, and arrive at

$$\begin{array}{rcl} \dot{z}_i & = & (\imath\omega_0 + \sigma\mu) z_i + g z_i |z_i|^2 + \mathbf{u}^* \cdot \mathbf{D}_E \cdot \mathbf{x} - \mathbf{u}^* \cdot \mathbf{D}_I \cdot (\mathbf{u} z_i + \overline{\mathbf{u} z_i}) \\ \dot{\mathbf{x}} & = & \frac{N\omega}{\Omega} \left(\mathbf{D}_I \cdot \frac{1}{N} \sum_i (\mathbf{u} z_i + \overline{\mathbf{u} z_i}) - \mathbf{D}_E \cdot \mathbf{x} \right) + (\mathbf{H}_E - j)\mathbf{x}. \end{array} \tag{7.9}$$

The dimension of this system is $2N + M$, which is considerably lower than the dimensions of Eqs. 7.4 and 7.5. The elimination of the fast modes from the intracellular kinetics also has the advantage that the system is no longer stiff, and can be integrated by explicit methods.

In the limit of $\Omega \to 0$, the variables of the external medium are eliminated, and the dynamic equations are reduced to

$$\begin{aligned}\dot{z}_i &= (\imath\omega_0 + \sigma\mu)z_i + g z_i|z_i|^2 \\ &\quad + \mathbf{u}^* \cdot \mathbf{D}_I \cdot (\mathbf{u}(\frac{1}{N}\sum_k z_k - z_i) + \overline{\mathbf{u}}(\frac{1}{N}\sum_k \overline{z_k} - \overline{z_i})) \qquad (7.10) \\ &= (\imath\omega_0 + \sigma\mu)z_i + g z_i|z_i|^2 + K(\frac{1}{N}\sum_k z_k - z_i) + L(\frac{1}{N}\sum_k \overline{z_k} - \overline{z_i}),\end{aligned}$$

which describes a population of Stuart-Landau oscillators with direct coupling.

Rescaling

For convenience, we will introduce the centroid $Z = \frac{1}{N}\sum_{i=1}^{N} z_i$. Any eigenvector $\tilde{\mathbf{u}} = \alpha\mathbf{u}$ obtained by multiplying $\mathbf{u}$ by any non-zero complex number α could be used in the transformations described above. From the normalisation $\mathbf{u}^*\mathbf{u} = 1$ we obtain $\tilde{\mathbf{u}}^* = \frac{1}{\alpha}\mathbf{u}^*$, and from the transformation $z = \mathbf{u}^*\mathbf{x}$ we have $\tilde{z} = \frac{1}{\alpha}z$. Substitution gives

$$\dot{\tilde{z}} = (i\tilde{\omega}_0 + \tilde{\mu}\tilde{\sigma})\tilde{z} + \tilde{g}\tilde{z}|\tilde{z}|^2 + \tilde{K}(\tilde{Z} - \tilde{z}) + \tilde{L}(\overline{\tilde{Z}} - \overline{\tilde{z}}),$$

but since $\tilde{z} = \frac{1}{\alpha}z$ we can also write this as

$$\frac{1}{\alpha}\dot{z} = (i\tilde{\omega}_0 + \tilde{\mu}\tilde{\sigma})\frac{1}{\alpha}z + \frac{1}{\alpha|\alpha|^2}\tilde{g}z|z|^2 + \tilde{K}\frac{1}{\alpha}(Z - z) + \tilde{L}\frac{1}{\overline{\alpha}}(\overline{Z} - \overline{z}).$$

However, this equation should still describe the same dynamical system, regardless of our choice of α. By comparison with Eq. 7.10 we therefore conclude that $\tilde{\omega}_0 = \omega_0$, $\tilde{\mu} = \mu$, $\tilde{\sigma} = \sigma$ and $\tilde{K} = K$, whereas $\tilde{g} = |\alpha|^2 g$ (a change of the modulus) and $\tilde{L} = \frac{|\alpha|^2}{\alpha^2}L$ (a rotation). This result is useful since we can use it to simplify Eq. 7.10. Let's consider the case where we choose an α with $|\alpha| = 1$. In this case $\tilde{g} = g$, so only $\tilde{L}$ is affected by the choice of eigenvector

$$\dot{\tilde{z}} = (i\omega_0 + \mu\sigma)\tilde{z} + g\tilde{z}|\tilde{z}|^2 + K(\tilde{Z} - \tilde{z}) + \frac{|\alpha|^2}{\alpha^2}L(\overline{\tilde{Z}} - \overline{\tilde{z}}).$$

It follows that we are free to rotate L independently of the other parameters. A convenient choice is to rotate L such that $L' = |L|$ and $L'' = 0$. Subsequently, we will choose a new rescaling β such that $\frac{|\beta|^2}{\beta^2} = \frac{|\alpha|^2}{\alpha^2}$. By this choice $\tilde{L} = L = |L|$, so we can now rescale the modulus of g independently of the other parameters. We choose to do this so that the radius of the limit cycle of a free-running oscillator is 1, which implies $g' = -\mu\sigma'$. With $\eta = g''/g'$ we can now rewrite Eq. 7.10 as

$$\dot{z}_i = (i\omega_0 + \mu(\sigma - \sigma'(1 + i\eta)|z_i|^2))z_i + K(Z - z_i) + |L|(\overline{Z} - \overline{z}_i) \tag{7.11}$$

without loss of generality. It is possible to rescale the time of this equation and obtain an even simpler form. However, we prefer to keep the physical time for the sake of clarity.

7.1.2 Complex coupling constants with negative real parts

Except for the counter-rotating term $|L|(\overline{Z} - \overline{z}_i)$, these equations are identical to equations for coupled Stuart-Landau oscillators, which have been studied in detail by the physics community. The dynamics of two identical, coupled Stuart-Landau oscillators are treated by Aronson *et al.* (1990) and de Vries *et al.* (1998), and populations of coupled Stuart-Landau oscillators with a distribution in their natural frequencies are treated by Matthews and Strogatz (1990) and Matthews *et al.* (1991) as well as by our collaborators Silvia De Monte and Francesco d'Ovidio at the Technical University of Denmark (De Monte and d'Ovidio, 2002; Danø *et al.*, 2001). The case of a globally coupled population of identical oscillators is treated by Hakim and Rappel (1992). See also Winfree (1967) where coupled oscillators were first discussed in a biological context, and d'Ovidio (2002) for a theoretical thesis on the topic.

An important result is that sufficiently close to the Hopf bifurcation, identical oscillators will always synchronize in phase (Hakim and Rappel, 1992). Apparently, this is a paradox since we do not see in-phase synchronization even if we model identical cells very close to the Hopf bifurcation. Of course, the first thing to check is that the above simplifications and transformations have not changed the synchronization properties of our model. As seen from Fig. 7.2, this is not the case: the cells still synchronize out of phase. This is also the case if we redo the simulation, but now with the coupling constant of the counter-rotating term $|L|$ set to zero (data not shown).

The Stuart-Landau parameters σ and g of the model do not fit the experimental observations very well (Table. 5.10). To test whether this is the cause of the out-of-phase synchronization, we substitute the Stuart-Landau parameters from the model with those determined from perturbation experiments (Fig. 4.8). As before, the coupling terms are calculated from the model

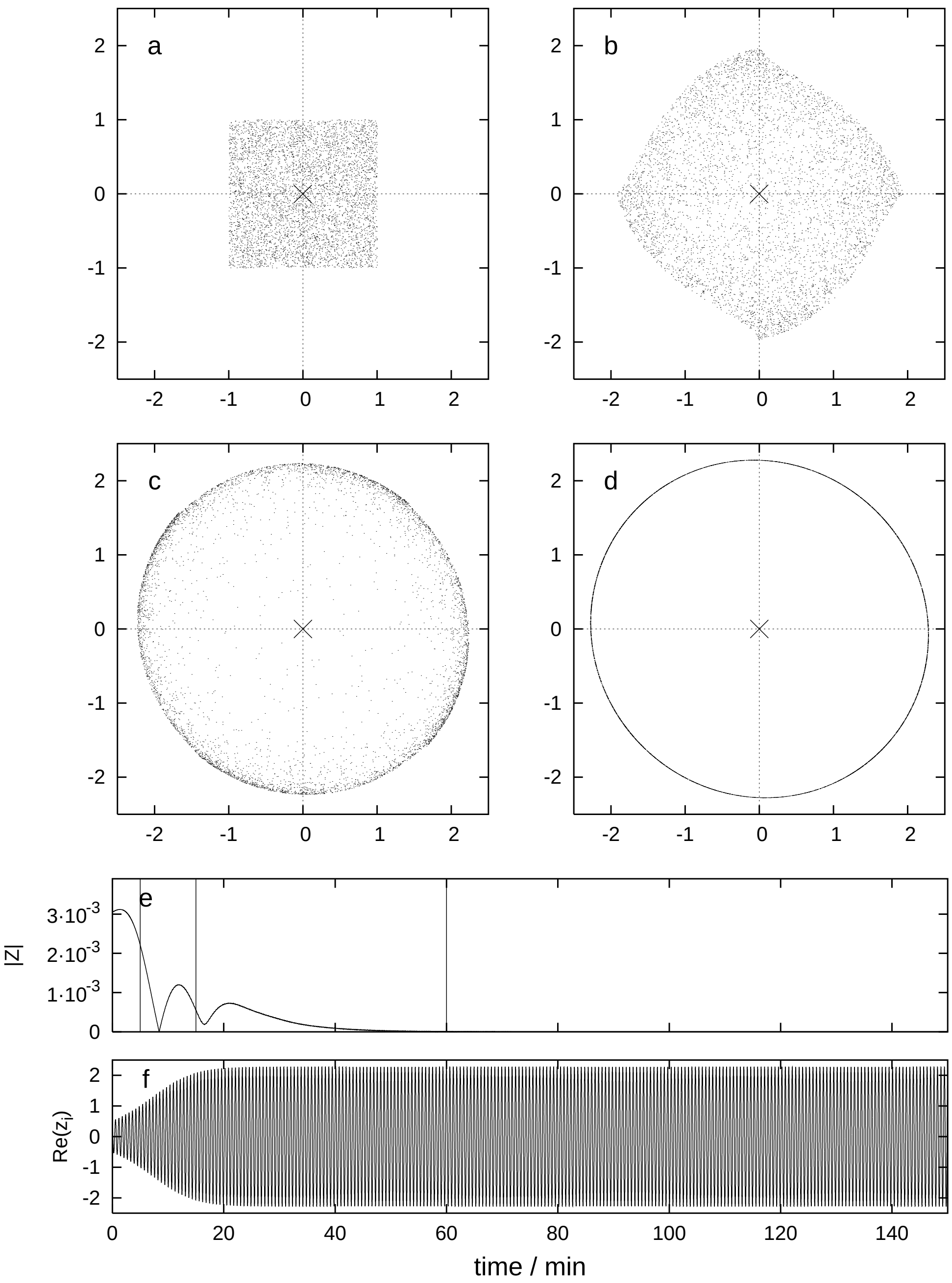

Figure 7.2: Out-of-phase synchronization in a simulation of 5000 directly coupled, identical Stuart-Landau oscillators with all parameters calculated from our glycolysis model according to Eq. 7.10 at $\mu = 0.5$, which corresponds to a mixed flow glucose concentration of 19 mM. The population shows out-of-phase synchronization in agreement with two cells and a medium modelled with the full glycolysis model. Panels (a-d) show snapshots of the plane of oscillations at different times. The centroid is indicated by a $\times$. (a): $t = 0$ min; (b): $t = 5$ min; (c): $t = 15$ min; and (d): $t = 60$ min. Panel (e) shows the time-course of the macroscopic amplitude. The vertical lines indicate the times of the snapshots shown in the panels above. Panel (f) shows the dynamics of a single oscillator in the population. g has been scaled so that $r_{1c} = 1$ for an isolated oscillator in a medium. η, σ and ω_0 according to Table 5.10; $K = -(0.12 + 0.34i)$ min^{-1} and $|L| = 0.36$ min^{-1}.

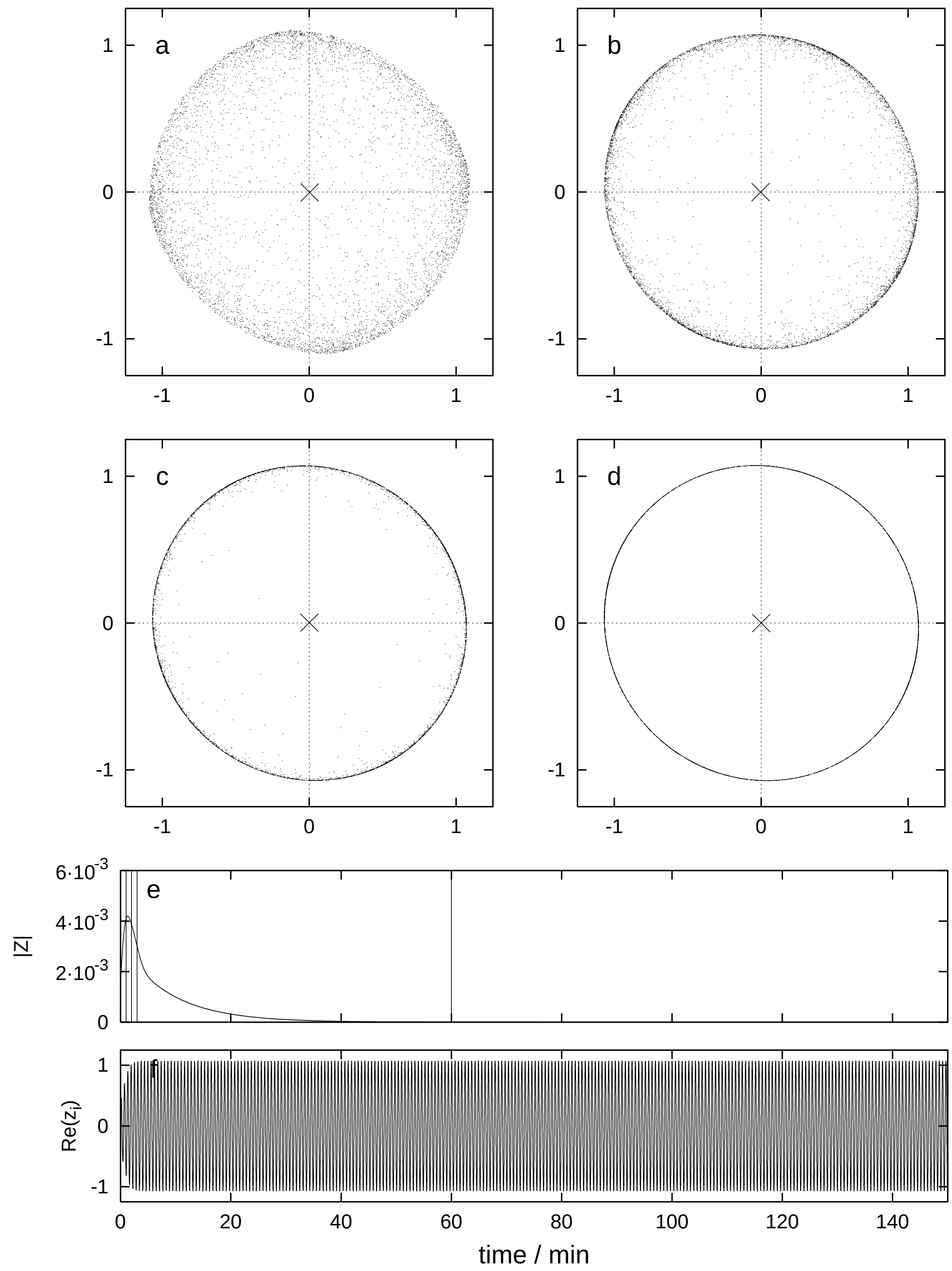

Figure 7.3: Out-of-phase synchronization in a population of directly coupled oscillators with experimentally determined Stuart-Landau parameters, but with K and $|L|$ calculated from the full-scale glycolysis model according to Eq. 7.10 at $\mu = 0$. Panels (a-d) show snapshots of the plane of oscillations at different times. The centroid is indicated by a $\times$. (a): $t = 1$ min; (b): $t = 2$ min; (c): $t = 3$ min; and (d): $t = 60$ min. Panel (e) shows the time-course of the macroscopic amplitude. The vertical lines indicate the times of the snapshots shown in the panels above. Panel (f) shows the dynamics of a single oscillator in the population. g has been scaled so that $r_{\mathrm{lc}} = 1$ for an isolated oscillator in a medium. η, $\mu\sigma$ and ω_0 from Fig. 4.8a, $K = -(0.13 + 0.35i)$ min^{-1} and $|L| = 0.38$ min^{-1}. Initial distribution of the 5000 oscillators as in Fig. 7.2a.

Table 7.1: Eigenvectors $\mathbf{u}$ and $\mathbf{u}^*$ for the intracellular species in the glycolysis model at the Hopf bifurcation. The last two columns display the norm of the components of $\mathbf{u}$ and the real part of the components of $\mathbf{u}^*\mathbf{u}$. The eigenvectors have no NAD^+ or AMP components, since the concentrations of these metabolites are given implicitly by conversion equations. The units of $\mathbf{u}$ and $\mathbf{u}^*$ are concentration and reciprocal concentration, respectively. Only the relative magnitudes of the vector components have physical significance.

s	$\mathrm{Re}(\mathbf{u}_s)$	$\mathrm{Im}(\mathbf{u}_s)$	$\mathrm{Re}(\mathbf{u}_s^*)$	$\mathrm{Im}(\mathbf{u}_s^*)$	$\lvert\mathbf{u}_s\rvert$	$\mathrm{Re}(\mathbf{u}_s^* \cdot \mathbf{u}_s)$
Glc	5.39e-02	-1.16e-02	-1.15e-02	-7.37e-02	5.51e-02	-1.47e-03
G6P	-4.68e-01	7.93e-02	-3.16e-01	7.44e-01	4.75e-01	2.07e-01
ATP	-2.46e-01	-2.11e-01	-8.94e-01	2.52e+00	3.24e-01	7.53e-01
ADP	1.43e-01	1.24e-01	-4.63e-01	1.27e+00	1.90e-01	-2.25e-01
F6P	-6.50e-02	-2.07e-03	-2.53e-01	-7.65e-01	6.50e-02	1.48e-02
FBP	5.69e-01	-3.51e-01	2.44e-01	1.88e-01	6.69e-01	2.05e-01
GAP	7.70e-03	-4.41e-03	4.98e-02	1.85e-01	8.88e-03	1.20e-03
DHAP	1.65e-01	-1.29e-01	1.64e-01	4.25e-02	2.09e-01	3.25e-02
BPG	-4.34e-05	-4.25e-05	-7.52e-01	2.40e+00	6.08e-05	1.35e-04
NADH	3.00e-02	0	5.44e-01	-1.89e+00	3.00e-02	1.63e-02
PEP	6.62e-04	-2.14e-04	-3.43e-01	1.17e+00	6.96e-04	2.40e-05
Pyr	2.27e-02	-1.20e-01	1.07e-02	-7.99e-05	1.22e-01	2.33e-04
ACA	-2.58e-02	7.51e-03	1.48e-02	5.47e-01	2.68e-02	-4.49e-03
EtOH	3.30e-02	-1.62e-02	0	0	3.68e-02	0
Glyc	-7.22e-03	-5.00e-02	0	0	5.05e-02	0

according to Eq. 7.10. As seen in Fig. 7.3, this still results in out of phase synchronization, but now the attraction of the individual oscillators to the limit cycle is faster. Therefore, the solution to the synchronization problem, as well as to the paradox, must be found in the coupling terms.

Indeed, closer inspection shows that the real part of the most important coupling constant K is negative. This case has been deliberately excluded from the analysis usually made of Eq. 7.11, because the coupling constant has been regarded as a physical diffusion constant, and thus a negative coupling constant (or a complex coupling constant with $\mathrm{Re}(K) < 0$) has been considered unphysical. In our case, however, there is nothing unphysical about a complex coupling constant with $\mathrm{Re}(K) < 0$ since the coupling is operating in a coordinate system defined in terms of dynamical modes rather than in the physical space of concentrations. From Eq. 7.10 it can be seen that K is a complex number composed of a linearised transport matrix multiplied from the left by $\mathbf{u}^*$ and from the right by $\mathbf{u}$. This means that it depends on the transport of chemical species through the cell membrane as well as on the eigenvectors of the Jacobian matrix. The negative real part of the coupling constant arises because only a few metabolites are capable of passing the cell membrane: if all species of the reaction system could pass the cell membrane, then the real part of K would always be positive. (If $\mathbf{D}_I = \mathbf{I}$ then $K = \mathbf{u}^*\mathbf{u} = 1$ and $L = \mathbf{u}^*\overline{\mathbf{u}} = 0$).

Indeed, if the calculations of the stability criterion for the in-phase solution of two coupled Stuart-Landau oscillators with no counter-rotating term given by de Vries *et al.* (1998) are redone without assuming $\mathrm{Re}(K) \geq 0$, one obtains two additional criteria from their Eqs. 40 and 41. The negative real part of K for our model violates these criteria. (See alternatively Eqs. 5.5 and 5.6 in Aronson *et al.* (1990)). We have not yet been successful in analysing the stability of the in-phase solution of Eq. 7.11. The calculations are complicated by the presence of the counter-rotating term, which prohibits the use of a rotating frame of reference. (As seen from Fig. 7.6, the radial symmetry of the problem is lost).

If the transport through the cell membrane is diffusive, or mediated by a simple carrier, the matrix $\mathbf{D}_I$ is a diagonal matrix with positive elements. The sign of the contribution to the transport term $K = \mathbf{u}^* \cdot \mathbf{D}_I \cdot \mathbf{u}$ in Eq. 7.10 can then be determined by inspection of the eigenvector components of the species, Table 7.1. For acetaldehyde, it can be seen that the real part of its contribution to K is always negative, independent of the size of the transport coefficient. This means that for the chosen operating point (*i.e.* the eigenvectors in Table 7.1), acetaldehyde works as an anti-phase synchronizing species[1]. A similar conclusion can be taken for glucose. The contributions from ethanol and glycerol are zero for our model. (As discussed in chapter 5, this is consistent with experiments). Since these four species are the only metabolites capable of passing the cell membrane, this explains why we get $\mathrm{Re}(K) < 0$ when the coupling constants are calculated from the model. The ACA membrane transport is modelled as simple diffusion, so the only ACA element of $\mathbf{D}_I$ is the diagonal element. Therefore, the contribution from ACA to K is given solely by its $\mathbf{u}_s^* \cdot \mathbf{u}_s$ component. This is different for the glucose transport.

[1]Note, however, that the presence of an extracellular medium will introduce an additional phase shift of the coupling substances, and this can cause a change of stability for the in-phase solution. See Reddy *et al.* (1999).

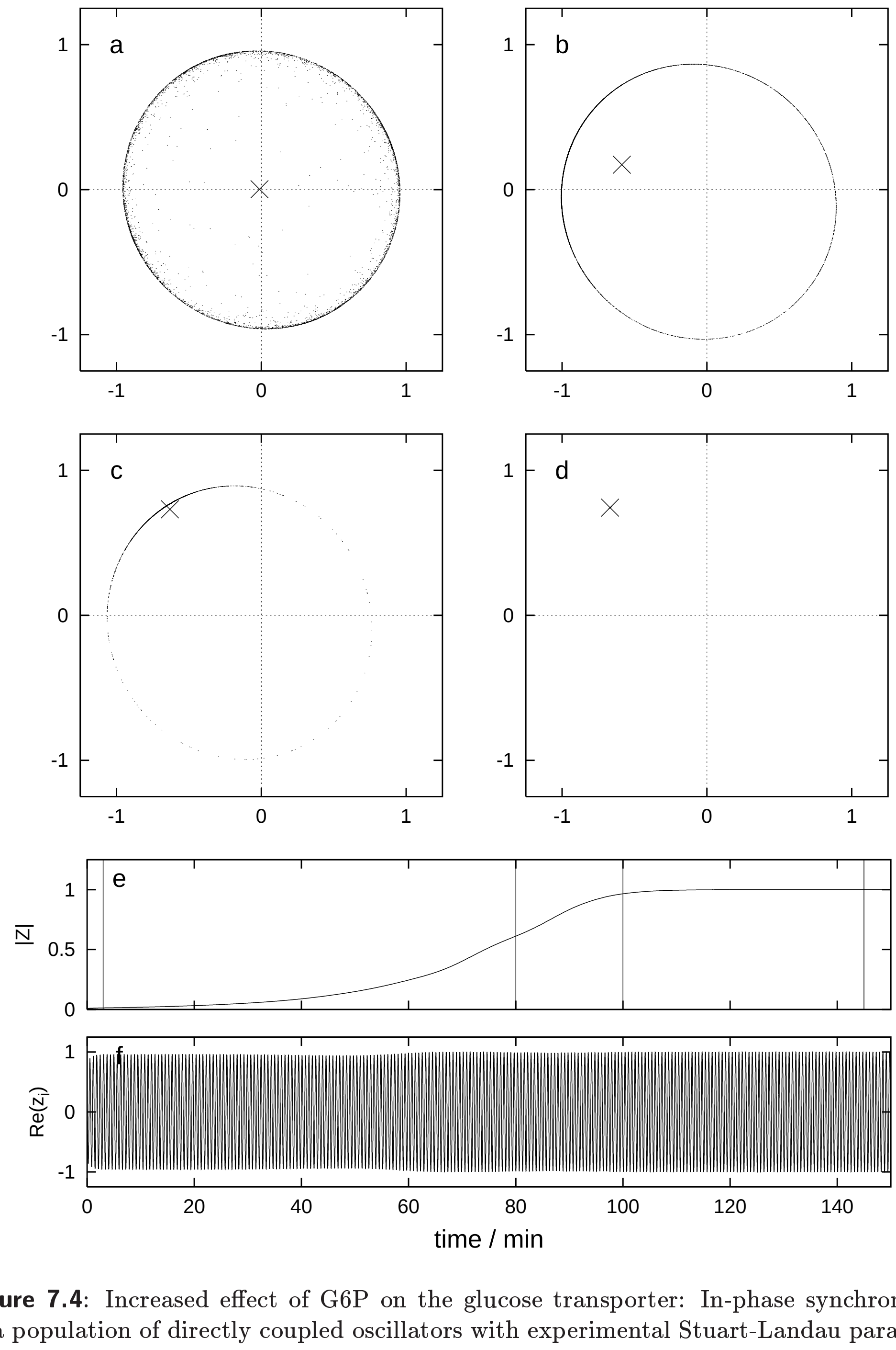

Figure 7.4: Increased effect of G6P on the glucose transporter: In-phase synchronization in a population of directly coupled oscillators with experimental Stuart-Landau parameters, and coupling constants K and L calculated from the eigenvectors of our model at $\mu = 0$, but now with the off-diagonal term of $\mathbf{D}_I$ increased from 6.6 min^{-1} to 24 min^{-1}. Panels (a-d) show snapshots of the plane of oscillations at different times. $\times$ indicates the position of the centroid Z. (a): $t = 3$ min; (b): $t = 80$ min; (c): $t = 100$ min; and (d): $t = 145$ min. Panel (e) shows the time-course of the macroscopic amplitude. The vertical lines in this panel indicate the times of the snapshots shown in the panels above. Panel (f) shows the dynamics of a single oscillator in the population. η, $\mu\sigma$ and ω_0 from Fig. 4.8a, $K = (0.071 + 0.23i)$ min^{-1} and $|L| = 0.27$ min^{-1}. Initial distribution of oscillators as in Fig. 7.2a. g has been scaled so that $r_{\text{lc}} = 1$ for an isolated oscillator in a medium. $N = 5000$.

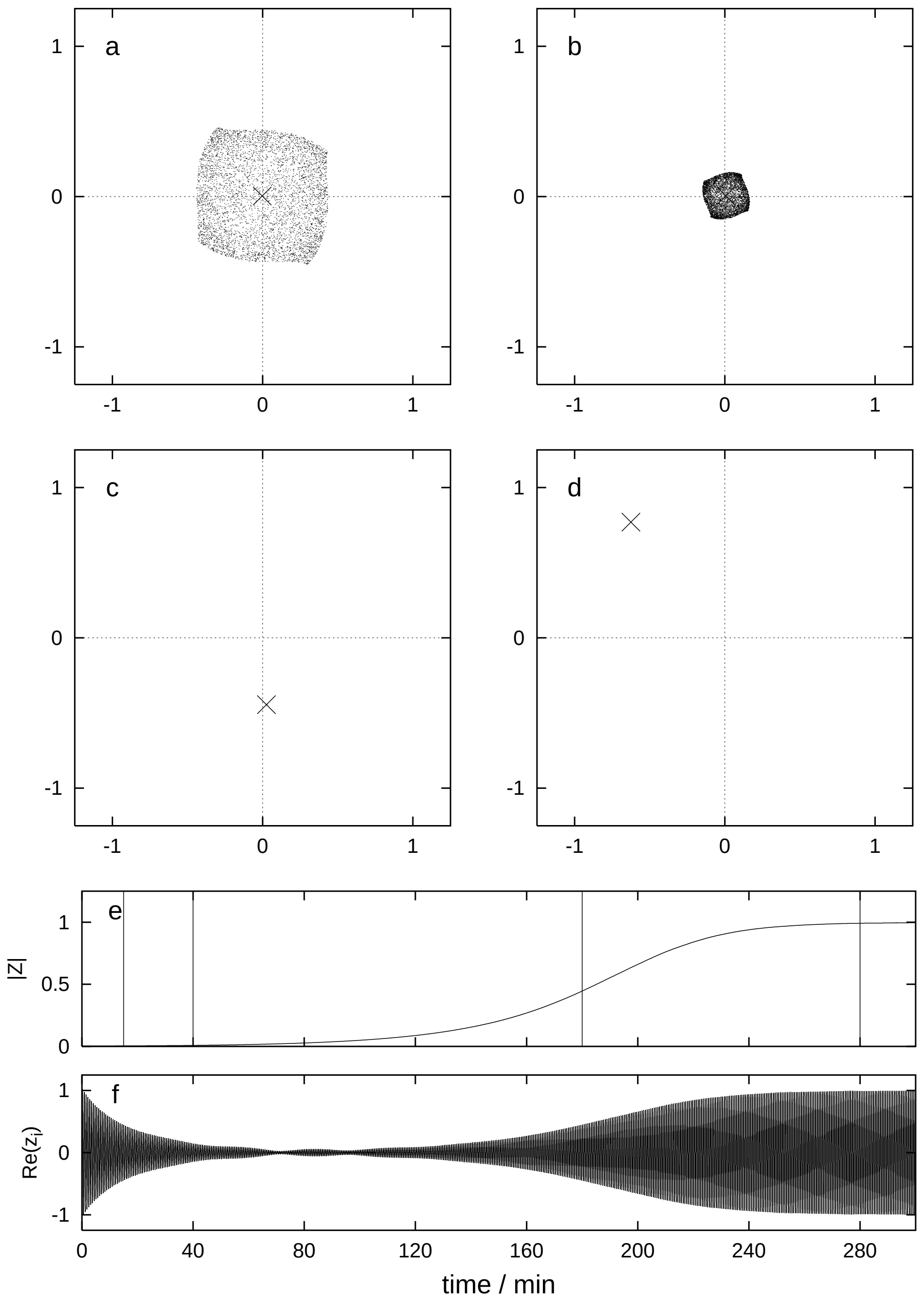

Figure 7.5: Very slow in-phase synchronization in a population of directly coupled oscillators with Stuart-Landau parameters from the full-scale model but with the off-diagonal term of $\mathbf{D}_I$ increased from 6.6 min^{-1} to 24 min^{-1} as in Fig. 7.4. Panels (a-d) show snapshots of the plane of oscillations at different times. $\times$ indicates the position of the centroid Z. (a): t = 15 min; (b): t = 40 min; (c): t = 180 min; and (d): t = 280 min. Panel (e) shows the time-course of the modulus of the centroid. The vertical lines in this panel indicate the times of the snapshots shown in the panels above. Panel (f) shows the dynamics of a single oscillator in the population. K and $|L|$ as in Fig. 7.4; all other parameters, scaling of g and initial conditions as in Fig. 7.2.

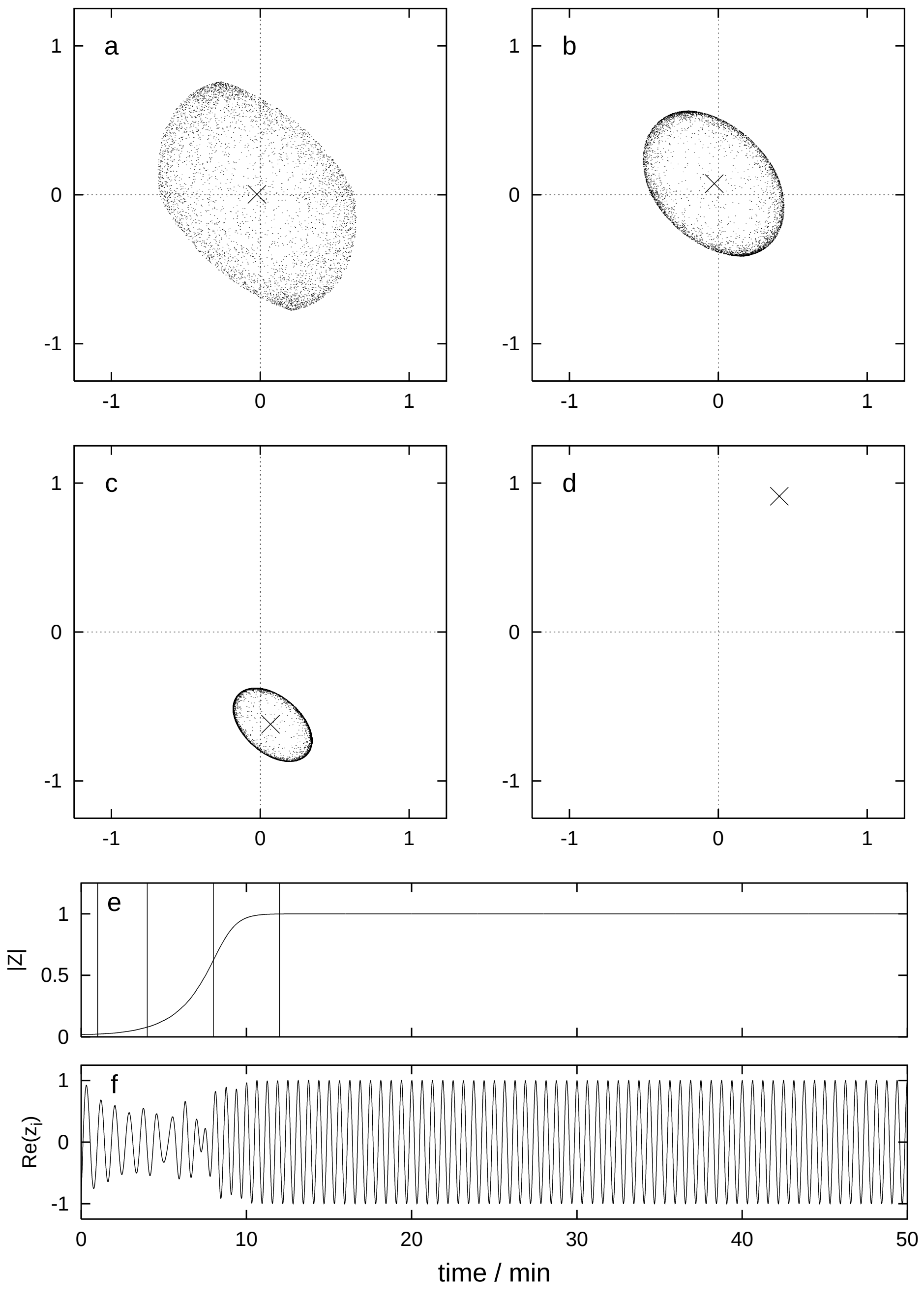

Figure 7.6: Faster in-phase synchronization is obtained by increasing the magnitudes of the coupling constants. All parameters, scalings and conditions are as indicated in Fig. 7.4 except for K and $|L|$ which have been increased by an order of magnitude ($K = (0.71+2.3i)$ min^{-1} and $|L| = 2.7$ min^{-1}). Panels (a-d) show snapshots of the plane of oscillations at different times. $\times$ indicates the position of the centroid Z. (a): $t = 1$ min; (b): $t = 4$ min; (c): $t = 8$ min; and (d): $t = 12$ min. Panel (e) shows the time-course of the macroscopic amplitude. The vertical lines in this panel indicate the times of the snapshots shown in the panels above. Panel (f) shows the dynamics of a single oscillator in the population.

Recall that we have modelled this transport with the rate equations

$$v_{\rightarrow} = \frac{V_m \frac{[\mathrm{Glc_x}]}{K_{\mathrm{Glc}}}}{1 + \frac{[\mathrm{Glc_x}]}{K_{\mathrm{Glc}}} + \frac{P\frac{[\mathrm{Glc_x}]}{K_{\mathrm{Glc}}}+1}{P\frac{[\mathrm{Glc}]}{K_{\mathrm{Glc}}}+1}\left(1 + \frac{[\mathrm{Glc}]}{K_{\mathrm{Glc}}} + \frac{[\mathrm{G6P}]}{K_{\mathrm{IG6P}}} + \frac{[\mathrm{Glc}][\mathrm{G6P}]}{K_{\mathrm{Glc}}K_{\mathrm{IIG6P}}}\right)}$$

$$v_{\leftarrow} = \frac{V_m \frac{[\mathrm{Glc}]}{K_{\mathrm{Glc}}}}{1 + \frac{[\mathrm{Glc}]}{K_{\mathrm{Glc}}} + \frac{P\frac{[\mathrm{Glc}]}{K_{\mathrm{Glc}}}+1}{P\frac{[\mathrm{Glc_x}]}{K_{\mathrm{Glc}}}+1}\left(1 + \frac{[\mathrm{Glc_x}]}{K_{\mathrm{Glc}}}\right) + \frac{[\mathrm{G6P}]}{K_{\mathrm{IG6P}}} + \frac{[\mathrm{Glc}][\mathrm{G6P}]}{K_{\mathrm{Glc}}K_{\mathrm{IIG6P}}}},$$

modelling a reversible glucose transporter regulated by G6P. This G6P regulation gives rise to the only off-diagonal term in $\mathbf{D}_I$, and the contribution of this term to K has a positive real part. The value of the off-diagonal term in $\mathbf{D}_I$ is 6.6 min^{-1} for the full-scale model, and this is not sufficient to change the out-of-phase synchronization behaviour. The result of a simulation with the experimental Stuart-Landau parameters, but with coupling constants calculated with an off-diagonal term of 24 min^{-1} instead of 6.6 min^{-1}, is shown in Fig. 7.4. A similar simulation with Stuart-Landau parameters calculated from the model is shown in Fig. 7.5. In both cases, the phases of the cells are now converging, and the centroid shows persistent oscillations corresponding to the behaviour observed in the experiments. Inspection of the K values shows that their real parts are now positive.

Still, if we compare the characteristic time of the synchronization process in both of these simulations with that of the mixing experiments (Pye, 1969; Ghosh *et al.*, 1971; Richard *et al.*, 1996a), we see that it is an order of magnitude too slow in the simulations. As shown in Fig. 7.6, this can be corrected by increasing the size of the two coupling terms by a factor of ten. Simulations where the initial conditions correspond to mixing experiments now show resynchronization that is comparable to that observed experimentally (data not shown). Biochemically, these observations indicate that the amplitude of the extracellular oscillations are too low in the model, and/or that their phases are wrong.

7.2 On the synchronization mechanism

Considering only the experimental data in the literature, ACA-mediated synchronization seems the best candidate for the synchronization mechanism (see the discussion in section 4.1.3). However, we have shown here that ACA functions as an anti-phase synchronizer when the transport matrix and the eigenvectors of the model are used. This will not change even for high coupling strengths (*i.e.* larger amplitude of the ACA oscillations).

Possibly, this is due to an error in the model. ACA interacts with the rest of glycolysis through the NAD^+/NADH system, and – as discussed in chapter 5 – the relative phases of NADH and ACA_x seem to be wrong, whereas the relative phases of most other species are correct (with G6P as a possible exception). Such an error for the NAD^+/NADH system is equivalent to errors in the eigenvector components of the relevant species, and therefore it will affect the contribution of the relevant species to K. The number of reactions in a pathway can affect the phase shift between its start and its end (Hunding, 1974; Rodríguez *et al.*, 2002), so a possible cause of the phase error of NADH and ACA_x is the lumping of three reactions (PGK, PGM and ENO) in the lower part of glycolysis into one (lpPEP). It is also possible that the delay introduced by the extracellular medium could cause a phase shift, such that ACA would contribute to in-phase synchronization.

This said, it is still problematic for the hypothesis of ACA-mediated synchronization that it has not yet been possible to model this synchronization mechanism quantitatively with a full-scale model; see the discussion of the synchronization problem in Winfree (1980).

Other models exist in which ACA synchronizes the glycolytic oscillations (Wolf and Heinrich, 2000; Bier *et al.*, 2000), but these models do not describe glycolytic oscillations in full detail or with quantitative agreement. A common problem to these models is that even though they can show in-phase synchronization, the timescale of synchronization in Pye's mixing experiment is much too slow compared to the period of oscillations. This problem is also found in our glycolysis model, and is associated with a too small $|\mathrm{Re}(K)|$ (compare Figs 7.4, 7.5 and 7.6).

Glucose-mediated synchronization?

The other synchronizer candidate is glucose. The analysis of the synchronization properties of the full-scale glycolysis model points to this substance as the most probable candidate, but a major problem exists: the glucose transporter is believed to be saturated in the transient experiments (see chapter 4), and since this implies that the yeast cells are insensitive to changes in the extracellular glucose concentration, it seems unlikely that modulations of the

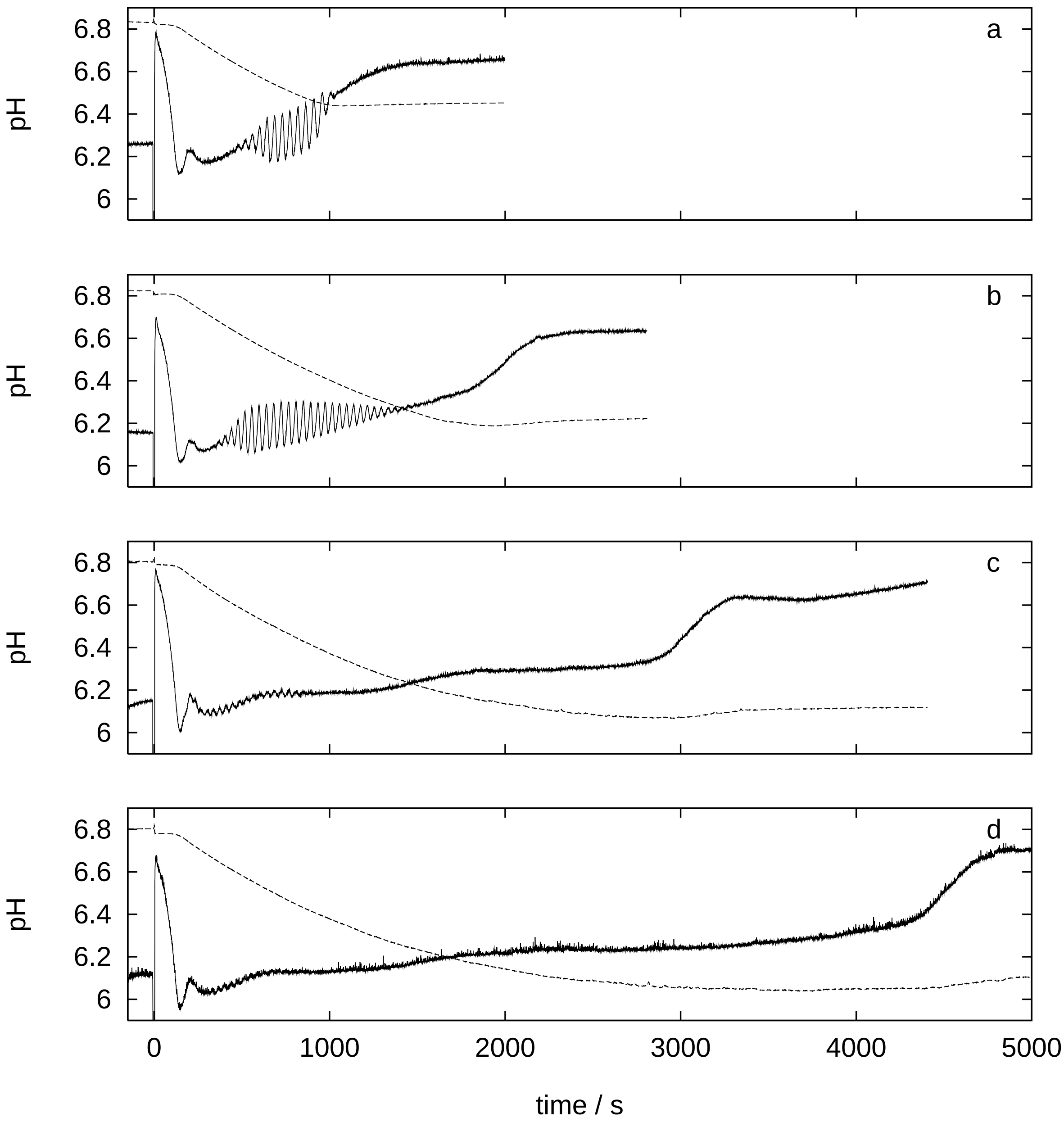

Figure 7.7: Macroscopic oscillations are suppressed by high initial glucose concentrations. Yeast cell suspensions at a final cell density of 28 (mg d.w.)/mL were given a KCN pulse of 5 mM final concentration at $t = -240$ s, and glucose pulses of equal volume but increasing concentrations at time $t = 0$, resulting in final glucose concentrations of 20 mM (a), 40 mM (b), 60 mM (c) and 80 mM (d).

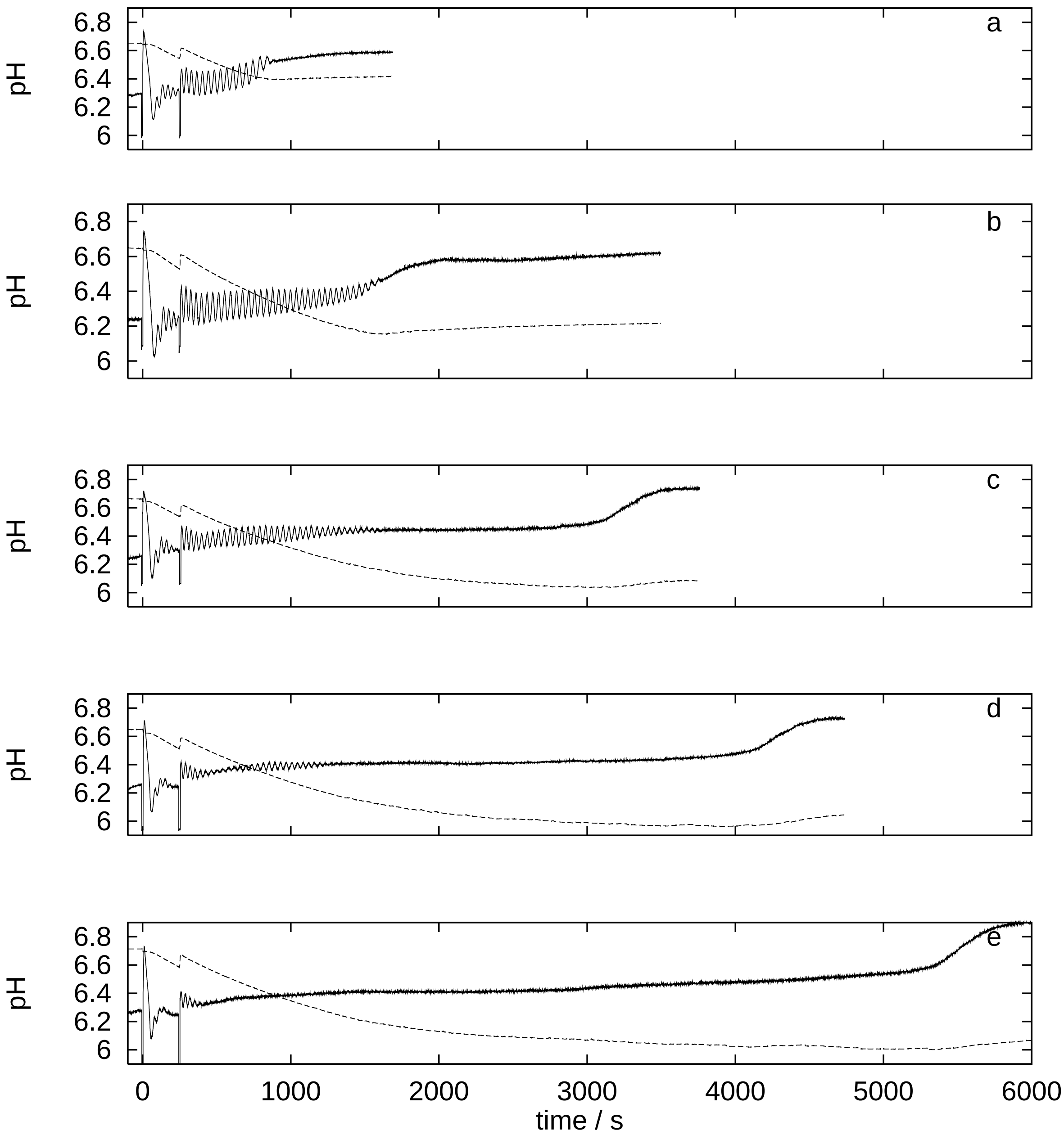

Figure 7.8: Macroscopic oscillations are suppressed by high initial glucose concentrations. Yeast cell suspensions were given a KCN pulse of 5 mM final concentration at $t = -240$ s, and glucose pulses at time $t = 0$ resulting in final glucose concentrations of 20 mM (a), 40 mM (b), 60 mM (c), 80 mM (d) and 100 mM (e). The final cell densities were either 28 (mg d.w.)/mL (a,b) or 26 (mg d.w.)/mL (c–e).

extracellular glucose concentration can transmit the signal necessary for the synchronization.

This seemingly rules out glucose as synchronization mechanism for glycolytic oscillations in yeast, but the experiments in Figs. 7.7 and 7.8 question this argument. If the initial glucose pulse is increased from the usual 20 mM to round 80 mM, macroscopic oscillations are no longer observed. Still, it appears that the yeast cells are running glycolysis normally, since the time from glucose addition to the shift to the high NADH state which indicates glucose run out, is proportional to the amount of glucose added. Furthermore, the pH time courses are practically identical (that is, up until the points of glucose depletion). So, at least it seems reasonable to suggest that the disappearance of macroscopic oscillations at high glucose concentrations is a desynchronization effect rather than a direct chemical or biochemical effect.

A possible explanation is that only at these high glucose concentrations have the yeast cells become insensitive to small glucose variations, either as a result of saturation, or because the high glucose concentration makes the relative size of such variations very small. Since glucose transport in yeast is very complicated with several glucose transporters operating at the same time (see Özcan and Johnston (1999) or appendix D), it might be possible that the glucose transporter responsible for the main flux is saturated, while other low-affinity transporters are not. This way, it would be possible to have glucose sensitive yeast cells under conditions where the glucose consumption rate seems constant (Fig. 6.10), but this requires a strong glucose response in oscillating yeast cells. The magnitudes of the glucose affinities of yeast hexose transporters could support this hypothesis: Before glucose depletion, the HXT1-encoded transporter with a K_{m} value of 50-100 mM is dominant, whereas the HXT7-encoded transporter found after the glucose depletion has a K_{m} value of 1-2 mM (Reifenberger *et al.*, 1997; Teusink *et al.*, 1998a).

If low-affinity components of the glucose transport system are needed in order to observe macroscopic oscillations, then this offers an explanation why long-lasting transient oscillations are only observed with yeast cells harvested at the point of glucose depletion, and not at a later stage: the high-affinity transporter should be dominating in order to set up a nearly constant glucose flux (see section 4.1), but some low-affinity components should still be present in order not to loose glucose sensitivity when the high-affinity components are saturated.

We tested this hypothesis by forcing experiments where the glucose inflow of the CSTR is pulsatile with a period close to the natural frequency of the yeast cells. This was obtained by running the burettes of the glucose inflow at double speed during half the forcing period, and stopping the glucose flow for the rest of the period. In the CSTR, the glucose supplied equalises the glucose consumed by the yeast cells plus that flowing out of the reactor. Therefore, this forcing represents the maximum glucose fluctuations that the yeast cells would be able to set up themselves. (Our CSTR setup is described in detail in Danø (1999)). Small samples of the cell suspension were removed from the CSTR and seperated from the yeast cells by filtering (0.45 μm, Milipore). The extracellular glucose concentrations in these samples were measured using a HK-based glucose kit purchased from Sigma. Results from such an experiment are shown in Figs. 7.9, 7.10 and 7.11. At low glucose concentrations, where the high-affinity transporter is not saturated, the yeast cells phase-synchronize their oscillations to the external forcing and show a marked response in both amplitude and frequency when a phase shift is introduced in the forcing (Fig. 7.9). We also found that the amplitude of the oscillations is larger during forcing than with a steady inflow of glucose solution (data not shown). In Fig. 7.10 the forcing is made at a somewhat higher glucose concentration. The yeast cells still respond to a phase shift, but the response is now mainly a frequency response and somewhat slower. In both cases, the maximum of the extracellular glucose concentration coincides with the quenching phase of glucose (cf. Fig. 4.8). The yeast cells are insensitive to the forcing when the high-affinity transporter is saturated at round $10 \times K_{\mathrm{m}}$ (Fig. 7.11).

From these experiments we conclude that even though extracellular glucose oscillations can entrain the glycolytic oscillations when the glucose transporter is not saturated, then glucose cannot be responsible for the synchronization process in yeast, since the transporter is saturated during the transient experiments.

I can think of one possible alternative explanation for the desynchronization phenomenon in Figs. 7.7 and 7.8. Like ACA, glucose is an aldehyde which might react with cyanide, so high initial glucose concentrations could deplete the cyanide otherwise needed for the synchronization (see section 4.1). However, the experiments in Fig. 7.12 show that glucose variations in the range from 10-40 mM affect the macroscopic dynamics even in the absence of cyanide. Moreover, we followed the cyanide concentration by UV absorbance measurements at 202 nm, and were unable to detect any absorbance change for 1 h in a solution of 30 mM KCN, 200 mM glucose and 100 mM phosphate buffer at 25°C and pH 6.8. Thus, the experiments in Figs. 7.7 and 7.8 remain unexplained.

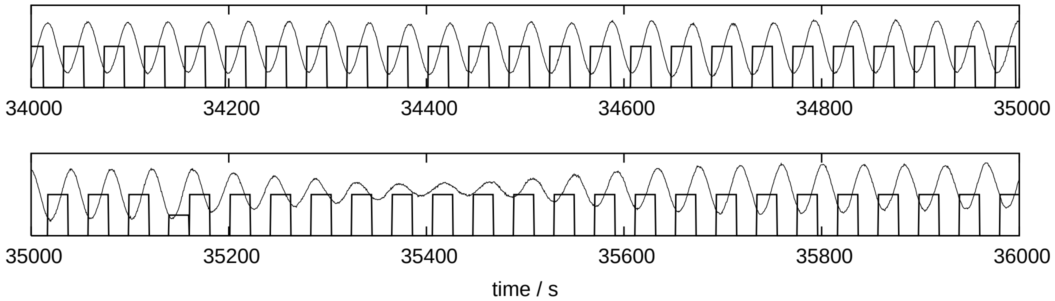

Figure 7.9: Forcing experiment at low glucose concentration. The oscillations of the yeast cells are entrained by the external glucose forcing, and the 180° phase shift in the forcing at time $t = 35140$ s gives rise to marked response in both frequency and amplitude. The thin line is the fluorescence signal in arbitrary units, but on a scale comparable to that of Figs. 7.10 and 7.11. The thick line shows the forcing: the glucose inflow is runnig at double speed when it is high, and it is stopped when it is low. The forcing period was set to 41 s in order to match that of the yeast cells. The average mixed flow glucose concentration of the CSTR was 20 mM, and we measured an extracellular glucose concentration of 2.4 mM. The final cell density was 31 (mg d.w)/mL, the mixed flow cyanide concentration was 5.7 mM and the specific flow rate was 23 min^{-1}.

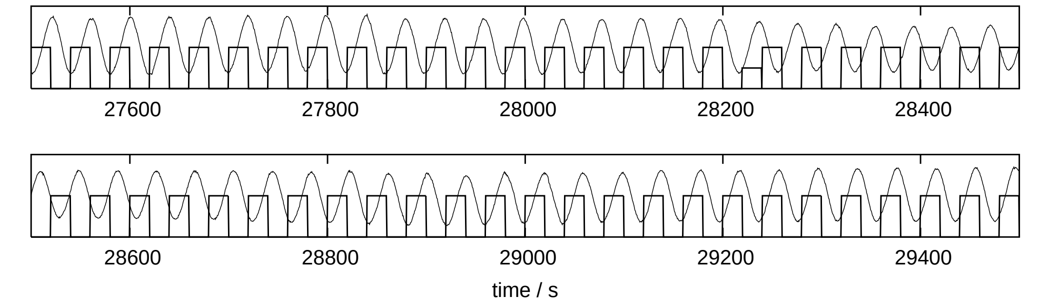

Figure 7.10: Forcing experiment at intermediate glucose concentration. The yeast cells respond to a 180° phase shift in the forcing at time $t = 28240$ s, but the response is mostly a frequency response The thin line is the fluorescence signal in arbitrary units, but on a scale comparable to that of Figs. 7.9 and 7.11. The thick line shows the forcing: the glucose inflow is runnig at double speed when it is high, whereas it is stopped when it is low. The forcing period was set to 40 s in order to match the period of the yeast cells at this operating point. The average mixed flow glucose concentration of the CSTR was 22mM, and we measured an extracellular glucose concentration of 4.2 mM. The specific flow rate and cell density were the same as in Fig 7.9, whereas the mixed flow cyanide concentration was 5.6 mM.

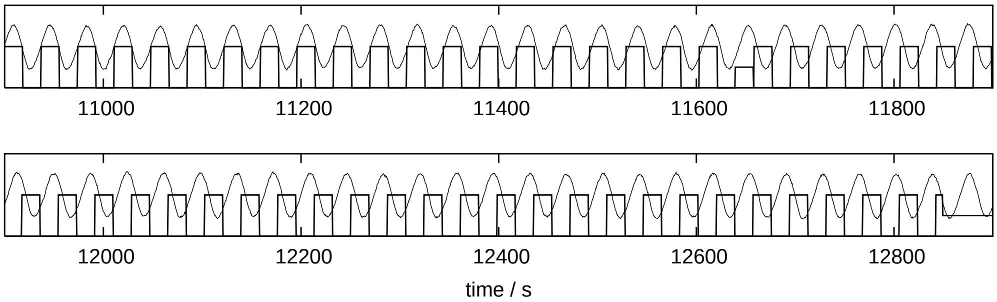

Figure 7.11: Forcing experiment at high glucose concentration. The yeast cells are unaffected by the forcing, and do not react to the $180°$ phase shift in the forcing at time $t = 11640$ s. The thin line is the fluorescence signal in arbitrary units, but on a scale comparable to that of Figs. 7.9 and 7.10. The thick line shows the forcing: the glucose inflow is runnig at double speed when it is high, and it is stopped when it is low. The forcing period was set to 37 s in order to match that of the yeast cells. The average mixed flow glucose concentration of the CSTR was 35 mM, and we measured an extracellular glucose concentration of 19 mM. The final cell density was 29 (mg d.w)/mL, the mixed flow cyanide concentration was 5.4 mM and the specific flow rate was 22 min^{-1}.

7.3 Conclusion

The main result of the work presented here is that when coupled Stuart-Landau oscillators are used for modelling the coupling dynamics of real, cellular oscillators where only a subset of the metabolites are exchanged, then one in general encounters complex coupling constants which might have negative real parts. As shown here, this is of primary importance for the coupling dynamics. Accordingly, the existing work on coupled Stuart-Landau oscillators should be extended to include these more general coupling constants. Likewise, it should be clear from our analysis why first reducing glycolysis to a core model, and subsequently analysing the synchronization properties as if the variables referred to physical concentrations, can lead to erroneous conclusions.

The specific results of the analysis of our full-scale model show that, in this otherwise realistic model and at the chosen operating point, ACA will always contribute to out-of-phase synchronization, whereas glucose might contribute to both in-phase and out-of-phase synchronization depending on subtleties of the glucose transport kinetics. On the basis of this, we have presented experimental evidence indicating that the oscillatory dynamics of the yeast cells are glucose sensitive, despite the saturation of the high-affinity component of the glucose transport. Still, our forcing experiments show that in general glucose

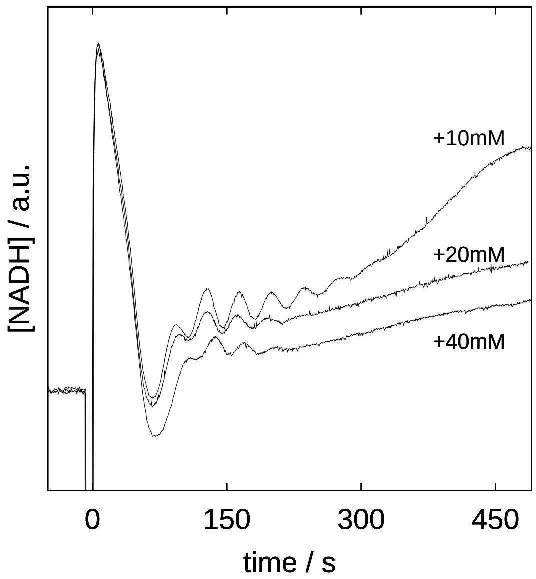

Figure 7.12: Variation of the initial glucose concentration in the absence of glucose. The plot shows the time traces of three different experiments where the yeast cell were given 10 mM, 20 mM and 40 mM glucose. The final cell density was 40 (mg d.w.)/mL in all three experiments.

does not mediate the synchronization of glycolytic oscillations: only at low glucose concentrations – when the high-affinity transporter is not saturated – do the yeast cells show phase-synchronization of their oscillations to our external glucose signal. Therefore, ACA remains the best synchronizer candidate for glycolytic oscillations in yeast, despite the difficulties of modelling the process. At present, we have no explanation for the glucose sensitivity found at high extracellular glucose concentrations.

If we broaden the perspective from yeast cells to cells showing glycolytic oscillations in general, then the observation that such oscillations can be entrained by a pulsatile glucose signal is interesting, since this allows for synchronization of glycolytic dynamics through modulation of *e.g.* the blood glucose level. By adjusting the affinity of the glucose transporters, different cell types can have different sensitivities towards such a signal. For animal tissues, this might provide an intimate link between function and regulation of cellular dynamics.

The explicit link between our full-scale model and the reduced equations provides a biochemical interpretation of the synchronization problem for this particular model: both the kinetic details of the glucose transporter and the phases of the metabolites in the lower part of glycolysis play crucial roles for the phenomenon, but at the same time the relation $K = \mathbf{u}^* \cdot \mathbf{D}_I \cdot \mathbf{u}$ states explicitly that the entire glycolytic system contributes to the coupling term according to

Table 7.1. This confirms the notion that cell synchronization is not a property of a single chemical species or enzyme, but a dynamic property of the entire glycolytic and fermentative network as well as the transport of metabolites through the cell membrane. Further progress on the understanding of active phase-synchronization in yeast cells could be obtained by combining more experimental data with the Direct Method of Optimization and the method for obtaining low-dimensional descriptions of populations of oscillators described here.

8

Nutritional control of bacterial colony front stability

Bacteria of the gram-negative species *Proteus mirabilis* form colonies with remarkable periodicity and circularity on standard laboratory media (Fig. 8.1). Complicated biological processes underlie this pattern formation: The colony expansion depends on a collective motility phenomenon called swarming carried out by specialised swarmer cells. Still, the pattern formation is well controlled and regular patterns occur under some conditions. Therefore, Proteus colonies are well suited as model systems of biological pattern formation.

Together with Kasper Dyring-Andersen, I have studied the pattern formation of this organism in the laboratory of Prof. James A. Shapiro at the University of Chicago. In this chapter I present the results of this work: The dynamics of the expanding front of the bacterial colony can be described phenomenologically as a simple reaction-diffusion system with autocatalytic front-propagation and a competing diffusion-induced lateral instability. Moreover, we show how simple experiments allow the components of this conceptual model to be identified biologically, thus linking function and dynamics.

Figure 8.1: The circular pattern which Proteus displays when grown on standard PA 2% agar plates with 0.4% glucose and 0.2% CAA. The picture is taken after 27 h of inoculation. The colony expands in time, whereas the terraces forming the bulls-eye pattern within the colony are stationary. Scale: all plates in all figures of this chapter are made in 9-cm Petri dishes.

Motivation

The goal of the present work is to elucidate the factors governing the remarkable circular symmetry of Proteus colonies. Is the symmetry a trivial consequence of medium homogeneity and the point inoculation, or does it require bacterial activity? If the agar surface is uniform on the length scale relevant to the motion of the bacteria, the circular shape of the inoculum will be retained. However, examination of the surface of an agar plate by reflected light shows that it is not uniform at all and displays macroscopic creases and folds. When other species of bacteria swarm on agar plates, they do not form patterns with such a high degree of circularity (*e.g. Serratia liquefaciens* in Eberl *et al.* (1999) or *Bacillus subtilis* in Matsushita (1997)). Moreover, mutants of Proteus are found which have lost the circularity of their pattern (Shapiro and Trubatch, 1991; Allison *et al.*, 1992; Shapiro, 1995). Even wildtype strains of *Proteus mirabilis* can show non-circular patterns when growth conditions are not optimal: In Fig. 8.2 we show how the circularity of the colony is lost as the amount of amino acids available to the colony is decreased. Thus, it seems reasonable to believe that the circularity of Proteus colonies is non-trivial, and that it has a biological basis. The challenge is to gain insights of the mechanisms involved by studying these expressive patterns in more detail. Work on the circularity of Proteus colonies has previously been presented by Sturdza (1973).

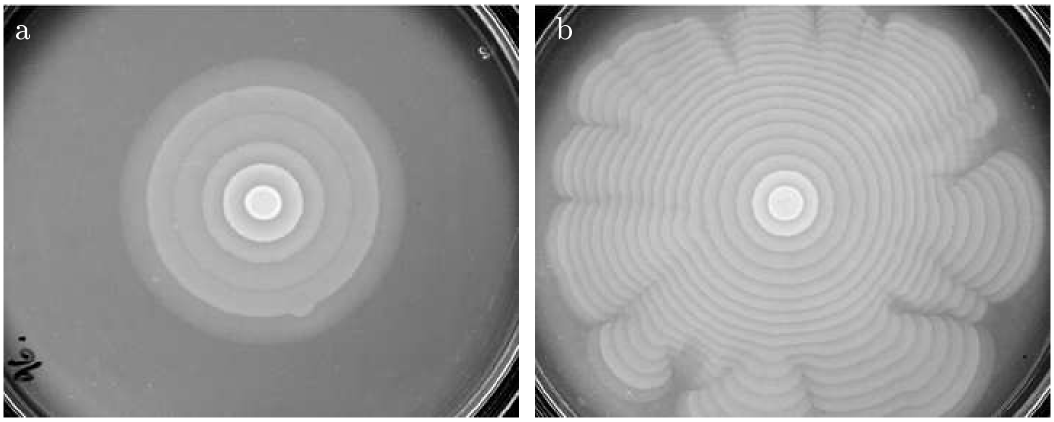

Figure 8.2: Proteus colonies on agar plates with different [CAA]. On the left a typical circular colony on an agar plate with standard nutrient composition (2% agar, 0.4% glucose and 0.2% CAA). On the right the concentration of CAA – a mixture of amino acids – is halved, and the colony now shows lateral front instabilities. Pictures are taken in a semi-darkfield setup after 26 h and 79 h of inoculation, respectively.

8.1 Background

8.1.1 Periodic nature of Proteus colony expansion

The periodicity of the patterns is far better understood than their circularity. The expansion of Proteus colonies involves two distinct cell types. The vegetative cell is a typical 2-3 μm long oligo-flagellated bacterium which swims in liquid media, but cannot migrate on solid agar surfaces. The other cell type, known as a "swarmer" cell, is a specialised cell type found exclusively on surfaces. Swarmer cells are multi-nucleate, hyper-flagellated filaments up to 80 μm long that can migrate collectively (swarm) on solid laboratory media at concentrations up to 3% agar. It is known that amino acids are required for the development of swarmer cells from vegetative cells (Jones and Park, 1967a). Allison *et al.* (1993) reported that glutamine alone will support the swarmer cell differentiation, but we have not been able to confirm this result. Instead, a mixture of amino acids is required. Casamino acid (CAA) is a convenient choice for this amino acid mixture.

Proteus colonies expand in a cyclic fashion on agar media. After inoculation, the swimmer cells begin to multiply in place and start to differentiate into swarmer cells. After a lag phase of a few hours, groups of swarmer cells emerge around the periphery and expand over the surface for a certain period of time. This period of active migration, during which swarmer cells septate and form new vegetative cells, is called the "swarming phase". After colony expansion ceases, there is a "consolidation phase," during which there is both swimmer cell proliferation and new swarmer cell differentiation. This cyclic behaviour creates the characteristic stationary "terraces" in the Proteus pattern. After some time in the consolidation phase, a new swarming phase begins and groups of swarmer cells again migrate over the agar surface. Under our standard conditions (32°C, 2% agar plates), swarmer cell groups can spread at a velocity of round 3 mm per hour, and thus the colony can fill an entire 9 cm plate within a day or two.

The swarmer cell motility is a cooperative phenomenon. One swarmer cell cannot migrate on its own, while groups (rafts) of swarmer cells can (Sturdza, 1975). Thus, the swarming ability depends on swarmer cell density in a nonlinear way, and population density dynamics play an important role in the formation of the colony (Matsuyama *et al.*, 2000). This density dependence is the key element of numerical simulations of the periodic colony expansion by Esipov and Shapiro (1998), Medvedev *et al.* (2000), Arouh (2001) and Czirók *et al.* (2001). (See also Matsushita (1997)). As we show below, the periodic nature of the Proteus behaviour is largely independent of the factors governing pattern circularity. Therefore, we are not concerned with the periodicity of the patterns *per se* in this study.

8.1.2 Proteus colonies as reaction-diffusion systems

Circular expanding fronts are not only found in Proteus colonies. They are particularly well known and well understood in chemical reaction-diffusion systems with autocatalysis like, *e.g.*, the Belousov-Zhabotinsky reaction. This understanding is based on the modulation of the front expansion velocity by the curvature of the front; see Horváth *et al.* (1993). We will show below that the theoretical framework which is used to explain circularity in these chemical systems applies equally well to the Proteus pattern on the macroscopic level, even though the bacterial system is very different from the chemical systems on the microscopic level.

The reason why the same mathematical framework can be used to explain the behaviour of such different systems is that their main components have equivalent dynamics. A key component is the diffusible autocatalyst (selfactivator; positive feedback). In the chemical systems, this is a substance which catalyses its own formation. So, when a little bit of this substance diffuses into the zone in front of the chemical front, a rapid increase of its concentration is triggered. This advances the chemical front. The autocatalyst is formed chemically from other substances, and when these substances are consumed, the concentration of the autocatalyst will stop increasing. Thus, another key component is the substances being consumed during the front propagation (negative feedback). In the bacterial system the diffusible autocatalyst is the population of motile swarmer cells. When a group of swarmers migrate into an uncolonised zone at the edge of the colony, more nutrients become available and they will increase their cell mass rapidly, thus advancing the bacterial front. If the increase in cell mass is too slow, then the colony expansion will result in a lower swarmer cell density. This will impair the collective motility of the swarmer cells and slow down the colony expansion. Therefore, the autocatalytic growth must be as important for the colony expansion as is the swarming capability. Obviously, the nutrients required for the growth of the swarmer cells are the equivalents of the chemicals being consumed during the chemical front propagation.

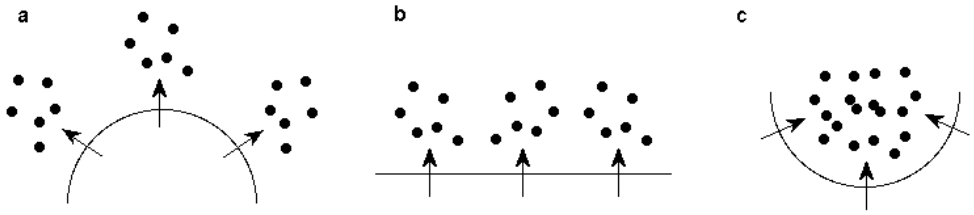

Figure 8.3: Autocatalytic front propagation. If part of the expanding front has increased outward curvature (a), then the autocatalyst will spread in a relatively larger area, and consequently the concentration of autocatalyst will be lower. This slows down the front propagation. Likewise, a part of the front which has inward curvature will have a larger concentration of the autocatalyst, and therefore expand faster (c). Thus, small lateral perturbations will decay, and a front with uniform curvature (c) is the stable solution.

As we shall now show, the lateral stability of the bacterial front governs whether the bacterial colony forms circular patterns or not. The simple description of front propagation given above provides an effective framework for the investigation of lateral front stability when two (or more) spatial dimensions are considered. If the growth and diffusion of the autocatalyst dominates the system (that is, the nutritional conditions of the bacterial colony are good and the bacterial motility is high) then the front will be stable towards spatial perturbations: If part of the front has increased outward curvature, then the autocatalyst will spread into a relatively larger area, and consequently the concentration of autocatalyst will be lower (Fig. 8.3a). This slows down the front propagation. Likewise, a part of the front which has inward curvature will have a larger concentration of the autocatalyst, and therefore expand faster (Fig. 8.3c). Thus, small lateral perturbations will decay, and a front with uniform curvature is the stable solution. If the bacteria are inoculated on a line, then this results in a planar front, and if the bacteria are inoculated in a single spot, then the uniform curvature solution is a circular pattern.

If the bacterial motility is poor or the nutrient availability is low (and, consequently, the bacterial growth is poor), then the dynamics of the front expansion will be governed by the diffusion of nutrients towards the colony. It can easily be seen (by inverting the arrows in Fig. 8.3) that this reverts the curvature dependence so that parts of the front with increased outward curvature now grow faster than the rest of the front. In its extreme form, the resulting diffusion-induced lateral instability leads to diffusion-limited aggregation (DLA) and fractal boundaries. Such patterns are well documented in many situations in physical, chemical and biological systems including electrodeposition, snow-flake formation, flame instabilities, and nutrient deficient bacterial colonies. (See Vicsek (1992) for a general reference, and Matsushita and Fujikawa (1990), Matsuyama and Matsushita (1993), Ben-Jacob and Cohen (1997) and Matsushita (1997) for references specific to bacterial colonies).

In Proteus colonies on standard laboratory medium we can expect both mechanisms to work simultaneously. Therefore, front stability is a balance between the autocatalytic growth and the diffusion of the autocatalytic substance on one hand, and the nutrient consumption and the diffusion of nutrients on the other hand. Consequently, we can expect a bifurcation from stable to unstable fronts to occur if the growth of swarmer cells (the autocatalyst) is impaired, when the swarming (the diffusion of the autocatalytic substance) is lowered or when the strength of the diffusion instability is increased by lowering the nutrient concentration.

In the experiments presented below, we change growth parameters and inoculation geometries systematically. This way, we show that the phenomenology of the Proteus system agrees with the framework presented above, and we identify the key elements of the reaction-diffusion description biologically.

8.2 Experiments

8.2.1 Methods

Strains

The strain used is the wild type strain PRM 1. This strain has been used in several previous studies, including Rauprich *et al.* (1996) and Itoh *et al.* (1999). The strain was maintained on 3% agar plates with 0.4% glucose and 0.2% CAA.

Media and culture conditions

Both solid and liquid media are composed of a PA minimal salt medium as described in Robinson (1964) and Nieder and Shapiro (1975), 0.0002% nicotinic acid and different concentrations of glucose and casamino acids (CAA) as specified. Plates were solidified with agar. In some experiments, single amino acids or additional amounts of ammonium chloride were added. When nothing else is explicitly specified, the glucose concentration is 0.4%, and the agar concentration is 2.0%. Note that the PA minimal salt medium contains 0.2% NH_4Cl. All experiments were performed at 32°C.

9-cm-diameter standard Petri dishes were used for the experiments. 25 mL of molten medium were poured into each of the Petri dishes, which were then left to cool on the table (lid on, no stacking). The plates were then dried for 20 h at 37° before they were stored at room temperature in sealed plastic bags. This procedure insures minimal intra-batch variation of the softness of the plates, but some variation occurs between batches. The effect of plate geometry was tested by using square Petri dishes in some geometrical experiments. No differences in colony patterns were found.

Inoculations were made from fresh overnight liquid cultures adjusted to an optical density at 650 nm of 0.5 ($\sim 10^9$ CFU/mL). Our standard inoculation volume was 2 μL pr. spot.

Photography and measurements

Most pictures are reflected-light photographs taken with a 35-mm camera using the ceiling light fixtures for illumination as described by Shapiro (1985). The photographs in Figs. 8.6c and d were taken with a WILD Makroskop 420 fitted with coaxial illumination, and the transmitted-light photographs in Figs. 8.6a and b were taken with a 35-mm camera fixed above the colony, which was placed on a glass plate and illuminated from the sides below by two flashes. Similarly, in the setup used for Fig. 8.2 the plate is illuminated from the sides below by a ring-shaped fluorescent tube. Expansion rates and swarming periods were measured in “human camera” experiments, where the colony radius is measured periodically with a ruler on the back of the Petri dish.

8.2.2 Basic nutrient effects

Microscopically, the bacterial system is very different from the chemical reaction-diffusion systems. Therefore, we can manipulate the bacterial reaction-diffusion system by means that are not available in the chemical reaction-diffusion systems. As reported by Rauprich *et al.* (1996), the bacterial motility can be changed simply by changing the hardness of the agar: when the agar content is increased, the colony expands slower. Probably, this is a purely physical effect. Rauprich *et al.* (1996) also investigated the effect of glucose concentration on colony expansion rate. As seen in figure 8.4, glucose only affects the rate of colony expansion below a very low threshold. At the standard 0.4% glucose concentration the swarmer cells are saturated with respect to glucose.

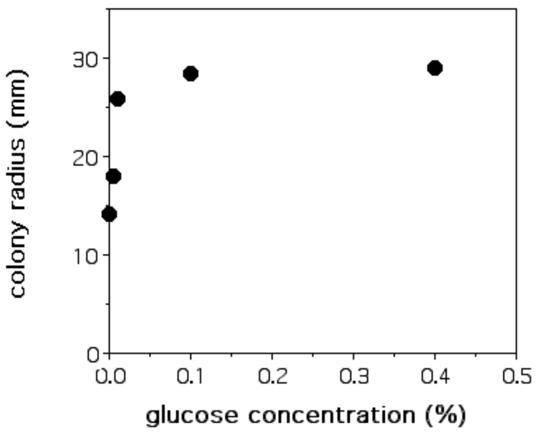

Figure 8.4: Radius of colonies after 17.6 h of inoculation as a function of glucose concentration. All plates were 2% agar plates with 0.2% CAA. (A similar experiment is described in Rauprich *et al.* (1996).)

In contrast, varying the concentration of the amino acid mixture (CAA) has a pronounced effect on the colony expansion rate. The colony expansion velocity v increases with the CAA concentration according to $v \propto \log[\mathrm{CAA}]$ with different proportionality constants at different agar concentrations (Fig. 8.5a).

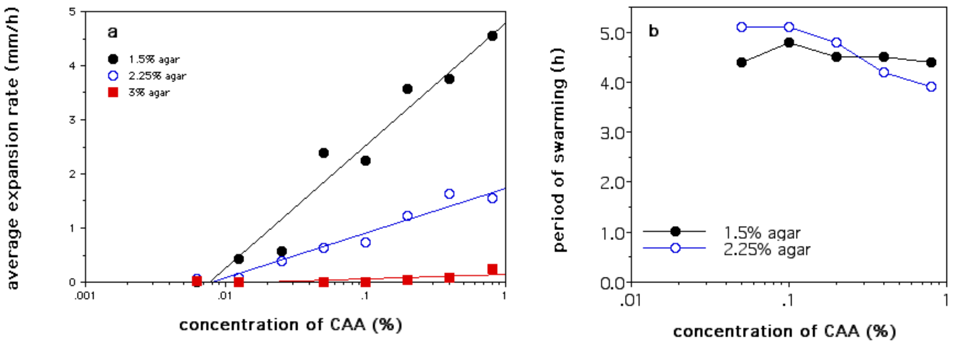

Figure 8.5: Swarming speed (a) and periodicity (b) measured on plates with different [CAA] and agar contents. The swarming period remains almost constant, whereas swarming speed shows a large increase as the concentration of CAA in increased.

Remarkably, the period of the swarming plus consolidation phase is roughly unaffected by such changes in the CAA concentration (Fig. 8.5b). This indicates that the periodicity and the front propagation of the colony can be viewed as two largely uncoupled phenomena (see also Rauprich *et al.* (1996)). This warrants separate investigations of the two phenomena. As a practical consequence, terrace widths can conveniently be taken as a measure of colony expansion rates.

The different effects of glucose and CAA on colony growth are highlighted by experiments with nutrient depleted zones. In these experiments, bacteria are inoculated along the edges of a large square. As they grow towards the center of the Petri dish, they gradually consume the nutrients in the agar plate until the colony expansion finally stops, leaving a nutrient depleted region in the center of the plate (Fig. 8.6). Subsequently, this zone can be used to test the effects of glucose and CAA directly on the colony. Addition of glucose to this sterile zone causes a marked increase in cell density (the light rim around the depleted zone in Fig. 8.6a) but no further swarming (Fig. 8.6c). Addition of CAA results in formation of new thin layers of swarmer cells (Fig. 8.6d), while no apparent increase in cells mass is seen (Fig. 8.6b). Thus, the two nutrients play different roles in the growing colony: Glucose supports cell growth but not swarming, whereas amino acids primarily support swarming or growth of swarmer cells.

Both swarmer cells and vegetative cells are present in expanding Proteus

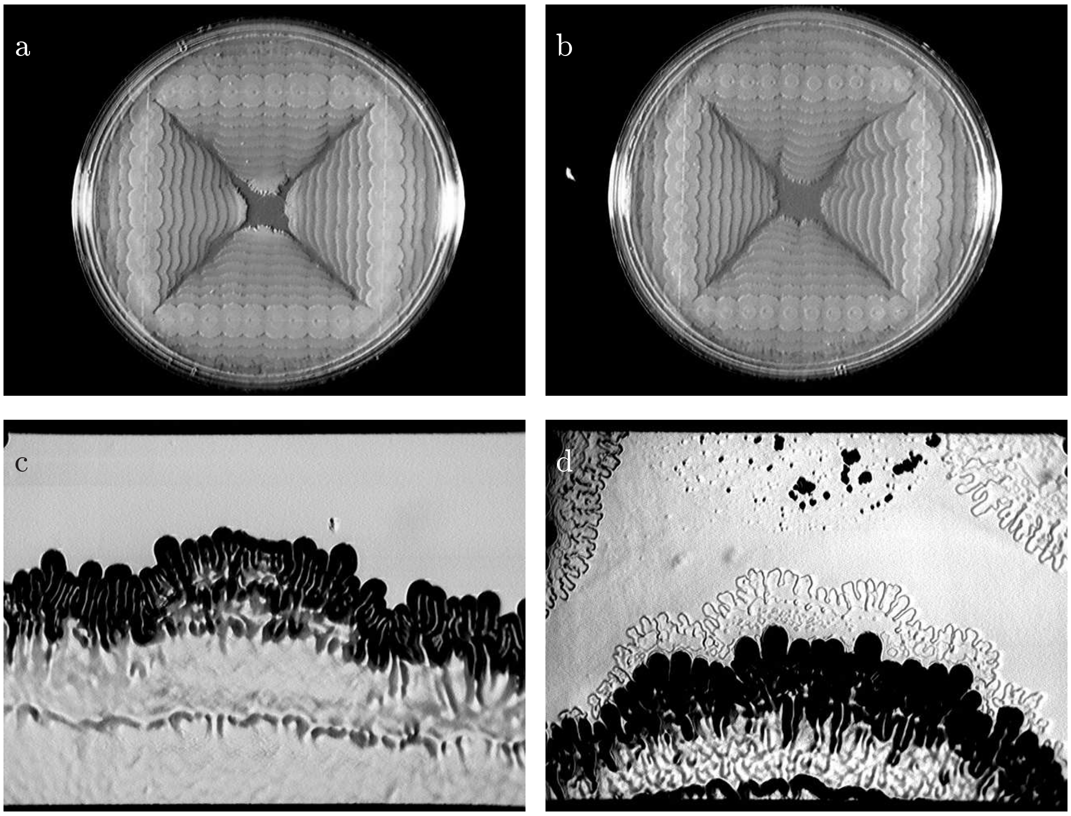

Figure 8.6: Direct tests of the effects of CAA and glucose. The effect of adding glucose or CAA in the nutrient-depleted, sterile centres that form when the bacteria are inoculated in spots along the sides of a 60 mm large square. After 65 hours of growth on 2.25% agar plates with 0.2% CAA and 0.4% glucose, the front has come to a complete stop. At this point either 10 μL of 40% glucose or 10 μL of 20% CAA is added to the centre. After an additional 23 h of inoculation, the plate given glucose shows a marked increase in cell mass around the sterile centre (a) but no swarming (c). The plate given CAA shows no apparent increase in cell mass (b), but instead a thin layer of cells has swarmed out from the original front towards the drop of CAA (d). Both (c) and (d) are 1.1 cm x 0.8 cm enlargements of the colony perimeter towards the sterile center.

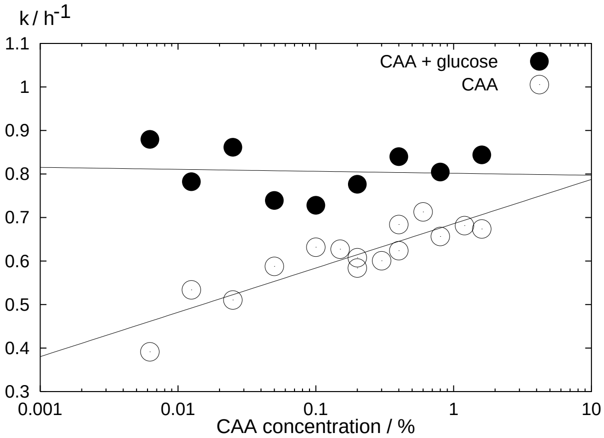

Figure 8.7: Results from liquid growth experiments, showing the effect of CAA concentration on the exponential growth rate k of swimmer cells. When growing on PA medium with 0.4% glucose and CAA (•), the growth rate is roughly independent of [CAA] with a mean growth rate of 0.81 $\pm$ 0.06 h^{-1}. When growing in PA medium with CAA but without glucose (○), the growth rate increases with increasing [CAA].

colonies. To differentiate the effects of glucose and amino acids further, we measured the growth rates in liquid cultures where only vegetative cells are present (Fig. 8.7). When CAA is the only carbon and energy source, the growth rate increases with CAA concentration. However, this increase is not as dramatic as the increase of colony expansion rate seen on solid media (Fig. 8.5), and the growth rate increases and becomes independent of the CAA concentration when the medium is supplemented with glucose.

Thus, it appears as if the preferred carbon and energy source of the vegetative cells is glucose, while amino acids are essential for the formation and the active motility of the swarmer cells. This finding is in line with Jones and Park (1967b), who found that swarmer cells differ from vegetative cells in having no detectable amino acid pool, and suggested that this is due to the vast flagellar synthesis by developing swarmer cells.

8.2.3 Spatial effects

These basic insights allow us to test our reaction-diffusion hypothesis by simple experiments. On standard agar plates, the key nutrient appears to be CAA. Lowering its concentration will decrease both the growth rate and the motility of the swarmer cells, so we expect the bacterial front to loose stability at low CAA concentrations. In Fig. 8.8a,b,c we show how the ability to regain colony circularity is lost, as the amount of amino acids available to the colony is decreased. For comparison, a picture showing laterally stable, travelling fronts in the autocatalytic Belousov-Zhabotinsky reaction is shown in Fig. 8.8d.

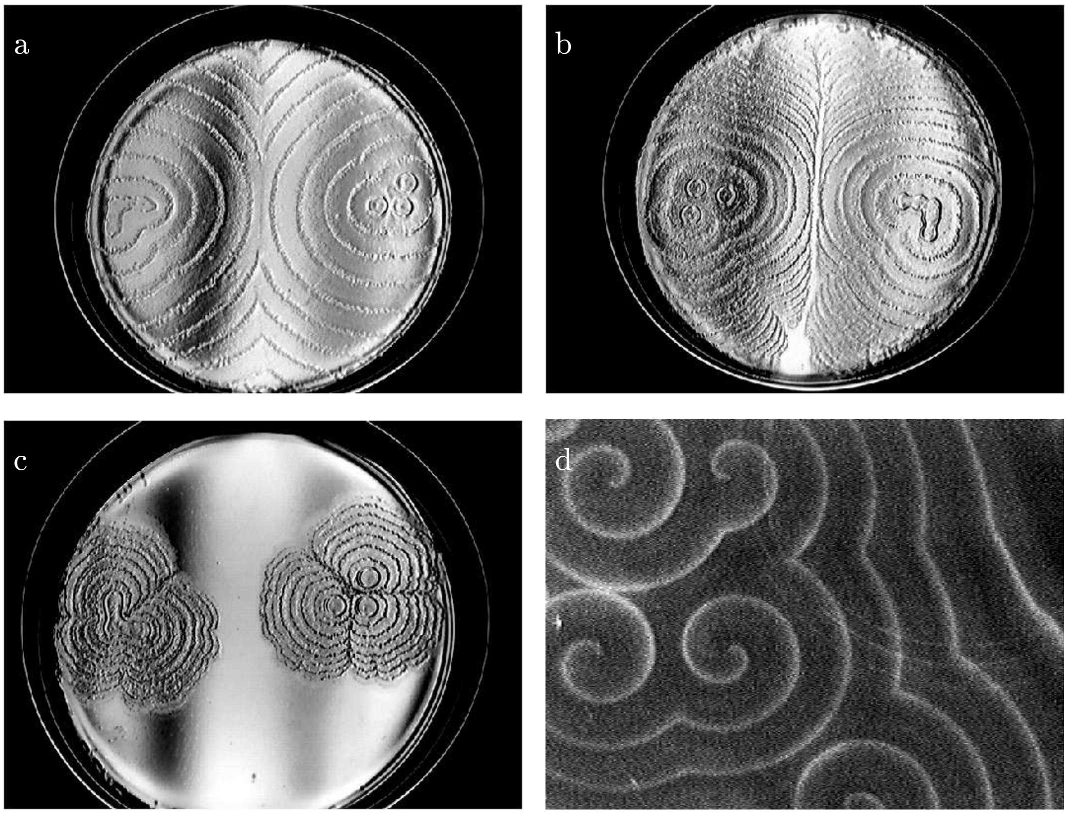

Figure 8.8: Demonstration of changes in front stability as the initial CAA concentration is decreased. On each of the plates bacteria were inoculated in an L-shape and in three spots marking the corners of this L-shape. This way two main colonies are formed, each consisting of three colonies. Depending on the initial CAA concentration, this results in plates with colonies showing regulation towards uniform curvature (a), regulation towards uniform curvature in the first swarming phase only (b) or no regulation towards uniform curvature (c). Note the sterile nutrient depleted cleft which forms between the two main colonies in experiment b. A snapshot from the Belousov-Zhabotinsky reaction is included for comparison: the stable fronts of the interacting spirals show regulation towards uniform curvature (d). All the plates are 2.25% agar with 0.4% glucose but with different concentrations of CAA. (a): 1.6% CAA after 74 h. (b): 0.4% CAA after 74 h. (c): 0.2% CAA after 47 h. The Belousov-Zhabotinsky picture is courtesy of Henrik Skødt at our department. (The size of this picture is roughly 1 cm by 0.7 cm).

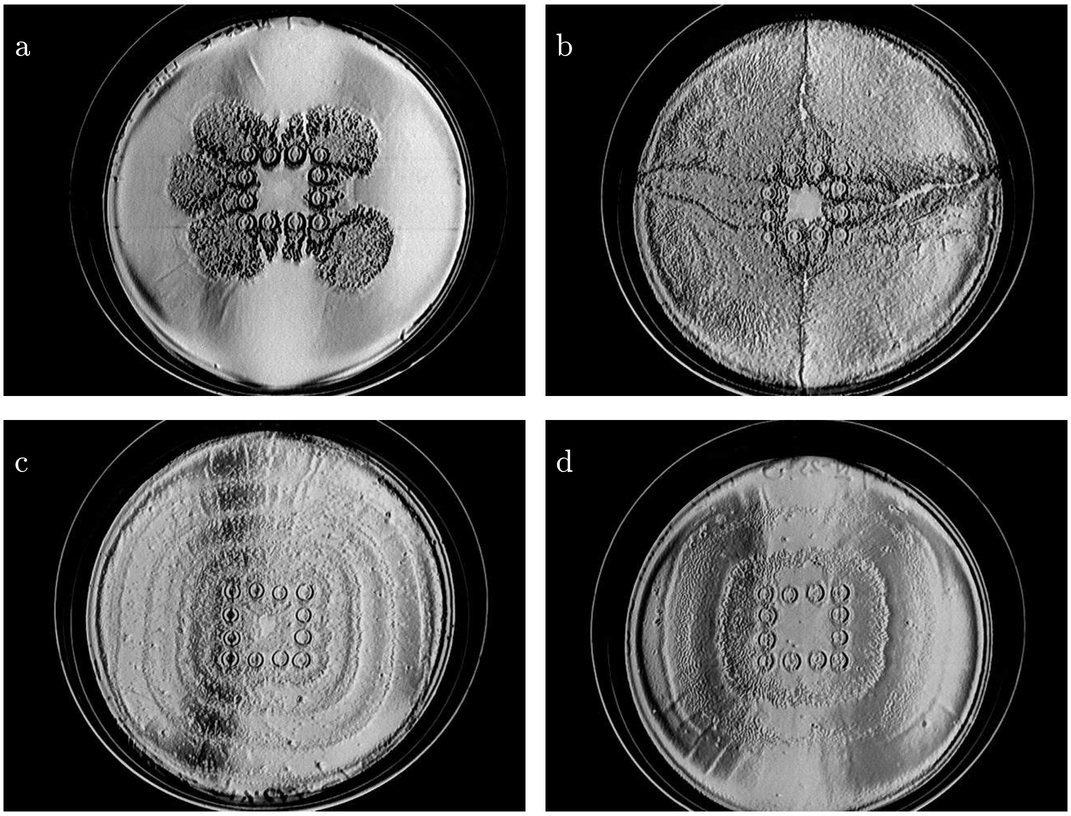

Figure 8.9: A series of square inoculations on PA 1.5% agar plates with 0.4% glucose and increasing CAA concentrations. The bacteria were inoculated in spots along the sides of a 15 mm square. The changing patterns reflect changes in front stability as the CAA concentration is varied. (a): [CAA] = 0.0125%, (b): [CAA] = 0.025%, (c): [CAA] = 0.1%, (d): [CAA] = 0.4%. All pictures are taken after 63 h of inoculation. See text for discussion.

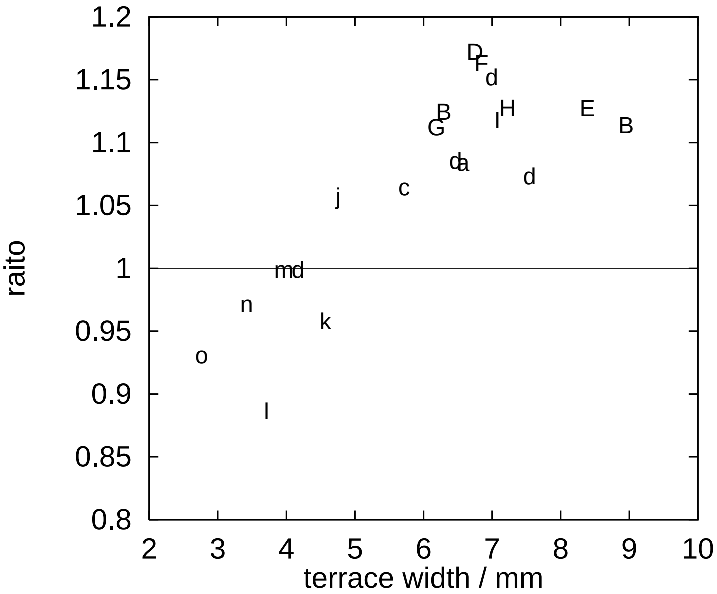

Figure 8.10: Regulation of colony perimeter towards a circular shape as a function of terrace width. As a measure of regulation towards a circular shape, small squares (15 mm on each side) were inoculated, and the ratio $r = v_{\mathrm{side}}/v_{\mathrm{corner}}$ of the expansion velocities at the sides and at the corners were determined. This ratio is plotted against the terrace width (measured at the corners), since this is a measure of the swarming ability on the actual plate. In this way, regulation on many different types of plates can be compared. v_{side} and v_{corner} are preferentially measured as the length of the second swarming phase, since this length is well defined as the distance between the two terrace edges. However, some squares regulate so fast that an almost circular shape is reached within the first swarming phase. Since, in such cases, there will be very little difference between v_{side} and v_{corner} in the second swarming phase, the regulation is instead measured in the first swarming phase. These cases are indicated by capital letters in the figure. Table 8.1 lists the different growth conditions in the experiment.

Another way to test the front stability is to inoculate the bacteria in small squares and note whether this spatial perturbation of the circular symmetry grows or decays. The results of such a series of experiments is shown in figure 8.9. As predicted, the circular geometry of the bacterial front is stable at high concentrations of CAA, but becomes unstable at low CAA concentrations.

In order to quantify the front stability, we carried out a number of these spatial perturbation experiments, and measured the colony expansion during one swarming cycle on the sides of the squares and in the corners (diagonally).

Symbol	Growth conditions
a	1.5% agar, 0.05% CAA
b	1.5% agar, 0.4% CAA
c	2.0% agar, 0.1% CAA
d	2.0% agar, 0.2% CAA
e	2.0% agar, 0.4% CAA
f	2.0% agar, 0.6% CAA
g	2.0% agar, 0.8% CAA
h	2.0% agar, 1.2% CAA
i	2.0% agar, 1.6% CAA
j	2.0% agar, 0.1% CAA + 0.1% glutamine
k	2.0% agar, 0.1% CAA + 0.1% glutamate
l	2.0% agar, 0.1% CAA + 0.04% urea
m	2.0% agar, 0.1% CAA + 0.03% $NH_4Cl^\dagger$
n	2.25% agar, 0.4% CAA
o	2.25% agar, 0.8% CAA

Table 8.1: The different growth conditions in the experiment shown in figure 8.10. All agar plates are PA agar plates with 0.4% glucose. †: In addition to the 0.2% NH_4Cl in the PA medium of all the plates.

From this we compute a metric for front stability:

$$r = \frac{v_{\text{side}}}{v_{\text{corner}}}, \quad r \begin{cases} > 1 & \text{regulation towards uniform curvature: stable front} \\ = 1 & \text{isotropic growth: neutrally stable front} \\ < 1 & \text{diffusion-induced lateral instability: unstable front} \end{cases}$$

This metric expresses the curvature dependence of the front-propagation velocity and thus the ability of the colony to regulate towards a circular shape. Since several factors, including the concentration of CAA and the percentage of agar in the medium, affect the front stability, we found it advantageous to plot the regulatory ability as a function of the actual swarming capacity of the colony. Thus, we plotted the ratio r as a function of the terrace width l_{side}, and we found that a bifurcation from unstable fronts to stable fronts takes place at a front-expansion velocity of about 1 mm/h. (Figure 8.10). Consistent data were obtained from plates where swarming capacity was altered either by changing concentrations of various nutrients or by changing the agar concentration. (Refer to table 8.1 for the actual plate compositions). In agreement with the proposed reaction-diffusion model, this result indicates that front stability is likely to be a function of the swarming capability in general, and not of any specific substance(s).

Like [CAA], the agar content affects the "diffusivity" of the bacteria: the more agar, the more difficult it is for the bacteria to move (Fig. 8.5a). However, changing the hardness of the agar plate is a purely physical affect, so we need not worry about other possible effects. Thus, it should be possible to change a stable front into an unstable front and back again by increasing first the agar content and then subsequently also the [CAA]. This is done in Fig. 8.11.

The reaction-diffusion model makes other testable predictions. By inoculating the bacteria on agar plates with very high CAA contents (1.6%) but no glucose, the swarming ability should be preserved while the autocatalytic growth will be impaired. This reduces the strength of the front stabilising dynamics. At the same time, the strength of the diffusion-induced instabilities are reduced because the very high CAA concentration and the complete absence of glucose prevents the formation of strong nutrient depletion gradients. Since both the stabilising and the destabilising mechanisms are impaired, we expect the resulting bacterial front to have neutral stability. This is seen in figure 8.12a: diffusion-induced instabilities are not seen, but still the inevitable small deviations from circularity are not corrected. The colony pattern changes dramatically when small amounts of glucose (0.1%) are added (Fig. 8.12b). Strong instabilities arise because the low glucose concentration generates diffusion-induced instabilities, while the autocatalytic growth – and hence the front-stabilising force – is still weak because of the low glucose concentration. In line with this explanation, front stability is restored when the glucose concentration is increased further towards the standard concentration of 0.4% (data not shown).

From the above experiments, we conclude that the remarkably simple reaction-diffusion model gives a description of expanding Proteus colonies which is both plausible and applicable. Its usefulness is illustrated by its ability to explain the "shadowing" phenomenon where an expanding Proteus colony does not spread into a zone behind a trench cut out of the agar (Fig. 8.13a; Shapiro and Trubatch (1991)). This effect was eliminated by increasing the CAA concentration in the medium (Fig. 8.13b). These observations can be explained using the reaction-diffusion model: When the expanding colony passes the trench, a large curvature is induced on the front. This slows down the colony expansion into the area behind the trench in analogy to spiral formation by front-breakage in the Belousov-Zhabotinsky reaction. Consequently the nearby

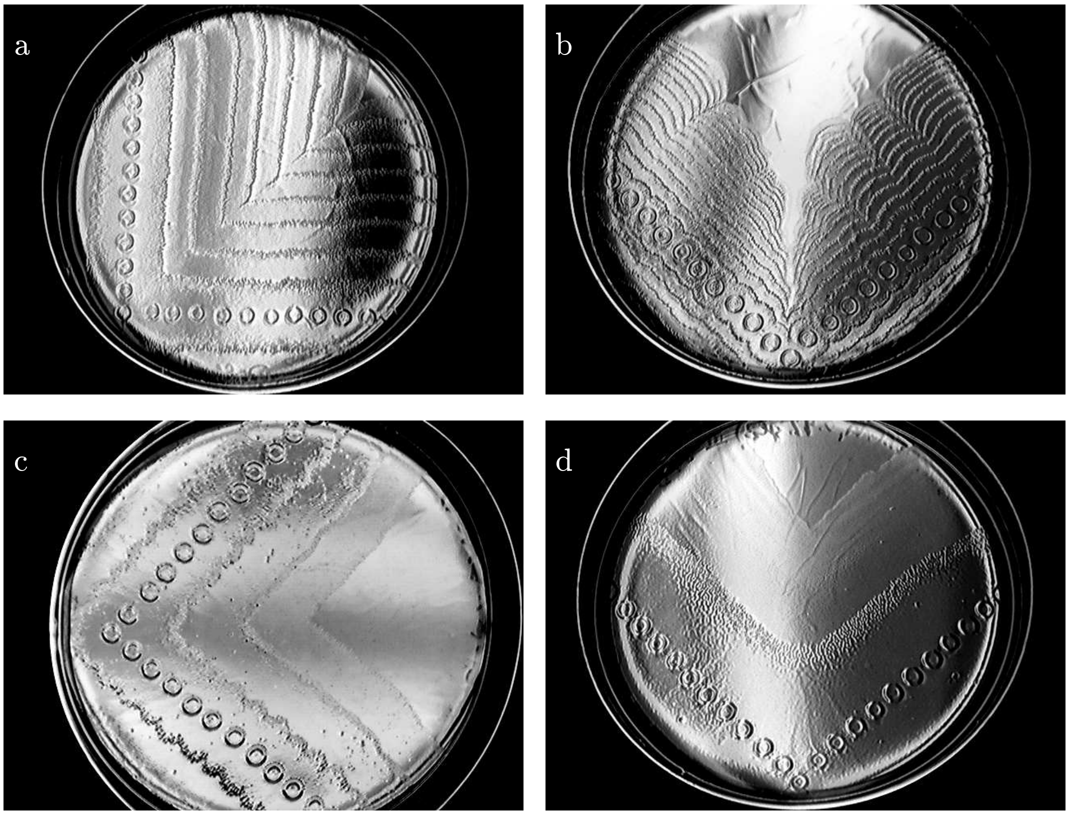

Figure 8.11: High [CAA] compensates for high agar content. The bacteria were inoculated in spots on two straight lines intersecting each other at 90° angle. (a): Standard plate after 42 h of inoculation. (b): The fronts become unstable when the agar content is increased form 2.0% to 2.25% (71 h). (c): Front stability is recovered on the 2.25% agar plates by increasing [CAA] from 0.2% to 0.8% (18 h). (d): On 1.5% agar plates with 0.2% CAA front stability is more pronounced and swarming is faster (17 h). The orientations of the plates are arbitrary.

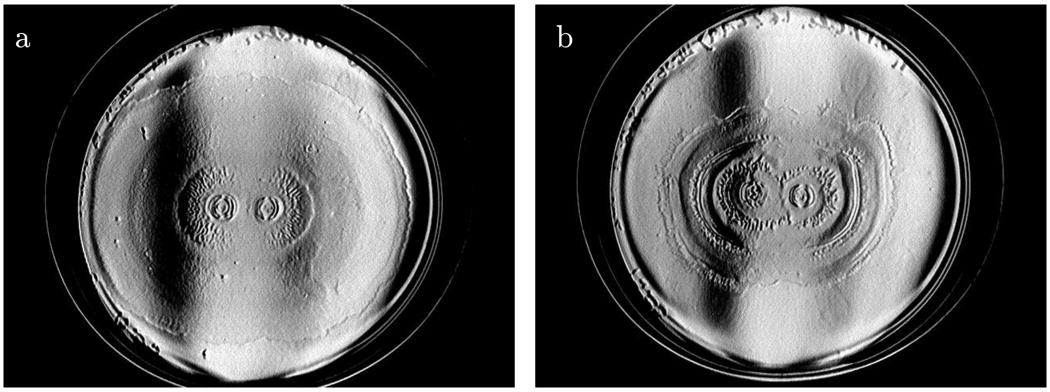

Figure 8.12: The effect of glucose on colony morphology. Two colonies inoculated 1 cm apart on 2% agar plates with high CAA concentration (1.6%) and either no glucose (a) or 0.1% glucose (b). Both plates are photographed after 20 h of inoculation.

colony will deplete this area of amino acids if the initial CAA concentration is not high enough, and the colony will then be unable to expand into this area. Thus, it appears that the trench did not block the diffusion of a swarm-stimulating colony metabolite into the "shadowed" region as previously suggested by Shapiro and Trubatch (1991).

Our explanation of the shadowing phenomenon is supported by the pattern formed by cells that have migrated along the edge of the trench (Fig. 8.13c). These bacteria cannot swarm at all and form tree-like structures reminiscent of the DLA-structures seen when bacteria are grown on plates with extremely low nutrient concentration (Matsushita and Fujikawa, 1990; Matsuyama and Matsushita, 1993; Nakahara *et al.*, 1996; Matsushita, 1997).

8.3 Conclusion

In the experiments presented above, we have shown that the circularity of Proteus colonies results from "active" front stability with a biological basis. It appears that this regulation depends on bacterial motility which results from the cooperative multicellular activity of a particular cell population, as well as on the bacterial growth. Our experiments show that the two main nutrients of the colonies, glucose and CAA, play quite distinct roles in these

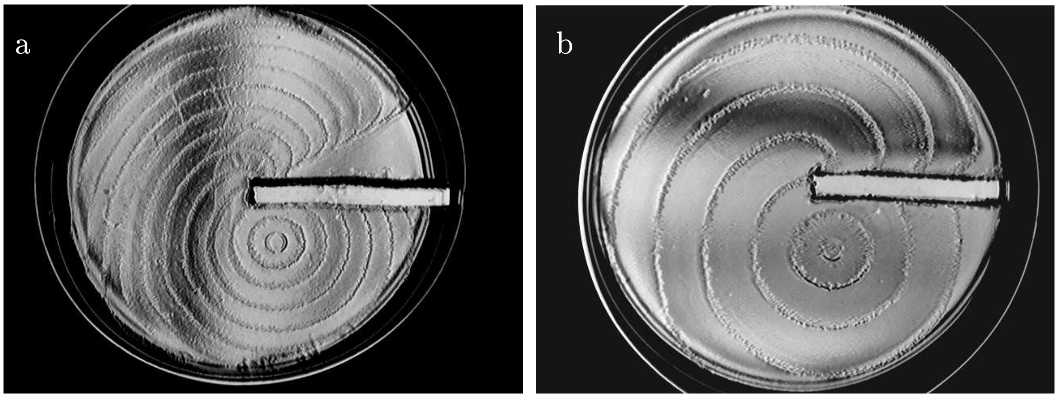

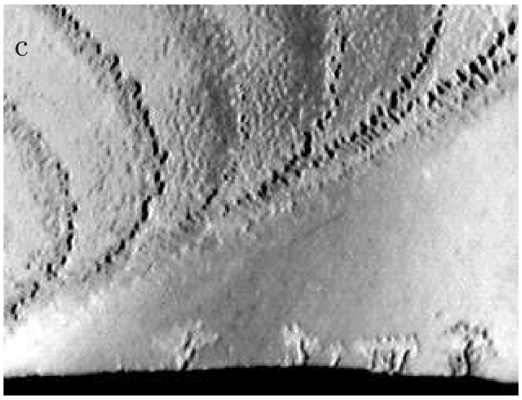

Figure 8.13: Shadowing experiments on plates with different concentrations of CAA. In these experiments, the colony grows out from a single inoculation spot and encounters a trench where a piece of agar is cut out. Both plates are PA 2% agar plates with 0.4% glucose, but with different concentrations of CAA. (a): 0.2% CAA after 210 h of inoculation. (b): 0.8% CAA after 40 h of inoculation. Panel (c) is an enlargement of picture (a) showing DLA-like structures growing from the trench into the shadowed area.

aspects, and their influence on the two different cell types in Proteus colonies are rather different. In particular, we have assigned the functional roles of the two nutrients: glucose promotes cell growth, whereas the swarming ability depends intimately on the availability of an amino acid mixture. This finding could very well apply to other swarming bacteria as well. Since Proteus is a pathogen bacterium causing urinary tract or kidney infections, the observation that amino acids are required for swarming could be of medical importance.

The specific roles of the different nutrients allow us to manipulate the growing colonies in well defined ways. Exploiting these findings, we showed that the qualitative macroscopic dynamics of the expanding colonies are well described by a simple phenomenological model identical to those known from chemical reaction-diffusion systems. That is, the observed changes in stability of the expanding bacterial front are explained without the use of nonlinear density-dependent diffusion or chemotaxis. Despite its simplicity, the model is capable of explaining striking phenomena like the "shadowing" effect (Fig. 8.13a; Shapiro and Trubatch (1991)).

Although they show similar dynamics, the chemical and bacterial systems are very different on the microscopic level. Especially, the bacteria are dense on the surface of the agar, and they possess active, collective motility with complex responses to changes in nutrient availability. This might give rise to phenomena which are not easily explained in the simple reaction-diffusion framework. An obvious example of this is the periodic nature of the Proteus pattern which we have not addressed in this study.

Other bacterial pattern-forming systems involve actively migrating cells; see Medvinsky *et al.* (1993), Shapiro (1995), Woodward *et al.* (1995), Matsushita (1997), Ben-Jacob and Cohen (1997), Kessler and Wojciechowski (1997) or Wakita *et al.* (2001) for examples. It is possible that nutrient-dependent morphology shifts in these systems, such as the transition from circular to dense-branching colonies seen with *Bacillus subtilis*, may be effectively modelled by similar reaction-diffusion systems where the size and directionality of the migrating populations are determined by gradients of specific nutrients.

The detailed understanding of the relations between specific nutrients, bacterial function and the resulting patterns also provides a novel tool for characterising phenotypes of mutants showing swarming defects or altered colony morphology (Williams *et al.*, 1976; Shapiro and Trubatch, 1991; Belas *et al.*, 1991, 1995, 1998; Gygi *et al.*, 1995; Hay *et al.*, 1997, 1999) or the effect of inhibitors of the swarming process (Gram *et al.*, 1996).

A
Abbreviations

This appendix contains an alphabetic listing of the abbreviations used. The list is divided into enzymes, metabolites and miscellaneous.

Enzymes

ADH	alcohol dehydrogenase
AK	adenylate kinase
ALD	aldolase
ENO	enolase
G3PDH	glycerol 3-phosphate dehydrogenase
GAPDH	glyceraldehyde 3-phosphate dehydrogenase
HK	hexokinase
PDC	pyruvate decarboxylase
PFK	phosphofructokinase-1
PFK2	phosphofructokinase-2
PGI	phosphoglucoisomerase
PGK	phosphoglycerate kinase
PGM	phosphoglycerate mutase
PK	pyruvate kinase
TIM	triosephosphate isomerase

Metabolites

2PG	2-phosphoglycerate
ACA	acetaldehyde
ACA_x	extracellular acetaldehyde
ADP	adenosine 5'-diphosphate
AMP	adenosine 5'-monophosphate
ATP	adenosine 5'-triphosphate
DHAP	dihydroxyacetone phosphate
BPG	1,3-bisphosphoglycerate
EtOH	ethanol
$EtOH_x$	extracellular ethanol
F6P	fructose 6-phosphate
F26BP	fructose 2,6-bisphosphate
FBP	fructose 1,6-bisphosphate
G6P	glucose 6-phosphate
GAP	glyceraldehyde 3-phosphate
Glc	glucose
Glc_x	extracellular glucose
Glyc	glycerol
$Glyc_x$	extracellular glycerol
NAD^+	nicotinamide adenine dinucleotide (oxidised form)
NADH	nicotinamide adenine dinucleotide (reduced form)
PEP	phosphoenol pyruvate
Pyr	pyruvate
T6P	trehalose 6-phosphate
UTP	uridine 5'-triphosphate

Miscellaneous

a.u.	arbitrary units
CAA	casamino acid (a mixture of amino acids)
DLA	diffusion-limited aggregation
d.w.	dry weight
CFU	colony forming units
CSTR	continuous-flow stirred tank reactor
FFT	fast Fourier transform

MCA	metabolic control analysis
OD	optical density
ODE	ordinary differential equation
PDE	partial differential equation
TCA cycle	tricarboxylic acid cycle
YNB	yeast nitrogen base

B
Stuart-Landau parameters from perturbation experiments

This appendix describes the fitting of Stuart-Landau parameters to perturbation experiments, as we have previously described it in Danø *et al.* (2000) and Danø *et al.* (2001).

We want to fit the parameters of the Stuart-Landau equation

$$\dot{z} = (i\omega_0 + \mu\sigma)z + gz|z|^2 \tag{B.1}$$

to time traces from perturbation experiments where a small amount of a given substance is added to an oscillating chemical system close to a supercritical Hopf bifurcation. (In this equation, μ and ω_0 are scalars whereas z, σ and g are complex).

For a given operating point μ we can scale the radius of the limit cycle in z space to one without loss of generality; this implies $g' = -\mu\sigma'$. Furthermore, we define $\eta = g''/g'$ and $\omega_{\mathrm{lc}} = \omega_0 + \mu(\sigma'' - \sigma'\eta)$ which is the frequency of oscillations on the limit cycle. By rewriting z in polar coordinates $z = re^{i\theta}$ we get $\dot{z} = \dot{r}e^{i\theta} + i\dot{\theta}re^{i\theta}$, and by inserting $z = re^{i\theta}$ in Eq. B.1 and collecting terms we obtain

$$\begin{aligned} \dot{r} &= \mu\sigma'(1 - r^2)r \\ \dot{\theta} &= \omega_0 + \mu(\sigma'' - \sigma'\eta r^2). \end{aligned} \tag{B.2}$$

Using standard tables of integrals, we can write up the explicit solution to these differential equations:

$$\begin{aligned} r(t) &= \frac{1}{\sqrt{1+(1/r_0^2-1)e^{-2\mu\sigma' t}}} \\ \theta(t) &= \omega_{\mathrm{lc}} t - \frac{\eta}{2}\ln\left(r_0^2 + (1-r_0^2)e^{-2\mu\sigma' t}\right) + \theta_0 \end{aligned} \tag{B.3}$$

where r_0 is the radius at time $t = 0$ and θ_0 is the phase at $t = 0$. We might need to take additional slow modes into account. To lowest order, such modes are described by an amplitude p_i satisfying the amplitude equation $\dot{p}_i = \lambda_i p_i$. If higher orders were to be considered, coupling modes between z and p modes should have been considered as well (Ipsen *et al.*, 2000).

Assuming a linear measuring function and using the transformations from amplitude space (*i.e.* z and p space) to concentration space described in Ipsen *et al.* (1998) we obtain

$$y(t) = y_0 + r(t)\cos(\theta(t)) + ar(t)^2\cos(2\theta(t) + \theta_d) + \sum_i b_i e^{\lambda_i t} \tag{B.4}$$

which can be directly compared to an experimental time trace $y(t)$ scaled so that the amplitude of the limit cycle is 1. The adjustable parameters of the fit come in two classes. The parameters y_0, r_0, θ_0 and b_i specify the initial conditions, whereas the parameters $\mu\sigma'$, ω_{lc}, η, a, θ_d and λ_i describe the dynamics of the system.

We could not resolve the terms arising from the nonlinearity of the transformation from amplitude space to concentration space in our experiments, so we use $a = 0$. Furthermore, we could identify two different, non-oscillatory slow modes, one excited by Glc perturbations and one excited by ACA perturbations. This immediately simplifies Eq. B.4 to

$$y(t) = y_0 + r(t)\cos(\theta(t)) + b_1 e^{\lambda_1 t} + b_2 e^{\lambda_2 t}$$

which was used in the actual fitting of the parameters characterising the dynamic properties of the system: ω_{lc}, $\mu\sigma'$, η, λ_1 and λ_2.

C
Extreme currents from biochemical reasoning

The extreme currents of the model developed in chapter 5 are calculated from the stoichiometric matrix as indicated in chapter 3. However, their form can also be reasoned biochemically as we described in Hynne *et al.* (2001). This argument is reproduced below.

We look at stationary *net velocities, i.e.* for reversible reactions the differences between forward and reverse velocities. We note that the network of reactions shown in Fig. 5.1 has chains of reactions branching like a tree. This structure makes it easy to determine all possible stationary net velocities. These are linear combinations with nonnegative coefficients of suitably normalised net velocities for each of just four definite subpathways, which cannot themselves be expressed similarly in terms of linear combinations of simpler subpathways. They are shown in Fig. C.1. We might call such subpathways "irreducible". The stationary velocities of such networks are the "extreme currents" (Clarke, 1980).

Each subpathway must start with extracellular glucose entering the system, and end with one or more extracellular species leaving the system or with accumulation of glycogen. (We do not require stationarity for glycogen). The possible branchings are limited by the stationarity condition for the conserved pair, NADH and NAD^+. So if a subpathway contains reactions producing NADH, it must also contain other reactions consuming the same number of molecules NADH. The same applies to ATP and ADP, when we take into consideration

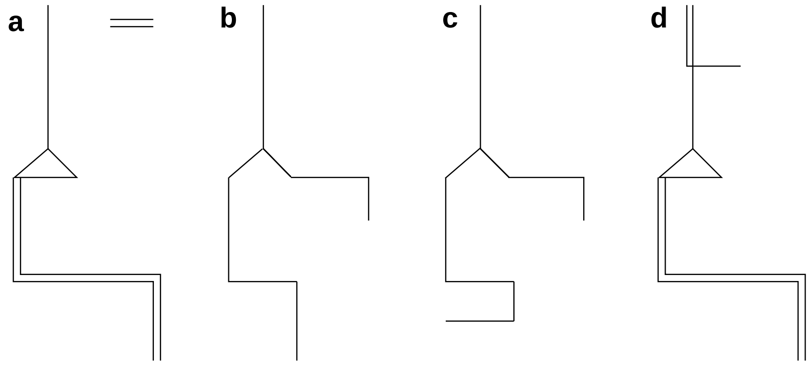

Figure C.1: Schematic representation of the four irreducible subnetworks patterned on Fig. 5.1. (a) glycolysis and fermentation, $\mathbf{E}_{\mathrm{ferm}}$. (b) glycerol production, $\mathbf{E}_{\mathrm{glyc}}$. (c) glycerol production and lactonitrile formation, $\mathbf{E}_{\mathrm{lact}}$. (d) glycolysis, fermentation and glycogen formation, $\mathbf{E}_{\mathrm{stor}}$.

other reactions in the cell external to glycolysis producing ADP from ATP. These reactions are represented by the schematic reaction R23 in the model (and see the discussion of glycogen formation below). Consequently, from the point of view of glycolysis proper, there is the restriction on stationary (sub-) networks that although ATP may be produced, it must not be consumed, and *vice versa* for ADP. For glycolysis plus reaction R23, ATP and ADP together are conserved at stationarity. We include the adenylate kinase reaction, R24, between ATP and AMP for the sake of dynamics. It has net velocity zero at stationarity, so AMP can be ignored as far as stationarity is concerned.

Glycolysis followed by fermentation and outflow of extracellular ethanol can be stationary together with R23, and cannot be expressed as a combination of simpler stationary networks, see Fig. C.1a. The NADH formed in the GAPDH reaction is reoxidized in the ADH reaction. Two molecules of ATP is formed (per molecule Glc), which are used elsewhere in the cell, reaction R23.

If acetaldehyde escapes the cell, it is lost for the last step of fermentation, the reduction to ethanol, and the NADH produced in the GAPDH reaction must be reoxidized elsewhere. Consequently, glycerol must be produced and flow out. So the GAP and DHAP formed together in the ALD reaction proceed along different branches: while GAP is oxidized by NAD^+, DHAP is reduced by NADH, and there is no net production of either NAD^+ or NADH. The extracellular acetaldehyde formed in the branched process just described, can either flow out or react with cyanide to lactonitrile, giving rise to two distinct irreducible subpathway, Figs. C.1b and C.1c. The two molecules of ATP hydrolysed in the upper part of glycolysis are reproduced in the branch from GAP in the lower part.

Finally, we consider glycogen formation via G6P. This reaction cannot occur alone at stationarity because ATP is consumed. The only way this can be compensated is if one molecule glucose is degraded through glycolysis and fermentation (all the way to extracellular ethanol flowing out) for each molecule of glucose that is build into glycogen, see Fig. C.1d. Note that although this subpathway in a sense contains glycolysis with fermentation as a part, it cannot be expressed in simpler terms because the two parts always must take place together in order to maintain stationarity, when glycogen is formed. In summary, the net reactions of these four irreducible subpathways are

$$\begin{array}{lrcl}
\mathbf{E}_{\mathrm{ferm}}: & C_6H_{12}O_6 & \to & 2\,CH_3CH_2OH + 2\,CO_2 \\
\mathbf{E}_{\mathrm{glyc}}: & C_6H_{12}O_6 & \to & CH_3CHO + C_3H_8O_3 + CO_2 \\
\mathbf{E}_{\mathrm{lact}}: & C_6H_{12}O_6 + HCN & \to & CH_3CHOHCN + C_3H_8O_3 + CO_2 \\
\mathbf{E}_{\mathrm{stor}}: & [\mathrm{glycogen}]_n + 2\,C_6H_{12}O_6 & \to & [\mathrm{glycogen}]_{n+1} + 2\,CH_3CH_2OH + 2\,CO_2.
\end{array}$$

Note that each of these subpathways are pH neutral, and that the ratio of produced CO_2 to consumed Glc is 2 for $\mathbf{E}_{\mathrm{ferm}}$ and 1 for the others.

Now we may choose a stationary net velocity vector for each of the four irreducible subpathways (a matter of scaling or "normalisation"), $\mathbf{E}_{\mathrm{ferm}}$, $\mathbf{E}_{\mathrm{glyc}}$, $\mathbf{E}_{\mathrm{lact}}$, and $\mathbf{E}_{\mathrm{stor}}$. Then any stationary net velocity, $\mathbf{w}$, can be expressed as a linear combination with nonnegative coefficients of these four extreme net velocities,

$$\mathbf{w} = \jmath_{\mathrm{ferm}}\,\mathbf{E}_{\mathrm{ferm}} + \jmath_{\mathrm{glyc}}\,\mathbf{E}_{\mathrm{glyc}} + \jmath_{\mathrm{lact}}\,\mathbf{E}_{\mathrm{lact}} + \jmath_{\mathrm{stor}}\,\mathbf{E}_{\mathrm{stor}}.$$

(The indices refer to the irreducible subpathways representing fermentation, glycerol production with outflow of ACA, glycerol production with lactonitrile formation, and storage buildup, respectively).

D
Comments to rate equations

This appendix contains comments to the rate equations given in Table 5.3. It is not intended to give a detailed discussion of the forms of the rate equations and the significance of the parameters. For such information, please see the references given below.

Reactions 1, 14, 17, 19 and 21: mechanical flows

These reactions are purely mechanical flows determined by the pumps of the flow system. k_0 is the specific flow of the reactor, and the factor y_{vol} scales the velocity according to Eq. 5.2.

Reaction 2: glucose transport

We have adopted the rate equation of the glucose transporter with G6P inhibition from Rizzi *et al.* (1996) who obtained their rate expression by fitting kinetic parameters to Glc and G6P transients, caused by addition of a glucose pulse to a growing culture of glucose limited *Saccharomyces cerevisiae.*[1] The question of whether the glucose transporter is in fact inhibited by G6P is unsettled (Azam and Kotyk, 1969; Teusink, 1999). We tested it with and

[1]Note that the lack of symmetry between the rate equations for the forward and reverse reactions is indeed correct; the equation for the reverse reaction is quoted incorrectly in Rizzi *et al.* (1997).

without inhibition and found that the model generally makes a better fit if it is included.

Glucose transport in yeast is very complicated with 20 known glucose transporters, several of which are expressed at the same time. We, however, only model one glucose transporter corresponding to the main glucose transport component. See Smits *et al.* (1996), Reifenberger *et al.* (1997), Teusink *et al.* (1998a), Özcan and Johnston (1999) or page 20 of Teusink (1999).

Reactions 3, 10 and 12: HK, PK and ADH

Initially, the reactions catalysed by HK, PK, and ADH were modelled as ordered bi-bi reactions Cleland (1963), reduced to irreversible form. See also Viola *et al.* (1982) for details of HK kinetics. In the course of the optimization, it turned out that the rate equations for the PK and ADH reactions could be simplified to the forms given in Table 5.3, whereas this was not the case for the HK reaction.

We have neglected some known regulatory effects of HK and PK. For HK, we have left out the inhibition by ATP (see references cited in Larsson *et al.* (2000)), G6P (see Mathews and van Holde (1990)) and T6P (Blazquez *et al.*, 1993), and for PK we have left out the inhibition by ATP and acetyl-CoA and the activation by FBP (Hess *et al.*, 1966; Mathews and van Holde, 1990).

These omissions are made because too little experimental data is available. In particular, extending the model to describe T6P or acetyl-CoA would be very difficult. According to Larsson *et al.* (2000) the ATP inhibition of PK is only marginally effective at the ATP concentrations in our experiments, and the effect of ATP on HK is either not there or too little to be distinguished from the effect of ATP on PFK in their assays. Hess *et al.* (1969) claim that [FBP] does not exert any effect on PK under the conditions observed during glycolytic oscillations.

Reactions 4 and 7: PGI and TIM

These reactions are modelled according to Richter *et al.* (1975). They both have well described enzyme kinetics, and I know of no regulatory effectors of these enzymes. Note that the K_{eq} of TIM is inconsistent with the measurements of metabolite concentrations and metabolic fluxes.

Reaction 5: PFK

PFK is a highly regulated enzyme with numerous allosteric effectors: AMP, ADP, FBP, and F26BP are activators, and ATP and citrate are inhibitors. At high concentrations, FBP is an inhibitor instead of an activator. Apparently, the effects of FBP and F26BP are interdependent, probably due to competition for the same binding site. Kreuzberg (1978) report that fructose and fructose 1-phosphate are activators in low concentrations, whereas they are competitive inhibitors at high concentrations. F26BP is sometimes considered the physiologically most important regulator of glycolysis, because it regulates glycolysis and glyconeogenesis at the same time; often as a response to a second messenger reflecting changes in the environment of the cell. For details about PFK kinetics and regulation see Mathews and van Holde (1990), Teusink *et al.* (2000) or Larsson *et al.* (2000) and references therein.

It is obvious that we cannot include all of these effectors in a sensible way if, at the same time, we want to keep down the number of parameters in the model. (But see the extensive fitting of PFK kinetics in Teusink *et al.* (2000)). We have therefore simply kept the functional form which works well in the extract model by Nielsen *et al*, except that a negligible term of the denominator has been left out. This rate expression includes the cooperative binding of F6P, the inhibition by ATP and the activation by AMP. So considering the above summary of PFK regulation, this rate expression is clearly a simplification. Nevertheless, it is still derived from a mechanistic description (of the Monod type) as described in Termonia and Ross (1981).

The measurements by Richard *et al.* (1996b) show that the level of F26BP is almost constant in oscillating yeast cells, and Yuan *et al.* (1990) report that the metabolite is not an essential part of the oscillations, since the F26BP concentration in oscillating extracts is too low to have any significant effect. Also, they report that oscillations can be seen in mutants with no detectable F26BP. So, at least this omission seems to be justified. According to Teusink, the role of ADP in PFK regulation is much less than that of AMP and ATP, and Betz (1973) arrives at the conclusion that AMP controls PFK . Larsson *et al.* (2000) conclude that the ATP inhibition is evident in their experiments whereas the effects of both AMP and ADP on PFK are insignificant. Thus, it appears that the most important omission in our rate equation is the effect of FBP, but it is unclear what this effect will actually be.

Reaction 6: ALD

Aldolase is described by an ordered uni-bi reaction in which GAP dissociates first (Cleland, 1963; Richter *et al.*, 1975).

Reaction 8: GAPDH

The kinetics of GAPDH are complicated, and the enzyme is also remarkable in that it is found in extremely high concentrations (Hess *et al.*, 1973). NAD^+ and NADH bind cooperatively to GAPDH, but this effect is only significant at $p\mathrm{H} > 7.5$ (Byers, 1982). The rate equation which we use is adopted from Teusink *et al.* (2000).

Reactions 9, 22, 23 and 24: schematic rate equations

The lumped reactions lpPEP, the reaction describing glycogen formation, the AK reaction and the ATP consumption are all modelled by mass action kinetics because this is the simplest form which at the same time is physically realistic (in the sense that the reaction will not proceed if the concentration of one of the substrates goes to zero). During the optimization, we tried to model the general ATPase by irreversible Michaelis-Menten kinetics as advocated by Richter *et al.* (1975), but found this to be of no advantage.

Reaction 11: PDC

Following Nielsen *et al.* (1998), we simply modelled the PDC reaction by irreversible Michaelis-Menten kinetics. At the time of writing this seems an oversimplification (see Boiteux and Hess (1970)).

Reactions 13, 16 and 18: diffusion through the cell membrane

Glycerol, EtOH and ACA diffuse passively through the cell membrane. (However, under certain conditions facilitated glycerol diffusion takes place in yeast (Luyten *et al.*, 1995)). As a first approximation, we can think of the passing of the cell membrane as composed of three steps:

- Transition from the aqueous phase to the lipid phase.
- Diffusion across the membrane.
- Transition from the lipid to the aqueous phase.

If the diffusion of the three water-soluble substances is about equal, which is reasonable here since they are of approximately the same size, then the membrane permeability can be estimated from the partitioning coefficients of the substances. From empirical formulas in Jain and Wagner (1980) the relative permeabilities can be calculated to 13 : 8.8 : 1 (given as ACA : EtOH : Glyc) as also indicated in Table 5.5.

Reaction 15: lpGlyc

We model the kinetics of the glycerol branch by the G3PDH reaction as described by Cai *et al.* (1996).

Reaction 20: lactonitril formation

Cyanide is a nucleophilic reagent in its deprotonated form, and as such it reacts with ACA to form lactonitril:

$$\mathrm{CH_3CHO} + {}^{-}\mathrm{CN} + \mathrm{H^+} \quad \rightarrow \quad \mathrm{CH_3CH(OH)CN}$$

As one could expect, this reaction has bimolecular reaction kinetics (Svirbely and Roth, 1953), and since CN^- is one of the reactive species, the rate constant increases with pH. According to Svirbely and Roth, this reaction is in practice irreversible. The factor y_{vol} scales the velocity as described near Eq. 5.2.

E

CO_2 calculations

This appendix describes the calculations of CO_2 production from pH measurements in the transient yeast oscillation experiments. Apart from water, three proteolysis systems are present in the suspension, namely the hydrocyanic acid, carbonic acid and phosphoric acid systems:

$$
\begin{array}{lcllcr}
\mathrm{HCN} & \rightleftharpoons & \mathrm{H^+ + CN^-}, & pK^{\ominus}_{\mathrm{HCN}} & = & 9.21 \\
\\
\mathrm{H_2CO_3} & \rightleftharpoons & \mathrm{H^+ + HCO_3^-}, & pK^{\ominus}_{\mathrm{H_2CO_3}} & = & 6.35 \\
\mathrm{HCO_3^-} & \rightleftharpoons & \mathrm{H^+ + CO_3^{2-}}, & pK^{\ominus}_{\mathrm{HCO_3^-}} & = & 10.33 \\
\\
\mathrm{H_3PO_4} & \rightleftharpoons & \mathrm{H^+ + H_2PO_4^-}, & pK^{\ominus}_{\mathrm{H_3PO_4}} & = & 2.16 \\
\mathrm{H_2PO_4^-} & \rightleftharpoons & \mathrm{H^+ + HPO_4^{2-}}, & pK^{\ominus}_{\mathrm{H_2PO_4^-}} & = & 7.21 \\
\mathrm{HPO_4^{2-}} & \rightleftharpoons & \mathrm{H^+ + PO_4^{3-}}, & pK^{\ominus}_{\mathrm{HPO_4^{2-}}} & = & 12.32
\end{array}
$$

Dissociation constants are from Lide (1994) p. 8-43; the cited value of $pK^{\ominus}_{\mathrm{H_2CO_3}}$ refers to the sum of $[\mathrm{H_2CO_3(aq)}]$ and $[\mathrm{CO_2(aq)}]$. By assuming equilibrium in these systems, we arrive at the following formulae which express the concentrations of each of the ions in terms of $[\mathrm{H^+}]$, the dissociation constants given above and the conserved moeity sums $c_{\mathrm{A}^{n-}} = \sum_{i=0}^{n}[\mathrm{H}_i\mathrm{A}^{(n-i)-}]$ for each of the three n-prote bases A^{n-}:

$$\begin{aligned}
[CN^-] &= \frac{c_{CN^-} K_{HCN}}{[H^+] + K_{HCN}} \\
[HCO_3^-] &= \frac{c_{CO_3^{2-}} [H^+] K_{H_2CO_3}}{[H^+]^2 + [H^+] K_{H_2CO_3} + K_{H_2CO_3} K_{HCO_3^-}} \\
[CO_3^{2-}] &= \frac{c_{CO_3^{2-}} K_{H_2CO_3} K_{HCO_3^-}}{[H^+]^2 + [H^+] K_{H_2CO_3} + K_{H_2CO_3} K_{HCO_3^-}} \\
[H_2PO_4^-] &= \frac{c_{PO_4^{3-}} [H^+]^2 K_{H_3PO_4}}{[H^+]^3 + [H^+]^2 K_{H_3PO_4} + [H^+] K_{H_3PO_4} K_{H_2PO_4^-} + K_{H_3PO_4} K_{H_2PO_4^-} K_{HPO_4^{2-}}} \\
[HPO_4^{2-}] &= \frac{c_{PO_4^{3-}} [H^+] K_{H_3PO_4} K_{H_2PO_4^-}}{[H^+]^3 + [H^+]^2 K_{H_3PO_4} + [H^+] K_{H_3PO_4} K_{H_2PO_4^-} + K_{H_3PO_4} K_{H_2PO_4^-} K_{HPO_4^{2-}}} \\
[PO_4^{3-}] &= \frac{c_{PO_4^{3-}} K_{H_3PO_4} K_{H_2PO_4^-} K_{HPO_4^{2-}}}{[H^+]^3 + [H^+]^2 K_{H_3PO_4} + [H^+] K_{H_3PO_4} K_{H_2PO_4^-} + K_{H_3PO_4} K_{H_2PO_4^-} K_{HPO_4^{2-}}},
\end{aligned}$$

and in addition we have $[OH^-] = K_w/[H^+]$. With these expressions inserted, the electroneutrality condition

$$0 = [K^+] + [H^+] - [OH^-] - [HCO_3^-] - [H_2PO_4^-] - 2[HPO_4^{2-}]$$

can readily be solved for $c_{CO_3^{2-}}$ when the pH value is known. (The CN^-, CO_3^{2-} and PO_4^{3-} terms have been omitted since their contributions are negligible in the pH range relevant here).

In the calculations, we need to correct for the nonzero ionic strength I of the solution. We do this by correcting the the thermodynamic $pK^{\ominus}$ values with appropriate factors before they are inserted into the equations above. For example, we use $K_{H_2CO_3} = \frac{\gamma_{H_2CO_3}}{\gamma_{H^+}\gamma_{HCO_3^-}} K^{\ominus}_{H_2CO_3} \approx \gamma_1^{-2} K^{\ominus}_{H_2CO_3}$ which we then calculate from the Debye-Hückel equation in the Güntelberg approximation $\log \gamma_i = -A z_i^2 \frac{\sqrt{I}}{1+B\sqrt{I}}$; A=0.509 $M^{\frac{1}{2}}$ and $B = 1$ $M^{\frac{1}{2}}$. For each experiment we first adjust $[K^+]$ as to have zero $c_{CO_3^{2-}}$ before the glucose addition, and then calculate the value of I from the starting pH and the total phosphate concentration. This constant value of I is used in the calculations throughout the dataset, even though it will change slightly as pH changes.

The pH is calculated from the electrode potential E according to $p\text{H}=\frac{E-d_0}{b_1}$ where $b_1 = \ln(10)RT/F$ and d_0 is adjusted to fit the pH of a calibration buffer.

The method should give a reasonable estimate of $c_{CO_3^{2-}}$, but underestimates the amount of CO_2 produced by the yeast cells, since some of the carbonate will leave the solution as gaseous CO_2. The kinetics of such processes can be very complicated, but as a reasonable estimate we can take $v_{\text{degas}} \propto [H_2CO_3]$. We have

$$[H_2CO_3] = \frac{c_{CO_3^{2-}}[H^+]^2}{[H^+]^2 + [H^+]K_{H_2CO_3} + K_{H_2CO_3}K_{HCO_3^-}}$$

so v_{degas} should increase in proportion to the total carbonate concentration and with the square of $[H^+]$. Therefore, it might be feasible to neglect the problem for short transient experiments, but for longer experiments where carbonate accumulates in the solution and pH is significantly reduced, it cannot be ignored. As mentioned, the ionic strength of the solution also changes during the experiment, so the assumption of constant I breaks down as well.

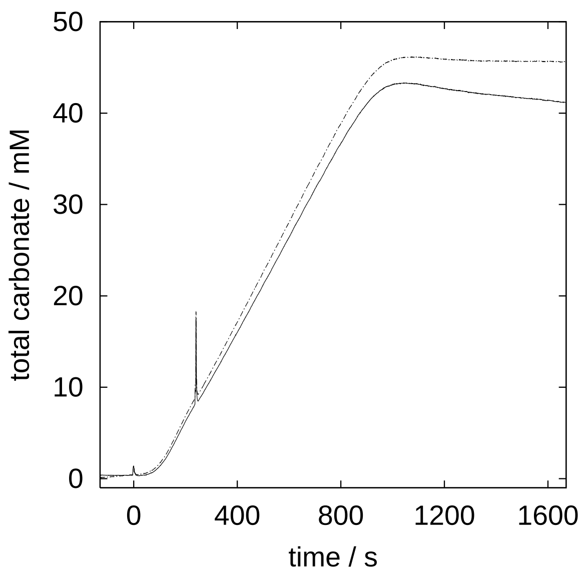

Figure E.1: The effect of degassing in the dataset of Fig. 6.11. The solid line is the actual $c_{CO_3^{2-}}$ of the solution calculated as described in this appendix. The dashed line is the same data, but now with a correction for a constant degassing rate estimated from the last 600 s of the pH recordings. The solid line gives an underestimation of the CO_2 produced by the yeast cells, whereas the dashed line gives an overestimation. In this short experiment (initial [Glc_x =] 20 mM, final pH = 6.5), the error is less than 10%.

We can estimate the importance of the degassing for a given transient experiment by looking at the change in $c_{CO_3^{2-}}$ when the yeast cells have run out of Glc; this will be the maximum degassing rate in the experiment. By making a correction for this (constant) maximum degassing rate throughout the entire experiment, we get an overestimation of the cellular CO_2 production. This can then be compared with the $c_{CO_3^{2-}}$ of the solution, which is an underestimate of the cellular CO_2 production. Such a comparison is made in Fig. E.1.

Bibliography

Albertyn, J., van Tonder, A. & Prior, B. A. (1992), Purification and characterization of glycerol-3-phosphate dehydrogenase of *Saccharomyces cerevisiae*, *FEBS Letters* **308**:130–132.

Allison, C., Lai, H.-C., Gygi, D. & Hughes, C. (1993), Cell differentiation of *Proteus mirabilis* is initiated by glutamine, a specific chemoattractant for swarming cells, *Molecular Microbiology* **8**:53–60.

Allison, C., Lai, H.-C. & Hughes, C. (1992), Co-ordinate expression of virulence genes during swarm-cell differentiation and population migration of *Proteus mirabilis*, *Mol. Microbiol.* **6**:1583–1591.

Aon, M. A., Cortassa, S., Westerhoff, H. V., Berden, J. A., van Spronsen, E. & van Dam, K. (1991), Dynamic regulation of yeast glycolytic oscillations by mitochondrial functions, *Journal of Cell Science* **99**:325–334.

Aronson, D., Ermentrout, G. & Kopell, N. (1990), Amplitude response of coupled oscillators, *Physica D* **41**:403–449.

Arouh, S. (2001), Analytic model for ring pattern formation by bacterial swarmers, *Phys. Rev. E* **63**:031908.

Aust, A., Yun, S.-L. & Suelter, C. H. (1975), Pyruvate Kinase from Yeast (*Saccharomyces cerevisiae*), *Methods Enzymol.* **42**:176–182.

Azam, F. & Kotyk, A. (1969), Glucose-6-phosphate as regulator of monosaccharide transport in baker's yeast, *FEBS Letters* **2**:333–335.

Babul, J., Clifton, D., Kretschmer, M. & Fraenkel, D. G. (1993), glucose Metabolism in *Escherichia coli* and the Effect of Increased Amount of Aldolase, *Biochemistry* **32**:4685–4692.

Barnard, E. A. (1975), Hexokinases from Yeast, *Methods Enzymol.* **42**:6–20.

Barwell, C. J. & Hess, B. (1972), Application of Kinetics of yeast Pyruvate Kinase in vitro to Calculation of Glycolytic Flux in the Anaerobic Yeast Cell, *Hoppe-Seyler's Z. Physiol. Chem.* **353**:1178–1184.

Becker, J.-U. & Betz, A. (1972), Membrane Transport as Controlling Pacemaker of Glycolysis in *Saccharomyces Carlsbergensis*, *Biochim. Biophys. Acta* **274**:584–597.

Belas, R., Erskine, D. & Flaherty, D. (1991), *Proteus mirabilis* Mutants Defective in Swarmer Cell Differentiation and Multicellular Behavior, *J. Bact.* **173**:6279–6288.

Belas, R., M., G. & K., A. (1995), Genetic Analysis of *Proteus mirabilis* Mutants Defective in Swarmer Cell Elongation, *J. Bact.* **177**:823–828.

Belas, R., Schneider, R. & Melch, M. (1998), Characterization of *Proteus mirabilis* precocious swarming mutants: identification of rsbA, encoding a regulator of swarming behavior, *J. Bact.* **180**:6126–6139.

Ben-Jacob, E. & Cohen, I. (1997), Cooperative Formation of Bacterial Patterns, in Shapiro, J. A. & Dworkin, M. (eds.), *Bacteria as Multicellular Organisms*, chap. 14, pp. 394–416, Oxford University Press.

Benevolensky, S. V., Clifton, D. & Fraenkel, D. G. (1994), The Effect of Increased Phosphoglucose Isomerase on Glucose Metabolism in *Saccharomyces cerevisiae*, *J. Biol. Chem.* **269**:4878–4882.

Bernasconi, C. (1976), *Relaxation Kinetics*, Academic Press.

Betz, A. (1973), Kinetics of Yeast Phosphofructokinase and the glycolytic oscillator, in Chance, B., Pye, E. K., Ghosh, A. & Hess, B. (eds.), *Biological and Biochemical Oscillators*, pp. 221–228, Academic Press, New York.

Betz, A. & Chance, B. (1965a), Influence of Inhibitors and Temperature on the Oscillations of Reduced Pyridine Nucleotides in Yeast Cells, *Arch. Biochem. Biophys.* **109**:579–584.

Betz, A. & Chance, B. (1965b), Phase Relationship of Glycolytic in Yeast Cells with Oscillatory Metabolic Control, *Arch. Biochem. Biophys.* **109**:585–594.

Betz, A. & Hinrichs, R. (1968), Incorporation of Glucose into an Insoluble Polyglycoside during Oscillatory Controlled Glycolysis in Yeast Cells, *Eur. J. Biochem.* **5**:154–157.

Bier, M., Bakker, B. & Westerhoff, H. (2000), How yeast cells synchronize their glycolytic oscillations: a perturbation analytic treatment, *Biophys. J.* **78**:1087–1093.

Bier, M., Teusink, B., Kholodenko, B. N. & Westerhoff, H. V. (1996), Control analysis of glycolytic oscillations, *Biophysical Chemistry* **62**:15–24.

Blazquez, M. A., Langunas, R., Gancedo, C. & Gancedo, J. M. (1993), Trehalose-6-phosphate, a new regulator of yeast glycolysis that inhibits hexokinases, *FEBS Lett.* **329**:51–54.

Boiteux, A. & Hess, B. (1970), Allosteric properties of yeast pyruvate decarboxylate, *FEBS Lett.* **9**:293–296.

Boiteux, A. & Hess, B. (1974), Oscillations in Glycolysis, Cellular Respiration and Communication, *Faraday Symp. Chem. Soc.* **9**:202–214.

BRENDA (2000), On-line database at http://www.brenda.uni-koeln.de.

Byers, L. D. (1982), Glyceraldehyde-3-phosphate Dehydrogenase from Yeast, *Methods Enzymol.* **89**:326–335.

Cai, J., Pietzsch, M., Theobald, U. & Rizzi, M. (1996), Fast purification and kinetic studies of the glycerol-3-phosphate dehydrogenase from yeast *Saccharomyces cerevisiae*, *Journal of Biotechnology* **49**:19–27.

Chance, B., Estabrook, R. W. & Ghosh, A. (1964), Damped Sinusoidal Oscillations of Cytoplasmic Reduced Pyridine Nucleotide in Yeast Cells, *Biochemistry* **51**:1244–1251.

Chance, B., Williamson, G., Lee, I. Y., Mela, L., DeVault, D., Ghosh, A. & Pye, E. K. (1973), Synchronization Phenomena in Oscillations of Yeast Cells and Isolated Mitochondria, in Chance, B., Pye, E. K., Ghosh, A. & Hess, B. (eds.), *Biological and Biochemical Oscillators*, pp. 285–300, Academic Press, New York.

Chevalier, T., Schreiber, I. & Ross, J. (1993), Towards a Systematic Determination of Complex Reaction Mechanisms, *J. Phys. Chem.* **97**:6776–6787.

Chou, H.-F., Berman, N. & Ipp, E. (1992), Oscillations of lactate released from islets of Langerhans: evidence for oscillatory glycolysis in β-cells, *Am. J. Physiol.* **262**:E800–E805.

Civelek, V. N., Deeney, J. T., Fusonie, G. E., Corkey, B. E. & Tornheim, K. (1997), Oscillations in Oxygen Consumption by Permeabilized Clonal Pancreatic β-Cells (HIT) Incubated in an Oscillatory Glycolyzing Muscle Extract. Roles of Free Ca^{2+}, Substrates, and the ATP/ADP Ratio, *Diabetes* **46**:51–56.

Civelek, V. N., Deeney, J. T., Shalosky, N. J., Tornheim, K., Hansford, R. G., Prentki, M. & Corkey, B. E. (1996), Regulation of pancreatic β-cell mitochondrial metabolism: influence of Ca^{2+}, substrate and ADP, *Biochem. J.* **318**:615–621.

Clarke, B. L. (1980), *Stability of complex reaction networks*, vol. 43 of *Adv. Chem. Phys.*, pp. 1–215, Wiley, New York.

Cleland, W. (1963), The kinetics of enzyme-catalyzed reactions with two or more substrates or products, *Biochim. Biophys. Acta* **67**:104–137.

Cohen, S. D. & Hindmarsh, A. C. (1994), CVODE, http://www.netlib.org/.

Crane, R. K. (1962), Hexokinases and Pentokinases, in Boyer, P. D., Lardy, H. & Myrbäck, K. (eds.), *The Enzymes*, vol. 6, pp. 47–66, Academic Press, New York, 2nd edn.

Crawford, J. (1995), Scaling and Singularities in the Entrainment of Globally Coupled Oscillators, *Phys. Rev. Lett.* **74**:4341–4344.

Cunningham, B. A., Deeney, J. T., Bliss, C. R., Corkey, B. E. & Thornheim, K. (1996), Glucose-induced oscillatory insulin secretion in perifused rat pancreatic islets and clonal β-cells (HIT), *Am. J. Physiol.* **271**:E702–E710.

Czirók, A., Matsushita, M. & Vicsek, T. (2001), Theory of periodic swarming of bacteria: Application to *Proteus mirabilis*, *Phys. Rev. E* **63**:031915.

Daido, H. (1994), Generic Scaling at the Onset of Macroscopic Mutual Entrainment in Limit-Cycle Oscillators with Uniform All-to-All Coupling, *Phys. Rev. Lett.* **73**:760–763.

Danø, S., Hynne, F. & Sørensen, P. (2000), Dynamics of Yeast Cell Populations, in *Physical Chemistry 2000*, pp. 12–19, Belgrade, Yugoslavia, http://theochem.ki.ku.dk/˜sdd/.

Danø, S. (1999), Glycolytic Oscillations in Yeast Cells, University of Copenhagen, http://theochem.ki.ku.dk/~sdd/.

Danø, S., Hynne, F., De Monte, S., d'Ovidio, F., Sørensen, P. G. & Westerhoff, H. (2001), Synchronization of glycolytic oscillations in a yeast cell population, *Faraday Discuss.* **120**:261–276.

Danø, S., Sørensen, P. G. & Hynne, F. (1999), Sustained oscillations in living cells, *Nature* **402**:320–322.

De Koning, W. & van Dam, K. (1992), A Method for the Determination of Changes of Glycolytic Metabolites in Yeast on a Subsecond Timescale Using Extraction at Neutral pH, *Anal. Biochem.* **204**:118–123.

De Monte, S. & d'Ovidio, F. (2002), Dynamics of order parameters for globally coupled oscillators, *Europhys. Lett.* **58**:21–27.

Dickenson, C. J. & Dickinson, F. M. (1976), Some Properties of an Alcohol Dehydrogenase Partially Purified from Baker's Yeast Grown without Added Zinc, *Biochem. J.* **153**:309–319.

Dickinson, F. M. & Monger, G. P. (1973), A Study of the Kinetics and Mechanism of Yeast Alcohol Dehydrogenase with a Variety of Substrates, *Biochem. J.* **131**:261–270.

d'Ovidio, F. (2002), *Modelling biological systems with coupled oscillators*, Ph.D. thesis, Technical University of Denmark.

Dujon, B. (1996), The yeast genome project: What did we learn?, *Trends in Genet.* **12**:263–270.

Duysens, L. N. M. & Amesz, J. (1957), Fluorescence spectrophotometry of reduced phosphopyridine nucleotides in intact cells in the near-ultraviolet and visible region, *Biochim. Biophys. Acta* **24**:19–26.

Eberl, L., Molin, S. & Givskov, M. (1999), Surface Motility of *Serratia liquefaciens* MG1, *Journal of Bacteriology* **181**:1703–1712.

Enzyme handbook (1969), Springer, New York.

Esipov, S. E. & Shapiro, J. A. (1998), Kinetic model of *Proteus mirabilis* swarm colony development, *Journal of Mathematical Biology* **36**:249–268.

Fell, D. (1997), *Understanding the Control of Metabolism*, Portland Press, London.

Fernández, R., Herrero, P. & Moreno, F. (1985), Inhibition and Inactivation of Glucose-phosphorylating Enzymes from *Saccharomyces cerevisiae* by D-Xylose, *J. Gen. Microbiol.* **131**:2705–2709.

Frenkel, R. (1968a), Control of Reduced Diphosphopyridine Nucleotide Oscillations in Beef Heart Extracts. I. Effects of Modifiers of Phosphofructokinase Activity, *Arch. Biochem. Biophys.* **125**:151–156.

Frenkel, R. (1968b), Control of Reduced Diphosphopyridine Nucleotide Oscillations in Beef Heart Extracts. II. Oscillations of Glycolytic Intermediates and Adenine Nucleotides, *Arch. Biochem. Biophys.* **125**:157–165.

Frenkel, R. (1968c), Control of Reduced Diphosphopyridine Nucleotide Oscillations in Beef Heart Extracts. III. Purification and Kinetics of Beef Heart Phosphofructokinase, *Arch. Biochem. Biophys.* **125**:166–174.

Ganzhorn, A. J., Green, D. W., Hershey, A. D., Gould, R. M. & Plapp, B. V. (1987), Kinetic Characterization of Yeast Dehydrogenases, *J. Biol. Chem.* **262**:3754–3761.

Ghosh, A. & Chance, B. (1964), Oscillations of Glycolytic Intermediates in Yeast Cells, *Biochem. Biophys. Res. Commun.* **16**:174–181.

Ghosh, A. K., Chance, B. & Pye, E. K. (1971), Metabolic Coupling and Synchronization of NADH Oscillations in Yeast Cell Populations, *Arch. Biochem. Biophys.* **145**:319–331.

Goffeau, A., Barrell, B. G., Bussey, H., Davis, R. W., Dujon, B., Feldmann, H., Galibert, F., Hoheisel, J. D., Jacq, C., Johnston, M., Louis, E. J., Mewes, H. W., Y., Y. M., Philippsen, P., Tettelin, H. & Oliver, S. G. (1996), Life with 6000 genes, *Science* **274**:546, 563–567.

Goldberg, R. N. (1999), Thermodynamics of Enzyme-Catalysed Reactions: Part 6 – 1999 Update, *J. Phys. Chem. Ref. Data* **28**:931–965.

Goldberg, R. N. & Tewari, Y. B. (1995a), Thermodynamics of Enzyme-Catalysed Reactions: Part 4. Lyases, *J. Phys. Chem. Ref. Data* **24**:1669–1698.

Goldberg, R. N. & Tewari, Y. B. (1995b), Thermodynamics of Enzyme-Catalysed Reactions: Part 5. Isomerases and Ligases, *J. Phys. Chem. Ref. Data* **24**:1765–1801.

Goldberg, R. N., Tewari, Y. B., Bell, D., Fazio, K. & Anderson, J. (1993), Thermodynamics of Enzyme-Catalysed Reactions: Part 1. Oxidoreductases, *J. Phys. Chem. Ref. Data* **22**:515–582.

Goldbeter, A. (1996), *Biochemical Oscillations and Cellular Rhythms*, Cambridge University Press, Cambridge.

Gram, L., de Nys, R., Maximilien, R., Givskov, M., Steinberg, P. & Kjelleberg, S. (1996), Inhibitory Effects of Secondary Metabolites from the Red Alga *Delisea pulchra* on Swarming Motility of *Proteus mirabilis*, *Applied and Environmental Microbiology* **62**:4284–4287.

Guckenheimer, J. & Holmes, P. (1983), *Nonlinear Oscillations, Dynamical Systems, and Bifurcations of Vector Fields*, Springer-Verlag, New York.

Gygi, D., bailey, M. J., Allison, C. & Hughes, C. (1995), Requirement for FlhA in flagella assembly and swarm-cell differentiation by *Proteus mirabilis*, *Mol. Microbiol.* **15**:761–769.

Hakim, V. & Rappel, W.-J. (1992), Dynamics of the globally coupled complex Ginzburg-Landau equation, *Phys. Rev. A* **46**:7347–7350.

Hale, J. & Kocak, H. (1991), *Dynamics and Bifurcations*, Springer-Verlag, New York.

Hay, N. A., Tipper, D. J., Gygi, D. & C., H. (1997), A Nonswarming Mutant of *Proteus mirabilis* lacks the Lrp Global Transcriptional Regulater, *J. Bact.* **179**:4741–4746.

Hay, N. A., Tipper, D. J., Gygi, D. & Hughes, C. (1999), A Novel Membrane Protein Influencing Cell Shape and Multicellular Swarming of *Proteus mirabilis*, *Journal of Bacteriology* **181**:2008–2016.

Hess, B. (1979), The Glycolytic Oscillator, *J. Exp. Biol.* **81**:7–14.

Hess, B. & Boiteux, A. (1968), Mechanism of Glycolytic Oscillation in Yeast, I, *Hoppe-Seyler's Z. Physiol. Chem.* **349**:1567–1574.

Hess, B. & Boiteux, A. (1971), Oscillatory Phenomena in Biochemistry, *Annual Review of Biochemistry* **40**:237–258.

Hess, B. & Boiteux, A. (1973), Substrate Control of Glycolytic Oscillations, in Chance, B., Pye, E. K., Ghosh, A. & Hess, B. (eds.), *Biological and Biochemical Oscillators*, pp. 229–241, Academic Press, New York.

Hess, B., Boiteux, A. & Krüger, J. (1969), Cooperation of Glycolytic Enzymes, *Adv. Enzyme Regul.* **7**:149–167.

Hess, B., Haeckel, R. & Brand, K. (1966), FDP-Activation of Yeast Pyruvate Kinase, *Biochem. and Biophys. Res. Commun.* **24**:824–831.

Hess, B., Kleinhans, H. & Kuschmitz, D. (1973), Component Structure of Oscillating Glycolysis, in Chance, B., Pye, E. K., Ghosh, A. & Hess, B. (eds.), *Biological and Biochemical Oscillators*, pp. 253–267, Academic Press, New York.

Higgins, J. (1964), A chemical mechanism for oscillation of glycolytic intermediates in yeast cells, *Proc. Nat. Acad. Sci.* **51**:989–994.

Hocker, C. G., Epstein, I. R., Kustin, K. & Tornheim, K. (1994), Glycolytic pH oscillations in a flow reactor, *Biophys. Chem.* **51**:21–35.

Horváth, D., Petrov, V., Scott, S. K. & Showalter, K. (1993), Instabilities in propagating reaction-diffusion fronts, *J. Chem. Phys.* **98**:6332–6343.

Hunding, A. (1974), Limit-Cycles in Enzyme-Systems with Nonlinear Negative Feedback, *Biophys. Struct. Mechanism* **1**:47–54.

Hynne, F., Danø, S. & Sørensen, P. (2003), A functional dynamics approach to modelling of glycolysis, in Deutsch, A., Falcke, M., Howard, J. & Zimmermann, W. (eds.), *Function and regulation of cellular systems: experiments and models*, Birkhauser, Basel, http://theochem.ki.ku.dk/˜sdd/.

Hynne, F., Danø, S. & Sørensen, P. G. (2001), Full-scale model of glycolysis in *Saccharomyces cerevisiae*, *Biophys. Chem.* **94**:121–163.

Hynne, F., Sørensen, P. G. & Møller, T. (1993a), Complete optimization of models of the Belousov-Zhabotinsky reaction at a Hopf bifurcation, *J. Chem. Phys.* **98**:219–230.

Hynne, F., Sørensen, P. G. & Møller, T. (1993b), Current and eigenvector analyses of chemical reaction networks at Hopf bifurcations, *J. Chem. Phys.* **98**:211–218.

Hynne, F., Sørensen, P. G. & Nielsen, K. (1990), Quenching of chemical oscillations: General theory, *J. Chem. Phys.* **92**:1747–1757.

Ipsen, M. (1996), *Amplitude Equations and Normal Forms*, Ph.D. thesis, University of Copenhagen.

Ipsen, M., Hynne, F. & Sørensen, P. (2000), Amplitude equations for reaction-diffusion systems with a Hopf bifurcation and slow real modes, *Physica D* **136**:66–92.

Ipsen, M., Hynne, F. & Sørensen, P. G. (1998), Systematic derivation of amplitude equations and normal forms for dynamical systems, *Chaos* **8**:834–852.

Itoh, H., Wakita, J., Matsuyama, T. & Matsushita, M. (1999), Periodic Pattern Formation of bacterial Colonies, *Journal of the Physical Society of Japan* **68**:1436–1443.

Jain, M. K. & Wagner, R. C. (1980), *Introduction to Biological Membranes*, Wiley.

Jones, H. E. & Park, R. W. A. (1967a), The Influence of Medium Composition on the Growth and Swarming of Proteus, *J. gen. Microbiol.* **47**:369–378.

Jones, H. E. & Park, R. W. A. (1967b), The Short Forms and the Long Forms of Proteus, *J. gen. Microbiol.* **47**:359–367.

Kessler, J. & Wojciechowski, M. (1997), Collective Behavior and Dynamics of Swimming Bacteria, in Shapiro, J. A. & Dworkin, M. (eds.), *Bacteria as Multicellular Organisms*, chap. 15, pp. 417–450, Oxford University Press.

Kohout, M., Schreiber, I. & Kubíèek, M. (2002), A computational tool for nonlinear dynamical and bifurcation analysis of chemical engineerig problems, *Comput. Chem. Eng.* **26**:517–527.

Kopetzki, E. & Entian, K.-D. (1985), Glucose repression and hexokinase isoenzymes in yeast, *Eur. J. Biochem.* **146**:657–662.

Kotyk, A. (1967), Mobility of the Free and of the Loaded Monosaccharide Carrier in *Saccharomyces cerevisiae*, *Biochim. Biophys. Acta* **135**:112–119.

Kreuzberg, K. (1978), Interaction of D-Fructose and Fructose 1-Phosphate with Yeast Phosphofructokinase and its Influence on Glycolytic Oscillations, *Biochem. Biophys. Acta* **527**:229–238.

Kreuzberg, K. H. & Betz, A. (1979), Amplitude and Period Length of Yeast NADH Oscillations Fermenting on Different Sugars in Dependence of Growth Phase, Starvation and Hexose Concentration, *J. interdiscipl. Cycle Res.* **10**:41–50.

Krietsch, W. K. G. (1975), Triosephosphate Isomerase from Yeast, *Methods Enzymol.* **41B**:434–438.

Kuramoto, Y. (1975), *Self-entrainment of a populaiton of coupled non-linear oscillators*, vol. 39 of *Lecture Notes in Physics*, pp. 420–422, Springer-Verlag, New York.

Kuramoto, Y. (1984), *Chemical Oscillations Waves and Turbulence*, Springer-Verlag, Berlin.

Larsson, C., Påhlman, I. & Gustafsson, L. (2000), The importance of ATP as a regulator of glycolytic flux in *Saccharomyces cerevisiae*, *Yeast* **16**:797–809.

Lide, D. R. (ed.) (1994), *CRC Handbook of Chemistry and Physics*, CRC Press, 75th edn.

Lorenzen, T. (1996), *Elaborated quenching analysis of the* $Ru(bipy)_3^{2+}$ *catalyzed Belousov Zhabotinsky reaction*, Master's thesis, University of Copenhagen.

Luyten, K., Albertyn, J., Skibbe, W. F., Prior, B. A., Ramos, J., Thevelein, J. M. & Hohmann, S. (1995), *Fps1*, a yeast member of the *MIP* family of channel proteins is a facilitator of glycerol uptake and efflux and is inactive under osmotic stress, *EMBO Journal* **14**:1360–1371.

Marynissen, G., Sener, A. & Malaisse, W. J. (1992), Oscillations in glycolysis: multifactorial quantitative analysis in the muscle extract, *Molecular and Cellular Biochemistry* **113**:105–121.

Mathews, C. K. & van Holde, K. E. (1990), *Biochemistry*, The Benjamin/Cummings Publishing Company, Redwood City.

Matsushita, M. (1997), Formation of Colony Patterns by a Bacterial Cell Population, in Shapiro, J. A. & Dworkin, M. (eds.), *Bacteria as Multicellular Organisms*, chap. 13, pp. 366–393, Oxford University Press.

Matsushita, M. & Fujikawa, H. (1990), Diffusion-limited bacterial colony growth, *Physica A* **168**:498–506.

Matsuyama, T. & Matsushita, M. (1993), Fractal Morphogenesis by a Bacterial Cell Population, *Critical Reviews in Microbiology* **19**:117–135.

Matsuyama, T., Takagi, Y., Nakagawa, Y., Itoh, H., Wakita, J. & Matsushita, M. (2000), Dynamic Aspects of the Structured Cell Population in a Swarming Colony of *Proteus mirabilis*, *J. Bact.* **182**:385–393.

Matthews, P. & Strogatz, S. (1990), Phase Diagram for the Collective Behaviour of Limit-Cycle Oscillators, *Phys. Rev. Lett.* **65**:1701–1704.

Matthews, P. C., Mirollo, R. E. & Strogatz, S. H. (1991), Dynamics of a large system of coupled nonlinear oscillators, *Physica D* **52**:293–331.

Medvedev, G. S., Kaper, T. J. & Kopell, N. (2000), A reaction-diffusion system with periodic front dynamics, *Siam J. Appl. Math.* **60**:1601–1638.

Medvinsky, A. B., Tsyganov, M. A., Kutyshenko, V. P., Shakhbazian, V. Y., Kresteva, I. B. & Ivanitsky, G. R. (1993), Instability of waves formed by motile bacteria, *FEMS Microbiology Letters* **112**:287–290.

Mihaliuk, E., Skødt, H., Hynne, F., Sørensen, P. G. & Showalter, K. (1999), Normal modes for chemical reactions from time series analysis, *J. Phys. Chem.* **103**:8246–8251.

Nakahara, A., Shimada, Y., Wakita, J., Matsushita, M. & Matsuyama, T. (1996), Morphological Diversity of the Colony Produced by Bacteria *Proteus mirabilis*, *Journal of the Physical Society of Japan* **65**:2700–2706.

Nieder, M. & Shapiro, J. (1975), Physiological Function of the *Pseudomonas putida* PpG6 (*Pseudomonas oleovorans*) Alkane Hydroxylase: Monoterminal Oxidation of Alkanes and Fatty Acids, *J. Bact.* **122**:93–98.

Nielsen, K., Sørensen, P. G., Hynne, F. & Busse, H.-G. (1998), Sustained oscillations in glycolysis: an experimental and theoretical study of chaotic and complex periodic behavior and of quenching of simple oscillations, *Biophysical Chemistry* **72**:49–62.

Nilsson, T., Schultz, V., Berggren, P.-O., Corkey, B. E. & Tornheim, K. (1996), Temporal patterns of changes in ATP/ADP ratio, glucose 6-phosphate and cytoplasmic free Ca^{2+} in glucose-stimulated pancreatic β-cells, *Biochem. J.* **314**:91–94.

O'Rourke, B., Ramza, B. M. & Marban, E. (1994), Oscillations of Membrane Current and Excitability Driven by Metabolic Oscillations in Heart Cells, *Science* **265**:962–966.

O'Rourke, B., Ramza, B. M., Romashko, D. N. & Marban, E. (1995), Metabolic Oscillations in Heart Cells, *Adv. Exp. Med. Biol.* **382**:165–174.

Ovádi, J. & Srere, P. A. (1996), Metabolic Consequences of Enzyme Interactions, *Cell Biochem. Funct.* **14**:249–258.

Perko, L. (1996), *Differential Equations and Dynamical Systems*, Springer-Verlag, New York, 2nd edn.

Petty, H. R., Worth, R. G. & Kinzelskii, A. L. (2000), Imaging Sustained Dissipative Patterns in the Metabolism of Individual Living Cells, *Phys. Rev. Lett.* **84**:2754–2757.

Prentki, M. (1996), New insights into pancreatic β-cell metabolic signaling in insulin secretion, *Eur. J. Endocrinol.* **134**:272–286.

Press, W. H., Flannery, B. P., Teukolsky, S. A. & Vetterling, W. T. (1989), *Numerical Recipes in Pascal*, Cambridge University Press, Cambridge.

Pye, E. K. (1969), Biochemical mechanisms underlying the metabolic oscillations in yeast, *Can. J. Botany* **47**:271–285.

Rauprich, O., Matsushita, M., Weijer, C. J., Siegert, F., Esipov, S. E. & Shapiro, J. A. (1996), Periodic Phenomena in *Proteus mirabilis* Swarm Colony Development, *Journal of Bacteriology* **178**:6525–6538.

Reddy, D., Sen, A. & Johnston, G. (1999), Time delay effects on coupled limit cycle oscillators at Hopf bifurcation, *Physica D* **129**:15–34.

Reifenberger, E., Boles, E. & Ciriacy, M. (1997), Kinetic characterization of individual hexose transporters of *Saccharomyces cerevisiae* and their relation to the triggering mechanism of glucose repression, *Eur. J. Biochem.* **245**:324–333.

Reijenga, K., Snoep, J., Diderich, J., van Verseveld, H., Westerhoff, H. & Teusink, B. (2001), Control of Glycolytic Dynamics by Hexose Transport in *Saccharomyces cerevisiae*, *Biophys. J.* **80**:626–634.

Reijenga, K., Westerhoff, H., Kholodenko, B. & Snoep, J. (2002), Control Analysis for Autonomously Oscillating Biochemical Networks, *Biophys. J.* **82**:99–108.

Richard, P., Bakker, B. M., Teusink, B., van Dam, K. & Westerhoff, H. V. (1996a), Acetaldehyde mediates the synchronization of sustained glycolytic oscillations in populations of yeast cells, *Eur. J. Biochem.* **235**:238–241.

Richard, P., Diderich, J. A., Bakker, B. M., Teusink, B., van Dam, K. & Westerhoff, H. V. (1994), Yeast cells with a specific cellular make-up and an environment that removes acetaldehyde are prone to sustained glycolytic oscillations, *FEBS Letters* **341**:223–226.

Richard, P., Teusink, B., Hemker, M. B., van Dam, K. & Westerhoff, H. V. (1996b), Sustained Oscillations in Free-energy State and Hexose Phosphates in Yeast, *Yeast* **12**:731–740.

Richard, P., Teusink, B., Westerhoff, H. V. & van Dam, K. (1993), Around the growth phase transition *S. cerevisiae*'s make-up favours sustained oscillations of intracellular metabolites, *FEBS Letters* **318**:80–82.

Richter, O., Betz, A. & Giersch, C. (1975), The Response of Oscillating glycolysis to Pertubations in the NADH/NAD System: A Comparison Between Experiments and a Computer Model, *BioSystems* **7**:137–146.

Rizzi, M., Baltes, M., Theobald, U. & Reuss, M. (1997), In Vivo Analysis of Metabolic Dynamics in *Saccharomyces cerevisiae*: II. Mathematical Model, *Biothechnology and Bioengineering* **55**:592–608.

Rizzi, M., Theobald, U., Querfurth, E., Rohrhirsch, T., Baltes, M. & Reuss, M. (1996), In Vivo Investigations of Glucose Transport in *Saccharomyces cerevisiae*, *Biothechnology and Bioengineering* **49**:316–327.

Roberts, A. (1997), Low-dimensional modelling of dynamical systems, Tech. rep., University of Southern Queensland, Australia.

Robinson, D. S. (1964), Oxidation of selected alkanes and related compounds by a *Pseudomonas* strain, *Antonie van Leeuwenhoek* **30**:303–316.

Rodríguez, Y., Torralba, A. & Montero, F. (2002), Periodic Signal Transduction through Metabolic Pathways with Michelian Kinetics, *J. Phys. Chem. B* **106**:5536–5542.

Schmidt, J. (2000), *A quantitative description of glycolysis by normal forms*, Master's thesis, University of Copenhagen, http://theochem.ki.ku.dk/ cats/library.html.

Sel'kov, E. E. (1968), Self-oscillations in glycolysis. A simple kinetic model, *Eur. J. Biochem.* **4**:79–86.

Shapiro, J. (1985), *ASM News* **51**:62–69.

Shapiro, J. A. (1995), The significances of bacterial colony patterns, *BioEssays* **17**:597–607.

Shapiro, J. A. & Trubatch, D. (1991), Sequential events in bacterial colony morphogenesis, *Physica D* **49**:214–223.

Siegel, G., Malmsten, M., Klüssendorf, D. & Hofer, H.-W. (1997), Vascular Smooth Muscle, a Multiply Feedback-Coupled System of High Versality, Modulation and Cell-Signaling Variability, *Int. J. Microcirc.* **17**:360–373.

Smits, H.-P., Smits, G. J., postma, P. W., Walsh, M. C. & van Dam, K. (1996), High-affinity Glucose Uptake in *Saccharomyces cerevisiae* is not Dependent on the Presence of Glucose-Phosphorylating Enzymes, *Yeast* **12**:439–447.

Sørensen, P. G. (1999), Chem, a program package for parsing, integration and continuation of chemical reaction dynamics.

Strogatz, S. H. (1993), *Norbert Wiener's Brain Waves*, vol. 100 of *Lecture Notes in Biomathematics*, Springer-Verlag.

Strogatz, S. H. (1994), *Nonlinear Dynamics and Chaos*, Addison Wesley, Reading, MA.

Sturdza, S. (1973), Sur la tendance des cultures envahissantes de *Proteus* à adopter des formes arrondes, *Arch. Roum. Path. Exp. Microbiol.* **32**:63–69.

Sturdza, S. A. (1975), Expansionserscheinungen der Proteuskulturen. I. Die Schwärmexpansion, *Zbl. Bakt. Hyg., I. Abt. Orig. A* **233**:505–530.

Svirbely, W. J. & Roth, J. F. (1953), Carbonyl Reactions. I. The Kinetics of Cyanohydrin Formation in Aqueous Solution, *J. Am. Chem. Soc.* **75**:3106–3111.

Termonia, Y. & Ross, J. (1981), Oscillations and control features in glycolysis: Numerical analysis of a comprehensive model, *Proc. Natl. Acad. Sci. USA* **78**:2952–2956.

Teusink, B. (1999), *Exposing a complex metabolic system: glycolysis in* Saccharomyces cerevisiae, Ph.D. thesis, University of Amsterdam.

Teusink, B., Bakker, B. & Westerhoff, H. V. (1996a), Control of frequency and amplitude is shared by all enzymes in three models for yeast glycolytic oscillations, *Biochem. Biophys. Acta* **1275**:204–212.

Teusink, B., Diderich, J., Westerhoff, H. V., van Dam, K. & Walsh, M. C. (1998a), Intracellular Glucose in Derepressed Yeast Cells Consuming Glucose Is High Enough To Reduce the Glucose Transport Rate by 50%, *J. Bact.* **180**:556–562.

Teusink, B., Larsson, C., Diderich, J., Richard, P., van Dam, K., Gustafsson, L. & Westerhoff, H. V. (1996b), Synchronized Heat Flux Oscillations in Yeast Cell Populations, *J. Biol. Chem.* **271**:24442–24448.

Teusink, B., Passarge, J., Reijenga, C. A., Esgalhado, E., van der Weijden, C. C., Schepper, M., Walsh, M. C., Bakker, B. M., van Dam, K., Westerhoff, H. V. & Snoep, J. L. (2000), Can yeast glycolysis be understood in terms of *in vitro* kinetics of the constituent enzymes? Testing biochemistry, *Eur. J. Biochem.* **267**:5313–5329.

Teusink, B., Walsh, M. C., van Dam, K. & Westerhoff, H. V. (1998b), The danger of metabolic pathways with turbo design, *TIBS* **23**:162–164.

Tornheim, K. (1988), Fructose 2,6-Bisphosphate and Glycolytic Oscillations in Skeletal Muscle Extracts, *J. Biol. Chem.* **263**:2619–2624.

Tornheim, K., Andrés, V. & Schultz, V. (1991), Modulation by Citrate of Glycolytic Oscillations in Skeletal Muscle Extracts, *J. Biol. Chem.* **266**:15675–15678.

Tornheim, K. & Lowenstein, J. M. (1974), The Purine Nucleotide Cycle. IV. Interactions with oscillations of the glycolytic pathway in muscle extracts, *J. Biol. Chem.* **249**:3241–3247.

Tornheim, K. & Lowenstein, J. M. (1975), The Purine Nucleotide Cycle. Control of phosphofructokinase and glycolytic oscillations in muscle extracts, *J. Biol. Chem.* **250**:6304–6314.

Vicsek, T. (1992), *Fractal growth phenomena*, World Scientific, Singapore.

Viola, R. E., Raushel, F. H., Rendina, A. R. & Cleland, W. W. (1982), Substrate synergism and the kinetic mechanism of yeast hexokinase, *Biochemistry* **21**:1295–1302.

de Vries, G., Sherman, A. & Zhu, H.-R. (1998), Diffusively Coupled Bursters: Effects of Cell Heterogeneity, *Bulletin of Mathematical Biology* **60**:1167–1200.

Wakita, J., Shimada, H., Itoh, H., T., M. & M., M. (2001), Periodic Colony Formation by Bacterial Species *Bacillus subtilis*, *Journal of the Physical Society of Japan* **70**:911–919.

Wiggins, S. (1990), *Introduction to Applied Nonlinear Dynamical Systems and Chaos*, Springer-Verlag, New York.

Wilkinson, J. H. & Reinsch, C. (1971), *Handbook for automatic computation*, Springer, New York.

Williams, F. D., Anderson, D. M., Hoffman, P. S., Schwarzhoff, R. H. & Leonard, S. (1976), Evidence Against the Involvement of Chemotaxis in Swarming of *Proteus mirabilis*, *J. Bact.* **127**:237–248.

Winfree, A. T. (1967), Biological Rhythms and the Behavior of Populations of Coupled Oscillators, *J. Theor. Biol.* **16**:15–42.

Winfree, A. T. (1972), Oscillatory Glycolysis in Yeast: The Pattern of Phase Resetting by Oxygen, *Arch. Biochem. Biophys.* **149**:388–401.

Winfree, A. T. (1980), *The Geometry of Biological Time*, Springer-Verlag, New York.

Wolf, J. & Heinrich, R. (1997), Dynamics of two-component biochemical systems in interacting cells; Synchronization and desynchronization of oscillations and multiple steady states, *BioSystems* **43**:1–24.

Wolf, J. & Heinrich, R. (2000), Effect of cellular interaction on glycolytic oscillations in yeast: a theoretical investigation, *Biochem. J.* **345**:321–334.

Wolf, J., Passarge, J., Somsen, O. J. G., Snoep, J. L., Heinrich, R. & Westerhoff, H. V. (2000), Transduction of Intracellular and Intercellular Dynamics in Yeast Glycolytic Oscillations, *Biophysical Journal* **78**:1145–1153.

Woodward, D. E., Tyson, R., Myerscough, M. R., Murray, J. D., Budrene, E. O. & Berg, H. C. (1995), Spatio-Temporal Patterns Generated by *Salmonella typhimurium*, *Biophysical Journal* **68**:2181–2189.

Wurster, B. & Schneider, F. (1970), Kinetik der Glucosephosphat-Isomerase (EC 5.3.1.9) aus Hefe in vitro und ihre Anwendung auf Flußberechnungen durch die Gärungskette der anaeroben Hefezelle, *Hoppe-Seyler's Z. Physiol. Chem.* **351**:961–966.

Yaney, C. G., Schultz, V., Cunningham, B. A., Dunaway, G. A., Corkey, B. E. & Tornheim, K. (1995), Phosphofructokinase Isozymes in Pancreatic Islets and Clonal β-Cells (INS-1), *Diabetes* **44**:1285–1289.

Yuan, Z., Medina, M. A., Boiteux, A., Müller, S. & Hess, B. (1990), The role of fructose 2,6-bisphosphate in glycolytic oscillations in extracts and cells of *Saccharomyces cerevisiae*, *Eur. J. Biochem.* **192**:791–795.

Özcan, S. & Johnston, M. (1999), Function and Regulation of Yeast Hexose Transporters, *Microbiol. Mol. Biol. Rev.* **63**:554–569.